School of Science

Self-assembly of amphiphiles for the modular formation of catalysts and sensors

Chloe Zhijun Ren

A Thesis Submitted to

Auckland University of Technology

in Fulfilment of the Requirements for the Degree of

Doctor of Philosophy

December 2022

Abstract

This thesis describes a new strategy for the formation and optimisation of cooperative catalysts utilising reversible hydrophobic interactions. This involves the self-assembly of pre-catalyst amphiphiles into vesicular structures, where the catalytically active head groups are brought into close proximity to work in a synergistic manner. These proof-of-concept studies focused on the combination of two pre-catalyst amphiphiles, C_{16}TACN **20** and C_{16}Gua **23**. The two amphiphiles were self-assembled in 20% DMSO solution, resulting in a significant enhancement in the rate of hydroxypropyl *p*-nitrophenyl phosphate (**HPNPP**) cleavage. One of the key advantages of this self-assembled system is its modular nature, which allows the catalyst to be rapidly optimized by changing the composition of the self-assembled system. We were able to demonstrate this concept by modifying the ratio of C_{16}TACN **20** to C_{16}Gua **23**, arriving at an optimised system consisting of two C_{16}Gua **23** units for every single C_{16}TACN **20** unit.

To gain insight into the self-assembly process and the composition of the vesicular structures formed in situ, we synthesised fluorescent analogues of our pre-catalytic amphiphiles C_{16}TACN **20** and C_{16}Gua **23**. The idea was that changes in FRET intensity could be used to follow the self-assembly of different amphiphiles, and allow insight into the dynamic changes that occur when additional amphiphiles are added in situ. During investigation of the fluorescent properties of the fluoro-amphiphiles, we observed that C_{12}-I-Coum-TACN **54** demonstrated unexpected turn-on fluorescence in the presence of Zn^{2+} and dimethyl phosphate. We propose that the turn-on fluorescence is due to the triple interplay between photoinduced electron transfer (PET), chelation-enhanced fluorescence (CHEF) and aggregation induced emission (AIE) effects. Control studies demonstrated the importance of self-assembly for the observed properties, as the shorter chain analogues did not display significant enhancement of fluorescence upon the addition of dimethyl phosphate. We show that C_{12}-I-Coum-TACN **54** possesses high selectivity for dimethyl phosphate over ATP and pyrophosphate, which is highly unusual given the higher charge density of the latter polyatomic anions. Most literature

examples of phosphate sensors target the detection of ATP and pyrophosphate, and therefore we believe our unique observations could lead to the development of sensors selective for dialkyl phosphates, which have applications for the detection of pesticides.

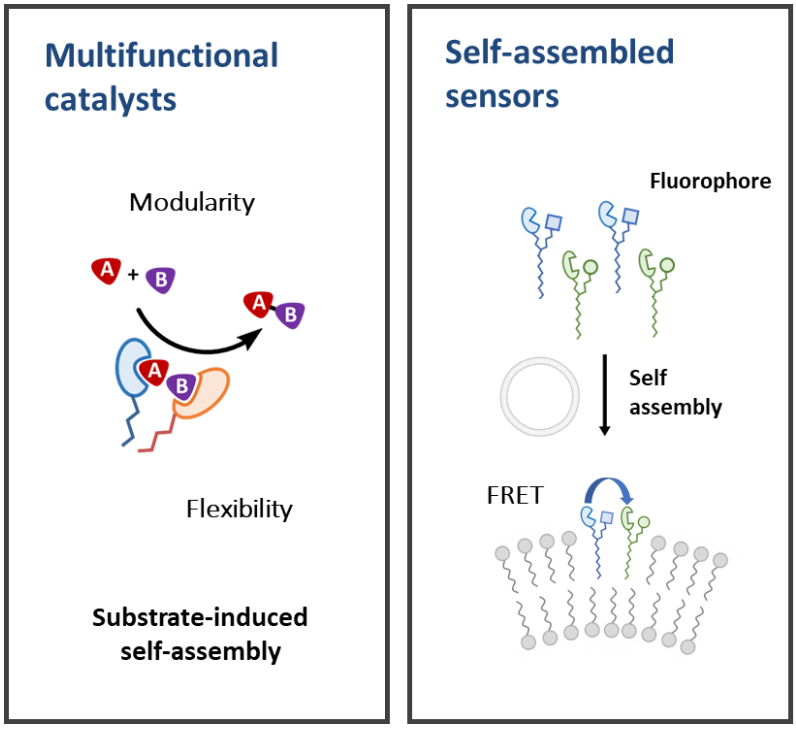

Acknowledgments

First and foremost, I would like to express my gratitude to my supervisor, Dr Jack L.-Y. Chen, for the opportunity to join his research group and for introducing me to such interesting and complicated projects. Throughout my Ph.D. journey, his infinite help and guidance led me in the right direction for my research. I can always get the motivation to be a better chemist and a better person from his enthusiasm and optimism in chemistry and in life. Thanks for the endless support and warm encouragement on my “lost and bad” days. He gave me the assurance that I was not alone on my tough journey since I knew that he was always available to have valuable discussions whenever I needed them. Thanks to Professor Allan Blackman for the endless support whenever I need.

I am grateful to Dr Cassandra Fleming for the kind discussions about organic synthesis and the fluorescence studies in my project, also for releasing my anxiety during my stressful days with her Ph.D. stories and for playing music to build a relaxing lab atmosphere. I want to thank Professor Leonard Prins and his team for providing me one-month research opportunity to gain experience in his lab at Padova University. Also, thanks to Professor Gregory G. Warr for his professional ideas and suggestions in SAXS and SANS experiments, and for the collaboration of a publication with good quality. I would also like to thank Dr Andrew Whitten from ANSTO for the technical help and data analysis for SANS during our visits to the Australia centre for neutron scattering in Sydney. Thanks to Dr Mark Johnstone for bringing interesting reaction mechanisms to the group meetings.

I would also want to express my thanks to Auckland University and Technology for giving me the opportunity to study here and awarding me the Vice Chancellor’s Doctoral Scholarship for the financial support during my stay in New Zealand. I want to thank the University and the Faculty for allowing me to use the facilities and the working spaces, and also for giving me the Covid scholarship extension and the enrolment to finalize my research and the thesis. Thanks

to the New Zealand Institute of Chemistry and the MacDiarmid Institute for providing my student membership and the valuable workshops and conferences.

I would also like to thank the past and present members of the Chen group, especially Adam Chopdat who trained me with all the lab techniques when I was an undergraduate in the lab five years ago, Pablo Solís-Muñana who accompanied me in the daily working routine and the trips to Italy and Australia, also for the warm discussions about the research, and Bryan Andres Tiban for bringing fun and energy to me anytime and anywhere. Thanks to Giada Arena and Mohinder Naiya for their valuable help and company whenever I needed them. Thanks to Bhanu Lokesh, Joanne Salam, and all of the group members for their company in the lab. Thanks to Dora, Bronte, Jess, Anau, Cameron, Franko, and Vinay for their friendships. All of you are wonderful colleagues in the lab, and I am so grateful for all of your friendships in my daily life.

Last but not least, I am so grateful to my family and my friends. 慈母爱子，非为报也，感谢父母的谆谆教诲，让我读万卷书，行万里路。感谢父母倾尽一生的爱护和付出，让我没有后顾之忧的追求自我理想和自我价值。我想感谢我的挚友们，你们给我带来了欢笑和陪伴，在我辛苦低落时的一句安慰和一个拥抱给了我坚持下去的勇气和决心。Thanks to my special one for the love.

感谢所有我爱的人们和爱我的人们，是你们给了我力量和信心去历经风雨，终见彩虹！

Thank you all! I could not finalize the tough Ph.D. journey without the help and encouragement from all of you.

Table of Contents

Abbreviations

δ	chemical shift
°C	degree Celsius
µ	micro
µL	microliter
µM	micromolar
γ-CD	γ-cyclodextrin
λ_{em}	emission wavelength
λ_{ex}	excitation wavelength
A	adenine
AcOH	acetic acid
ADP	adenosine diphosphate
AIE	aggregation induced enhancement
ApA	adenylyl(3'→5')phosphoadenine
Asp	aspartic acid
ATP	adenosine triphosphate
a.u.	arbitrary unit
AuNPs	gold nanoparticles
Boc	*tert*-butyloxycarbonyl
$(Boc)_2O$	di-tert-butyl dicarbonate
BPNPP	bis(*p*-nitrophenyl) phosphate
br s	broad singlet
Brij S2	polyethylene glycol octadecyl ether
C	cytosine
CAC	critical aggregation concentration
CAPS	*N*-cyclohexyl-3-aminopropanesulfonic acid
CAPSO	3-(cyclohexylamino)-2-hydroxy-1-propanesulfonic acid
Cbz	carbobenzoxy group

CD_3OD	deuterium methanol
CHES	*N*-cyclohexyl-2-aminoethanesulfonic acid
CHEF	chelation enhanced fluorescence effect
CMC	critical micelle concentration
Coum	coumarin
cP	cyclic phosphate
C_{pp}	critical packing factor
cryo-TEM	cryo-transmission electron microscope
CTAB	hexadecyltrimethylammonium bromide
Cys	cysteine
d	doublet
DBF	dibenzofulvene
DBU	1,8-diazacyclo[5.4.0]undec-7-ene
DCC	N,N′-dicyclohexylcarbodiimide
DCL	dynamic combinatorial library
dd	doublet of doublets
DET	diethylenetriammonium
DFT	density function theory
DOPC	1,2-dioleoyl-sn-glycero-3-phosphocholine
DPA	3,5-bis[(bispyridin-2-ylmethylamino)methyl]-4-hydroxyphenyl
DPH	1,6-diphenyl-1,3,5-hexatriene
DPPC	dipalmitoylphosphatidylcholine
dt	doublet of triplets
DIAD	diisopropyl azodicarboxylate
DIPA	*N*,*N*-diisopropylaminoethanol
DIPEA	*N*,*N*-diisopropylethylamine
DLS	dynamic light scattering
DMAP	4-dimethylaminopyridine
DMF	dimethylformamide

DMP	dimethyl phosphate
DMSO	dimethyl sulfoxide
DNA	deoxyribonucleic acid
DNPP	2,4-dinitrophenyl phosphate
DPA	di-2-picolyamine
EDC·HCl	*N*,*N*-diisopropylethylamine hydrochloride
E_m	emission
EM	electron microscopy
ER	endoplasmic reticulum
et al.	and others
EtOAc	ethyl acetate
EtOH	ethanol
eq.	equivalent(s)
E_x	excitation
FAM	carboxylfluorescein
FI	fluorescence intensity
FRET	fluorescence resonance energy transfer
Fmoc	Fluorenylmethyloxycarbonyl
g	gram
G	guanine
Gu	guanidine
GUVs	giant unilamellar vesicles
Glu	glutamic acid
h	hour(s)
HEPES	2-[4-(2-hydroxyethyl)piperazin-1-yl]ethanesulfonic acid
His	histidine
HoBt	hydroxybenzotriazole
HOMO	highest occupied molecular obital
HPNPP	2-hydroxypropyl *p*-nitrophenyl phosphate

HRESIMS	high resolution electrospray ionisation mass spectrometry
Hz	hertz
ICT	intramolecular charge transfer
IFE	inner filter effect
IR	infrared
J	coupling constant
LDA	linear discrimination analysis
LUVs	large unilamellar vesicles
m	multiplet
M	molar
Me	methyl group
MeCN	acetonitrile
MeOH	methanol
MES	2-(*N*-morpholino)ethanesulfonic acid
mg	milligram(s)
min	minute(s)
mM	millimole(s)
mmol	millimole(s)
MOFs	metal-organic frameworks
mQ water	milli-Q water
m/z	mass to charge ratio
NI	napthalimide fluorophore
nm	nanometer
NMR	nuclear magnetic resonance
NTA	nitrilotriacetic acid
$OPPh_3$	triphenyl phosphine oxide
PAP	purple acid phosphatase
PCA	principal component analysis
Pd/C	palladium on carbon

PET	photoinduced energy transfer
PMA	phosphomolybdic acid
PNP	*p*-nitrophenolate
Ph_7C_7H	*syn*-heptaphenylcycloheptatriene
PPh_3	triphenylphosphine
ppm	parts per million
q	quarte
R	unspecified alkyl group
R_0	Förster distance
R_f	retention factor
RNA	ribonucleic acid
RT	room temperature
s	singlet
SANS	small angle neutron scattering
SDS	sodium dodecyl sulfate
Ser	serine
t	triplet
T	thymine
TACN	1,4,7-triazacyclononane
THF	tetrahydrofuran
TLC	Thin Layer Chromatography
TMR	tetramethylrhodamine
Trp	tryptophan
TSA	transition state analogue
UV-Vis	ultraviolet-visible
UpNP	uridine-3'-*p*-nitrophenylphosphate
wt.%	percentage weight

List of Figures

from ref. 26. Copyright (2016) Nature Publishing Group.

Figure 12. Schematic illustration of a liposome and a micelle.

Figure 13. Schematic illustration of the aggregation progresses involved in micelle formation

Figure 14. Nanoreactors for organic reactions in water. Reprinted with permission from ref. 35. Copyright (2019) Nature Publishing Group.

Figure 15. Breslow's cyclodexdrin-based catalyst **5** for the hydrolysis of cyclic phosphates **6**

Figure 16. The protein structure of α-chymotrypsin contains the catalytic triad of aspartic acid, histidine, and serine in the catalytic pocket. Reprinted with permission from ref. 40. Copyright (2018) American Chemical Society.

Figure 17. Proposed mechanism of amide hydrolysis with an Asp-His-Ser catalytic triad. Reprinted with permission from ref. 40. Copyright (2018) American Chemical Society.

Figure 18. Manifestation of cooperativity in various fields. Reprinted with permission from ref. 44. Copyright (2016) American Chemical Society.

Figure 19. Proposed mechanism of **DNPP** hydrolysis using the catalyst by Comba and co-workers. Reprinted with permission from ref. 50. Copyright (2012) Royal Society of Chemistry.

Figure 20. Proposed mechanism of **HPNPP** cleavage for a complex **8** described by Williams et al. Reprinted with permission from ref. 51. Copyright (2008) American Chemical Society.

Figure 21. Structure of the control complex **10** (top) and proposed mechanism for cleavage of DNA by Fe-L_b **9** (bottom). Reprinted with permission from ref. 52. Copyright (2008) Elsevier Inc.

Figure 22. More O'Ferrall-Jencks diagram showing the limiting mechanisms for phosphate ester hydrolysis. Reprinted with permission from ref. 53. Copyright (2012) Royal Society of Chemistry.

Figure 23. Proposed mechanisms of phosphodiesters hydrolysis by (A) Lewis acid activation; (B) nucleophile activation; (C) base catalysis; (D) leaving group stabilization. Reprinted with permission from ref. 55. Copyright (2019) Frontiers Media S.A.

Figure 24. Transesterification of **HPNPP** to afford a **PNP** and a cyclic phosphate (**cP**) as two products.

Figure 25. Chemical structure of the control molecule Zn(L1OH) **11** and the catalyst Zn_2(L20) **12** for **HPNPP** cleavage. Reprinted with permission from ref. 56. Copyright (2003) American Chemical Society.

Figure 26. Catalyst structure of $Zn_2([12]aneN_3)_2$ **13** for **HPNPP** cleavage. Adapted with permission from ref. 58. Copyright (2006) American Chemical Society.

Figure 27. Chemical structure of the 1,3-distal bimetallic calix[4]-arene-based catalyst **14** and the 1,2-vicinal catalyst **15**. Reprinted with permission from ref. 59. Copyright (2006) American Chemical Society.

Figure 28. Schematic illustration of gold nanoparticles **16** covered by a monolayer of TACN-Zn amphiphiles and the C_{12}TACN **17** ligands

Figure 29. a) The chemical structure of ligand **18** and host **γ-CD**; b) proposed mechanism of **HPNPP** cleavage; c) Schematic illustration of the allosteric modulation of the activity of catalyst studied. Reprinted with permission from ref. 62. Copyright (2020) American Chemical Society.

Figure 30. Different strategies for the pre-organization of functional groups to induce cooperativity. Reprinted with permission from ref. 66. Copyright (2021) Wiley-VCH GmbH, Weinheim.

Figure 31. An animated illustration of the “lock and key” model

Figure 32. An animated illustration of the transition state theory. Substrate induces the change in the conformation of an enzyme to form a complementary enzyme-substrate complex.

Figure 33. Schematic illustration of ligand-induced conformational change. Reprinted with permission from ref. 74. Copyright (1965) American Society for Biochemistry and Molecular Biology.

Figure 34. Schematic model of the induced fit model. Reprinted with permission from ref. 72. Copyright (1994) Wiley-VCH GmbH, Weinheim.

Figure 35. A schematic illustration of molecular recognition processes involving ubiquitin.

Reprinted with permission from ref. 81. Copyright (2009) Nature Publishing Group.

Figure 36. Schematic illustration of cooperative catalysis induced by neighbouring TACN·Zn^{2+} complexes **20**·Zn^{2+} upon assembly in vesicular structures. Reprinted with permission from ref. 89. Copyright (2018) Wiley-VCH GmbH, Weinheim.

Figure 37. Initial rates of **HPNPP** cleavage at a fixed concentration of 50 μM of C_{16}TACN **20** amphiphiles and 500 μM of **HPNPP** in aqueous buffer (10 mM of **HEPES**, pH 7) at 40 °C. Reprinted with permission from ref. 89. Copyright (2018) Wiley-VCH GmbH, Weinheim.

Figure 38. Critical aggregation concentration of **20**·Zn^{2+} amphiphiles measured in the presence of different concentrations of **HPNPP**. Adapted with permission from ref. 89. Copyright (2018) Wiley-VCH GmbH, Weinheim.

Figure 39. Substrate-induced self-assembled catalysts for **HPNPP** cleavage. Adapted with permission from ref. 89. Copyright (2018) Wiley-VCH GmbH, Weinheim.

Figure 40. The structure of **TPGS-750-M** and S**PGS-550-M** reported by Lipshutz. Adapted with permission from ref. 32. Copyright (2021) Elsevier Inc.

Figure 41. Micellar catalysis of **HPNPP** cleavage

Figure 42. Photo-responsive self-assembled catalyst **21**·Zn^{2+} switching between catalysis 'ON' and 'OFF' states following irradiation. Adapted with permission from ref. 95. Copyright (2019) Wiley-VCH GmbH, Weinheim.

Figure 43. a) The interconversion of *E*- and *Z*-configuration of amphiphile **21**·Zn^{2+}; b) UV spectrum of both configurations of amphiphile **21**·Zn^{2+}.

Figure 44. Sequential switching between *E*- and *Z*-configuration of amphiphile **21** (150 μM) in CD_3OD by ^1H NMR.

Figure 45. The determination of the CACs of *E*- and *Z*-**21**·Zn^{2+} and the control molecule ***E*-22**·Zn^{2+} by fluorescence spectroscopy in the presence of 2 μM of **Nile red** (λ_{ex} = 570 nm) and 500 μM of **HPNPP** in 5 mM of HEPES buffer pH 7.0 at 20 °C.

Figure 46. Initial rate of **HPNPP** cleavage at increasing concentration of **21**·Zn^{2+} and control molecule **22**·Zn^{2+} in the presence of 500 μM of **HPNPP** in 5 mM of HEPES buffer pH 7.0 at 40 °C.

Figure 47. Initial rates of **HPNPP** cleavage following sequential photoisomerization of catalyst **21**·Zn^{2+}.

Figure 48. General representations of a cooperative catalyst formed by a multicomponent cooperative catalyst (C_{16}TACN·Zn^{2+} **20**·Zn^{2+} and C_{16}Gua **23**) formed by self-assembly.

Figure 49. Two-point hydrogen bonding between a protonated guanidinium and a phosphodiester.

Figure 50. a) Chemical structures of artificial phosphodiesterases **24a** – **24d** reported by Salvio and co-workers; b) proposed mechanism of **HPNPP** cleavage involving guanidinium cooperativity. Adapted with permission from ref. 96. Copyright (2015) Wiley-VCH GmbH, Weinheim.

Figure 51. Chemical structure of the cooperative guanidinium catalyst system supported on gold nanoparticles and its proposed mechanism of **HPNPP** cleavage. Reprinted with permission from ref. 105. Copyright (2014) Royal Society of Chemistry.

Figure 52. Self-assembly of C_{16}Gua **23** into vesicular aggregates for **HPNPP** cleavage. Reprinted with permission from ref. 107. Copyright (2020) American Chemical Society.

Figure 53. Initial rate of **HPNPP** cleavage in the presence of 70 μM of C_{16}Gua **23** at varying pHs. [**HPNPP**] = 500 μM, [aqueous buffer] = 5 mM (buffers used were: **MES** for pHs 6.0-6.5, **HEPES** for pHs 7.0-8.1 and **CHES** for pHs 8.6-10.0), 40 °C.

Figure 54. a) Chemical structure of **coumarin 153**, b) fluorescence spectra of **coumarin 153** in aqueous solutions of **SDS** (λ_{ex} = 410 nm, [**coumarin 153**] = 1 μM) and b) plot of the fluorescence intensity and c) plot of the wavenumber at the maximum of the fluorescence band of **coumarin 153** as a function of molar concentration of **SDS**. Adapted with permission from ref. 114. Copyright (2012) Elsevier Inc.

Figure 55. Chemical structure of **Nile red**

Figrue 56. Emission intensity of **Nile red** (1 μM, λ_{ex} = 570 nm, λ_{em} = 635 nm) at increasing concentration of C_{16}Gua **23** in aqueous **CHES** buffer solution (5 mM, pH 9.1), plotted a) in normal scale and b) in logarithmic scale.

permission from ref. 118. Copyright (2008) Royal Society of Chemistry.

Figure 67. Synergistic effect of a guanidinium and a metal ion trapped by a TACN group in an artificial model for a) RNA and b) DNA model cleavage. Reprinted with permission from ref. 97. Copyright (2016) American Association for the Advancement of Science.

Figure 68. Representation of C_{16}TACN·Cu^{2+} (**20**·Cu^{2+}) and C_{16}Gua **23** a) in a heterogeneous self-assembled state and b) in a self-sorted homogeneously assembled state. Reprinted with permission from ref. 107. Copyright (2020) American Chemical Society.

Figure 69. Initial rate of **HPNPP** cleavage at different proportion between C_{16}Gua **23** and **20**·Cu^{2+}, [total catalyst] = 200 μM, [**HPNPP**] = 500 μM, [**CHES**] = 5 mM, at pH 9.1, 40 °C.

Figure 70. Emission intensity profile for **Nile red** (1 μM, λ_{ex} = 570 nm, λ_{em} = 635 nm) at increasing concentration of 1:1 C_{16}Gua **23**/**20**·Cu^{2+} in aqueous buffer solution, [**CHES**] = 5 mM, pH 9.1, [**HPNPP**] = 500 μM.

Figure 71. a) Chemical structure of **HPNPP** and **model HPNPP**; b) Emission intensity profile for **Nile red** (1 μM, λ_{ex} = 570 nm, λ_{em} = 635 nm) at increasing concentration of 1:1 C_{16}Gua **23**/**20**·Cu^{2+} in aqueous buffer solution, **[CHES**] = 5 mM, pH 9.1, [**model HPNPP**] = 500 μM.

Figure 72. Hydrodynamic diameters of assemblies measured with dynamic light scattering (DLS) in the presence of **model HPNPP** for the combined C_{16}Gua **23** and **20**·Cu^{2+} system in CHES buffer aqueous solution, [**CHES**] = 5 mM, pH 9.1 in water, [total catalyst] = 200 μM, [**model HPNPP**] = 500 μM.

Figure 73. The initial rate of **HPNPP** cleavage in catalytic systems of only C_{16}Gua **23**, only **20**·Cu^{2+} and the combined 1:1 C_{16}Gua **23**/**20**·Cu^{2+} in aqueous buffer solution ranging from pH 5.5 to pH 10, [catalyst] = 60 μM, [**HPNPP**] = 500 mM, [buffer] = 5 mM at 40 °C. (MES for pH 5.5 – 6.5; HEPES for pH 7 – 8.2; CAPS for pH 8.6 – 10)

Figure 74. Chemical structure of the 1,2-vicinal catalyst **35** designed by Salvio and co-workers. Adapted with permission from ref. 97. Copyright (2016) American

Association for the Advancement of Science.

Figure 75. Initial rate of **HPNPP** cleavage of different systems of only C_{16}Gua **23**, only **20**·Cu^{2+} and the combined 1:1 **20**·Cu^{2+}/C_{16}Gua **23** in 80% DMSO in water mixtures in the presence of 100 mM of base (blue dots) or 5 mM **CHES** buffer at pH 9.1 (orange dots), [catalyst] = 200 μM, [**HPNPP**] = 500 mM at 40 °C.

Figure 76. The initial background rate of **HPNPP** cleavage in the presence of 1 mM or 100 mM of DIPEA in absence of any catalysts, [**HPNPP**] = 500 mM at 40 °C.

Figure 77. The initial rate of **HPNPP** cleavage of three representative catalytic systems in different proportion of DMSO in water mixtures, [total catalyst] = 200 μM, [**HPNPP**] = 500 mM, [DIPEA] = 1 mM at 40 °C.

Figure 78. Chemical structure of **DPH** fluorophore

Figure 79. Emission intensity profile of **DPH** (1 μM, λ_{ex} = 350 nm, λ_{em} = 440 nm) at increasing concentration of 1:1 **20**·Cu^{2+}/C_{16}Gua **23** in 20% DMSO in water, [**model HPNPP**] = 500 μM, [DIPEA] = 1 mM at 20 °C.

Figure 80. Hydrodynamic diameter of assemblies measured with dynamic light scattering (DLS) in the presence of **model HPNPP** for the combined C_{16}Gua **23** and **20**·Cu^{2+} systems in 20% DMSO in water, [total catalyst] = 200 μM, [**model HPNPP**] = 500 mM and [DIPEA] = 1 mM at 20 °C.

Figure 81. Representive TEM images of the vesicular structures of 1:2 **20**·Cu^{2+}/C_{16}Gua **23** system in 20% DMSO in water mixture, [total catalyst] = 200 μM, [**HPNPP**] = 500 μM and [DIPEA] = 1 mM.

Figure 82. I(q) vs q plot of SANS for the mixed catalyst system **20**·Cu^{2+}/C_{16}Gua **23** (1:3) compared to a control system containing **20**·Cu^{2+}/C_4Gua **29** (1:3).

Figure 83. Initial rate of **HPNPP** cleavage with increasing concentration of a) the combined 1:1 **20**·Cu^{2+}/C_{16}Gua **23** and b) the combined 1:3 **20**·Cu^{2+}/C_{16}Gua **23** in 20% DMSO in water, [total catalyst] = 200 μM, [**HPNPP**] = 500 μM, [DIPEA] = 1 mM at 20 °C.

Figure 84. Initial rate of **HPNPP** cleavage with different proportion of C_{16}Gua **23** and **20**·Cu^{2+} in 20% DMSO in water, [total catalyst] = 200 μM, [**HPNPP**] = 500 μM, [DIPEA] = 1 mM at 20 °C. The control reaction was with different proportion of C_4Gua **29** and

20·Cu^{2+} (grey dots) under the same conditions.

Figure 85. Saturation profiles of catalytic efficiency of three catalytic systems with 1:1 (grey dots), 1:2 (orange dots) and 1:3 (green dots) proportions of **20**·Cu^{2+}/C_{16}Gua **23** at increasing concentration of **HPNPP** in 20% DMSO in water, [total catalyst] = 200 μM, [DIPEA] = 1 mM at 20 °C. The solid lines are fits for a Michaelis-Menten mechanism.

Figure 86. Artificial transphosphorylases containing guanidinium and TACN·M^{2+} functional groups attached to a) a cone-calixarene scaffold[97]; and b) a xylylene scaffold[120]

Figure 87. Catalyst structures featuring TACN·M^{2+} in combination with two guanidiniums as reported by Graham[119] and Anslyn[124].

Figure 88. Saturation profiles of catalytic efficiency of the 1:2 **20**·Cu^{2+}/C_{16}Gua **23** at increasing concentration of **HPNPP** in 20% DMSO in water, [total catalyst] = 200 μM, [DIPEA] = 3 mM at 20 °C. The solid lines are the data fits for a Michaelis-Menten mechanism.

Figure 89. The initial rate of **HPNP**P cleavage with different proportion of C_{16}Gua **23** and **20**·Cu^{2+} in 20% DMSO in water, [total catalyst] = 200 μM, [**HPNPP**] = 3 mM, [DIPEA] = 3 mM at 20 °C.

Figure 90. Absorption at 410 nm as a function of time demonstrating the a) up- and b) down-regulation of the combined **20**·Cu^{2+}/C_{16}Gua **23** system, [total catalyst] = 200 μM, [**HPNPP**] = 500 μM, [DIPEA] = 1 mM at 20 °C.

Figure 91. a) Chemical structure of the membrane probe **NR18**; b) the solvatochromic and colorimetric changes of **NR18** in solvents of varying polarity, including dioxane, THF, CH_2Cl_2, acetone, MeOH (from left to right). The fluorescence intensity image of a mixed POPC/sphingomyelin/cholesterol 1:1:1 GUV labelled with **NR18**. Reprinted with permission from ref. 130. Copyright (2021) Elsevier Inc.

Figure 92. Fluorescence emission from excitation state to the ground state (green arrow)

Figure 93. FRET processes between two molecules

Figure 94. a) Graphical representation of spectral overlap between the emission of donors and excitation of acceptors. b) FRET efficiency with the function of Förster

distance R_0 between fluorescence pairs. Adapted with permission from ref. 132. Copyright (2018) Royal Society of Chemistry.

Figure 95. A graphical illustration of membrane fusion resulting in changes in the spatial distance between fluorescence donors and acceptors.

Figure 96. Signal transduction through a membrane bilayer using FRET to generate an output. Reprinted with permission from ref. 34. Copyright (2021) Wiley-VCH GmbH, Weinheim.

Figure 97. a) Chemical structures of receptor amphiphiles and the peptide **P1**; b) A graphical illustration of the fusion of receptor amphiphiles induced by peptides **P1**. Adapted with permission from ref. 136. Copyright (2020) Wiley-VCH GmbH, Weinheim.

Figure 98. Chemical structures of two amphiphilic receptors and peptide **P2**. Reprinted with permission from ref. 136. Copyright (2020) Wiley-VCH GmbH, Weinheim.

Figure 99. a) A graphical illustration of the fusion of labelled membrane receptors induced by peptides resulting in a FRET output; b) Fluorescence spectra of DOPC vesicles containing labelled receptors **Zn-DPA-FAM** amphiphiles and **Cu-NTA-TMR** amphiphiles (0.5 mol% each) in the absence (red) and presence (green) of peptide **P2**. Relative FRET emission ratio ($I_{580\,nm}/I_{520\,nm}$) of **P2** and monovalent $\mathbf{P_H}$ and $\mathbf{P_P}$ as control (inset). Reprinted with permission from ref.136. Copyright (2020) Wiley-VCH GmbH, Weinheim.

Figure 100. Summary of commonly used fluorophores arranged according to their brightness and absorption maximum.

Figure 101. a) Chemical structures of fluorophore pair **FL1** and **FL2**; b) schematic representation of the FRET-based assays. Reprinted with permission from ref. 141. Copyright (2019) Royal Society of Chemistry.

Figure 102. Schematic representation of the three forms of **49** and the effects of PET, FRET and ICT at different pH values. Reprinted with permission from ref. 144. Copyright (2019) Royal Society of Chemistry.

Figure 103. a) The chemical structures of L-tryptophan **50**, coumarin derivative **51** and

Figure 114. A PET-FRET based chemosensor **95** (top) and a schematic illustration of frontier orbital energy changes (bottom). Reprinted with permission from ref. 151. Copyright (2016) Royal Society of Chemistry.

Figure 115. Fluorescence spectrum of C_{12}-I-Coum-TACN·Zn^{2+} (**54**·Zn^{2+}) (33 μM), C_{12}-I-Naph-Gua **55** (67 μM) and 1:2 ratio of C_{12}-I-Coum-TACN **54** and C_{12}-I-Naph-Gua **55** (total 100 μM) in the presence of 250 μM of DMP in CHES buffered solution (5 mM, pH = 9.1), slit 2.5/2.5.

Figure 116. Fluorescence spectrum of C_{12}-I-Coum-TACN·Zn^{2+} (**54**·Zn^{2+}) (133 μM), C_{12}-I-Naph-Gua **55** (67 μM) and 2:1 ratio of C_{12}-I-Coum-TACN **54** and C_{12}-I-Naph-Gua **55** (total 200 μM) in the presence of 500 μM of DMP in 20% DMSO in water, slit 2.5/2.5.

Figure 117. Fluorescence profile of 50 μM of C_{12}-I-Coum-TACN **54** (blue bars) excited at 325 nm, slit 2.5/5, following the addition of 50 μM of Zn^{2+} and 500 μM of DMP in CHES buffer solution (5 mM, pH 9.1). And fluorescence profile of 100 μM of C_{12}-I-Coum-TACN **54** (orange bars) excited at 325 nm, slit 2.5/5, following the addition of 100 μM of Zn^{2+} and 500 μM of DMP in 20% DMSO in water and 1 mM of DIPEA.

Figure 118. UV-Visible profile of a) 100 μM of C_{12}-I-Coum-TACN **54** (blue curve), with the addition of 100 μM of Zn^{2+} ions (orange curve) and with the further addition of either 500 μM of DMP (grey curve); b) 250 μM of C_{12}-I-Coum-TACN **54** (blue curve), with the addition of 250 μM of Zn^{2+} ions (orange curve) and with the further addition of either 500 μM of DMP (grey curve) in 20% DMSO in water and in the presence of 1 mM of DIPEA.

Figure 119. Proposed PET, CHEF and AIE mechanisms for the unique fluorescence increase observed with C_{12}-I-Coum-TACN **54** in the presence of Zn^{2+} and DMP.

Figure 120. The chemical structure of C_{12}-I-Coum-TACN **54** and the control molecules, C_0-I-Coum-TACN **96** and C_4-I-Coum-TACN **97**.

Figure 121. UV-Visible spectrum of 100 μM of the C_0-I-Coum-TACN **96**, the C_4-I-Coum-TACN **97** and the C_{12}-I-Coum-TACN ligand **54** in 20% DMSO in water and 1 mM of DIPEA.

Figure 122. The fluorescence intensity of 100 μM of each C_0-I-Coum-TACN **96**, C_4-I-Coum-TACN **97** and C_{12}-I-Coum-TACN ligand **54** (blue bar), with the addition of 100 μM

Figure 142. Fluorescence intensity of 250 μM of a) C_4-I-Coum-TACN **97** and b) C_0-I-Coum-TACN **96** with increasing concentration of Zn^{2+} ions in 20% DMSO in water and 1 mM of DIPEA, excited at 327 nm for C_4 ligand and 344 nm for C_0 ligand **96**, slit 2.5/2.5 at 25 °C

Figure 143. Fluorescence response of C_{12}-I-Coum-TACN to various metal ions in 20% DMSO in water. Experimental conditions: [C_{12}-I-Coum-TACN] = [metal ions] = 250 μM, [DIPEA] = 1 mM in 20% DMSO in water, excited at 327 nm, slit 2.5/5 at 25 °C.

Figure 144. Fluorescence response of a) C_4-I-Coum-TACN **97** and b) C_0-I-Coum-TACN **96** to various metal ions in 20% DMSO in water and 1 mM of DIPEA. Experimental conditions: [C_x-I-Coum-TACN] = [metal ions] = 250 μM, [DIPEA] = 1 mM in 20% DMSO in water, excited at 327 nm for C_4 ligand **97** or 344 nm for C_0 ligand **96**, slit 2.5/2.5 at 25 °C.

Figure 145. Schematic representation of AIE with **54**·Zn^{2+} in the presence of dimethylphosphate

Figure 146. Schematic illustration of aggregation caused quenching (ACQ) in perylene. Adapted with permission from ref. 169. Copyright (2019) MDPI.

Figure 147. Schematic illustration of aggregation induced emission (AIE) due to restriction of intramolecular motion. Reprinted with permission from ref. 173. Copyright (2014) Wiley-VCH GmbH, Weinheim.

Figure 148. a) Steady-state photoluminescence spectra of Ph_7C_7H suspensions in difference proportion of H_2O in DMF and b) DFT minimum energy geometries calculated for the S_0 (purple) and S_1 (orange) of Ph_7C_7H. Adapted with permission from ref. 175. Copyright (2017) American Chemical Society.

Figure 149. a) Fluorescence profile of different concentrations of C_{12}-I-Coum-TACN·Zn^{2+} in the presence of 500 μM of DMP; b) Amphiphilic solution of C_{12}-I-Coum-TACN·Zn^{2+} at 50 μM, 100 μM, 150 μM and 250 μM in the presence of 500 μM of DMP in quartz cuvettes. Experimental condition: [C_{12}-I-Coum-TACN **54**] = [Zn^{2+}] = 50 μM, 100 μM, 150 μM or 250 μM, [DMP] = 500 μM, [DIPEA] = 1 mM in 20% DMSO in water, slit 2.5/2.5, excited at 327 nm, 25 °C.

Figure 150. Fluorescence emission profile of 100 μM of C_X-I-Coum-TACN amphiphile (n = 0, 4, 12) at increasing concentrations of DMP in the presence of 100 μM of Zn^{2+} in 20% DMSO/water and 1 mM of DIPEA at 25 °C.

Figure 151. Fluorescence emission profile of C_{12}-I-Coum-TACN **54** amphiphiles in the presence of 500 μM of dimethyl phosphate in 20% DMSO in water mixture, [C_{12}-I-Coum-TACN] = [Zn^{2+}], [DIPEA] = 1 mM, slit 2.5/2.5 at 25 °C.

Figure 152. The fluorescence intensity of 100 μM of each of C_0-I-Coum-TACN **96**, C_4-I-Coum-TACN **97** and C_{12}-I-Coum-TACN ligand **54** (blue bars), with the addition of 100 μM of Zn^{2+} (orange bars) and 500 μM of PPi substrates (grey bars) in 20% DMSO in water.

Figure 153. The fluorescence intensity of 100 μM of each of C_0-I-Coum-TACN **96**, C_4-I-Coum-TACN **97** and C_{12}-I-Coum-TACN ligand **54** (blue bars), with the addition of 500 μM of **PPi** (orange bars) and 100 μM of Zn^{2+} ions (grey bars) in 20% DMSO in water and 1 mM of DIPEA.

Figure 154. Fluorescence emission profile of 100 μM of C_{12}-I-Coum-TACN **54** amphiphile at increasing concentration of pyrophosphate in the a) presence of 100 μM of Zn^{2+} and b) absence of Zn^{2+} in 20% DMSO in water mixture, [C_{12}-I-Coum-TACN **54**] = 100 μM, [DIPEA] = 100 μM, slit 2.5/2.5 at 25 °C.

Figure 155. Fluorescence profile of 100 μM of **54**·Zn^{2+} in the presence of various of phosphates in 20% DMSO in water. [C_{12}-I-Coum-TACN **54**] = [Zn^{2+}] = 100 μM, [phosphate] = 500 μM, [DIPEA] = 1 mM, excited at 327 nm, slit 2.5/2.5 at 25 °C.

Figure 156. A hydrolase-inspired cosurfactant catalyst. Reprinted with permission from ref. 39. Copyright (2020) American Association for the Advancement of Science.

Figure 157. A general selection scheme for generating receptors or catalytic cavities capable of recognition and catalysis. Reprinted with permission from ref. 186. Copyright (1997) Wiley-VCH GmbH, Weinheim.

Figure 158. The chemical structures of dithiol precursors **100**, **101** and **102** for the distribution of DCL. The Diels-Alder reaction was used and product **103** was used as TSA for the selection of macrocycles **104** and **105** from DCL. Adapted with permission

List of Tables

Candidate contributions to co-author papers

Chapter 1 Solis Munana, P.; Ragazzon, G.; Dupont, J.; Ren, C. Z.; Prins, L. J.; Chen, J. L.-Y., Substrate-Induced Self-Assembly of Cooperative Catalysts. *Angew. Chem. Int. Ed.* **2018**, 57 (50), 16469-16474. https://doi-org.ezproxy.aut.ac.nz/10.1002/anie.201810891	Solis-Munana Ragazzon Dupont **Ren** Prins Chen	35% 35% 5% **5%** 10% 10%
Chapter 1 Ren, C. Z.; Solis Munana, P.; Dupont, J.; Zhou, S. S.; Chen, J. L.-Y., Reversible Formation of a Light-Responsive Catalyst by Utilizing Intermolecular Cooperative Effects. *Angew. Chem. Int. Ed.l* **2019**, 58 (43), 15254-15258. https://doi-org.ezproxy.aut.ac.nz/10.1002/ange.201907078	**Ren** Solis-Munana Dupont Zhou Chen	**80%** 4% 3% 3% 10%
Chapter 2 Ren, C. Z.-J.; Solís-Muñana, P.; Warr, G. G.; Chen, J. L.-Y., Dynamic and Modular Formation of a Synergistic Transphosphorylation Catalyst. *ACS Catal.* **2020,** *10*, 8395-8401. https://doi-org.ezproxy.aut.ac.nz/10.1021/acscatal.0c01321	**Ren** Solís-Muñana Warr Chen	**85%** 2% 5% 8%

Jack L.-Y. Chen

Signed: 

Pablo Solís-Muñana

Signed: 

Giulio Ragazzon

Signed: 

Julien Dupont

Signed: 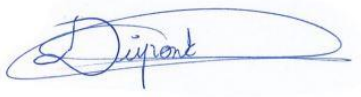

Leonard J. Prins

Signed: 

Siru Zhou

Signed: 

Gregory Warr

Signed: 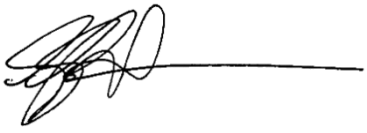

Attestation of Authorship

I hereby declare that this submission is my own work and that, to the best of my knowledge and belief, it contains no material previously published or written by another person (except where explicitly defined in the acknowledgments), nor material which to a substantial extent has been submitted for the award of any other degree or diploma of a university or other institution of higher learning.

Chloe Zhijun Ren

Chapter One: Introduction and Literature Review

1.1 Supramolecular Chemistry

The roots of supramolecular chemistry were established in the beginning of the 20th century with the discovery and acceptance of non-covalent interactions in natural systems. Supramolecular chemistry has since been referred to as "Chemistry beyond the molecule" by Nobel Laureate Jean-Marie Lehn, and encompasses a broad field of research concerned with studying the structural complexity and organisation of chemical systems composed of a discrete number of molecular building blocks. The study of spatial organisation of these building blocks, controlled by weak and reversible non-covalent interactions is a key feature of supramolecular chemistry, as is the study of systems that are highly dynamic and modular due to the reversible nature of the non-covalent interactions. Much of the inspiration for this area of research is to provide greater understanding of many biological processes that rely on concepts such as molecular folding and molecular recognition for their structure and function.

Key concepts in supramolecular chemistry encompass molecular self-assembly, folding, imprinting, molecular recognition, host-guest chemistry and dynamic covalent chemistry. Despite the categorisation of these different concepts, each of which have diverse applications in various fields, the essence behind each concept is the assembly from a disordered into a highly ordered system, driven by non-covalent interactions. A relatively new area of supramolecular chemistry is the construction of mechanically-interlocked molecular architectures, and the use of these structures to perform work. Pioneering research in this area has been carried out by Jean-Pierre Sauvage, Sir J. Fraser Stoddart and Bernard L. Feringa, who were awarded the 2016 Nobel Prize for Chemistry for their work on molecular machines, including the molecular lift and molecular motors.[1-2]

This thesis will focus on the self-assembly of amphiphilic molecules to form self-assembled vesicles capable of performing catalysis and acting as supramolecular sensors. In these studies,

we use hydrophobic interaction as the driving force to bring catalytically active sites into proximity and induce cooperative effects that result in an enhancement in the catalytic rate. The use of a self-assembly strategy to induce cooperativity allows for the modular combination of different catalytic units to rapidly screen different catalytic combinations for rapid optimisation of the catalyst. We then demonstrate that the self-assembly of fluorescent amphiphiles can give unexpected effects that are conducive for the construction of supramolecular sensors. With these examples, we aim to show that self-assembly is a powerful strategy for the construction of complex catalysts and sensors in a way that is synthetically accessible, and highly modular and flexible.

1.1.1 Types of non-covalent interactions

In contrast to traditional chemistry, which focuses on chemical reactions that involve the formation of intramolecular covalent bonds, supramolecular chemistry examines the weaker and reversible non-covalent interactions between molecules. These non-covalent forces include van der Waals forces, hydrogen bonding, π-π interactions, and hydrophobic interactions, amongst others. The existence of intermolecular forces was first verified by Johannes Diderik van der Waals in 1873.[3] Van der Waals forces are now used to describe attractive or repulsive interactions between atoms and molecules that have a distance dependence, and which do not occur through a chemical bond. Although this intermolecular force is much weaker than an ionic or a covalent bond, it plays a fundamental role in the field of supramolecular chemistry.

Latimer and Rodebush coined the term hydrogen bond in 1920, which is an example of an electrostatic dipole-dipole interaction.[4] The hydrogen, being a $\delta+$ region, is attracted by the electronegative atom such as nitrogen, oxygen, fluorine, which has partial negative charge, allowing temporary electron donation between hydrogen bond donors and acceptors (Figure 1). Hydrogen bonds are stronger than van der Waals forces, but are still much weaker than the

fully covalent bond. The hydrogen bond as one of the most important non-covalent interactions that occur both intramolecularly and intermolecularly, and is used to explain numerous phenomena in biochemistry, such as the secondary and tertiary structures of proteins, the formation of double-helical structures of DNA, as well as mechanisms of enzyme catalysis.

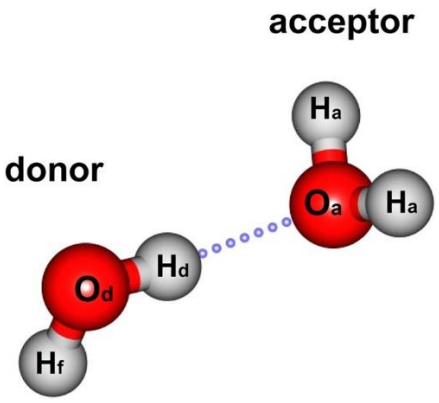

Figure 1. A formation of a hydrogen bond formed between two water molecules

The hydrophobic effect was first described by Walter Kauzmann in 1959.[5-6] He observed that non-polar substances tend to aggregate together and expel polar substances in an aqueous solution. This effect was driven by a reduction in free energy due to the decrease of disorder of the system. This hydrophobic effect is driven by entropy, and is not due to a specific interaction between molecules, and therefore many people do not consider it to be a non-covalent interaction. However, the hydrophobic effect is nevertheless an important phenomenon in supramolecular chemistry that helps to explain the formation of micelles, vesicles and cell membranes.

Numerous other types of noncovalent interactions exist, including ionic interactions, halogen bonding and π effects (π-π interactions, cation-π interaction, anion-π interaction). With the gradual increase in the understanding of these different kinds of noncovalent interactions, biologists and chemists have been able to gain greater understanding of important processes such as protein folding and enzymatic catalysis.

1.1.2 Mimicking nature

Chemists have been able to take the concepts gleaned from studying intermolecular interactions in nature and apply them to synthetic systems. A significant breakthrough in this area was made by Charles J. Pedersen in the 1960s, who found crown ethers had a strong affinity to cations due to the ability to form multiple electrostatic-dipole interactions (Figure 2).[7] Following this work, Donald J. Cram and Jean-Marie Lehn further explored the shape- and ion-selective effect of crown ether-like receptors for the recognition of either cations, anions or neutral molecules.[8-10] This resulted in the award of the 1987 Nobel Prize for Chemistry to Donald J. Cram, Jean-Marie Lehn, and Charles J. Pedersen in honour of their contributions in "structure-specific interactions of high selectivity". This discovery of selective host-guest complexes, in which crown ether-like host molecules could identify and preferentially bind certain guests, mimicked the action of enzyme selectivity and represented a fundamental finding in supramolecular chemistry.

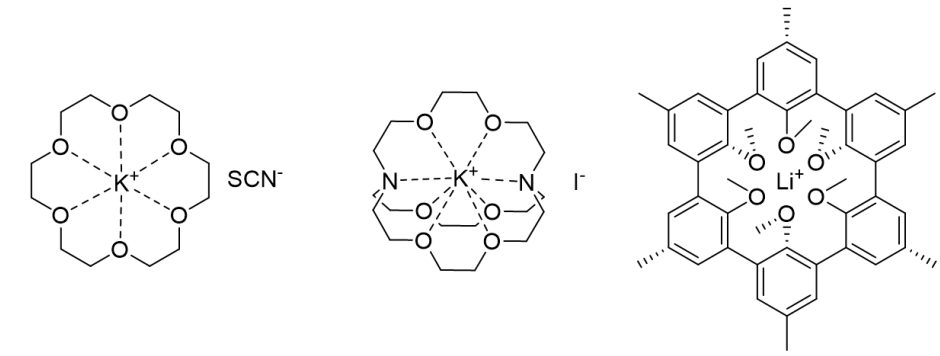

Figure 2. Crown ether and crown ether-like receptors reported by Charles J. Pedersen, Jean-Marie Lehn and Donald J. Cram, respectively.

By the 1990s, the focus had shifted to the study of mechanically-interlocked molecular architectures. Jean-Pierre Sauvage was able to devise a high-yielding synthesis of the now famous catenane family of interlocked compounds. In one example in 1994, he demonstrated

that interlocked rings in a [2]catenane could be induced to rotate in a controlled manner (Figure 3).[11-13] The driving force came from the redox reactions of Cu(I) and Cu(II), resulting in conversion between a five-coordinate Cu(II) complex and a four-coordinate Cu(I) complex. Therefore, copper coordination to either the bidentate or tridentate polypyridyl ligand on macrocycle **1** would shift upon redox conversion between Cu(II) and Cu(I), which allowed for circumrotation under electrochemical control. This was the first-ever non-biological molecular machine to mimic controlled movements in nature, such as ATP synthases.

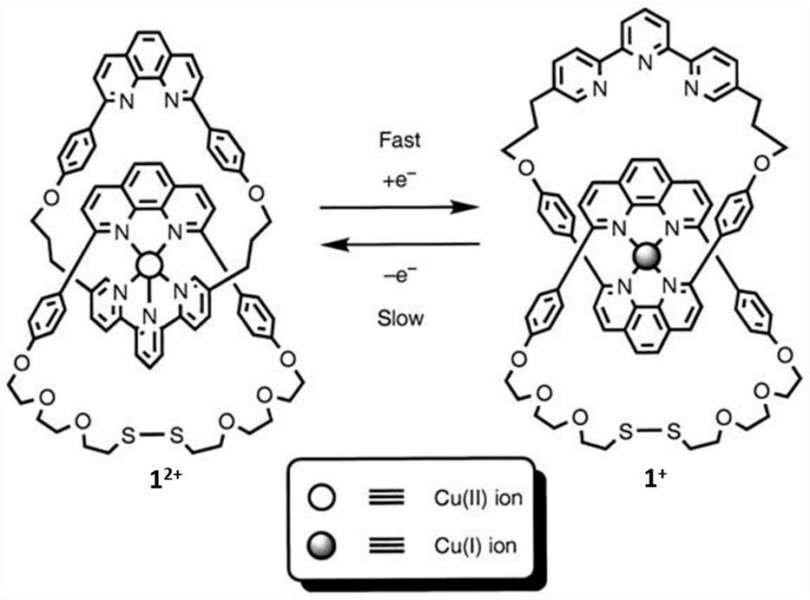

Figure 3. A two-geometry [2]catenane constructed **1** around copper(I); the gliding motion of one ring within the other is triggered by oxidizing or reducing the metal centre (Cu^{I} /Cu^{II}). Reprinted with permission from ref. 13. Copyright (2005) Springer.

Similarly, Sir James Fraser Stoddart developed a linear molecular shuttle based on a rotaxane structure, in which a ring-shaped molecule was mechanically interlocked with an axle.[14] The movement of a threaded ring on an axle could be controlled by artificial triggers such as a redox reaction (Figure 4, left). He also used rotaxane-based structures to create a molecular elevator[15] (Figure 4, right), and highly complex assembled systems such as molecular muscles.[16] At around the same time, Ben L. Feringa was creating molecular motors based on

the spin of molecular rotor blades under light irradiation.[17] The importance of their work was affirmed by the 2016 Nobel Prize for Chemistry, awarded to Jean-Pierre Sauvage, Sir J. Fraser Stoddart and Ben L. Feringa for their contributions to the study of molecular machines.[1-2]

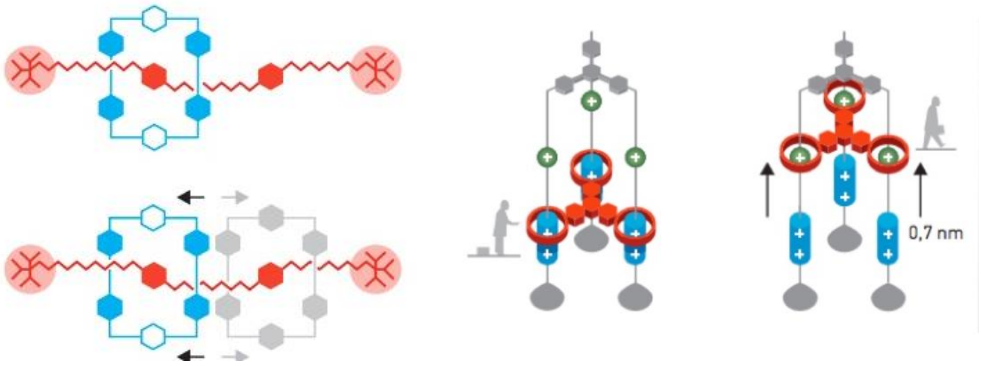

Figure 4. Schematic representation of a linear molecular shuttle (left) and a molecular elevator (right).

1.1.3 Supramolecular assemblies

Although supramolecular chemistry encompasses a wide variety of concepts and systems, including molecular self-assembly, folding, imprinting, molecular recognition, host-guest chemistry, mechanically interlocked molecular architectures and dynamic covalent chemistry, the essence behind each system is an assembly from a disordered into a highly ordered system, driven by non-covalent interactions. The types of supramolecular constructions can be broadly classified into two categories: self-assembled constructions and host-guest constructions with respect to the size and shape of molecular building blocks. Host-guest constructions are in alignment with the lock-and-key model of enzymatic catalysis, since the correct sizes and geometries of the host and guest are of great importance for binding, which is driven by non-covalent interactions.[18]

An example of an artificial host-guest complex is shown in Figure 5.[19] Pillar[6]arene **2** acts as an artificial host, providing a cavity for the trans form of azobenzene-derivative **3**. Binding of

this guest into the pillar[6]arene **2** is driven by the hydrophobic effect. The host-guest complex cannot form with the smaller host pillar[5]arene due to the smaller size of the cavity. Moreover, the formation of the host-guest complex, is reversible under light irradiation due to the isomerization of the azobenzene moiety in the guest. The dissociation of the host-guest complex can be triggered by the conversion of host molecule from the trans to the cis form by irradiation with UV light at 365 nm. The mismatch of the size between the host and the guest forbade the threading of the cis-azobenzene guest **3** through the cavity of pillar[6]arene-based host **2**. Upon visible light irradiation, threading of the guest through the host cavity was again allowed due to isomerization back to the trans isomer. This is a direct example showing the importance of both the size and shape of both the host and guest for successful binding based on the lock-and-key model.

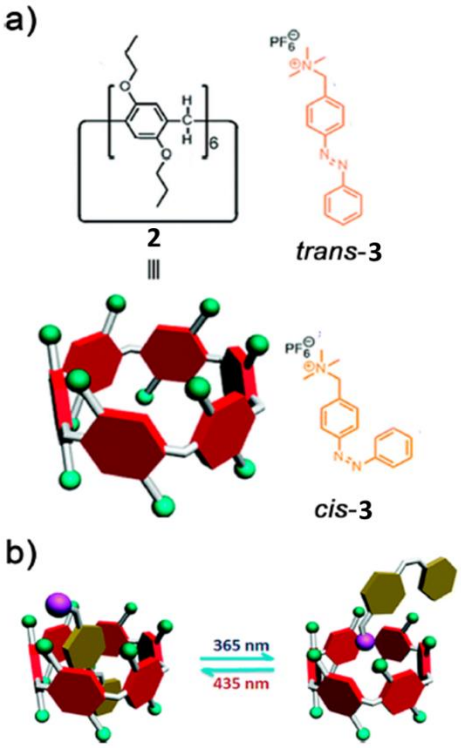

Figure 5. a) Chemical structures of pillar[6]arene host **2** and azobenzene guest **3** and b) their complexing and decomplexing. Reprinted with permission from ref. 19. Copyright (2015) American Chemical Society.

With self-assembled constructs, molecular building blocks orientate into highly ordered systems by non-covalent interactions, where the individual molecules do not show significant differences in size. Therefore, the evenly sized species would not typically provide cavities for trapping other building blocks. In nature, there are numerous examples of self-assembly, for example, the formation of the double-helical structure of DNA and the assembly of phospholipids into membrane structures. Taking the structure of DNA as example (Figure 6), two strands of a DNA molecule self-assemble and distort slightly into a double-helical structure with the assistance of hydrogen bonds between guanine (G) and cytosine (C) or thymine (T) and adenine (A). [20] There is no significant difference in size between the two strands of DNA.

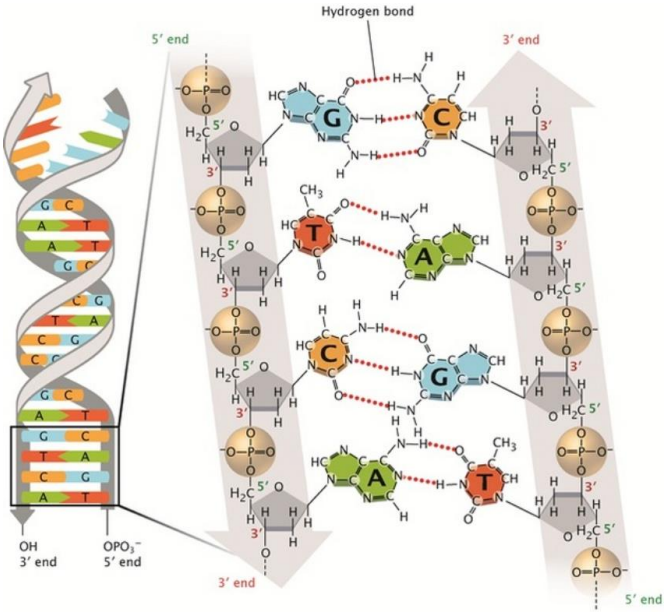

Figure 6. A graphical illustration of the double-helical structure of DNA. Reprinted with permissionon from ref. 20. Copyright (2008) Nature Publishing Group.

Artificial systems have also been designed that incorporate both host-guest chemistry and self-assembly constructions, allowing generation of yet more complex systems. Typical examples of such systems include metal-organic frameworks (MOFs) for catalysis,[21] molecule storage and separation.[22] Figure 7 shows an example of an optically-controlled hydrolase model for the catalysis of p-NPA hydrolysis.[23] The supramolecular catalyst was constructed by the

hierarchical self-assembly of peptide-based supra-amphiphiles, in which methylviologen-modified peptides (**MV-HGC** and **MV-RGC**) and azo-linked amphiphiles (3,4,5-tris(n-dodecyloxy)benzoylamide; **Azo-TBA**) act as guest molecules that are bound by cucurbit[8]uril **CB[8]** to form a stable 1:1:1 heteroternary host-guest complex. Supramolecular assembly and disassembly of this complex was achieved by the photoisomerisation of **azo-TBA** by irradiation with light. The trans to cis isomerization upon irradiation with UV for 60s caused aggregate dissociation, while the cis to trans isomerization through irradiation with visible light at 362 nm for 10 mins caused the reformation of vesicular structures. The interconversion was completely reversible up to five cycles with negligible switching fatigue as confirmed by dynamic light scattering (DLS. The authors investigated the catalytical activity of model hydrolase by monitoring the substrate *p*-nitrophenyl acetate (***p*-NPA)** hydrolysis and followed the UV absorbance of the product *p*-nitrophenolate at 400 nm. The assembly of the **V-$H_{10}R_1$** vesicle through visible light gave the best catalytic activity due to the induced synergistic effect of His/Arg under spatial organization of 10:1, whereas the imidazolyl group of His activated a water molecule to generate a hydroxide ion that attacked the carbonyl of ***p*-NPA** to yield a tetrahedral transition state stabilized by the guanidyl group of Arg for C–O bond cleavage. Moreover, the reversibility of light-induced activity changes of **V-$H_{10}R_1$** vesicles was explored by multiple assembly and disassembly cycles. This was conducted by sequentially irradiating **V-$H_{10}R_1$** with UV light treatment for 10 mins followed by Visible light treatment for 30 mins under ultrasonic conditions at room temperature. The up- and down- regulation of its catalytic activity indicated the photo-responsive assembly and disassembly was reversible under optical control over five cycles.

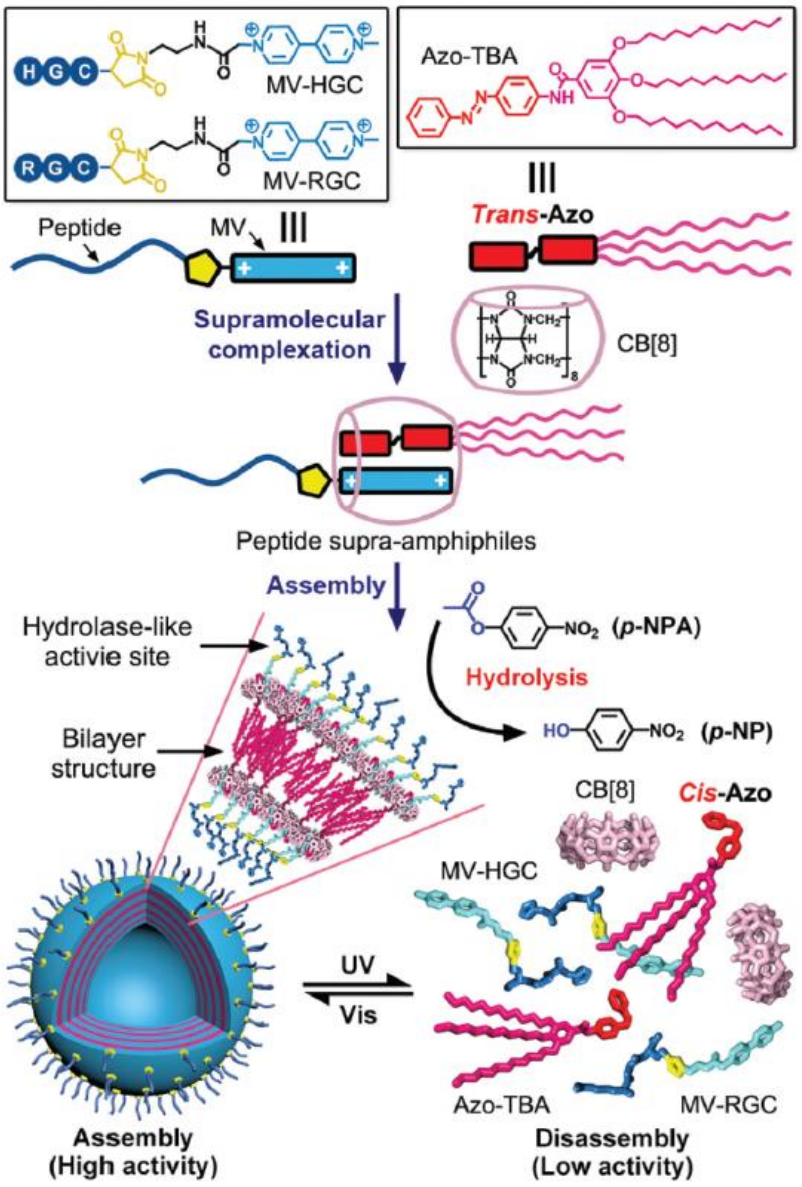

Figure 7. Schematic representation of the design of the photoresponsive hydrolase model through light-induced assembly/disassembly of His/Arg-containing peptide supra-amphiphiles. Reprinted with permission from ref. 23. Copyright (2019) Royal Society of Chemistry.

The focus of this thesis is on the self-assembly on amphiphilic molecules to give supramolecular constructs. The vesicular structures are believed to have binding pockets on its surface that can bind the substrate for both catalysis and sensing applications. Our constructs therefore have elements of both self-assembly and host-guest chemistry, however,

the modular self-assembly of a host on the surface of a vesicular structure is a concept that has been sparingly investigated in the literature and will be the focus of this thesis.

1.1.4 Self-assembly of supramolecular systems

Self-assembly (Figure 8) describes a spontaneous process where isolated components orientate into a highly ordered system by non-covalent interactions, rather than by guidance from outside sources. In self-assembled systems, molecular building blocks do not show a significant difference in size, and no species would act as a host for another within the self-assembled structure, in contrast to host-guest systems. The aggregation processes have their own equilibrium, which is influenced by factors such as the structure of the molecules, solvent, and temperature. Compared with traditional covalent bonding within molecules, the weaker and reversible non-covalent interactions are more dynamic and allow the possibility of reversal, or switchable control. Taking advantage of the dynamic nature of self-assembled systems, the abundance of possible applications has fuelled the abundant development of supramolecular chemistry, leading to applications in catalysis and biomedical technologies.[24]

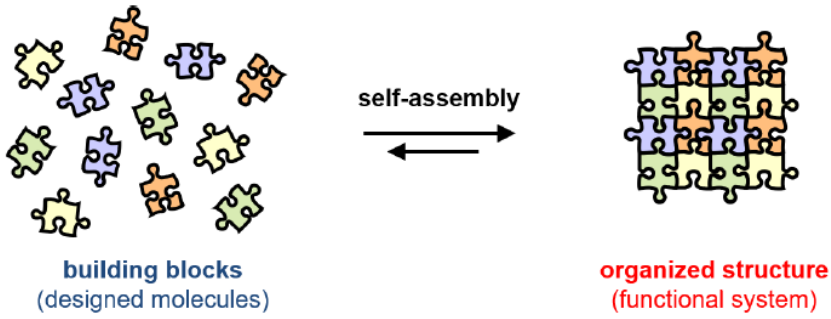

Figure 8. A graphical representation of self-assembly

Self-assembly in supramolecular chemistry was first studied in sophisticated structures and systems in nature. The diversity of self-assembled structures was observed in living organisms,

not only the bilayer of phospholipids but also in the folding of proteins and the formation of DNA. For nature's proteins, their folding and organisation in 3-dimensional space establishes their biological function. Figure 9 shows that the structure of a protein is organised in a hierarchical manner, from primary to quaternary. The linear sequence of amino acids is defined as its primary structure, which self-organises into its secondary structure, with common examples being alpha helixes or beta sheets. These domains containing secondary structure are further folded and organised to form the tertiary structure of a protein, which is dominated by intermolecular interactions and hydrophobic effects. Finally, some proteins will be further organised to form quaternary structures, with a classic example being haemoglobin, where the functional protein contains two pairs of peptides. The correct folding of proteins via self-assembly is extremely important for its three-dimensional structure, and ultimately, function.

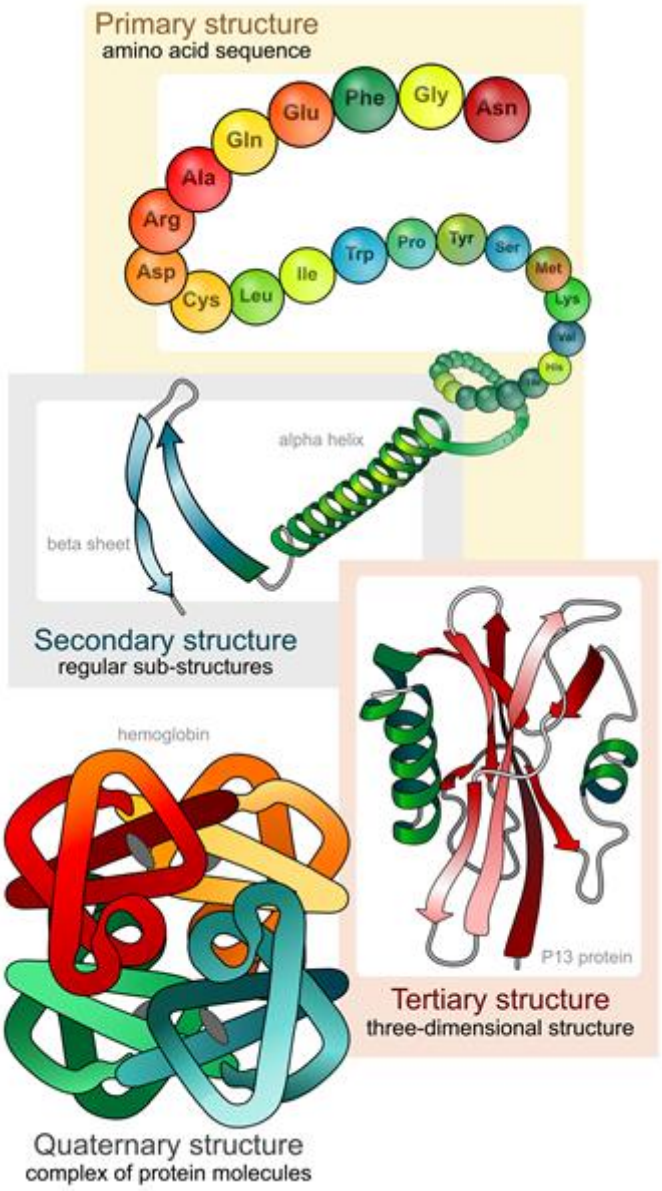

Figure 9. Four hierarchically arranged structures of protein.

In attempts to mimic nature, synthetic chemists have created numerous examples of artificial self-assembled systems utilizing non-covalent interactions. Figure 10 shows work by Stupp and co-workers, who reported peptide nanofibers formed by multiple stages of hierarchical organisation by self-assembly and biomineralization, to mimic bone tissues.[25] Thousands of the designed monomers **4** were self-assembled to form nanofibers, and the size of the hydrated state of nanofibers was measured by cryo-transmission electron microscope (cryo-TEM) to have a diameter of 7.6 ± 1 nm and lengths up to several micrometres.

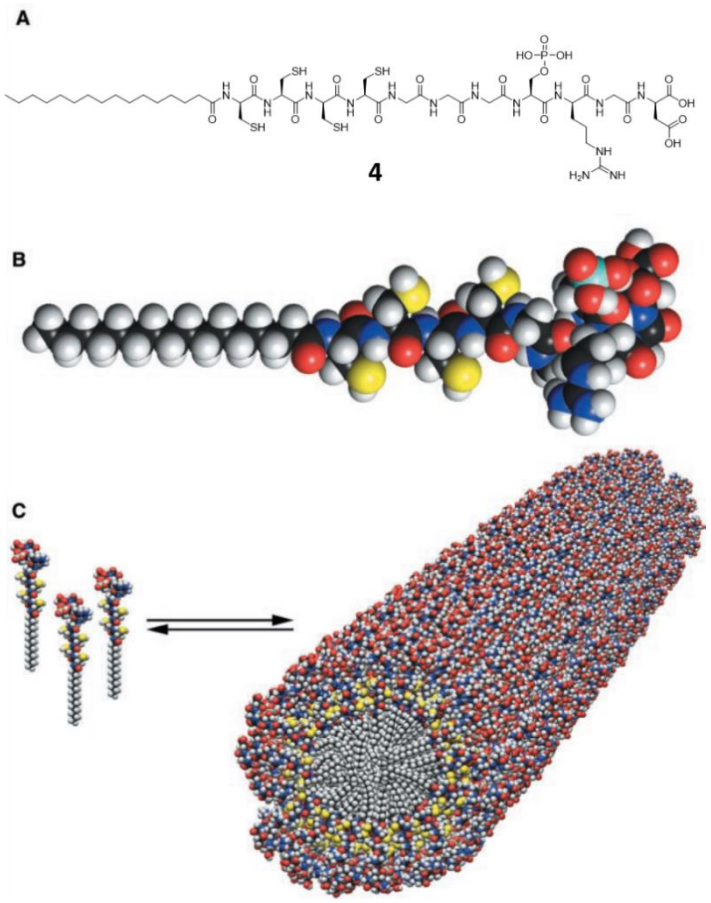

Figure 10. a) Chemical structures of peptide-amphiphiles **4**. B) Molecular model of the peptide-amphiphiles showing the overall conical shape of the molecule going from the narrow hydrophobic tail to the bulkier peptide region. C) Schematic illustration of the self-assembly of peptide-amphiphiles into a nanotube. Reprinted with permission from ref. 25. Copyright (2001) American Association for the Advancement of Science.

Another important example nature-inspired mimicry is the formation of self-assembled polyhedral reported by Fujita.[26] In this case, they were able to form geometrically designed cavities, some of which were able to perform catalytic reaction by acting as an efficient host for the substrates. They demonstrated the successful synthesis of several giant Pd_nL_{2n} assemblies containing n Pd ions and 2n ligands (n = 6, 12, 24, 30) (Figure 11). The geometrically restricted rules constrained self-assembly into roughly spherical, isotropic structures to reduce their surface energy. Numerous other examples of artificial self-assembled systems can be found and can involve the formation of nanotubes[27], and metalloorganic frameworks (MOFs)[21],

etc.

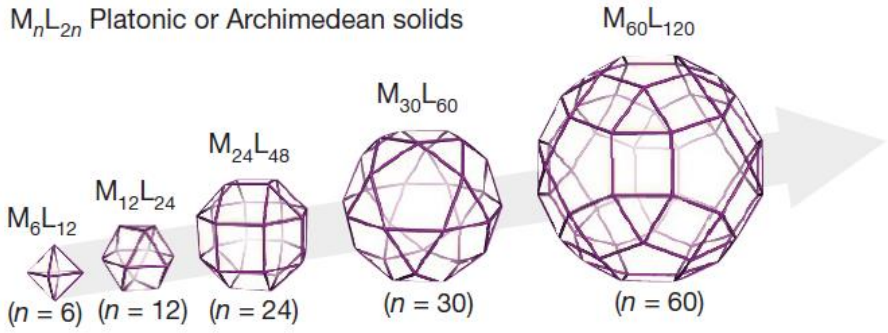

Figure 11. Schematic illustration of M_nL_{2n}-type polyhedral metal-organic ligand complexes with the symmetry of Platonic or Archimedean solids. Reprinted with permission from ref. 26. Copyright (2016) Nature Publishing Group.

1.1.4.1 Micelles and vesicles

This thesis focuses mainly on using the hydrophobic effect as the driving force to induce the self-assembly of molecular building blocks. Micelles and vesicles are one of the simplest self-assembled structures driven by the hydrophobic effect. These supramolecular structures contain thousands of molecular building blocks (or amphiphiles), that contain hydrophobic (oil-loving) alkyl tails and hydrophilic (water-loving) head groups. The formations of micelles and vesicles are mainly driven by the hydrophobic effect, where the hydrophobic tails are hidden away from aqueous media while hydrophilic heads point outwards and help to solubilise the entire structure within an aqueous solution. Although the concept of a 'hydrophobic bond' has been widely accepted, the true reason for the strong desire of hydrophobic groups to assemble in water is due to the configurational rearrangement of water molecules within the system.[28] The hydrophilic heads of the amphiphiles orient themselves towards the exterior of the micelles and vesicles, while the polar heads form hydrogen bonds with water and achieves solubility.

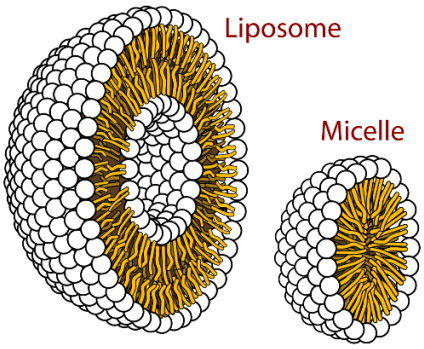

Figure 12. Schematic illustration of a liposome and a micelle.

A key characteristic of self-assembled structures is the critical aggregation concentration (CAC) or critical micellar aggregation (CMC) for micelles. This is the minimal concentration needed for the commencement of the self-assembly of amphiphiles. The key processes of micellar aggregation are shown pictorially in Figure 13, and other types of aggregation formation work in a similar way. During the initial addition of amphiphiles into aqueous media, the amphiphiles are dispersed at the air-water interface. This reduces the free energy of the system by minimizing the contact of hydrophobic tails with water. With the gradual saturation of the air-water interface, amphiphiles disperse freely into the water phase while the concentration is still too low to form aggregates (below CAC). Subsequently, upon reaching the CAC, amphiphiles aggregate in water to form micelles, and the free energy of the whole system also reaches its lowest point due to the shielding of the hydrophobic tail of the amphiphiles away from water. It is important to note that the CAC is independent of the properties of the interface.

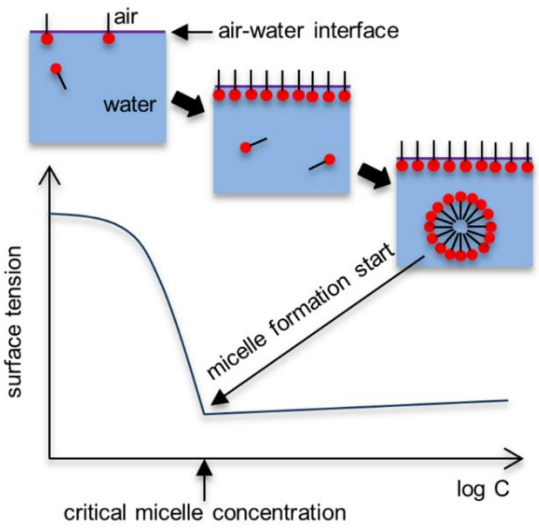

Figure 13. Schematic illustration of the aggregation progresses involved in micelle formation

Self-assembled micelles and vesicles/liposomes have been used in a wide variety of applications, including drug delivery[29], cancer therapy[30], catalysis[31-32], transmembrane sensing[33-34] and as nanoreactors.[35] For example, Lipshutz and co-workers reported that nanomicelles can be used as nanoreactors for a variety of chemical transformations including palladium-catalysed cross-coupling reactions.[35-37] They employed the designer surfactant **TPGS-750-M** that contained a vitamin E lipophilic core, which allowed a variety of organic reactions to take place in water. Higher rates of reaction were possible due to the ability of the system to solubilise the substrates and catalyst in the interior of the nanomicelles, causing significant enhancement of concentration.

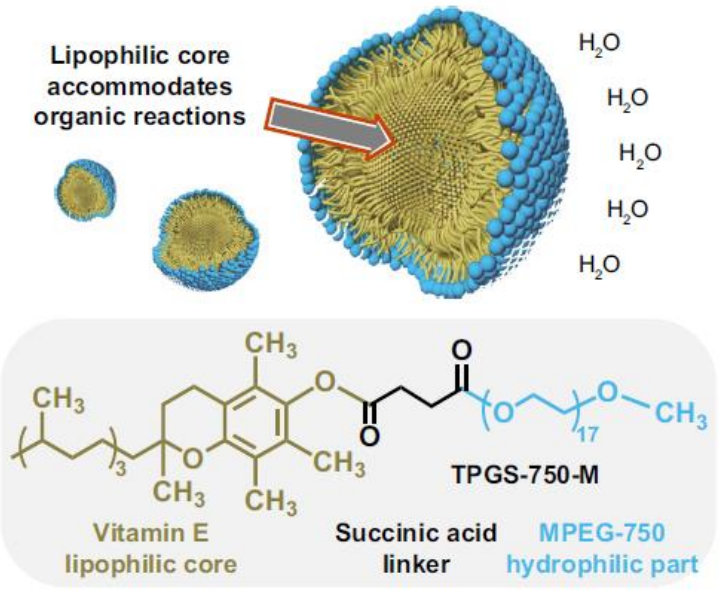

Figure 14. Nanoreactors for organic reactions in water. Reprinted with permission from ref. 35. Copyright (2019) Nature Publishing Group.

1.2 Supramolecular Catalysts and Cooperativity

Supramolecular catalysts have historically been designed to imitate the microenvironment of enzymes by building molecular architectures that mimic the enzymatic active site. Conventional design concepts include the confinement of the substrate within a rigid binding pocket, and the precise positioning of the functionality required for catalysis. An example includes Breslow's cyclodexdrin-based catalyst **5** for the hydrolysis of cyclic phosphates **6**.[38] The cyclodexdrin **5** provides the binding pocket for the substrate **6** and two imidazole units appended to the cyclodexdrin stabilise the transition state of the reaction and promotes the hydrolysis.

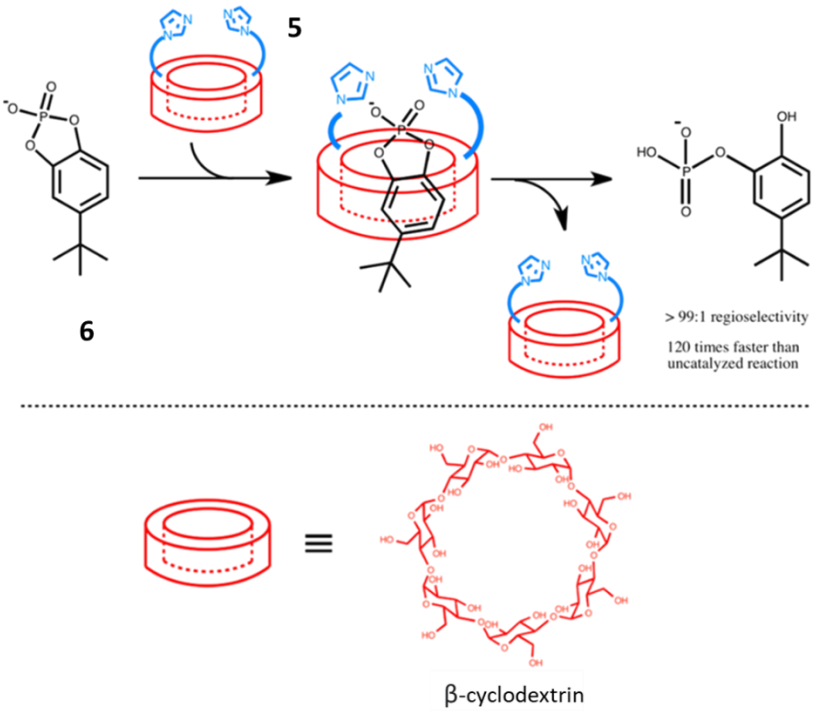

Figure 15. Breslow's cyclodexdrin-based catalyst **5** for the hydrolysis of cyclic phosphates **6**

Another hallmark of natural enzymes are the cooperative interactions that occur between multiple functional groups in the catalytic pocket. Take for example α-chymotrypsin, a well-studied serine protease that uses a serine residue as the nucleophile for the hydrolysis of amide bonds. The active site of the catalytic pockets contain the amino acid residues aspartic acid, histidine and serine, which work together in a synergistic manner, and is known as a catalytic triad.[39-40]

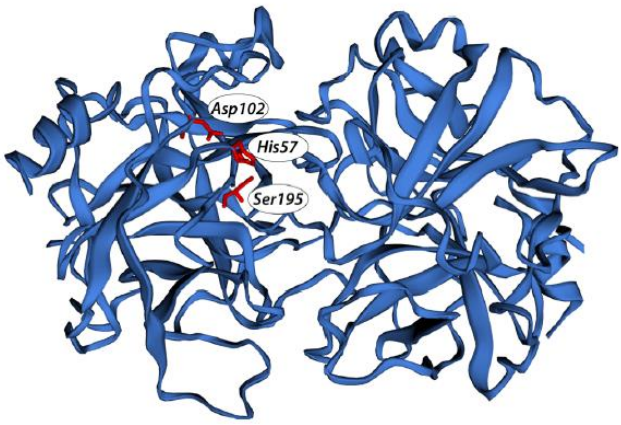

Figure 16. The protein structure of α-chymotrypsin contains the catalytic triad of aspartic acid, histidine, and serine in the catalytic pocket. Reprinted with permission from ref. 40. Copyright (2018) American Chemical Society.

Figure 17 summarises how the Asp-His-Ser catalytic triad acts to cleave an amide bond.[40] The key is the formation of a reactive serine residue, which begins by interaction of the carboxylate group from an aspartic acid residue with the histidine residue. The carboxylate acts as a hydrogen bond acceptor which increases the pKa of the basic nitrogen on the imidazole. With this assistance, the imidazole can act as a base to deprotonate the hydroxyl group of Ser, which produce a powerful nucleophile to attack the carbonyl group (in blue) of the amide in the substrate. The resulting transition state is further stabilized by stabilisation of the anionic oxygen via hydrogen bonding of guanidine which acts as an oxyanion hole (in green), as well as the electrostatic interaction via the nearby charged imidazole ring. The stabilization of the tetrahedral intermediate reduces the activation energy needed to accelerate the reaction. The electrons from the negatively charged oxygen are then pushed back to regenerate the carbonyl group and break the amide bond, allowing the release of an amine (in red) as the product.

To expel the carboxylic acid from the catalytic site, a water molecule from the solution gets assistance from the imidazole to act as a nucleophile, attacking the carbonyl functional group of the ester. The tetrahedral transition state is similarly stabilized via amino acid residues in the catalytic pocket. Once the carboxylic acid is eliminated and the hydroxyl group is

protonated by the conjugate acid of the imidazole, the Asp-His-Ser catalytic triad is regenerated for further reaction cycles.

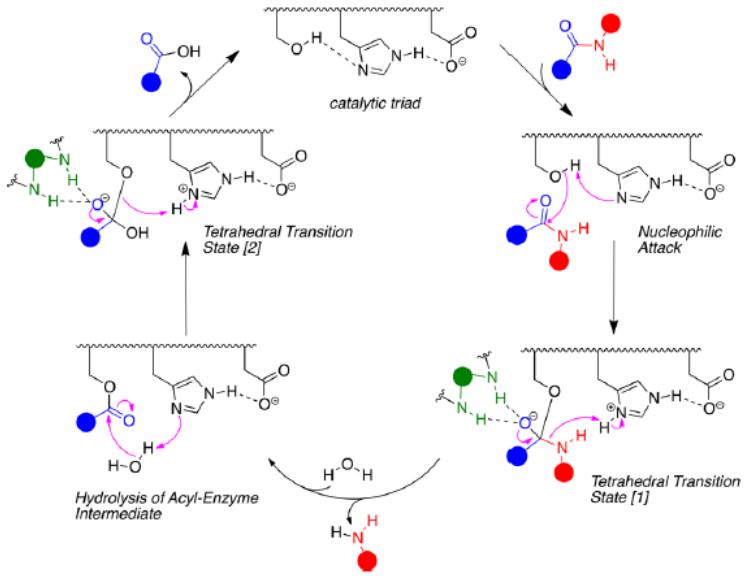

Figure 17. Proposed mechanism of amide hydrolysis with an Asp-His-Ser catalytic triad. Reprinted with permission from ref. 40. Copyright (2018) American Chemical Society.

This complicated interplay between three amino acid residues and an extra oxyanion hole in the active site of α-chymotrypsin allows the hydrolysis of an amide bond in a much shorter time period compared to non-catalysed proteolysis which takes hundreds of years. Such significant rate acceleration can only be achieved by the synergistic interaction between multiple functional groups in a confined space and is commonly seen in natural enzymes. Other well-known hydrolytic enzymes contain different catalytic triads such as Cys-His-Asp, Ser-His-His, Ser-Glu-Asp.[41-42]

When viewed from a broader perspective, cooperativity can be seen to operate at different levels of organisation, from single molecules to large multimolecular systems, and up to complex biological systems.[43] The term cooperativity or cooperative interactions, however, can have different meanings in different fields and can have origins other than the combination of

non-covalent interactions (Figure 18).[44] One of the most commonly used examples to illustrate cooperativity in biology is the binding of oxygen to mammalian haemoglobin, where four tetrameric proteins bind oxygen in an allosteric manner, with their affinity for oxygen increasing following binding of the first molecule of oxygen.[45] Another example of cooperativity is the folding of proteins into secondary and tertiary structures due to the cooperativity of non-covalent interactions between different amino acids, crucial for a variety of biological properties.[46] In chemistry, cooperativity has widely been used to describe the formation of self-assembled structures,[47] where monomers associate via multiple non-covalent interactions; and multifunctional catalysis, where multiple functional groups work together in a synergistic manner, with an example being the simultaneous activation of both the nucleophile and the electrophile to dramatically accelerate a chemical reaction.[48]

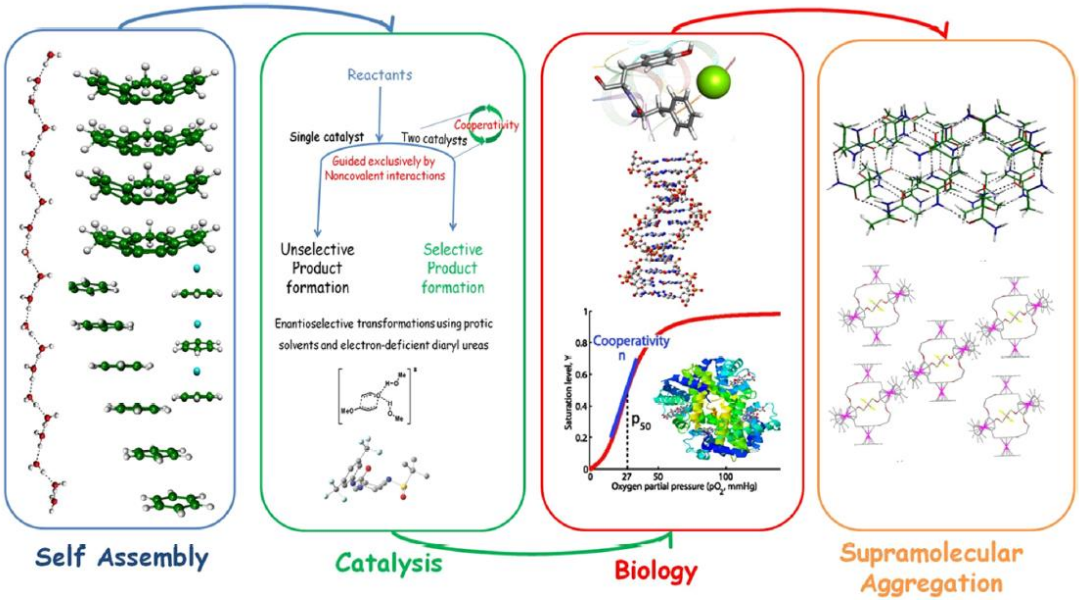

Figure 18. Manifestation of cooperativity in various fields. Reprinted with permission from ref. 44. Copyright (2016) American Chemical Society.

Despite at times having different underlying mechanisms, the essential feature of cooperativity is that the interplay of two or more interactions gives unique properties that are absent in the presence of each of the interactions on their own.[49] This is often referred to as

an ‘emergent’ property in self-assembled systems, where the ‘emergent’ property is a feature of the self-assembled system, which is not found in the individual components of that system. A classic example is a living cell, where the properties of being alive are not found in each of the components that cell, but is a result of complex interactions between the cell membrane, metabolic apparatus, cytoskeleton, etc. In this thesis, we will use the term ‘cooperativity’ in the context of cooperative catalysis, where the synergistic effect between multiple functional groups give rise to rate accelerations not seen with each of the individual functional groups on their own.

1.2.1 Artificial metalloenzymes

A popular target for the study of cooperative mechanisms in enzymes is a family of metalloenzymes known as phosphodiesterases. These enzymes are used in nature to cleave ribonucleic acid (RNA) and deoxyribonucleic acid (DNA), in reactions that are assisted by metal ions.

Comba and co-workers synthesised a functional mimic of purple acid phosphatase (**PAP**) that was able to hydrolyse the model compound 2,4-dinitrophenyl phosphate (**DNPP**).[50] As shown in Figure 19, phosphatase-like activity was observed when **DNPP** was able to be correctly orientated and activated within the catalyst structure **7**. With the help of the protonated tertiary amine on the crown ether binding to the phosphoryl group, **DNPP** was positioned in a manner that allowed further activation by one of the ferric ions from above. A second ferric ion promoted the formation of a hydroxyl group and nucleophilic attack. This mechanism is in agreement with **PAP** hydrolysis in nature and is a very good example of a specific synthetic catalyst that mimics a natural enzyme.[50]

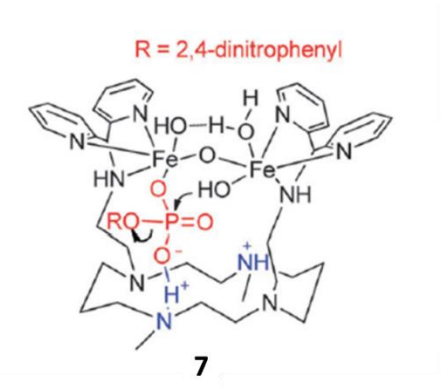

Figure 19. Proposed mechanism of **DNPP** hydrolysis using the catalyst by Comba and co-workers.

Reprinted with permission from ref. 50. Copyright (2012) Royal Society of Chemistry.

There are several other literature examples that suggest the cooperative interaction between precisely positioned functional groups is crucial for activating a substrate for a chemical reaction. Williams and co-workers synthesised a dinuclear metal ion complex **8** for the cleavage of model RNA in neutral pH (Figure 20).[51] In this example, the stabilisation of 2-hydroxypropyl-4-nitrophenyl phosphate (**HPNPP**) was enhanced by the cooperativity between hydrogen bonds provided by multiple amines and double Lewis acid activation by zinc binding. Following activation, an intramolecular attack by a hydroxyl group results in **HPNPP** cleavage.

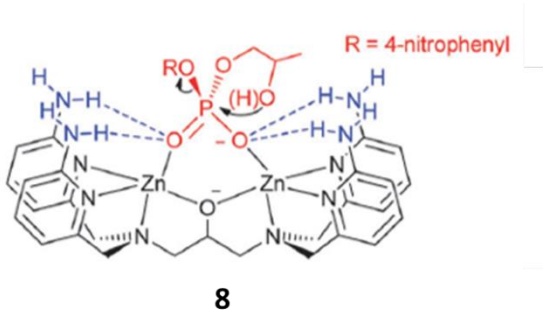

Figure 20. Proposed mechanism of **HPNPP** cleavage for a complex **8** described by Williams et al.

Reprinted with permission from ref. 51. Copyright (2008) American Chemical Society.

Even more challenging is DNA cleavage, which is an intermolecular process. Peng *et al.* reported an artificial diferric complex Fe-L_b **9** that was able to imitate the activity of

nucleases.[52] The diferric centre provided two different functions – one was to stabilise the negatively charged phosphate by an ion-ion interaction, and the other was to facility the formation of an hydroxide anion and nucleophilic attack. Interestingly, the cleavage of DNA only occurred with the assistance of bisguanidinium groups, which bound to the adjacent phosphate groups and pulled the DNA molecule closer to the diferric centre. The diferric centre and bisguanidinium groups worked in a synergistic manner to achieve DNA cleavage that was one order of magnitude faster than the artificial catalyst **10** without bisguanidinum groups (Figure 21, top).

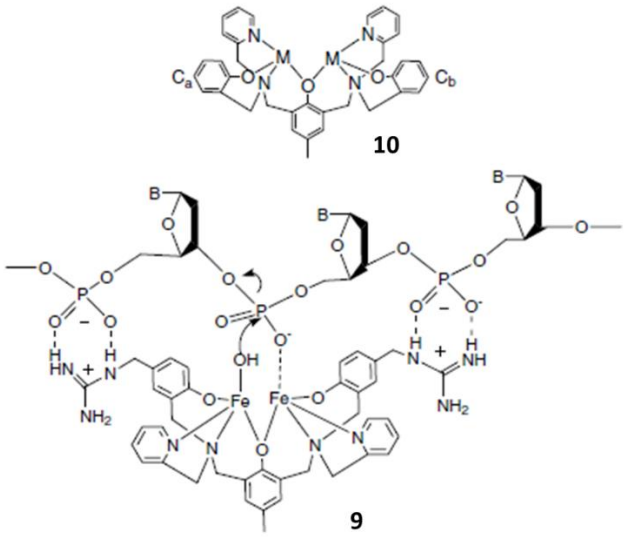

Figure 21. Structure of the control complex **10** (top) and proposed mechanism for cleavage of DNA by Fe-L_b **9** (bottom). Reprinted with permission from ref. 52. Copyright (2008) Elsevier Inc.

1.2.2 Cooperativity in phosphate ester cleavage

Artificial phosphodiesterase enzymes that cleave ribonucleic acid (RNA) and deoxyribonucleic acid (DNA) has been extensively studied, and a number of possible reaction mechanisms have been proposed.[53] In essence, the mechanism of phosphate ester cleavage is a substitution reaction, and it may follow three critical mechanisms as shown in Figure 22.[53-54]

i. A dissociative (D_N + A_N) mechanism, where the expulsion of the leaving group precedes nucleophilic attack. This allows the formation of the metaphosphate intermediate (Figure 22, bottom right).

ii. An associative two-step (A_N + D_N) mechanism, where nucleophilic attack on phosphorus to form the phosphorane intermediate occurs before departure of the leaving group (Figure 22, top left).

iii. A concreted A_ND_N mechanism, where there is no intermediate observed. The formation of the P-nucleophile bond and the cleavage of the P-leaving group bond occurs simultaneously (Figure 22, middle).

Out of these three critical mechanisms, the A_N + D_N and A_ND_N mechanisms are considered to be the most likely due to the presence of a negative charge on the phosphoryl group following nucleophilic attack. Such an intermediate or transition state would benefit from extra binding between the negatively charged phosphoryl group and the positively charged transition metal, as seen with many enzyme mimics. However, whether this reaction occurs via an associative or a dissociative mechanism is still under debate, as this is likely to depend on the nature of the substrate and the nature of the leaving group.

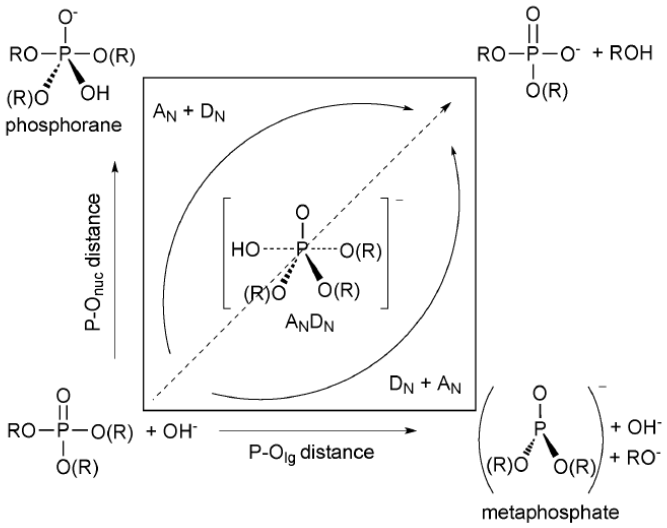

Figure 22. More O'Ferrall-Jencks diagram showing the limiting mechanisms for phosphate ester hydrolysis. Reprinted with permission from ref. 53. Copyright (2012) Royal Society of Chemistry.

There are numerous ways by which a metal centre is able to promote phosphodiester cleavage (Figure 23).[55] The mononuclear centre may act as a Lewis acid to polarize a phosphorus-oxygen and activate the phosphorus for nucleophilic attack (Figure 23, A), or it can enhance the nucleophilicity of water by stabilising the hydroxide anion for direct nucleophilic attack in neutral conditions (Figure 23, B). Moreover, Figure 23C shows that the metal can act as a general base for nucleophilic attack in alkaline conditions. Last but not least, the metal could stabilise the leaving group, as shown in the two structures in Figure 23, D. It is worth noting that one metal centre could activate more than one of these pathways at the same time. In addition, dinuclear complexes are common, which could result in multiple simultaneous site activations.

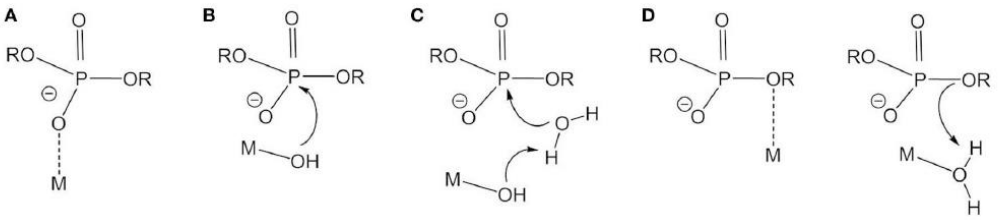

Figure 23. Proposed mechanisms of phosphodiesters hydrolysis by (A) Lewis acid activation; (B) nucleophile activation; (C) base catalysis; (D) leaving group stabilization. Reprinted with permission from ref. 55. Copyright (2019) Frontiers Media S.A.

With respect to this thesis, we were interested in systems for phosphodiester cleavage that involves cooperativity of dinuclear centres, where binary or multiple activations could combine to achieve higher catalytic activity, for example, where one metal centre acted through a Lewis acid activation pathway, and the other through a nucleophile activation pathway. As the substrate, we utilised 2-hydroxypropyl *p*-nitrophenyl phosphate (**HPNPP**, Figure 24), a popular RNA model known to be cleaved by dinuclear zinc or copper complexes. Upon cleavage, the leaving group *p*-nitrophenol (**PNP**) allowed the reaction to be easily followed by UV spectroscopy by measuring at 400 nm.

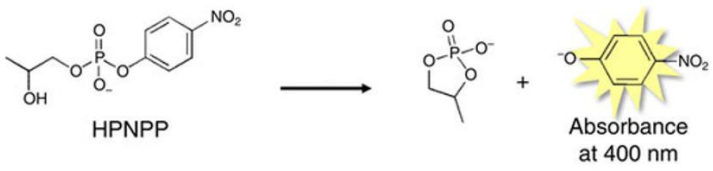

Figure 24. Transesterification of **HPNPP** to afford a **PNP** and a cyclic phosphate (**cP**) as two products.

A simple way to form a di-metallic complex is to use metal-chelating ligands such as 1,4,7-triazacyclononane (TACN). By joining two TACN units together in a covalent way, Morrow and Richard were able to demonstrate efficient cooperativity between two Zn^{2+} ions for the cleavage of **HPNPP** (Figure 25).[56-57] The catalytic activity of Zn_2(L20) **12** in water was almost 120-fold faster than the corresponding mononuclear Zn(L1OH) control analogue **11**, while the catalytic activity in methanol was further enhanced due to the weaker solvent polarity which resulted in stronger Zn^{2+} chelation at the TACN catalytic sites.

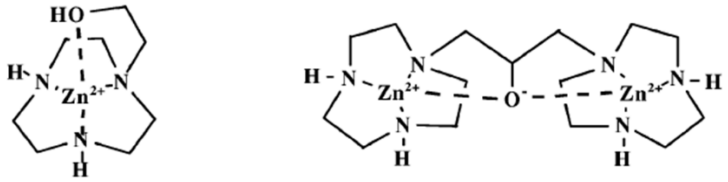

Figure 25. Chemical structure of the control molecule Zn(L1OH) **11** and the catalyst Zn_2(L20) **12** for **HPNPP** cleavage. Reprinted with permission from ref. 56. Copyright (2003) American Chemical Society.

Moreover, Brown and co-workers reported a more efficient di-Zn complex (Zn_2([12]aneN$_3$)$_2$, **13**) for the hydrolysis of neutral carboxylate esters, activated amides and neutral phosphates with a 10^6-10^9-fold rate acceleration in the presence of 1 equivalent of methoxide in methanol (pH 9.5) when compared to water.[58] And relative to the background reaction at pH 9.5, Zn_2([12]aneN$_3$)$_2$ **13** accelerates cleavage of each phosphate diester by a remarkable factor of 10^{12}-fold. The main accelerating effects of the solvent change are proposed to be due to increased pre-association and Zn^{2+}/P=O binding and an enhanced activity of the metal-bound

methoxide which drives the actual phosphoryl transfer subsequent to the binding process.

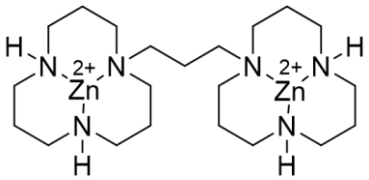

$Zn_2([12]aneN_3)_2$ **13**

Figure 26. Catalyst structure of $Zn_2([12]aneN_3)_2$ **13** for **HPNPP** cleavage. Adapted with permission from ref. 58. Copyright (2006) American Chemical Society.

Ungaro and co-workers have also shown the possibility of **HPNPP** cleavage by cooperativity between copper ions.[59] Two Cu^{2+} ions were bound by 1,4,7-triazacyclononane (**TACN**) head groups that were covalently anchored to a calix[4]arene body in 1,2-vicinal relationship (Figure 27, left). The structure forces these metal ions to be close which allows cooperativity for stabilisation of the substrate and activation of the hydroxyl group at the same time. Once the hydroxyl group is activated, **HPNPP** can be cleaved by an intramolecular attack. Interestingly, the 1,3-distal bimetallic copper **15** (Figure 27, right) did not show catalytic activity due to the *pinched cone* conformation where the two TACN units were brought together in a nearly parallel fashion. This squeezed the **HPNPP** substrate into a narrow cavity where the 2-hydroxylpropyl chain was prevented from forming the pseudocyclic conformation required for phosphodiester cleavage. This was therefore not a good host for **HPNPP** cleavage.

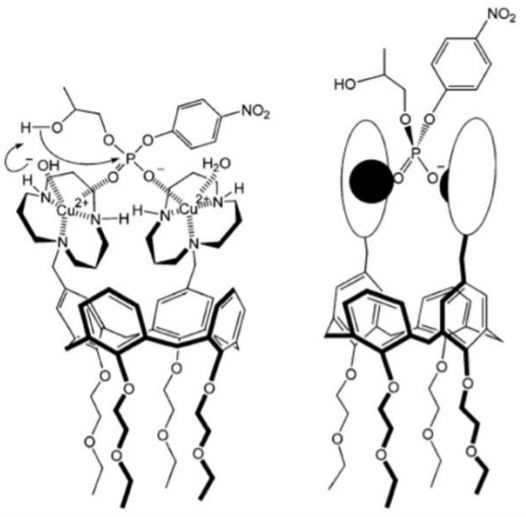

14 **15**

Figure 27. Chemical structure of the 1,2-vicinal bimetallic calix[4]-arene-based catalyst **14** and the 1,3-distal catalyst **15**. Reprinted with permission from ref. 59. Copyright (2006) American Chemical Society.

Moreover, this 1,2-vicinal calix[4]-arene-based catalyst **14** was also able to cleave diribonucleoside monophosphates such as UpU and UpG.[60] Di- and tri-nuclear copper(II) complexes with the calix[4]-arene scaffold also gave good reactivity in the cleavage of oligoribonucleotides which is an even closer mimic of ribonuclease and RNase A.

Pasquato and Scrimin observed that TACN-Zn^{2+} moieties anchored onto the surface of gold nanoparticles achieved efficient acceleration of RNA cleavage.[61] The TACN moieties were anchored to sub 2 nm gold nanoparticles through strong thiol-gold bonds to form a monolayer of organic molecules on the gold surface. This demonstrated another way to bring the Zn^{2+} ions together to close proximity and to promote cooperativity. In this example, these cooperative effects resulted in catalysis with the nanoparticles **16** being approximately 160-times faster than the isolated C_{12}TACN **17** ligands in solution.

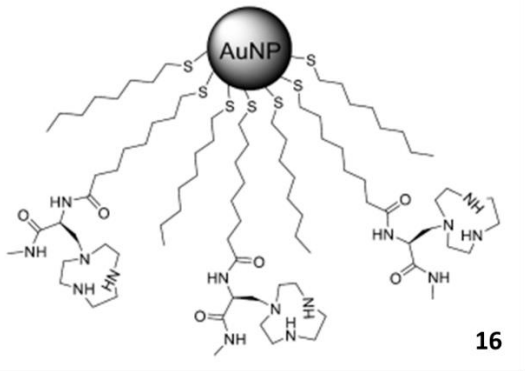

Figure 28. Schematic illustration of gold nanoparticles **16** covered by a monolayer of TACN-Zn amphiphiles and the C_{12}TACN **17** ligands

Scrimin and Mancin demonstrated how control over cooperativity could be used to regulate catalytic activity. They devised a host-guest system consisting of a γ-cyclodextrin (**γ-CD**) host and a precatalyst **18** that consisted of a C_{10} alkyl chain containing two terminal TACN-Zn catalytic sites (Figure 29).[62] The bimetallic compound **18** has the two metallic sites far away when free in solution and does not possess catalytic activity. However, upon addition of **γ-CD** as a host, the hydrophobic alky chain of precatalyst **18** self-assembles into the hydrophobic cavity of host **γ-CD** to reduce the free energy of the system, forcing the TACN-Zn catalytic sites into close proximity and activating **HPNPP** cleavage. Their proposed mechanism showed the two zinc centres acting as Lewis acids to provide simultaneously stabilization of the increasing charge in the transition state (Figure 29, b). Allosteric modulation was facilitated by the addition of 1-adamantane carboxylate **19** as a competitive guest of **γ-CD** to release catalyst **18** back into solution. This allowed reversible modulation of catalysis depending on the relative concentrations of the components in the system.

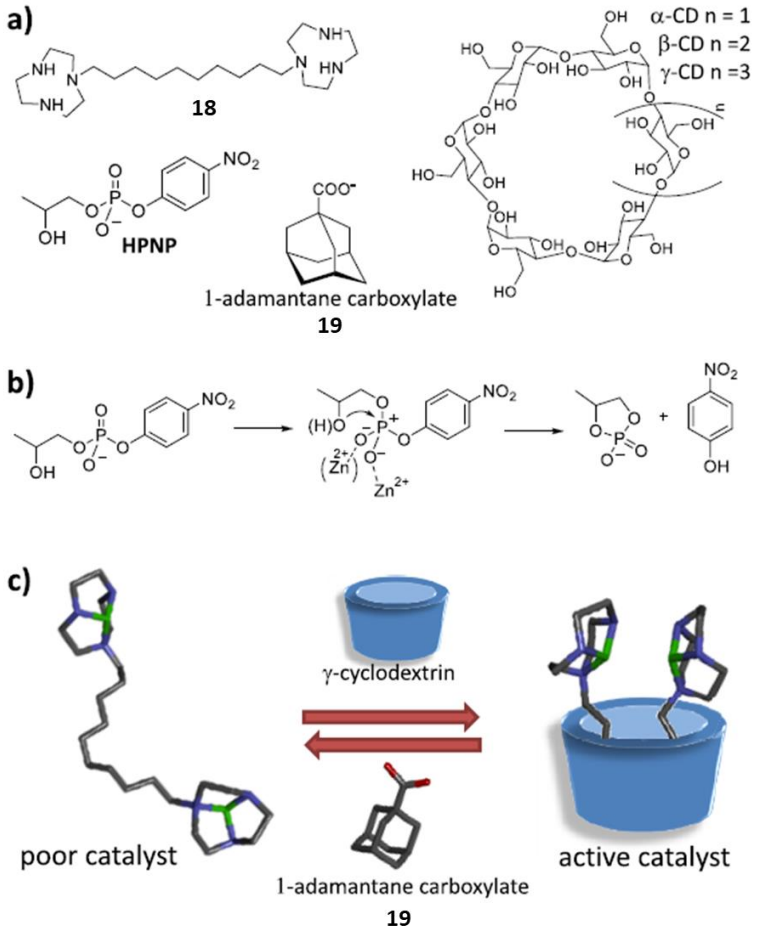

Figure 29. a) The chemical structure of ligand **18** and host **γ-CD**; b) proposed mechanism of **HPNPP** cleavage; c) Schematic illustration of the allosteric modulation of the activity of catalyst studied. Reprinted with permission from ref. 62. Copyright (2020) American Chemical Society.

Up until a few years ago, the design of these bimetallic catalysts was based on the direct linkage of zinc-binding units through an alkyl chain,[56-58] or their immobilisation onto molecular scaffolds,[59-60] dendrimers,[63-64] or onto nanoparticles.[61, 65] This was done with the objective of inducing cooperativity between zinc centres by pre-organising the zinc-binding sites in close proximity. [66] The majority of these approaches were inspired by the classic idea of the lock-and-key theory of enzyme catalysis. This theory supported the notion that highly rigid binding pockets, with precise positioning of functional groups were necessary for effective catalysis. While numerous successful artificial catalysts have been designed using this theory, the ideas around enzyme catalysis have since evolved greatly, meaning that much more dynamic

methods for forming supramolecular catalysts may be possible.

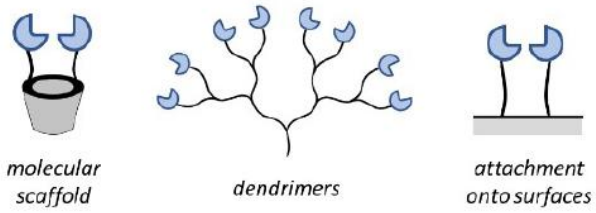

Figure 30. Different strategies for the pre-organization of functional groups to induce cooperativity. Reprinted with permission from ref. 66. Copyright (2021) Wiley-VCH GmbH, Weinheim.

1.2.3 Mechanisms of Enzyme Action

With greater understanding of non-covalent interactions within chemical and biological systems, several hypotheses have emerged and evolved in attempts to describe enzymatic catalysis. These include the classic lock and key model, the induced fit model, and the conformational selection model. All the theories have evolved over time and has helped us build a better understanding of enzyme catalysis and has given us important clues for the design of more efficient supramolecular catalysts.

1.2.3.1 The lock and key hypothesis

Supramolecular chemistry was fundamentally inspired by the enzyme-substrate interaction first described by Emil Fisher, who proposed the lock and key model while conducting research on yeast fermentation in 1894.[67-68] To explain the high specificity of enzymes, Fisher proposed that the enzyme and the substrate must have complementary shapes to closely fit with one another, which can be represented by the animation of a key and a lock in Figure 31. Only the correct key can fit into the keyhole of the lock, in close analogy to how only specific substrates

with the correct size and shape are able to bind with the specific geometric shape of an enzyme active site.

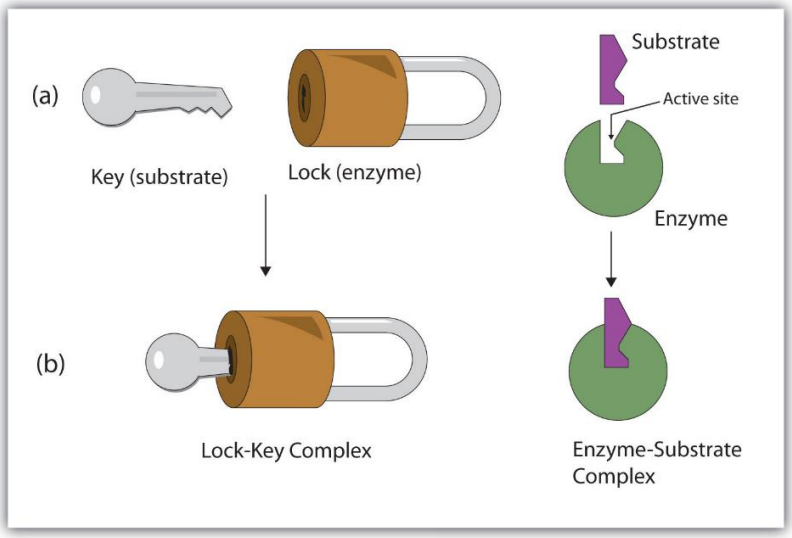

Figure 31. An animated illustration of the "lock and key" model

Up until the middle of the twentieth century, the lock and key model met the conceptual needs of chemistry, biology, and medicinal science. It led to the development of key areas in the supramolecular field such as molecular recognition and host-guest chemistry. However, the lock and key model had some limitations. It could not explain the formation of transition states, the unstable transient structures that are formed during chemical reactions. With respect to the changing three-dimensional structure of transition states, it was difficult to explain why the lock (enzymes) could still be opened by a modified key (transition state).

1.2.3.2 The transition state hypothesis

Four decades later, Haldane and Pauling refined the lock and key model and proposed an early variation of the transition state model.[69,70] Linus Pauling found that the conformation of gamma globulin (antibodies acting as enzymes) was highly dynamic, and only one specific conformation of the antibody was selected in the presence of an antigen (substrate), which

was stabilized by the attractive forces between the polypeptide chain of the antibody and the antigen to achieve closely complementarity. Importantly, this led to the production of specific bonds between the antibody and the antigen, allowing the formation of the activated complex (transition state). In the substrate-enzyme complex, the enzyme was not in the normal conformation, but rather in a strained conformation which was induced by attractive forces with the substrate. This is an early description of the transition state theory. What is widely accepted now is that the transition state is an unstable intermediate, which is a hypothetical "in between" status in a reaction where reactant bonds are partially broken, and product bonds are partially made. The formation of transition states leads to a decrease in activation energy and an acceleration of reaction rate.

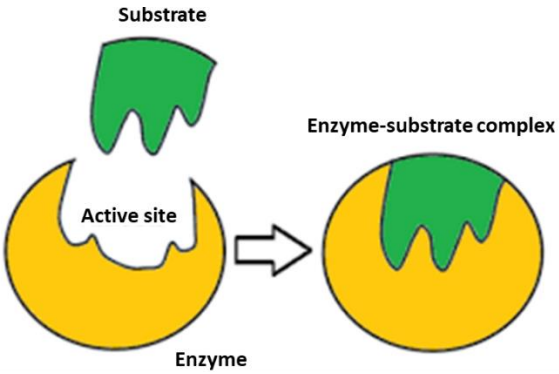

Figure 32. An animated illustration of the transition state theory. Substrate induces the change in the conformation of an enzyme to form a complementary enzyme-substrate complex.

1.2.3.3 The induced fit hypothesis

As the idea of the changing conformation of enzymes was gradually accepted, the dynamic nature of proteins gained the attention of scientists. In 1958, Daniel Koshland proposed the induced fit model for enzymatic catalysis.[71-72] In this model, the perfect complementary substrate is not the only species that can bind with specific enzymes, but smaller and bigger molecules could also bind tightly without reacting. He found that beta-amylose had a structurally much larger inhibitor, cyclohexaamylose. This could not be explained by the lock

and key model, which said that poor reactivity was due to failure in binding.[73]

Additional support for the induced fit model was demonstrated by the enzyme phosphoglucomutase.[74] In Figure 33, the original configuration of phosphoglucomutase is shown which have the phosphate and SH groups buried inside the enzyme. Upon addition of a substrate, there is an interaction with the phosphate, and site X, which results in exposure of the SH group. This change in conformation and exposure of the SH group resulted in higher catalytic activity, and demonstrated the existence of induced configurational change.

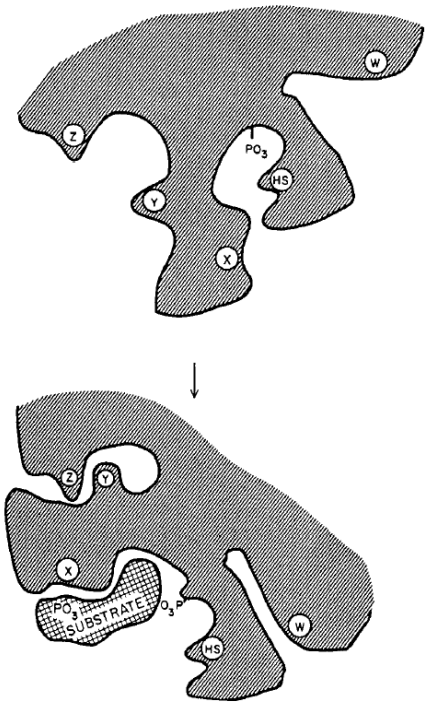

Figure 33. Schematic illustration of ligand-induced conformational change. Reprinted with permission from ref. 74. Copyright (1965) American Society for Biochemistry and Molecular Biology.

In addition, the complementary binding between a substrate and an enzyme is necessary for successful catalysis, which is in agreement with the lock and key model.[72] Koshland described his theory as “hand-in-glove”, which added flexibility compared to the lock and key model. Substrates play an important role in determining the final configuration of enzymes. The active

configuration is formed only when the active sites of enzymes align complementarily with the binding group of substrates (Figure 34, top right). All active sites A, B and C works in synergistic manner. However, poor catalysis would happen if any active site was too far in distance for cooperativity (Figure 34, bottom left) or was buried in a non-active position (Figure 34, bottom right). Overall, the induced fit model combined the high flexibility of enzymes, with the lock and key model describing the complementarity of substrates and enzymes. These ideas helped to further the understanding of enzyme catalysis.

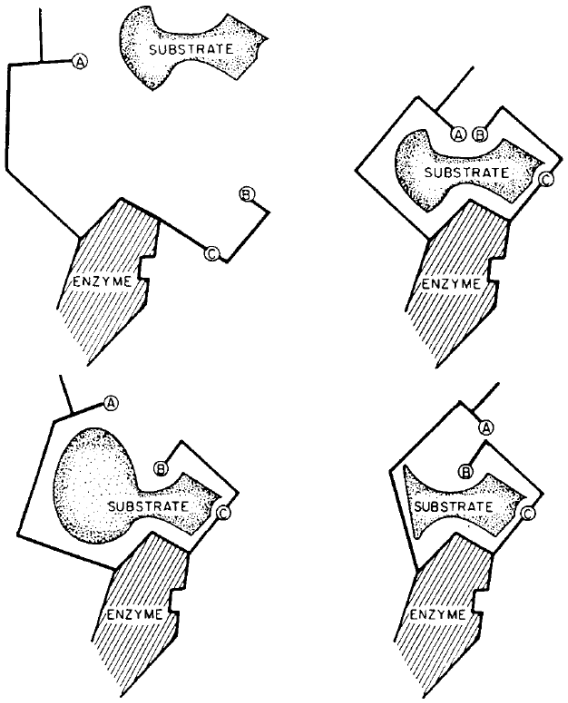

Figure 34. Schematic model of the induced fit model. Reprinted with permission from ref. 72. Copyright (1994) Wiley-VCH GmbH, Weinheim.

1.2.3.4 The conformational selection hypothesis

It is worth noting that both the lock and key and induced-fit models are based on the assumption that proteins exist in one single stable conformation under experimental conditions. In contrast to the prevailing view of these two models, Straub in 1964 proposed the conformational selection paradigm.[75] In this hypothesis, the ligand selects one

conformation of a dynamically fluctuating protein, which pre-exists as numerous diverse conformations. Zavodszky and co-workers then proved this hypothesis with initial experimental evidence in 1966.[76] Over two decades later, the general concept of conformational selection and population shift was established by Sligar and Holynes in 1999 based on the energy landscape of a protein.[77-79] Experimental evidence showed the pre-existence of a very large number of conformational ensembles of a protein in solution, which could be confirmed by NMR, X-ray and cryo-electron microscopy, kinetics studies, and single-molecule fluorescence.

Taking ubiquitin as the enzyme of interest, Lange and co-workers reported the presence of all "bound" conformations of ubiquitin in the absence of their binding partners.[80] Figure 35 showed only five conformations of ubiquitin for clarity out of all 46 of the known X-ray crystal structures.[81] Although the relative population of each pre-existing conformational ensemble and energy barrier are unknown, the binding conformation could be shifted from other existing conformations rather than induction of a new conformation not observed in the free protein. Therefore, the population shift involved in conformational selection model could be understood as induced fit processes. Nowadays, it is well understood that the distinction of each binding theory is not absolute as new examples emerge.[82-83] The modern conformational selection theory has been extended to include the basic ideas from the induced fit model and the lock and key model.[84]

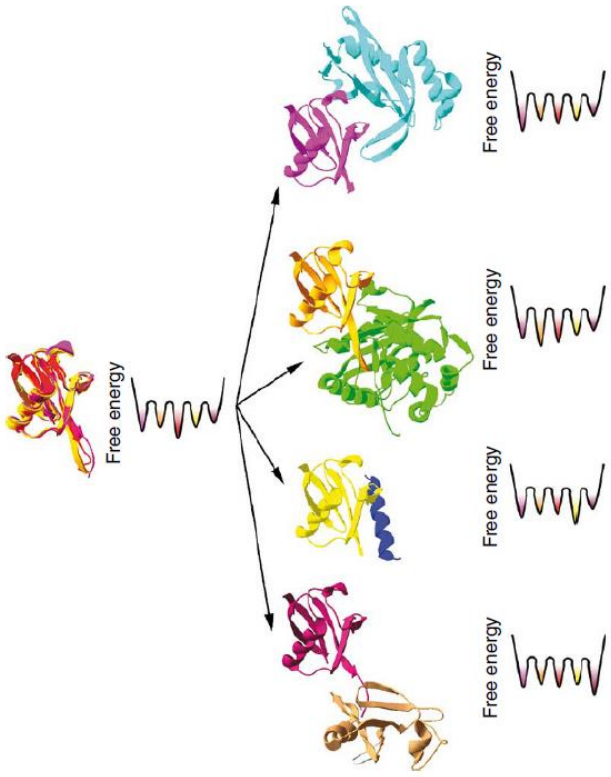

Figure 35. A schematic illustration of molecular recognition processes involving ubiquitin. Reprinted with permission from ref. 81. Copyright (2009) Nature Publishing Group.

It is now very well-accepted that enzymes are highly dynamic and conformationally diverse structures that flex and mould in response to its surrounding environment.[85-87] This flexibility is required for the enzyme to adopt the various conformations required for substrate binding, stabilisation of the transition state, and release of the product. Artificial enzyme mimics have traditionally focused on the careful pre-organization of functional groups in rigid binding pockets which act as an "entropy trap".[88] However, such rigid systems potentially risk binding to the substrate too effectively, which would lower catalyst turnover.

In this thesis, we will investigate the possibility form cooperative catalysts by bringing together the required functional groups using hydrophobic interactions. We envisage that amphiphilic molecules can self-assemble into micellar or vesicular structures to induce cooperativity in an intermolecular fashion. The modularity and flexibility of such systems will allow for easy

modification and optimisation of the catalytic system. This concept bears resemblance to the conformational selection hypothesis in that the self-assembled system represents a dynamic system with a range of possible arrangements for the individual building blocks. The addition of a substrate has the potential to select the most effective supramolecular assembly to catalyse the reaction, and the dynamic nature of the system would allow for the flexibility required for substrate binding, stabilisation of the transition state, and product release. This should limit issues such as substrate or product-induced inhibition of the supramolecular catalyst and may be a better imitation of enzyme catalysis in nature. Our aim is to demonstrate this concept for the self-assembly of catalytically active building blocks to design novel cooperative catalyst systems.

1.3 Previous work in our group

Demonstration of intermolecular cooperativity began in our research group with the synthesis of the amphiphilic molecule C_{16}TACN **20**. We found that C_{16}TACN·Zn^{2+} (**20**·Zn^{2+}) formed vesicular structures in aqueous solution buffered at pH 7.[89] This was able to efficiently cleave **HPNPP** with a k_{cat} of 1.4×10^{-3} s^{-1} as determined by fitting into Michaelis-Menten kinetics. This rate was comparable to the k_{cat} of 4.2×10^{-3} s^{-1} when the TACN ligands were anchored directly onto the surface of gold nanoparticles. This suggests that these vesicular structures had enough dynamic stability to enable cooperativity between adjacent C_{16}TACN **20** groups and the formation of catalytic pockets. The average diameter of the vesicular aggregates was measured by dynamic light scattering (DLS) to be 20-30 nm, and their vesicular structure was confirmed by electron microscopy (EM) and small angle neutron scattering (SANS).

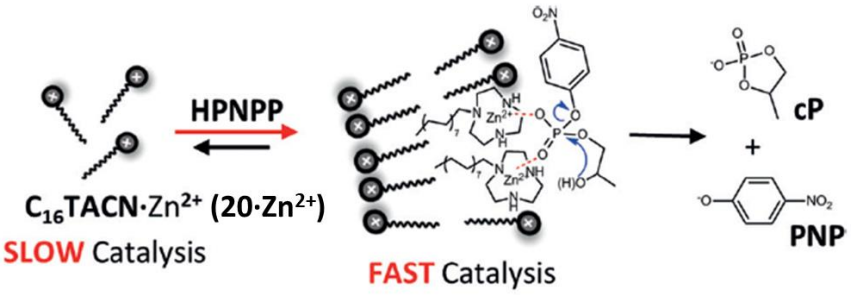

Figure 36. Schematic illustration of cooperative catalysis induced by neighbouring TACN·Zn^{2+} complexes **20**·Zn^{2+} upon assembly in vesicular structures. Reprinted with permission from ref. 89. Copyright (2018) Wiley-VCH GmbH, Weinheim.

The transphosphorylation of **HPNPP** was possible due to the formation of catalytic pockets on the surface of the vesicles. Figure 37 shows a plot of the initial rates of **HPNPP** cleavage with increasing concentration of Zn^{2+} ions in the presence of 50 μM of C_{16}TACN **20** amphiphiles and 500 μM of **HPNPP** substrates in an aqueous buffer (10 mM of **HEPES**, pH 7). Under these conditions, the system was above the critical aggregation concentration either in the presence or absence of Zn^{2+} (vesicles are formed at all zinc concentrations). At below 0.3 equivalents of Zn^{2+}, the increase of the initial reaction rate was limited. This was due to the fact that a small amount of Zn^{2+} ions would be bound to the TACN head groups, and they would not be neighbouring to each other, due to the repulsion of the positively charged Zn^{2+} ions. As the addition of Zn^{2+} ions approached 0.5 equivalents and higher, the initial reaction rate increased rapidly. This is because the additional Zn^{2+} ions would have to occupy TACN sites that already have a neighbouring TACN·Zn^{2+} complex. With a further increase of Zn^{2+} ions, the initial reaction rate starts to plateau as all the TACN headgroups become saturated with Zn^{2+} ions. This sigmoidal curve is characteristic of cooperative systems and gives evidence for the effective formation of a cooperative catalyst from self-assembly of **20**·Zn^{2+}.

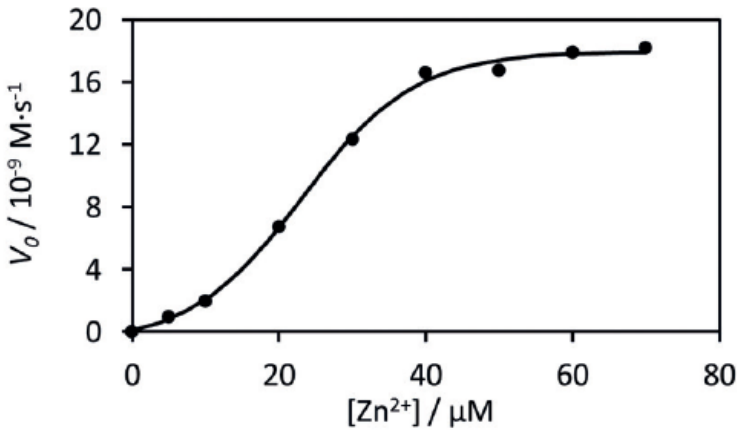

Figure 37. Initial rates of **HPNPP** cleavage at a fixed concentration of 50 μM of C_{16}TACN **20** amphiphiles and 500 μM of **HPNPP** in aqueous buffer (10 mM of **HEPES**, pH 7) at 40 °C. Reprinted with permission from ref. 89. Copyright (2018) Wiley-VCH GmbH, Weinheim.

1.3.1 Substrate-induced catalyst formation

One key observation of the vesicular structures formed from C_{16}TACN·Zn^{2+} (**20**·Zn^{2+}), was that the CAC decreased significantly with increasing concentrations of **HPNPP** (Figure 38). The CAC of **20**·Zn^{2+} was determined to be 93 μM in the absence of **HPNPP**. With increasing concentrations of **HPNPP**, the CAC progressively dropped, eventually reaching a value of ~10 μM in the presence of 1 mM **HPNPP**. This is likely due to the negatively charged phosphate of **HPNPP** having strong ionic interactions with the TACN·Zn^{2+} complex, decreasing the charge repulsion between adjacent TACN·Zn^{2+} groups and decreasing the CAC of the amphiphiles **20**·Zn^{2+}. This indicates that the presence of the **HPNPP** substrate induces the formation of the vesicular structures that allow cooperative catalysis to occur – an interesting phenomenon that is often seen in natural systems, but that has so far not been exploited in synthetic systems.

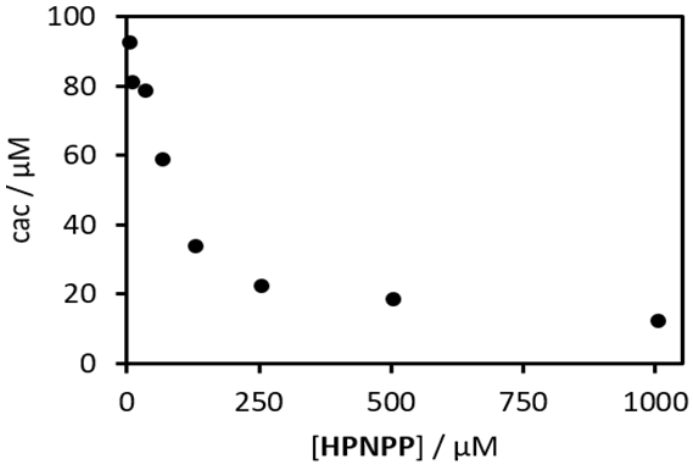

Figure 38. Critical aggregation concentration of **20**·Zn^{2+} amphiphiles measured in the presence of different concentrations of **HPNPP**. Adapted with permission from ref. 89. Copyright (2018) Wiley-VCH GmbH, Weinheim.

In this substrate-induced system, **HPNPP** can be treated as a chemical fuel that drives the formation of self-assembled catalysts that consumes the **HPNPP** itself. Ideally, the decomposition of the **HPNPP** fuel should lead to the disassembly of the self-assembled catalysts to their monomeric amphiphiles, resulting in dissipation of the activated state. This would have created an out-of-equilibrium system with analogies to natural systems such as the production of microtubules from tubulin polymerisation. These out-of-equilibrium systems are currently gaining an increasing amount of attention from researchers worldwide as they imitate living systems which require a constant input of fuel to main a functional and 'alive' state. Our system has some of the features of an out-of-equilibrium system, but we found the cleavage products **cP** and **PNP** are also able to promote the assembly of the C_{16}TACN·Zn^{2+} (**20**·Zn^{2+}) amphiphiles, preventing the dissipation of the system. As a result, the conversion of fuel to waste did not allow the disassembly of **20**·Zn^{2+} amphiphiles. Nevertheless, we were able to demonstrate the substrate-induced formation of a cooperative catalyst, which is one key component in the design of an out-of-equilibrium system. Work is currently ongoing for the design of new substrates whose waste products are not able to stabilize the vesicular assemblies.

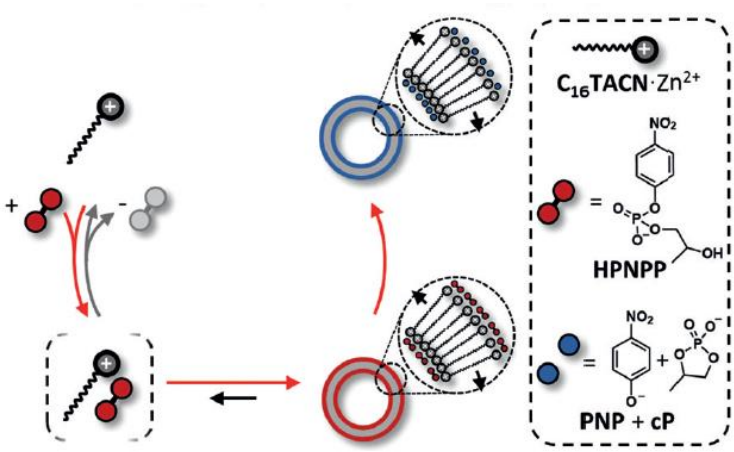

Figure 39. Substrate-induced self-assembled catalysts for **HPNPP** cleavage. Adapted with permission from ref. 89. Copyright (2018) Wiley-VCH GmbH, Weinheim.

1.3.2 Micellar versus vesicular catalysis

It is important to note that the above system is distinctly different to conventional micellar catalysis. Micellar catalysis usually refers to rate accelerations that are due to concentration effects occurring when the reactants are solubilised in the hydrophobic interior of micelles.[31] Some of the most famous examples utilise the designer surfactants **TPGS-750-M** and **SPGS-550-M**, reported by Lipshutz and co-workers.[36] His group has shown that numerous commonly used reactions in organic synthesis can be catalysed in micelles in water media, including a variety of Pd-catalysed cross-coupling reactions.[36] It is widely accepted that the hydrophobic interior of micelles acts to concentrate the reaction components resulting in rate acceleration.

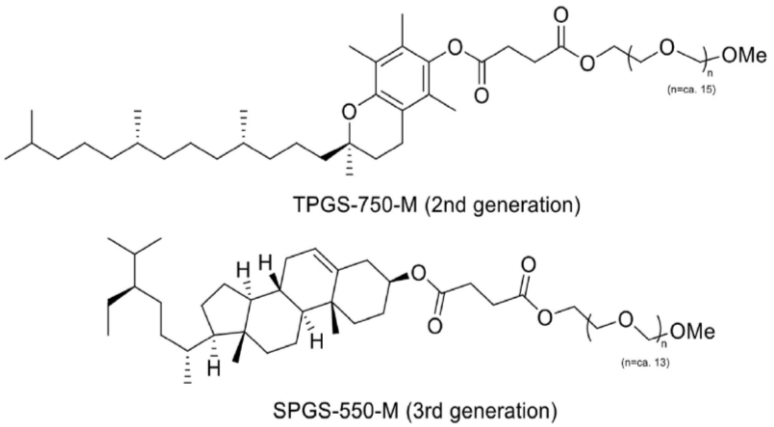

Figure 40. The structure of **TPGS-750-M** and S**PGS-550-M** reported by Lipshutz. Adapted with permission from ref. 32. Copyright (2021) Elsevier Inc.

The cooperative catalysts described in our previous studies involves the self-assembly of C_{16}TACN·Zn^{2+} (**20**·Zn^{2+}) amphiphiles to form vesicular structures. The catalysis in this case is due to synergistic effects that occur between the polar head groups of the amphiphiles, rather than solubilization effects in the hydrophobic portion, as for conventional micellar catalysis. Moreover, it has been shown that cooperativity between the polar headgroups is less likely to occur on the surface of micelles due to their highly dynamic nature. Scrimin and co-workers have reported micellar systems containing C_{12}TACN·Zn^{2+} (**17**·Zn^{2+}) amphiphiles (Figure 41),where ineffective catalysis was observed, with activity two orders of magnitude lower than their nanoparticle-based counterparts **16** (see Figure 28).[61] The low catalytic activity was attributed to the inability to form cooperative binding sites due to the rapid exchange of amphiphiles between the micellar structure and the bulk of the solution. Amphiphiles are estimated to have a residence time in the order of 10^{-5} to 10^{-6} seconds, which would limit the possibility to form cooperative interactions.[90-92]

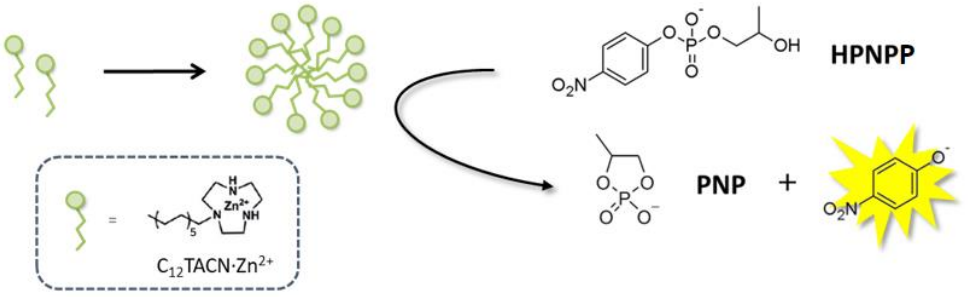

Figure 41. Micellar catalysis of **HPNPP** transesterification

On the other hand, vesicles are known to have much greater stability, with much slower exchange of amphiphiles between the vesicle bilayers and the bulk.[93-94] This gives the possibility of cooperative catalysis occurring in the surface of vesicles in between the polar headgroups.

1.3.3 A dynamic stimuli-responsive system

The first 6 months of my PhD was spent completing a project on a stimuli-responsive system[95] which I began during my Honours. This stimuli-responsive system was based on a catalytically active amphiphile similar to the $C_{16}TACN{\cdot}Zn^{2+}$ (**20**$\cdot Zn^{2+}$) system described above. Taking advantage of the reversibility of the self-assembly process, we designed a catalyst system that could switch between assembled and disassembled states, upon application of an external stimuli. The stimulus that we used was light, which has the advantage of being able to have high temporal and spatial control.

The amphiphile that we designed was based on the **20**$\cdot Zn^{2+}$ amphiphile, and contained a diazobenzene moiety embedded in the hydrophobic alkyl chain (see Figure 42). The diazobenzene is able to respond to external light irradiation by *E*/*Z*-isomerization, and the key feature is that the *E*- and *Z*- configured amphiphiles have different propensities for self-

assembly, resulting in switching between catalysis 'ON' and 'OFF' states.

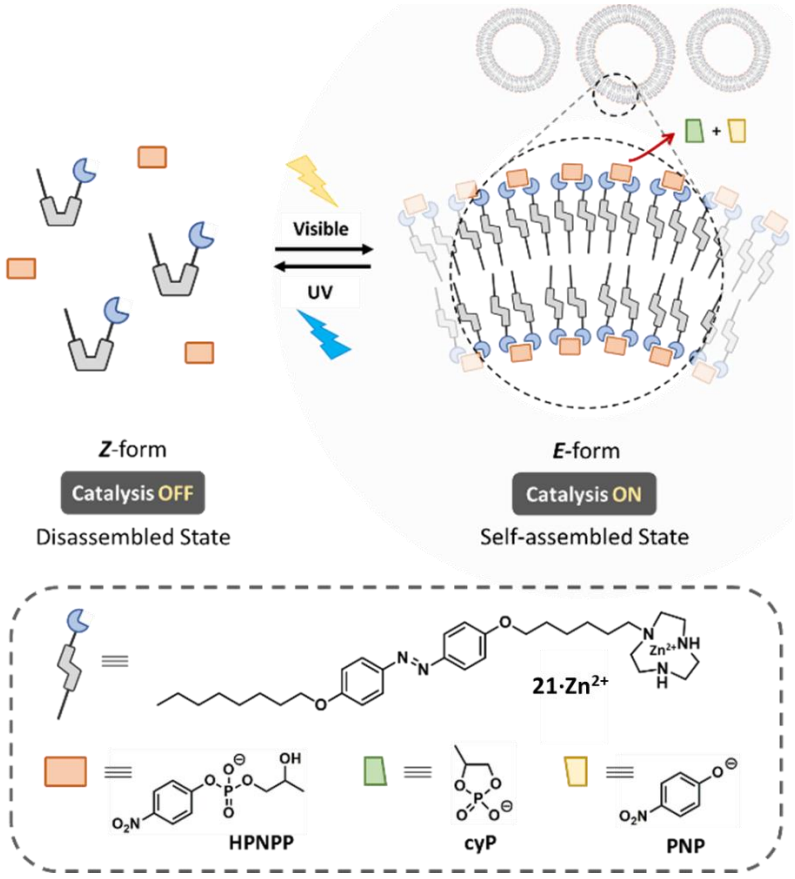

Figure 42. Photo-responsive self-assembled catalyst **21**·Zn^{2+} switching between catalysis 'ON' and 'OFF' states following irradiation. Adapted with permission from ref. 95. Copyright (2019) Wiley-VCH GmbH, Weinheim.

We first investigated the photoisomerization of the designed **21**·Zn^{2+} upon irradiation with UV and visible light. Figure 43 shows that the *E* configuration of **21**·Zn^{2+} had strong absorption at 365 nm in a solution buffered at pH 7 ([**HEPES**] = 5 mM), and its *Z* configuration can be formed following under irradiation at 365 nm for 15 mins, giving two bands at 320 nm and 450 nm.

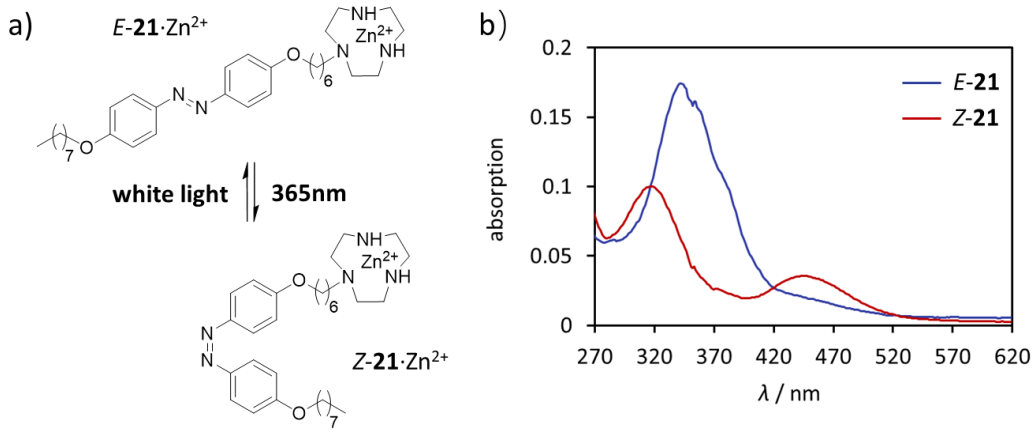

Figure 43. a) The interconversion of *E*- and *Z*-configuration of amphiphile **21**·Zn^{2+}; b) UV spectrum of both configurations of amphiphile **21**·Zn^{2+}.

The photoisomerization of **21** was then conducted in ^{1}H NMR to more precisely study the photostationary state following *E*/*Z*-isomerisation. Under irradiation of 365 nm, the NMR spectrum of 150 µM solution of **21** in CD_3OD gave a photostationary state ratio of *E*-**21**:*Z*-**21** = 78:22, while irradiation with white light for 15 mins converted the compound to exclusively the *E*-configuration (*Z*-**21**:*E*-**21** ≥ 98:2). It was important to note that the interconversion between the *E*- and *Z*-configurations was both solvent and concentration dependent. A 150 µM solution of **21** in CD_3OD could be cycled between a predominantly *E*-configuration (around 80%) and *Z*-configuration (around 98%) for at least 8 cycles using sequential irradiation at 365 nm and with white light, without loss of efficiency and the formation of side products.

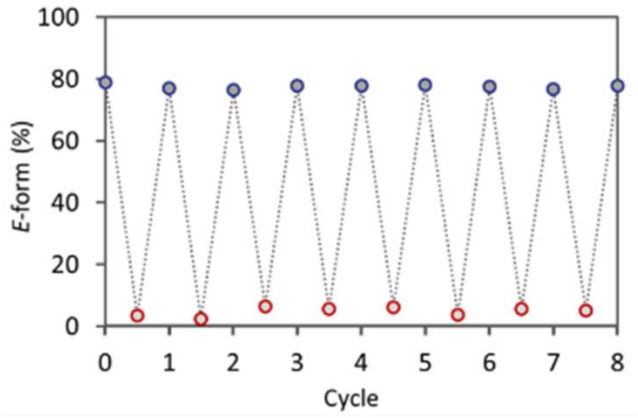

Figure 44. Sequential switching between *E*- and *Z*-configuration of amphiphile **21** (150 µM) in CD_3OD by ^1H NMR.

The CACs of both *E*- and *Z*-**21**·Zn^{2+} enriched solutions were measured using fluorescence titrations in the presence of 500 µM of **HPNPP** substrate and the fluorescence probe **Nile red** (λ_{ex} = 570 nm). With addition of increasing amounts of the amphiphile **21**·Zn^{2+}, the CAC can be identified as the point where there is a significant change in fluorescence intensity and often also a shift in the maximum wavelength of fluorescence, due to the solubilisation of the **Nile red** into the hydrophobic interior of the self-assembled vesicular structure. These fluorescence titrations revealed a CAC of 20 µM for a solution containing predominantly the *E*-isomer and a CAC of 60 µM for the *Z*-isomer. This difference in CAC was due to differences in the propensity for packing of the *E*- and *Z*-isomers, where the *E*-isomers more readily assembled into vesicular structures. This narrow window between the CACs of *E*- and *Z*-**21**·Zn^{2+} gave us the possibility to demonstrate control over the self-assembly process, which required the catalyst concentration to be above the CAC of the *E*-isomer, but below the CAC of the *Z*-isomer.

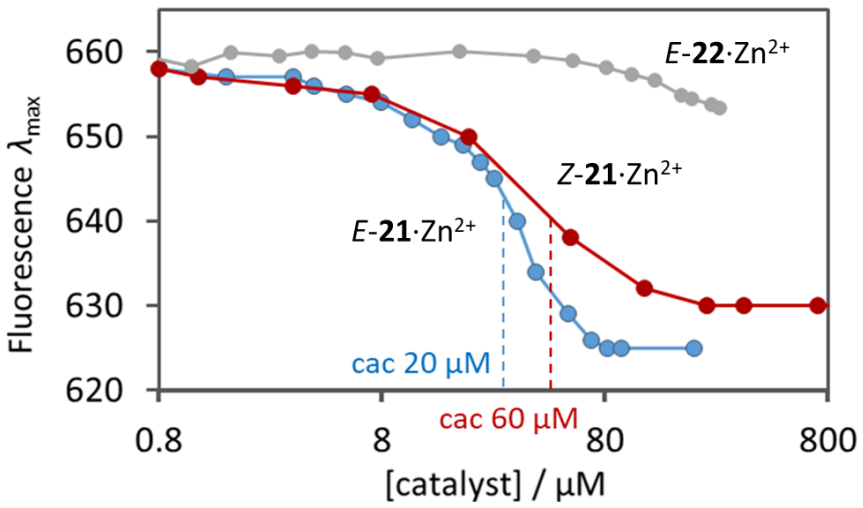

Figure 45. The determination of the CACs of *E*- (blue) and *Z*-**21**·Zn^{2+} (red) and the control molecule ***E*-22**·Zn^{2+} (grey) by fluorescence spectroscopy in the presence of 2 µM of **Nile red** (λ_{ex} = 570 nm) and 500 µM of **HPNPP** in 5 mM of HEPES buffer pH 7.0 at 20 °C.

The catalytic activity of *E*- and *Z*-**21**·Zn^{2+} were examined in the presence of excess **HPNPP** (500 µM) as shown in Figure 46. The initial rates of reaction were determined at varying concentrations of *E*- and *Z*-**21**·Zn^{2+} in an aqueous buffer solution at pH 7 ([**HEPES**] = 5 mM). The initial reaction rates of both configurations of **21**·Zn^{2+} were reasonably low at concentrations below 20 µM. Once the catalyst concentration was increased to 20 µM, there was an obvious increase in **HPNPP** cleavage with *E*-**21**·Zn^{2+} (blue dots), while the catalytic activity of *Z*-**21**·Zn^{2+} remained relatively low (red dots). This observation occurred at 20 µM, which matched the CAC value determined by fluorescence titration, and indicates that the formation of vesicular structures was crucial to induce cooperative catalysis. This concentration also gave the biggest difference in the ratio of catalytic activities between the two isomers, as above this concentration, *Z*-**21**·Zn^{2+} also begins to have significant catalytic activity. This is likely due to the fact that *Z*-**21**·Zn^{2+} may also be able to form dimers or self-assembled structures at these higher concentrations. Control experiments were conducted using **22**·Zn^{2+}, which possessed much shorter C_2 alkyl chains to prevent hydrophobic interaction for self-assembly. The low observed catalytic activities of both *E*- and *Z*-**22**·Zn^{2+} (grey and yellow dots) indicated the lack of cooperative catalysis due to the inefficient self-

assembly.

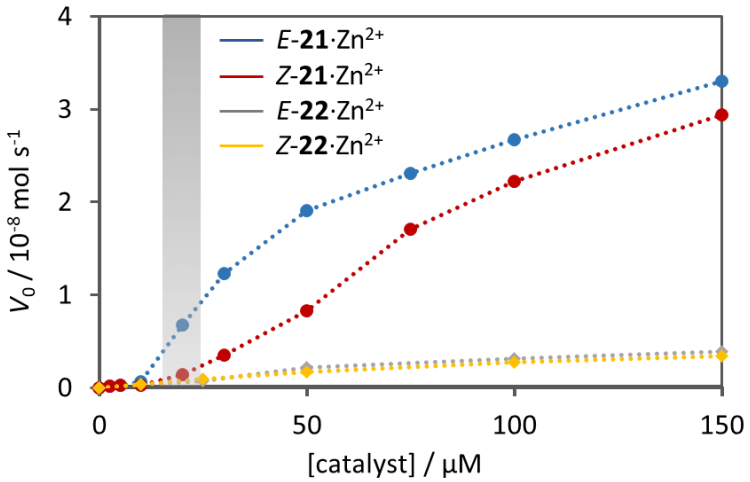

Figure 46. Initial rate of **HPNPP** cleavage at increasing concentration of **21**·Zn^{2+} and control molecule **22**·Zn^{2+} in the presence of 500 µM of **HPNPP** in 5 mM of HEPES buffer pH 7.0 at 40 °C.

At the end of this project, the reversible photo-modulation of catalyst activity was finally investigated. The cycling between catalysis 'ON' and 'OFF' states were conducted at 20 µM of catalysts in the presence of an initial 500 µM of **HPNPP** in an aqueous buffer solution at pH 7 ([**HEPES**] = 5 mM). As we observed in Figure 47, when we started the reaction with *E*-configuration of **21**·Zn^{2+} and irradiated the same sample with sequential irradiation of UV and white light for 5 cycles, the interconversion between self-assembled *E*-isomers and disassembled *Z*-isomers resulted in the in situ up- and down- regulation of catalytic activity. The decrease in the maximum catalytic activity was due to the depletion of the **HPNPP** substrate over time, since no additional substrate was added following each cycle. This catalytic system is a neat example of coupling structure formation with the emergent property of catalysis. In this case, by exploiting the reversible nature of the structure formation, an external stimulus was used to switch between the assembled and disassembled states, resulting in control over catalytic activity.

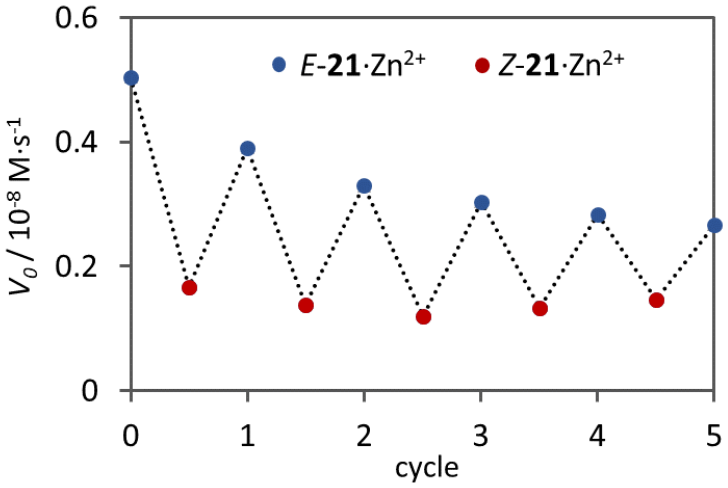

Figure 47. Initial rates of **HPNPP** cleavage following sequential photoisomerization of catalyst **21**·Zn^{2+}.

1.4 Our system of interest – a multifunctional catalyst

In the examples of catalysts formed by supramolecular self-assembly presented so far, we can see some unique properties due to the modular and reversible nature of how the catalysts are constructed. So far, we have only examined the self-assembly of catalysts from a single amphiphilic molecule. One of the objectives of this thesis is to examine more complex systems that are composed of more than a single amphiphile. We aim to take advantage of the modular nature of this system to mix and match multiple functional groups and to induce cooperativity and enhancement of cooperative activity. This also has the potential to modify the ratio of catalytic components to optimise catalytic activities, which is not possible when catalytic units are linked covalently or immobilised onto solid supports. Based on the promising preliminary studies presented in sections 1.3.1 - 1.3.3, we think self-assembled vesicles could be a new pathway to the imitation of nature enzymes in supramolecular chemistry, which would give us a high possibility to create more efficient catalytic systems in a more efficient way.

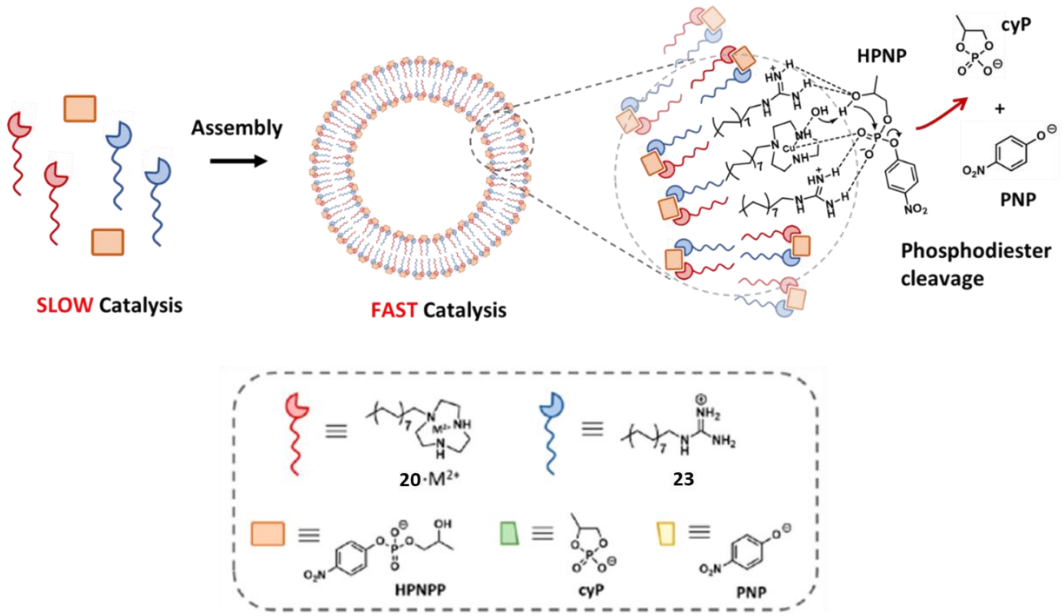

Figure 48. General representations of a cooperative catalyst formed by a multicomponent cooperative catalyst (C_{16}TACN·Cu^{2+} **20**·Cu^{2+} and C_{16}Gua **23**) formed by self-assembly.

Chapter Two: A Multifunctional Self-Assembled Catalyst

2.0 Overview

In our preliminary studies of self-assembled catalysts using C_{16}TACN **20** amphiphiles, cooperative catalysis was achieved by the formation of vesicular structures, which brought into proximity of two Zn^{2+}-binding TACN moieties to work together in a synergistic manner. One of the Zn^{2+} units is believed to increase the electrophilicity of the phosphate by acting as a Lewis acid, while the other stabilises the nucleophilic alkoxide anion. The objective of this research is to investigate other functional groups that can act cooperativity in the cleavage of **HPNPP**. This is inspired by natural enzymes, where it is common to find multiple functional groups acting together in synergism, such as the Asp-His-Ser catalytic triad discussed in Section 1.2. There are currently limited examples in the literature of artificial enzymes where cooperativity is provided by two or more different functional groups. This chapter focuses on following aspects.

- Formation of a heterogenous system involving two catalytic moieties for efficient cooperative catalysis
- Taking advantage of the high flexibility and modularity of the system, to demonstrate the rapid optimisation of a self-assembled cooperative catalyst

2.1 Use of Guanidinium moiety in cooperative systems

As we discussed in Section 1.2.2, phosphodiesters are commonly cleaved by the cooperativity of dinuclear metal centres, which are held by metal-binding ligands such as TACN, imidazole, di-pyridine and tri-picolyl. Our research group demonstrated the formation of self-assembled catalysts using TACN·Zn^{2+} as the cooperative functional group. Our initial aim was to find another functional group that could show cooperativity with the TACN·Zn^{2+} group for **HPNPP**

cleavage.

After an extensive search of the literature, we found a number of examples highlighting the ability of guanidinium groups to act as phosphodiesterases in supramolecular systems.[96-98] The guanidinium functional group is found in the amino acid arginine, which is present in many natural enzymes. They have been observed in nature to coordinate strongly with oxoanions, for example, carboxylates and phosphates as well as antibodies.[99-101] Interestingly, they are known to bind strongly with phosphates via a two-point hydrogen-bonding motif as seen in Figure 49.[100-102] This can be ascribed to its planar and rigid structure, which is geometrically complementary to oxoanions, as well as its high pK_a (12-14), which allows the guanidinium to remain in a protonated state over a wide pH range. It has also attracted the attention of researchers for molecular recognition studies[103] due to its unique two-point hydrogen binding with numerous oxoanions.

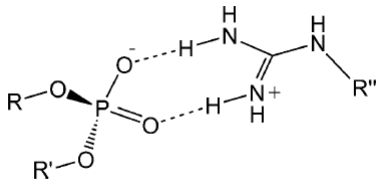

Figure 49. Two-point hydrogen bonding between a protonated guanidinium and a phosphodiester.

Salvio and co-workers have demonstrated cooperativity between guanidinium groups by incorporating two to four guanidinium moieties to the upper rim of a calixarene scaffold. (Figure 50).[96, 104] The di-functionalized guanidinium catalyst **24a** and **24b** is proposed to cleave **HPNPP** via the proposed mechanism shown in Figure 50 (bottom), in which the protonated guanidinium stabilises and binds strongly to the phosphate by two-point hydrogen bonding with the assistance of an ion-ion interaction. The other guanidinium group acts as a base to increase the nucleophilicity of the intramolecular hydroxyl group. This synergistic effect results in significant rate enhancement of **HPNPP** cleavage. The maximum catalytic activity in the reaction catalysed by the 1,3-distal bifunctional catalyst **24b** is in 2 orders of magnitude higher compared to the control mono-guanidinium molecule **24e**. Interestingly, the tri-functionalized

guanidinium catalyst **24c** could not further activate **HPNPP** catalysis and the additional guanidine/ium group was demonstrated to act as an innocent spectator. The tetra-functionalized guanidinium catalyst **24d** was shown to be slightly less effective for **HPNPP** cleavage, attributed to the greater steric hindrance within its structure.

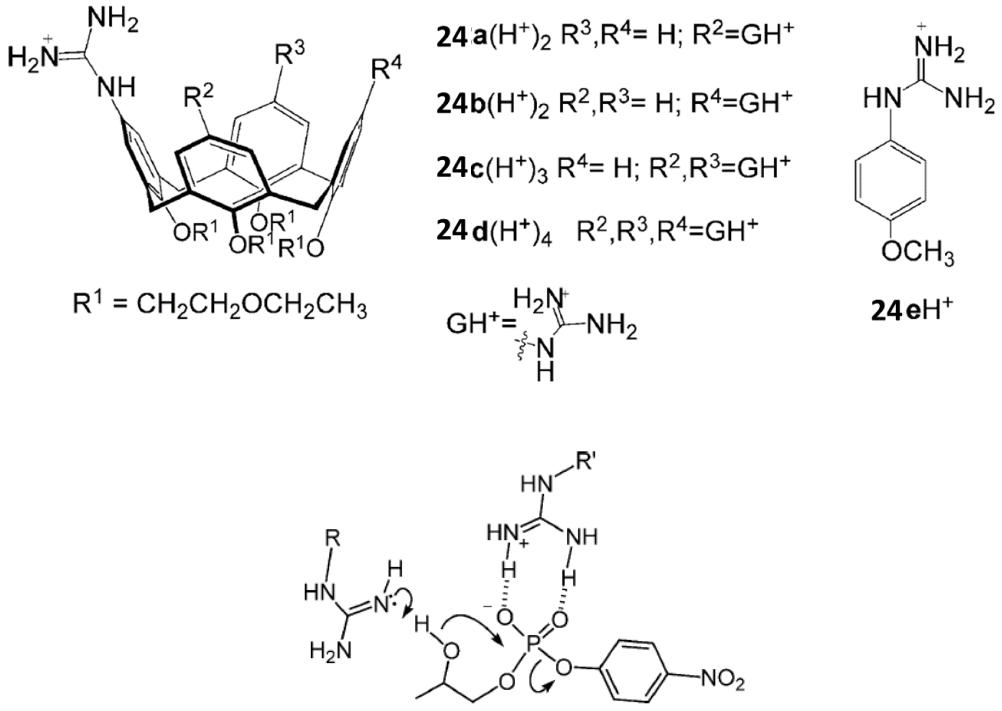

Figure 50. a) Chemical structures of artificial phosphodiesterases **24a** – **24d** reported by Salvio and co-workers; b) proposed mechanism of **HPNPP** cleavage involving guanidinium cooperativity. Adapted with permission from ref. 96. Copyright (2015) Wiley-VCH GmbH, Weinheim.

However, one issue with the above catalytic systems involving a molecular scaffold is the need for lengthy and complicated multi-step synthesis. Researchers have also investigated the use of supramolecular strategies that possess a greater degree of flexibility and modularity. Salvio and co-workers have demonstrated that guanidinium moieties can be incorporated onto the surface of gold nanoparticles to induce cooperativity (Figure 51).[105] In this study, phenoxyguanidine moieties with long alkanethiol chains were anchored onto the surface of gold nanoparticles, which produced monolayer-protected gold clusters **25** active for **HPNPP**

transesterification. Hollfelder and co-workers reported a polymeric system modified with guanidinium units that could achieve rate accelerations for **HPNPP** cleavage up to 10^4 (K_{cat}/K_{uncat}).[106]

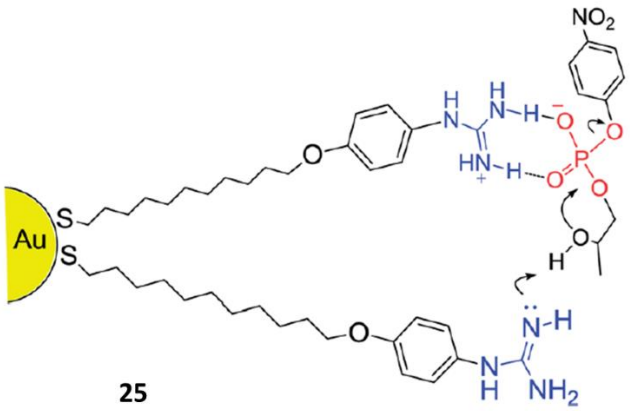

Figure 51. Chemical structure of the cooperative guanidinium catalyst system supported on gold nanoparticles and its proposed mechanism of **HPNPP** cleavage. Reprinted with permission from ref. 105. Copyright (2014) Royal Society of Chemistry.

Our initial aim was to demonstrate that cooperativity between guanidinium groups could be achieved in reversible structures formed by weak hydrophobic interactions. The idea would be to synthesise amphiphiles containing guanidinium amphiphiles, which could self-assemble from an inactive disassembled state into a catalytically active state when the catalyst concentration is above its CAC.[107] The assembled state would allow the two guanidinium groups to cleave the RNA model **HPNPP** by activation via two-point hydrogen bonding and general base catalysis.

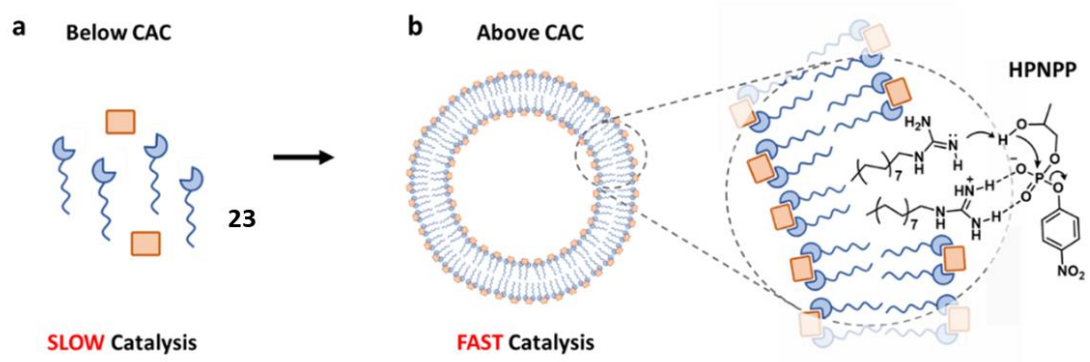

Figure 52. Self-assembly of C_{16}Gua **23** into vesicular aggregates for **HPNPP** cleavage. Reprinted with permission from ref. 107. Copyright (2020) American Chemical Society.

2.1.1 Design and synthesis of guanidinium amphiphiles and HPNPP

Following the simple design of C_{16}TACN **20**, we directly attached a guanidinium head group onto a C_{16} hydrocarbon tail to form C_{16}Gua amphiphile **23**. The reaction scheme started with the alkylation of C_{16} hexadecylamine onto a 1,3-di-Boc-2-(trifluoromethylsulfonyl) guanidine **26**, following by Boc deprotection with 6 M HCl to afford the desired C_{16}Gua amphiphile **23**. A control molecule (C_4Gua **29**) with a much shorter C_4 butyl chain was also synthesized, following the same reaction scheme.

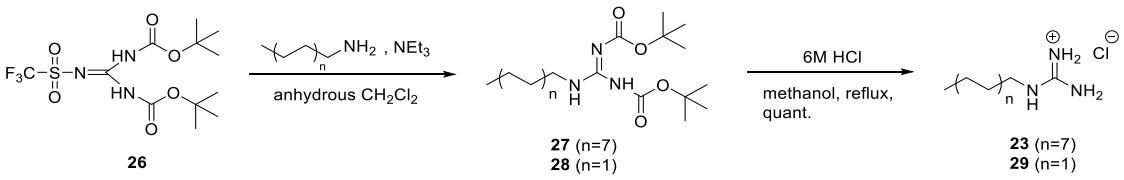

Scheme 1. Synthesis of the designed catalyst C_{16}Gua **23** and the control molecule C_4Gua **29**.

2.1.1.1 Mechanism of the alkylation

Coupling of the alkylamine and 1,3-di-Boc-2-(trifluoromethylsulfonyl)guanidine **26** began with nucleophilic attack by the amino group in the alkylamine onto a reactive guanidine group

activated with a trifluorosulfonyl group. The trifluorosulfonyl group is a strong electron withdrawing group that increases the electrophilicity of the guanidine carbon, enhancing nucleophilic attack. It also acts as a good leaving group, giving trifluoromethanesulfonamide as a side product.

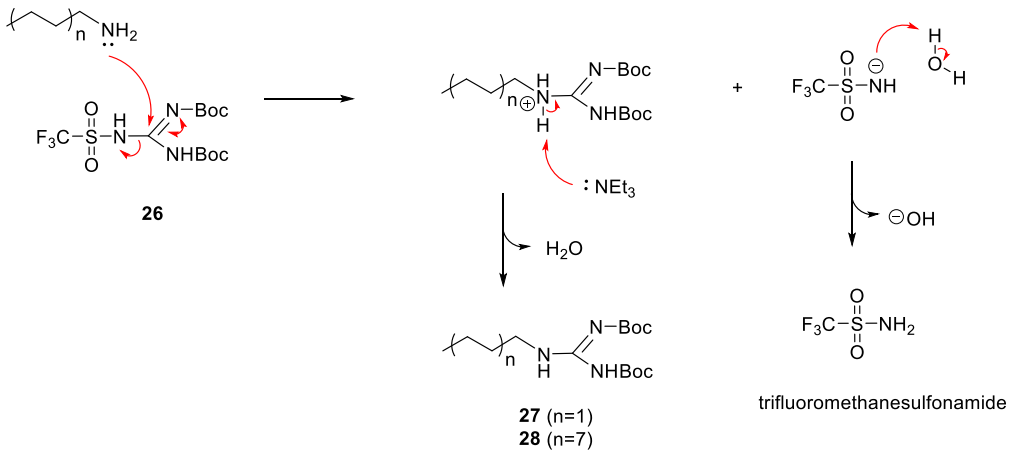

Scheme 2. Proposed mechanism for synthesis of guanidinium **27** and **28**

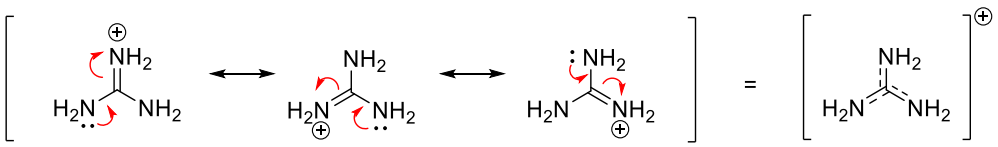

Scheme 3. Three resonance stable states of guanidinium ion

2.1.1.2 Mechanisms of the Boc deprotection

The deprotection of the Boc group was performed using a standard procedure involving 6 M HCl to afford the free amine. The mechanism involves an initial protonation of the carbamate oxygen followed by loss of the *tert*-butyl group as a carbocation. Deprotonation of the carbocation by a chloride ion allows the formation of isobutylene as a gas. At the same time, deprotonation of the carbamic acid results in the release of CO_2 gas and the formation of an amide anion which is immediately protonated to form the amine product.

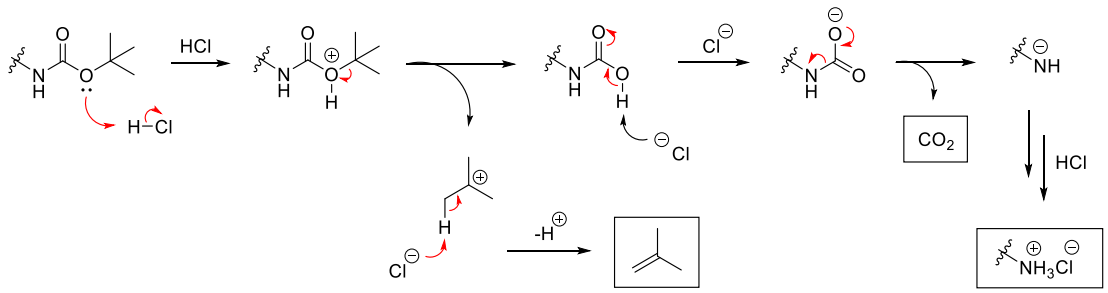

Scheme 4. Proposed mechanism for the deprotection of guanidinium **28** to afford the C_{16}Gua **23** and guanidinium **27** to afford the control molecule C_4Gua **29**.

2.1.1.3 Mechanisms of HPNPP and model HPNPP synthesis

The two-step synthesis of **HPNPP** was modified from the procedures reported by Brown[108]. It started with a cation exchange of the commercial disodium p-nitrophenyl phosphate **30** passed down to a column of IR-120 (H^+) resin in water, followed by a pH adjustment (pH ~8) with aqueous ammonia. Coupling of the corresponding p-nitrophenyl phosphate **31** and 1,2-epoxypropane **32** in water obtained **HPNPP**.

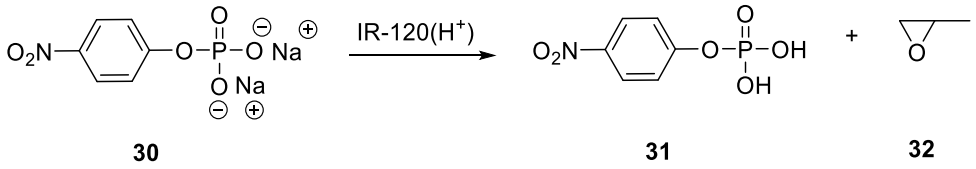

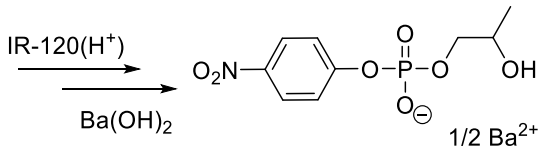

Scheme 5. Synthesis of **HPNPP**

Model HPNPP is an analogue of **HPNPP** but does not contain a secondary hydroxyl group preventing the intramolecular transphosphorylation. The procedures modified from Pezzato[109] started with the slow addition of pyridine to a solution of p-nitrophenol and phosphorous oxychloride in anhydrous toluene, giving the aryl phosphorodichloridate

intermediate **33**. Coupling of phosphorodichloridates **33** with propan-1-ol in anhydrous THF with triethylamine as base obtained **model HPNPP** as triethylammonium salts.

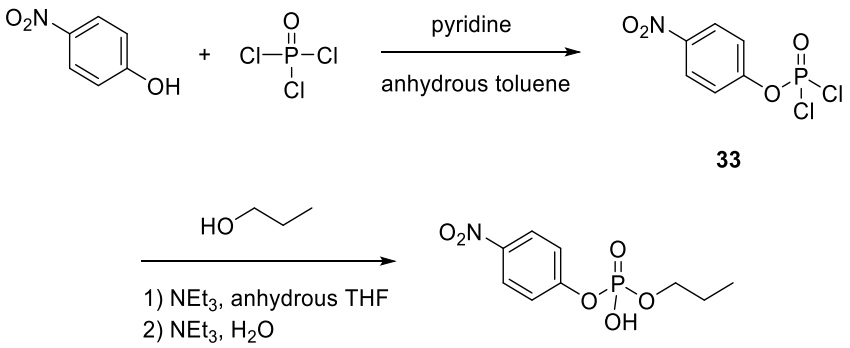

Scheme 6. Synthesis of **model HPNPP**

2.1.2 Activity of Guanidium-based catalysts in HPNPP cleavage

The catalytic activity of C_{16}Gua **23** for the cleavage of **HPNPP** was first examined in a number of different aqueous buffers ranging from pH 6 to 10. The buffers used were: 2-(N-morpholino)ethanesulfonic acid (**MES**) for pHs 6.0-6.5, 2-[4-(2-hydroxyethyl)piperazin-1-yl]ethanesulfonic acid (**HEPES**) for pH's 7.0-8.1, and N-cyclohexyl-2-aminoethanesulfonic acid (**CHES**) for pH's 8.6-10.0. As we can see in Figure 53, the initial rate of **HPNPP** cleavage (blue dots) was quite low at pH 6-7 in the presence of 70 μM of C_{16}Gua **23**. The initial rate then gradually increased when the pH was raised from 7 to 9.1, followed by a dramatic jump after pH 9.6. This suggested that the pH of the reaction mixture plays a key role in the catalytic activity of C_{16}Gua **23**, even if the charged guanidinium form is expected to be the predominant species present at pH 6-10, due to the high pK_a (13.6) of the guanidine head group. In order to be certain that the catalytic activity observed was due to cooperativity between proximal guanidinium groups, we performed control experiments in the absent of catalysts, which showed very low catalytic activity from pH 6-9.1 and rose slightly with increasing pH from pH 9.1-10. Moreover, an additional control experiment was conducted with the addition of hexadecyltrimethylammonium bromide (**CTAB**). Their initial rates (Figure 53, grey dots) were

almost at the same level as the rates measured in the absent of catalysts (red dots). This control experiment demonstrated that the acceleration of **HPNPP** cleavage was not due to a buildup of local positive charges on the surface of the vesicles.

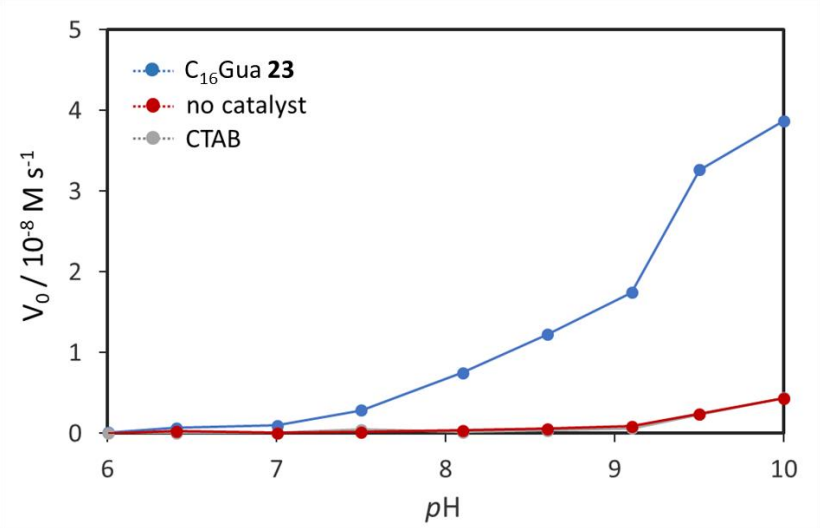

Figure 53. Initial rate of **HPNPP** cleavage in the presence of 70 µM of C_{16}Gua **23** at varying pHs. [**HPNPP**] = 500 µM, [aqueous buffer] = 5 mM (buffers used were: **MES** for pHs 6.0-6.5, **HEPES** for pHs 7.0-8.1 and **CHES** for pHs 8.6-10.0), 40 °C.

After observing the results shown in Figure 53, we decided to use CHES buffer at pH 9.1 for the subsequent experiments. At pH 9.1, there was significant rate enhancement with the biggest difference in ratio between using C_{16}Gua **23**, and the background rate of the control systems, which was close to zero.

2.1.3 Determination of CAC and structural data

The CAC is the critical concentration of amphiphile at which aggregation occurs and is one of the key parameters measured when studying amphiphilic molecules. Several methods for CAC determination have been published, including light scattering[110], electrical conductivity[111], surface tension, and spectrophotometric methods[112]. Although electrical conductivity and

surface tension are easy techniques to use in terms of sample preparation, they are not suitable for samples with low CAC values due to their low sensitivity and because the results can be highly dependent on the method used for data analysis.[113] Recently, spectrophotometric methods have for CAC determination concerning their precision and high sensitivity. Spectrophotometric methods are suitable even for CAC values below 0.1 mM.[113] Fluorescence titration for the determination of the CAC had been reported by Prazeres utilizing **coumarin 153** as the fluorescence probe, where the shift in the emission intensity (Figure 54b) and its maximum wavelength (Figure 54c) was plotted against the addition of sodium dodecyl sulfate (**SDS**).[114] The significant change in slope indicated a change in the surrounding environment of **coumarin 153**, illustrated the aggregation of **SDS** amphiphiles in solution. A similar method was also reported by Stuart and co-workers using **Nile red** as the fluorescence probe.[115]

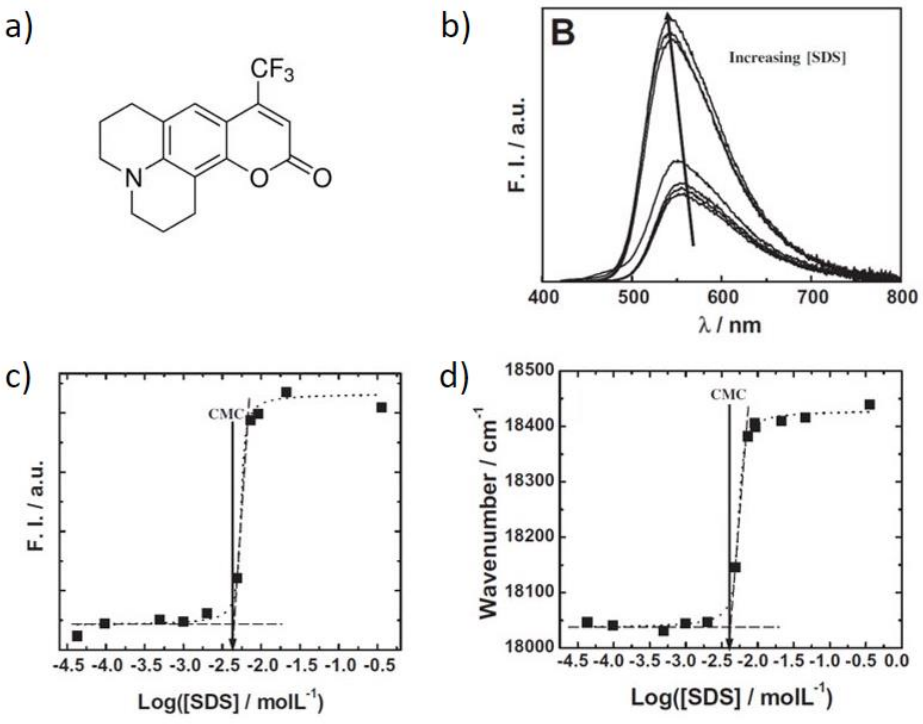

Figure 54. a) Chemical structure of **coumarin 153**, b) fluorescence spectra of **coumarin 153** in aqueous solutions containing **SDS** (λ_{ex} = 410 nm, [**coumarin 153**] = 1 µM) and c) plot of the fluorescence intensity and d) plot of the wavenumber at the maximum of the fluorescence band of **coumarin 153**

as a function of molar concentration of **SDS**. Adapted with permission from ref. 114. Copyright (2012) Elsevier Inc.

In this thesis, we determined the CAC of our amphiphiles of interest by utilizing fluorescent techniques. We used **Nile red** (λ_{ex} = 552 nm, λ_{em} = 636 nm in methanol) due to its high sensitivity and remarkable change in fluorescence intensity upon the formation of aggregates. **Nile red** is an apolar fluorescence probe, that does not show strong fluorescence in most polar solvents but becomes intensely fluorescent in hydrophobic environments. Its solvatochromic shift depending on the polarity of the surrounding environment is particularly useful for monitoring the formation of aggregates and giving CAC values.[115] Moreover, it is often reasonable to neglect the effect of the fluorescent probe on aggregation conformation, as the concentration of fluorophores in solution is relatively low, compared to the concentration of the amphiphiles.[116]

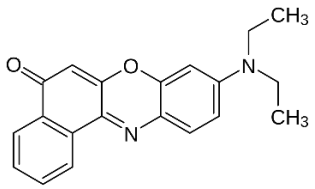

Figure 55. Chemical structure of **Nile red**

In practice, the CAC is determined by monitoring the changes in fluorescence intensity during the addition of amphiphiles to a solution in the presence of **Nile red**. The CAC is usually the point where there is a change in the slope a plot of the fluorescence vs amphiphile concentration. This is because the apolar **Nile red** probe becomes solubilised in the hydrophobic interior of the formed aggregates and causes significant changes in the fluorescence intensity.

We determined the CAC of C_{16}Gua **23** by titrating an increasing amount of C_{16}Gua **23** to **CHES** buffer solution (pH 9.1), in the presence of an excess amount of **HPNPP** (500 μM), and **Nile**

red (1 µM) as a fluorescence probe. When a small amount of C_{16}Gua **23** is added to the solution, there is an increase in the fluorescence intensity at 635 nm (excitation at 570 nm), which may be due to the formation of micellar structures. Interestingly, the fluorescence intensity does not increase between 40 and 60 µM, before a sudden jump in the fluorescence intensity as the concentration of the amphiphile is further increased. This change in slope occurred at 62 µM and is an estimation of the CAC of the amphiphile under these conditions. When the emission intensity vs amphiphile concentration is plotted on a logarithmic scale (Figure 56b), the intercept of the trend lines can be used to estimate the CAC. Using this method, we obtained a value of 55 µM for the CAC, which is in close agreement with 62 µM and matches with the jump in catalytic efficiency (described later).

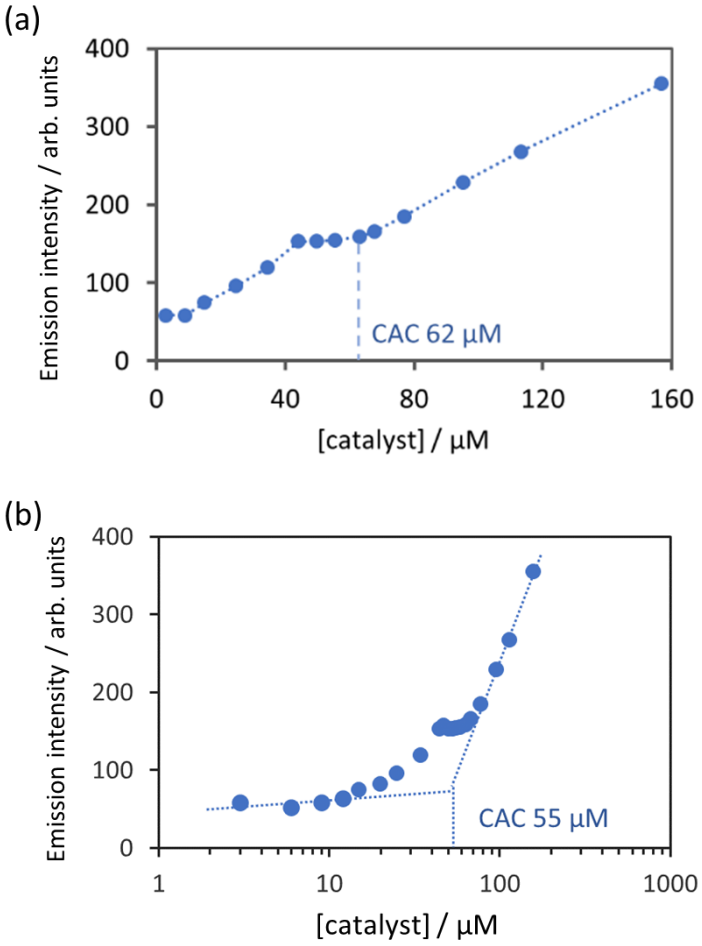

Figrue 56. Emission intensity of **Nile red** (1 µM, λ_{ex} = 570 nm, λ_{em} = 635 nm) at increasing concentration of C_{16}Gua **23** in aqueous **CHES** buffer solution (5 mM, pH 9.1), plotted a) in normal scale

and b) in logarithmic scale.

As discussed in Chapter One, we observed substrate-induced formation of the vesicular catalysts when using C_{16}TACN·Zn^{2+} (**20**·Zn^{2+}) amphiphiles. Therefore, we performed experiments to determine if this phenomenon was also present with the C_{16}Gua **23** system. The CAC values of C_{16}Gua **23** in the presence of various **HPNPP** concentrations (0 µM, 63 µM, 125 µM, 250 µM and 500 µM) was measured in aqueous **CHES** buffer pH 9.1 and data were plotted in a logarithmic scale (Figure 57). The CAC of C_{16}Gua **23** was 146 µM, 75 µM, 60 µM and 50 µM in the presence of 63 µM, 125 µM, 250 µM and 500 µM of **HPNPP** substrate, respectively.

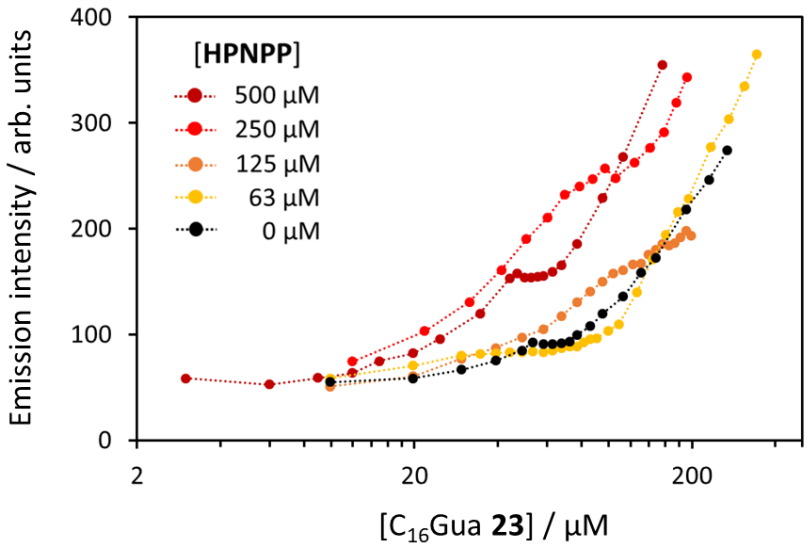

Figure 57. Emission intensity profiles for **Nile red** at increasing concentration of C_{16}Gua **23**, in the absence (black dots) and the presence of **HPNPP** (62.5 µM, yellow dots; 125 µM, orange dots; 250 µM, red dots and 500 µM, dark red dots); the dotted lines serve as a guide for the eye.

After plotting the CAC values against **HPNPP** concentration as shown in Figure 58, it is clear to see the decrease of the CAC of C_{16}Gua **23** when the concentration of **HPNPP** is increased. This confirms that the substrate-induced effect existed in the C_{16}Gua **23** system as well, indicating that the strong binding between the guanidinium head groups and the **HPNPP** substrate acts

to induce the formation of vesicular structures.

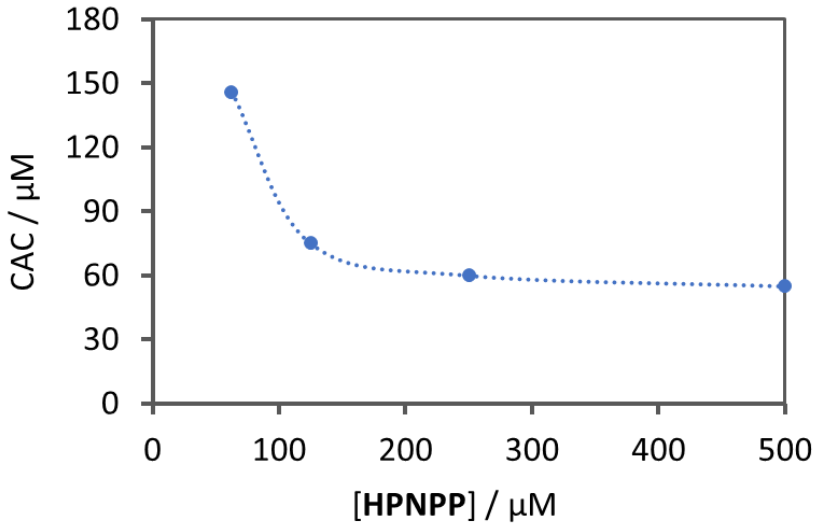

Figure 58. Critical aggregation concentrations (CAC) of C_{16}Gua **23** measured in the presence of various concentrations of **HPNPP** in **CHES** buffered solution with **Nile red** as a fluorescence probe.

To confirm the formation of aggregates above the CAC of C_{16}Gua **23**, we measured the average size of the formed structures by dynamic light scattering (DLS), a technique commonly used for determination of the size distribution of small particles. Aggregates and particles dispersed in solution scatters light to different extents, and the scattering information can be used to determine the hydrodynamic diameter of the particles in solution. These experiments were performed in the presence of **model HPNPP** (Figure 59a) rather than **HPNPP**. **Model HPNPP** is a derivative of **HPNPP** which lacks a hydroxyl group on the alkyl chain, and therefore intramolecular transphosphorylation is not possible. Therefore, **model HPNPP** would not be cleaved in the timeframe of the experiments, unlike **HPNPP**. We added 70 µM of C_{16}Gua amphiphiles **23** in the presence of 500 µM of **model HPNPP** and observed a monodisperse sample with an average hydrodynamic diameter of ~100 nm (Figure 59b).

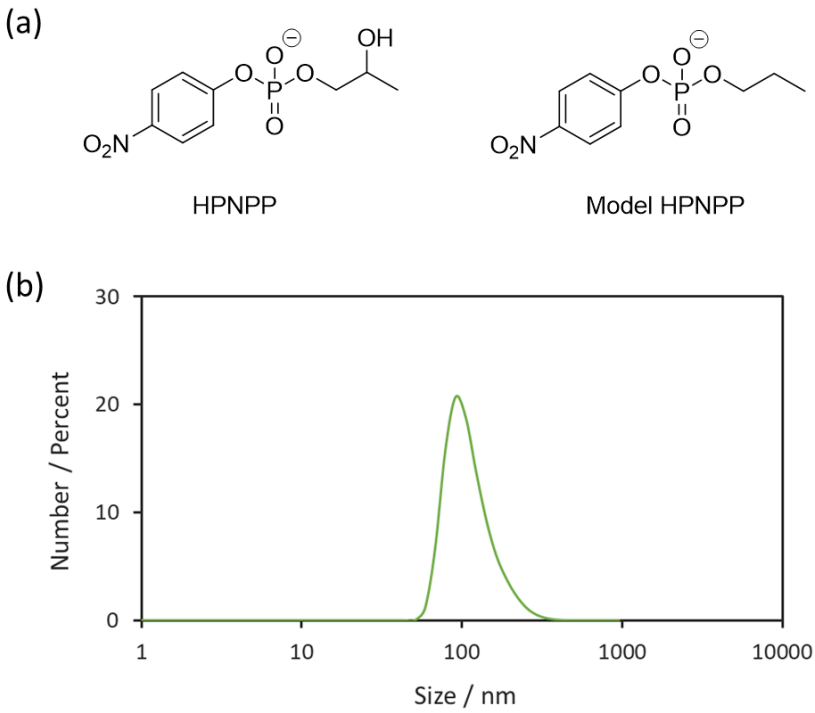

Figure 59. a) Chemical structure of **HPNPP** and **model HPNPP**; b) The hydrodynamic diameter of assemblies measured with dynamic light scattering (DLS) in the presence of **model HPNPP** for C_{16}Gua **23** system in aqueous **CHES** buffer pH 9.1, [C_{16}Gua **23**] = 70 µM, [**model HPNPP**] = 500 µM.

The obtain more information on the nature of the aggregates formed, a solution of C_{16}Gua **23** (70 µM) in the presence of **HPNPP** (500 µM) in an aqueous **CHES** buffered solution was also analysed using transmission electron microscopy (TEM). Uranyl acetate was used to stain the samples in order to provide sufficient contrast for visualisation. The observed black hollow circles confirmed the presence of vesicular structures rather than micelles, and these were observed with an average size of ~90-100 nm, which was in close agreement with the data obtained by DLS.

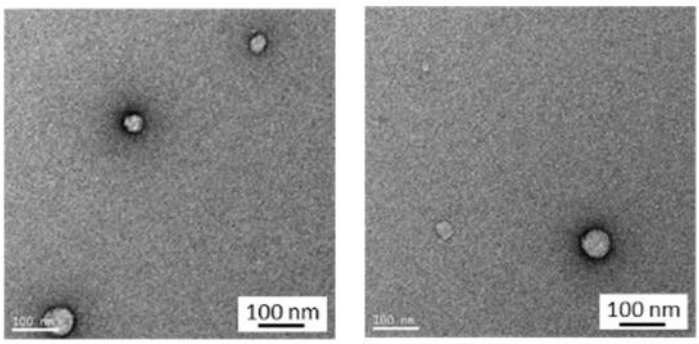

Figure 60. Representative TEM images of the vesicular structures of C_{16}Gua **23** (70 μM) in CHES buffer solution pH = 9.1 ([**CHES**] = 5 mM), [**HPNPP**] = 500 μM.

2.1.4 Kinetics of HPNPP cleavage with C_{16}Gua 23

To investigate the catalytic functionality of the self-assembled guanidinium amphiphiles, we measured the initial rates of **HPNPP** cleavage by following the formation of the cleavage product **PNP** at 410 nm. Figure 61 showed a plot of the initial reaction rate against increasing concentrations of C_{16}Gua **23**, in the presence of 500 μM **HPNPP** in **CHES** buffer at pH 9.1. At low concentrations of C_{16}Gua **23** (from 0 to 40 μM), low catalytic activity was observed, which was expected due to the concentration being below the CAC for C_{16}Gua **23**. When we increased the concentration of C_{16}Gua **23** to above 60 μM, a significant increase in the rate of **HPNPP** cleavage was observed, which continued to increase in a linear manner. The intercept of the two trend lines converged at ~55 μM, which closely matched the CAC of C_{16}Gua **23** (~60 μM) as measured by fluorescence spectroscopy. Importantly, the initial reaction rates with the control molecule C_4Gua **29** remained at a low level even at high concentrations of the ligand. This clearly demonstrated that **HPNPP** cleavage required the formation of self-assembled structures, which is not possible with C_4Gua **29** due to the presence of the shorter alkyl chains which does not provide enough hydrophobicity to drive self-assembly under the conditions examined. This data also provided additional evidence for the requirement for cooperativity between proximal guanidinium head groups in order to observe efficient catalysis.

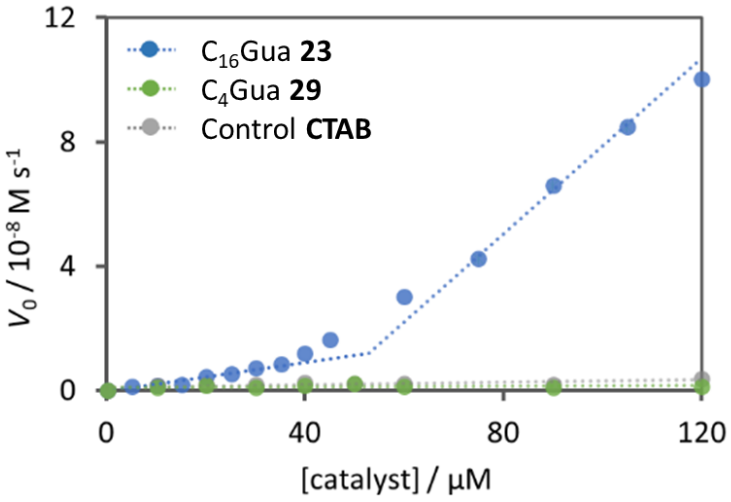

Figure 61. The initial rate of **HPNPP** cleavage with increasing concentration of C_{16}Gua **23** (blue dots), C_4Gua **29** (green dots) and **CTAB** (grey dots) in 5 mM of CHES buffer pH 9.1, [**HPNPP**] = 500 µM at 40 °C.

CTAB was examined as a second control amphiphile, and low catalytic activity in **HPNPP** cleavage was also observed (Figure 61, grey dots). This control molecule was used to confirm that the catalytic activity was not induced by the local pH changes due to the accumulation of positive ions on the surface of the vesicular structures.

To further investigate the substrate-induced activation of catalysis, we measured the initial rates of **HPNPP** cleavage at varying concentrations of C_{16}Gua **23** in the presence of specific concentrations of **HPNPP**. In the presence of 63 µM of **HPNPP**, no significant rate enhancement was observed at any concentration of C_{16}Gua **23**, which would be expected due to the small amount of **HPNPP** present, which would be consumed quickly and not be efficient at promoting formation of the vesicular assemblies.

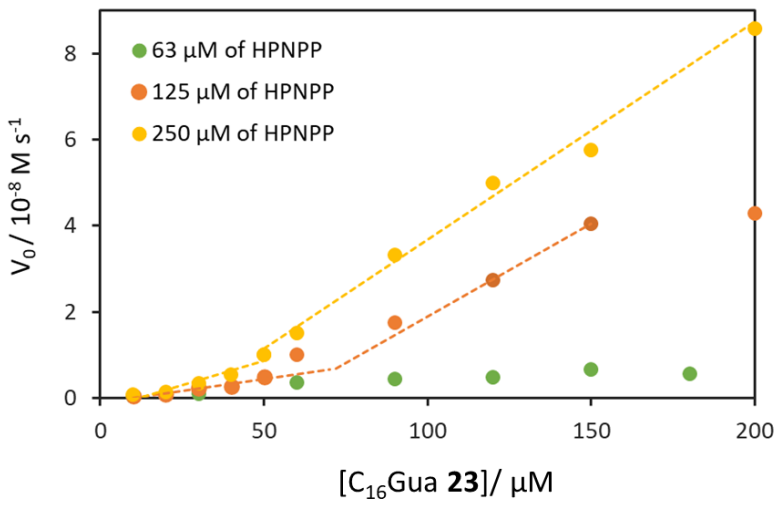

Figure 62. The initial rate of **HPNPP** cleavage with increasing concentration of C_{16}Gua **23** in 5 mM **CHES** buffer at pH 9.1, [**HPNPP**] = 63 µM (green dots), 125 µM (orange dots) and 250 µM (yellow dots) at 40 °C.

In the presence of 125 µM of **HPNPP**, the reaction rate increased slowly up to a concentration of 70 µM C_{16}Gua **23**. After that point, the reaction rate rapidly increased and could be fitted to a line of best fit with higher slope. The intercept between the two slopes occurs at 70 µM, which closely matches the CAC (75 µM) determined by fluorescence in the presence of 125 µM of **HPNPP**. The last data point in this experiment was off the linear line of best fit likely because of the high loading of C_{16}Gua **23** which consumed the **HPNPP** so quickly that it may have reduced the ability of the **HPNPP** to stability formation for the vesicular structures.

In the presence of 250 µM of **HPNPP**, the intercept between the two linear lines of best fit occurred at 50 µM, which was in close agreement with the CAC (60 µM) determined by fluorescence spectroscopy. In this example, there was no decrease in catalysis at higher C_{16}Gua **23** concentrations as the substrate concentration was more than three times that of the catalyst concentration. Overall, a higher concentration of **HPNPP** resulted in a decrease in the concentration of C_{16}Gua **23** at which the jump in the catalytic rate was observed. This observation was in agreement with the hypothesis that the **HPNPP** substrate induced formation of vesicular structures.

To further examine the importance of cooperativity for catalysis, we measured the catalytic activity of C_{16}Gua **23** when combined with different ratios of a non-catalytically active amphiphile. The inactive catalyst we chose was polyethylene glycol octadecyl ether (**Brij S2**), which is a commercially available, non-ionic surfactant terminating in polyethylene glycol. Figure 63 shows a plot of the initial rate of **HPNPP** cleavage against the proportion of C_{16}Gua **23** over **Brij S2**. The plot shows a sigmoidal curve where low catalytic activity is observed with low loadings of C_{16}Gua **23** up to 40%. With increasing proportions of C_{16}Gua **23** in solution, a significant increase in the observed rate is seen between 40% to 90% of C_{16}Gua **23**, after which a small increase is observed as the proportion reaches 100% C_{16}Gua **23**. This behaviour demonstrates that **Brij S2** co-assembles with C_{16}Gua **23** within the vesicular structure, resulting in poor cooperativity between C_{16}Gua **23** headgroups.

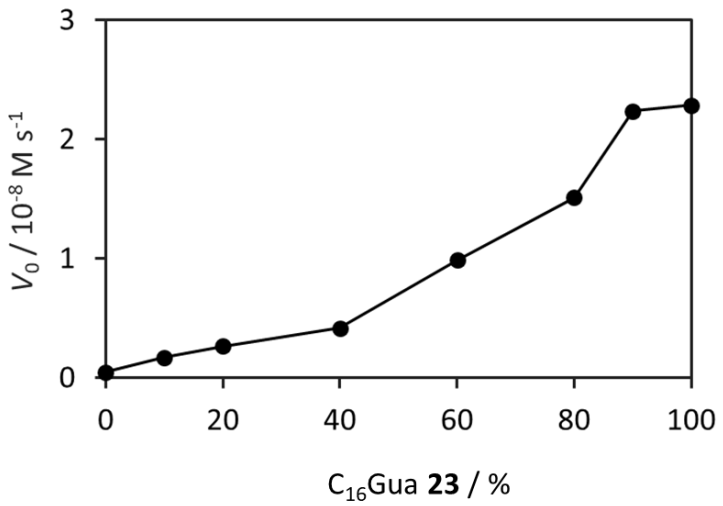

Figure 63. The initial rate of **HPNPP** cleavage with different proportion of C_{16}Gua **23** and **Brij S2** in **CHES** buffer solution pH 9.1, [**CHES**] = 5 mM, [**HPNPP**] = 250 µM, [catalyst] = 70 µM.

The Michaelis-Menten parameters of this guanidinium-based vesicular catalyst was determined by measuring the initial rate of **HPNPP** cleavage with increasing concentrations of **HPNPP** at a fixed C_{16}Gua **23** concentration of 70 µM. Fitting of the saturation profile into the Michaelis-Menten equation plotted in Figure 63 determined the V_{max} to be 3.5×10^{-8} mol s^{-1}

and the K_M to be 0.31 mM.

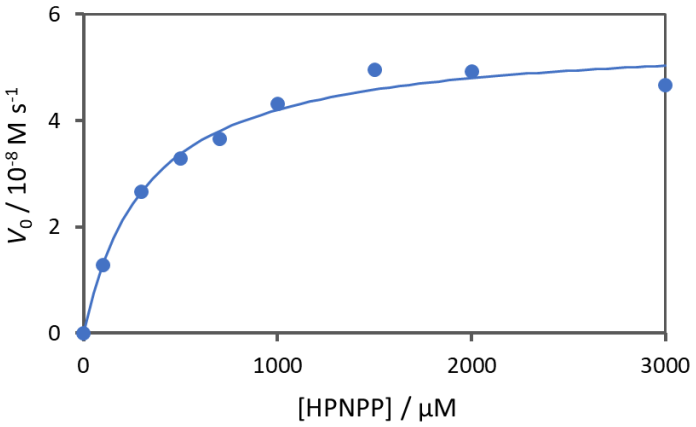

Figure 64. The initial rates of **HPNPP** cleavage at 70 µM of C_{16}Gua **23** with increasing concentrations of **HPNPP** in 5 mM CHES buffer solution at pH 9.1 and 40 °C.

The measured V_{max} of the C_{16}Gua **23** system is about half of that for the C_{16}TACN·Zn^{2+} (**20**·Zn^{2+}) system (7.2 ± 0.6 × 10^{-8} mol s^{-1}). The K_m is about one-third of that for the **20**·Zn^{2+} system K_m (1.0 ± 0.1 mM).[89] This suggests that the guanidinium head groups bind strongly to the **HPNPP** substrate, likely via two points hydrogen bonding as often described in the literature.[100-102] The ability to catalyse the cleavage of **HPNPP**, however, is weaker than for **20**·Zn^{2+}, potentially because the guanidinium group is not as effective at activating the nucleophilic oxygen required for the intramolecular transphosphorylation. While the system is less efficient than the **20**·Zn^{2+} system, to the best of our knowledge, this C_{16}Gua **23** system is the first example showing cooperativity between guanidium groups induced by weak hydrophobic interactions.

(Figure 52 was reprinted for clarity)

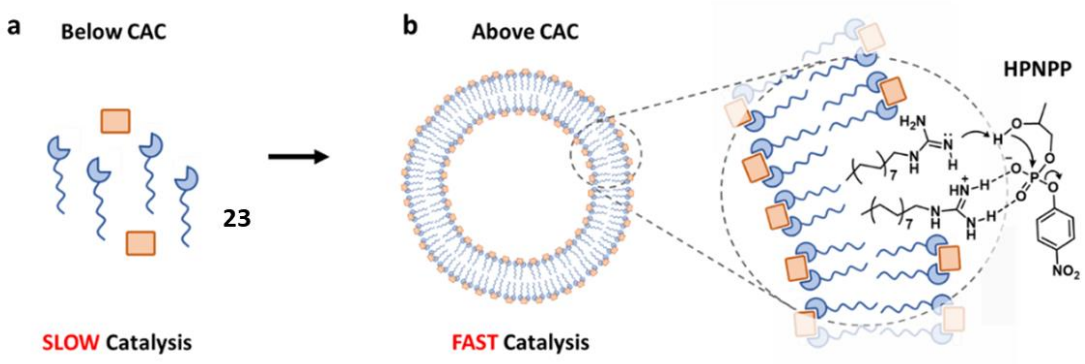

Figure 52. Self-assembly of C_{16}Gua **23** into vesicular aggregates for **HPNPP** cleavage. Reprinted with permission from ref. 107. Copyright (2020) ACS Catalysis.

2.2 Cooperativity in a multifunctional catalyst

The above vesicular catalytic system involved the assembly of a single amphiphilic molecule possessing a single functional group. Nature's enzymes, on the other hand, contain active sites where multiple functional groups act together cooperatively to catalyse chemical transformations. An alkaline phosphatase, for example, induces catalysis by the cooperative action of di-nuclear zinc centres, a serine and an arginine residue.[117] The guanidinium group of the arginine residue was shown to be involved in substrate activation and transition state stabilisation, while the hydroxyl group of the serine residue acted as a nucleophile in catalysis. Another example was reported by Cotton and co-workers.[101] They confirmed that guanidinium moieties cooperate with a metal ion in the enzyme staphylococcal nuclease, which is a DNA and RNA phosphodiesterase. The cooperation between two guanidiniums and the Ca^{II} ions played a critical role in binding with phosphates via hydrogen bonds and electrostatic interaction, respectively.

Not surprisingly, it has been popular for artificial phosphodiesterases to utilise cooperativity between guanidinium units and metal-bound ligands. The guanidinium unit is thought to help

in substrate binding and activation, as well as transition-state stability, and complements the catalytic activity of the metal ions. In commonly proposed mechanisms involving synergism between a metal ion and a guanidinium group, the guanidinium is shown to have two-point hydrogen bonding with the assistance of general base activation provided by a metal ion in both RNA and DNA cleavage (Figure 65).

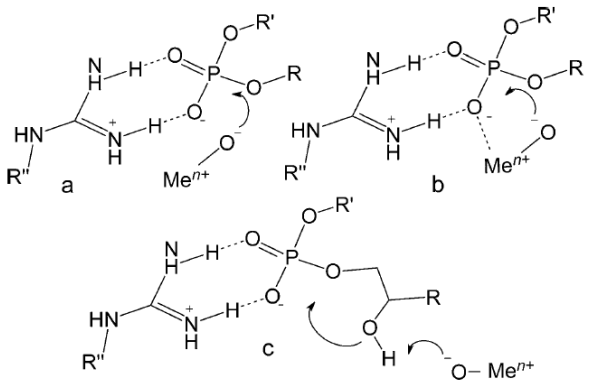

Figure 65. Proposed mechanism of a) and b) DNA and c) RNA model catalysis involving synergism of a guanidinium moiety and a metal ion. Reprinted with permission from ref. 96. Copyright (2015) Wiley-VCH GmbH, Weinheim.

Mao and co-workers reported a synthetic catalyst **34** containing two guanidiniums and a 2,2'-dipyridyl group for copper binding.[118] In their case, the two pendant guanidinium groups interacted with two adjacent phosphodiester units in a DNA strand via hydrogen bonding, resulting in association of the DNA molecule and the copper ion, which resulted in DNA degradation. This complex showed a rate enhancement that was 10-fold higher than the parent molecule of a 2,2'-dipyridyl group without pendant guanidiniums.

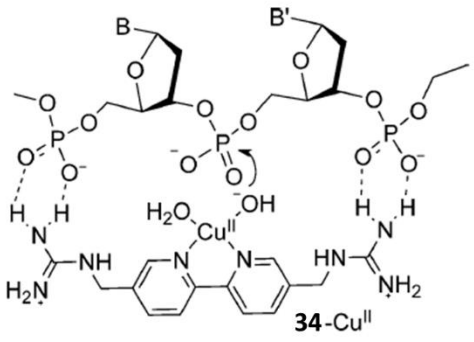

Figure 66. Proposed mechanism of the designed catalyst **34** involving two guanidinium moieties and a mono-nuclear copper centre for DNA hydrolysis. Reprinted with permission from ref. 118. Copyright (2008) Royal Society of Chemistry.

One key example that inspired our work was the demonstration of cooperativity between a guanidinium moiety and a TACN unit reported by Salvio and co-workers.[97] DNAase and RNAase mimics were formed by the covalent linkage of both a guanidinium and a TACN unit onto the upper rim of a cone-calixarene scaffold, where the functional groups were brought into close proximity for synergistic effects. From their proposed mechanisms for RNA and DNA cleavage, the guanidinium was involved in two-point hydrogen bonding to stabilize phosphodiester, while the function of the metal-TACN centre was as a general base is for either intramolecular or the intermolecular hydroxyl activation in RNA (Figure 67, left) and DNA model (Figure 67, right), respectively.

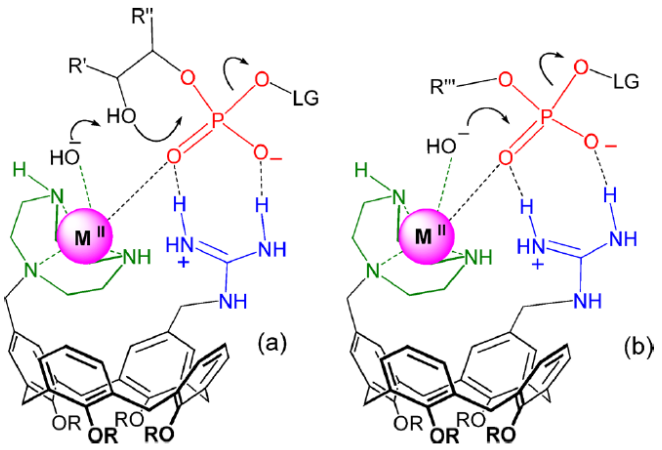

Figure 67. Synergistic effect of a guanidinium and a metal ion trapped by a TACN group in an artificial model for a) RNA and b) DNA model cleavage. Reprinted with permission from ref. 97. Copyright (2016) American Association for the Advancement of Science.

Inspired by Salvio's studies, we wanted to explore the possibility of using weak hydrophobic interactions as the driving force to induce cooperativity between guanidiniums and metal ions bound by TACN functional groups. Although Zn^{2+} was the metal ion used in the C_{16}TACN·Zn^{2+} (**20**·Zn^{2+}) system,[89] the majority of studies in the literature examining cooperativity between TACN·M^{2+} and the guanidinium ion used Cu^{2+} as the metal ion, which proved to be more effective at demonstrating cooperativity than Zn^{2+}.[119-120] Therefore, we proceeded to add Cu^{2+} to our TACN-based systems to investigate the synergistic effect between TACN·Cu^{2+} and guanidinium ions within vesicular structures. The idea was that we would mix together both guanidinium-based amphiphiles and TACN·Cu^{2+} amphiphiles into solution. Upon addition of the substrate **HPNPP**, the system is expected to form vesicular assemblies which induces the formation of catalytic pockets and the activation of synergistic catalysis (Figure 48).

(Figure 48 was reprinted for clarity)

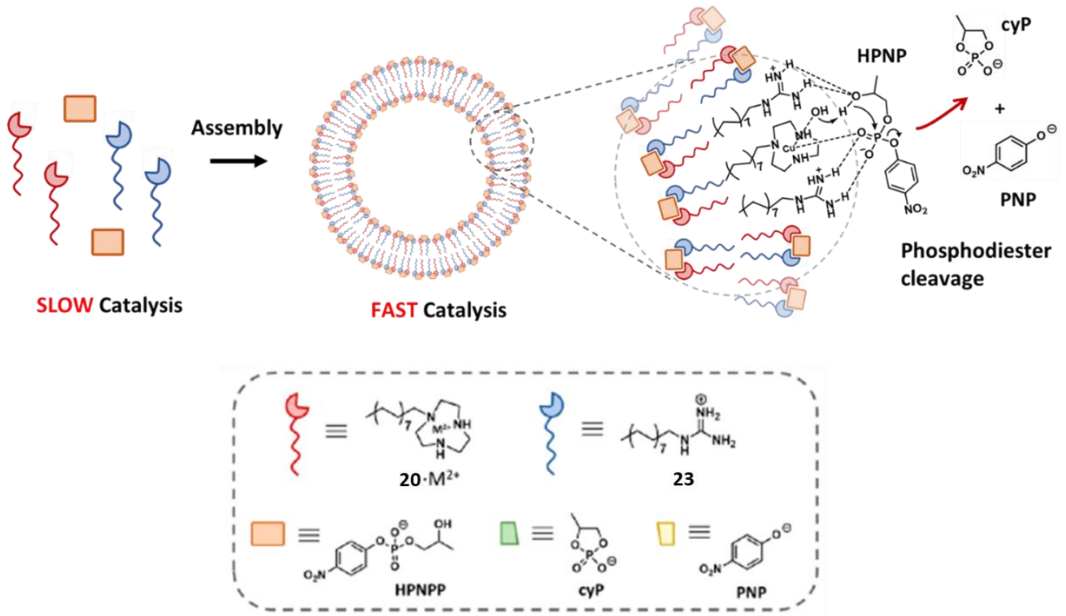

Figure 48. General representations of a cooperative catalyst formed by a multicomponent cooperative catalyst (C_{16}TACN·Cu^{2+} **20**·Zn^{2+} and C_{16}Gua **23**) formed by self-assembly.

However, upon addition of the two amphiphilic pre-catalysts into solution, it is uncertain whether heterogeneous self-assembly or self-sorted homogeneous assembly occurs (Figure 68). We wanted to find an answer to this issue by screening the catalytic activity of a combination system with two amphiphiles in an attempt to see whether there was any synergism between the two functional groups, resulting in a catalytic activity that was higher than each pre-catalyst working individually.

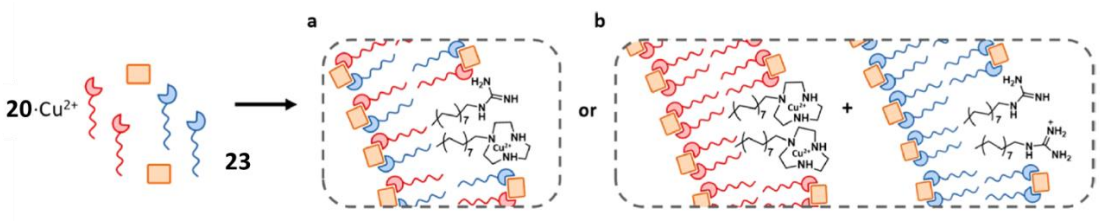

Figure 68. Representation of C_{16}TACN·Cu^{2+} (**20**·Cu^{2+}) and C_{16}Gua **23** a) in a heterogeneous self-assembled state and b) in a self-sorted homogeneously assembled state. Reprinted with permission from ref. 107. Copyright (2020) American Chemical Society.

In our search for cooperative effects between guanidinium and TACN·Cu^{2+} functional groups, we initially examined the catalytic activities of catalytic systems containing different proportions of C_{16}Gua **23** and C_{16}TACN·Cu^{2+} (**20**·Cu^{2+}) in the original aqueous buffer conditions (**CHES** buffer, pH 9.1). Figure 69 is a plot of the initial rate of **HPNPP** cleavage against an increasing percentage of C_{16}Gua **23**, with the total catalyst concentration being 200 μM, which was well above the CAC of C_{16}Gua **23** (62 μM) and **20**·Cu^{2+} (20 μM) on their own. We made sure that all catalytic systems at different ratios of two catalysts was operating above the CAC. The reaction rate in the presence of only **20**·Cu^{2+} was 7.2×10^{-8} mol L^{-1} s^{-1} (far left), while the reaction rate with only C_{16}Gua **23** was 4.0×10^{-8} mol L^{-1} s^{-1} (far right). Different proportions of C_{16}Gua **23** and **20**·Cu^{2+} did not result in an increase in the reaction rates, and in fact the value always sat in between the two extremes of C_{16}Gua **23** only and **20**·Cu^{2+} only. Therefore, there was no evidence of cooperativity between guanidinium and TACN groups, which should result in significant rate enhancement beyond the rates given at the two ends of the graph.

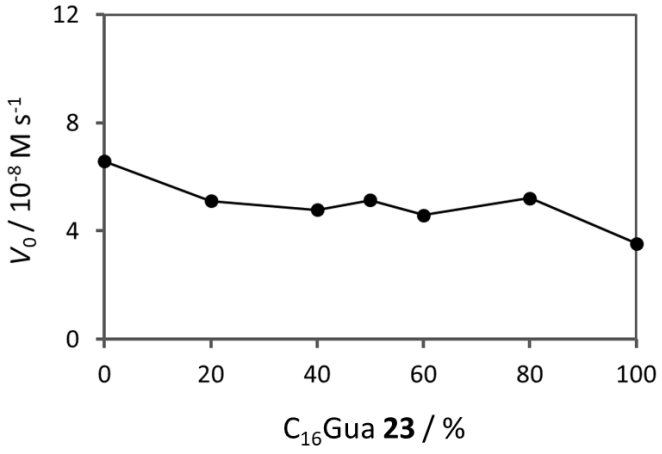

Figure 69. Initial rate of **HPNPP** cleavage at different proportion between C_{16}Gua **23** and **20**·Cu^{2+}, [total catalyst] = 200 μM, [**HPNPP**] = 500 μM, [**CHES**] = 5 mM, at pH 9.1, 40 °C.

To be sure that we were working at concentrations above the CAC of these self-assembled systems involving C_{16}Gua **23** and C_{16}TACN·Cu^{2+} (**20**·Cu^{2+}), we measured their CAC values using a fluorescent probe. We took the 1:1 C_{16}Gua **23** to **20**·Cu^{2+} system as the reference system.

Utilizing **Nile red** as the fluorescence probe, we measured the change in emission intensity as the concentration of C_{16}Gua **23** and **20**·Cu^{2+} (1:1) was increased within a **CHES** buffered solution (pH 9.1) in the presence of an excess amount of **HPNPP** (500 µM). From Figure 70, it can be seen that the emission intensity of **Nile red** decreased with the addition of amphiphilic ligands, with a change in slope occurring at around 40 µM. The change in fluorescence emission behavior at this point indicates the formation of self-assembled structures at this concentration. This measured CAC of the combined catalyst system was in line with expectations as it is between the CAC of C_{16}Gua **23** on its own (62 µM) and **20**·Cu^{2+} on its own (20 µM).

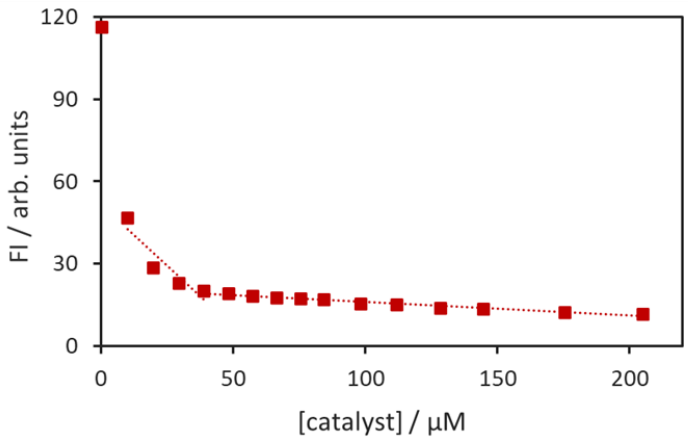

Figure 70. Emission intensity profile for **Nile red** (1 µM, λ_{ex} = 570 nm, λ_{em} = 635 nm) at increasing concentration of 1:1 C_{16}Gua **23**/**20**·Cu^{2+} in aqueous buffer solution, [**CHES**] = 5 mM, pH 9.1, [**HPNPP**] = 500 µM.

The CAC measurements were also conducted under the same conditions in the presence of **model HPNPP** instead of **HPNPP**. **Model HPNPP** does not have a hydroxyl group on the alkyl side chain, so it is not able to undergo hydrolysis, which we thought may interfere with the fluorescence measurements and/or the formation of vesicles. We found that the fluorescence emission intensity changes of **Nile red** followed the same pattern in the presence of **HPNPP** and **model HPNPP** and gave the same CAC value for the 1:1 C_{16}Gua **23**/**20**·Cu^{2+} system in an aqueous buffer solution. This showed that **model HPNPP** has the same ability to promote

vesicle formation as **HPNPP**, and therefore was suitable for structural investigation.

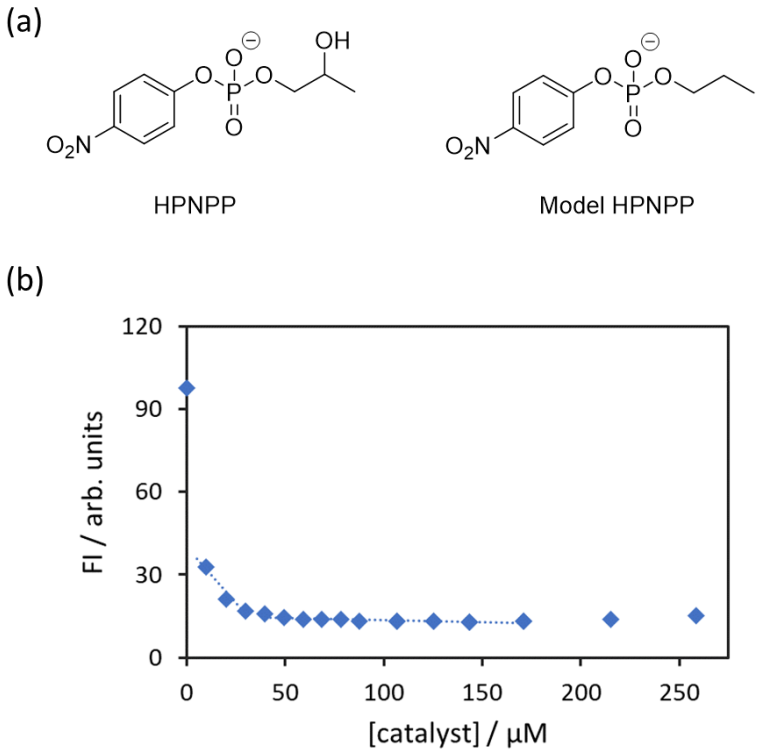

Figure 71. a) Chemical structure of **HPNPP** and **model HPNPP**; b) Emission intensity profile for **Nile red** (1 µM, λ_{ex} = 570 nm, λ_{em} = 635 nm) at increasing concentration of 1:1 C_{16}Gua **23**/**20**·Cu^{2+} in aqueous buffer solution, **[CHES]** = 5 mM, pH 9.1, [**model HPNPP**] = 500 µM.

Further structural investigation of the different systems of C_{16}Gua **23** to **20**·Cu^{2+} was measured by dynamic light scattering (DLS). The average size of 1:1 and 1:2 C_{16}Gua **23**/**20**·Cu^{2+} aggregates was determined to be 27-28 nm in aqueous buffered solution, and the 1:3 C_{16}Gua **23**/**20**·Cu^{2+} aggregates were slightly bigger with an average size of 30 nm. The size of these structures indicated the formation of vesicles rather than micellar structures. The confirmation that self-assembled structures were formed suggested that the lack of synergistic catalysis was not due to the inability of the supramolecular structures to form, but due to a lack of cooperativity between guanidinium and TACN in an aqueous buffer solution. Therefore, different experimental conditions were investigated in attempts to induce cooperativity between the C_{16}Gua **23** and **20**·Cu^{2+} amphiphiles.

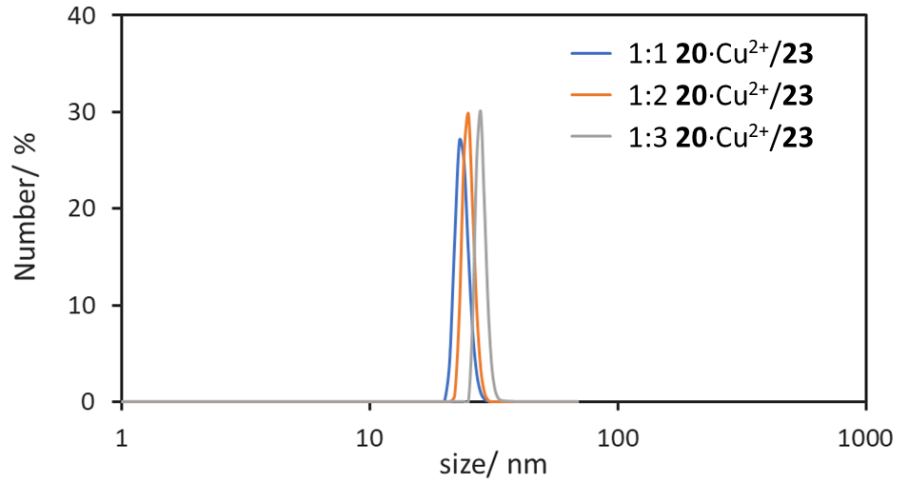

Figure 72. Hydrodynamic diameters of assemblies measured with dynamic light scattering (DLS) in the presence of **model HPNPP** for the combined C_{16}Gua **23** and **20**·Cu^{2+} system in CHES buffer aqueous solution, [**CHES**] = 5 mM, pH 9.1 in water, [total catalyst] = 200 µM, [**model HPNPP**] = 500 µM.

2.2.1 Reaction conditions in multifunctional catalytic systems

2.2.1.1 pH effects

In the search for cooperativity between the guanidinium and C_{16}TACN·Cu^{2+} moieties, we next examined the catalytic activities of the combined C_{16}Gua **23**/**20**·Cu^{2+} (1:1) system at different pH's. The catalytic activity of the combined C_{16}Gua **23**/**20**·Cu^{2+} (1:1) system (black) was compared directly with the C_{16}Gua **23** only (red) and **20**·Cu^{2+} only (blue) systems at pH's ranging from 5.5 to 10 (Figure 73). This plot showed that the catalytic activity of the **20**·Cu^{2+} only system increased from pH 5.5 to pH 8.1, followed by a decrease in catalytic activity at higher pH values. The catalytic activity in the presence of only C_{16}Gua **23** kept increasing at higher pH values up to pH 10. The reaction rate in absence of catalyst was at a reasonable low level below 0.2×10^{-7} M s^{-1}. Unfortunately, the 1:1 combined catalytic system did not show any hint of cooperativity, with no indication of rate enhancement over the two homogeneous systems.

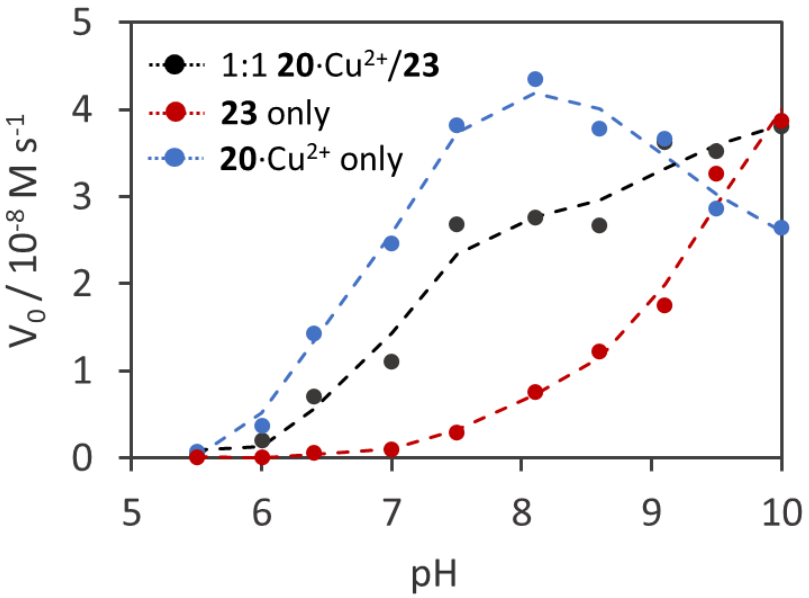

Figure 73. The initial rate of **HPNPP** cleavage in catalytic systems of only C_{16}Gua **23**, only **20**·Cu^{2+} and the combined 1:1 C_{16}Gua **23**/**20**·Cu^{2+} in aqueous buffer solution ranging from pH 5.5 to pH 10, [catalyst] = 60 μM, [**HPNPP**] = 500 mM, [buffer] = 5 mM at 40 °C. (**MES** for pH 5.5 – 6.5; **HEPES** for pH 7 – 8.2; CAPS for pH 8.6 – 10)

2.2.1.2 Solvent and base effects

After being initially disappointed, we looked back again at the examples Salvio reported in Figure 74. The calixarene scaffold fused with guanidinium and TACN groups at the upper rim was solubilized in a 80% DMSO in water mixture, and strong binding of the guanidinium groups to phosphates was reported in this solvent system.[97] Less aqueous solvent mixtures have been seen to benefit the binding between the guanidinium group and phosphates and for this reason a number of DMSO/water system have been used to examine the activity of phosphodiesterases.[120-122]

Moreover, Salvio reported the conditions for **HPNPP** cleavage and real RNA cleavage, where 100 mM of *N*, *N*-diisopropylaminoethanol buffered 80% DMSO in water mixtures to give pH 9.8 for Zn-coordinated catalyst **35** and pH 8.8 for Cu-coordinated catalyst **35**.[97] And copper

system gave a much better performance in strong binding to phosphates and much better cooperativity for rate enhancement.

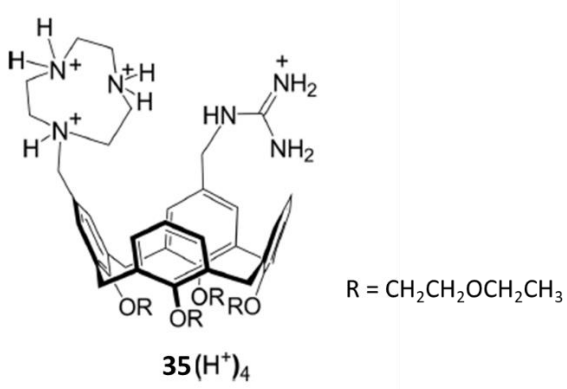

Figure 74. Chemical structure of the 1,2-vicinal catalyst **35** designed by Salvio and co-workers. Adapted with permission from ref. 97. Copyright (2016) American Association for the Advancement of Science.

Inspired by the positive cooperative system demonstrated by Salvio, we proceeded to investigate whether DMSO-water mixture could induce cooperativity in our self-assembled system. We examined the catalytic activity of three representative systems, the C_{16}Gua **23** only system, C_{16}TACN·Cu^{2+} (**20**·Cu^{2+}) only system and the combined 1:1 **20**·Cu^{2+}/C_{16}Gua **23** system in 80% DMSO in water mixtures. The catalytic rate was measured in the presence of 5 mM **CHES** buffer at pH 9.1. A high concentration of catalysts was used with the expectation of high CAC in DMSO/water mixtures. As can be seen in Figure 75, a very slow rate of **HPNPP** cleavage was observed with all catalytic systems in this **CHES** buffered DMSO solution. The rates observed were around 12 times slower than in our previous aqueous conditions at pH 8.8.

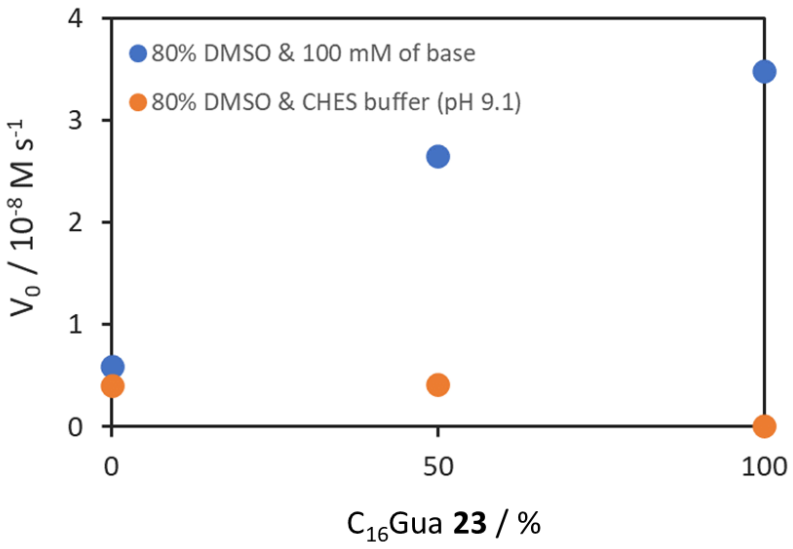

Figure 75. Initial rate of **HPNPP** cleavage of different systems of only C_{16}Gua **23**, only **20**·Cu^{2+} and the combined 1:1 **20**·Cu^{2+}/C_{16}Gua **23** in 80% DMSO in water mixtures in the presence of 100 mM of base (blue dots) or 5 mM **CHES** buffer at pH 9.1 (orange dots), [catalyst] = 200 μM, [**HPNPP**] = 500 mM at 40 °C.

However, when we added 100 mM of DIPEA as suggested by literature,[97] the reaction rate of the C_{16}Gua **23** system was significantly enhanced (Figure 75, right). The catalytic activity of the **20**·Cu^{2+} system was still depressed under these conditions, with a small increase on the activity without DIPEA (Figure 75, left). The reaction rate in the combined 1:1 **20**·Cu^{2+}/C_{16}Gua **23** system was increased, and the rate was not sitting in the linear line between the reaction rate of either C_{16}Gua **23** or **20**·Cu^{2+} only. This gave us a strong suggestion that there was cooperativity between the guanidinium and TACN·Cu^{2+}, assisted by the decrease in polarity of the solvent system and the presence of an amine base.

We next determined how the base concentration affected the rate of **HPNPP** cleave in the absence of any catalytic amphiphiles – background conditions. Figure 76 shows the initial rate of **HPNPP** cleavage in different proportions of DMSO in water and either 1 mM or 100 mM of DIPEA. The reaction rate with 100 mM of DIPEA increased when we decreased the proportion of DMSO from 80% to 40%. A dramatic rate enhancement up to 5.4×10^{-7} mol s^{-1} was observed

in a 20% DMSO in a water mixture in the presence of 100 mM of DIPEA. Such high background catalysis is not favourable, as it can obscure the effect of the catalyst of interest. We therefore investigated lower base concentrations and was able to show that with 1 mM of DIPEA, there was only a low rate of **HPNPP** cleavage, with the highest reaction rate seen at 0.47×10^{-7} mol s^{-1} in pure water. Since we wanted to keep the background reaction at a very low level that would not affect further catalysis studies, we continued our studies with a base concentration of 1 mM.

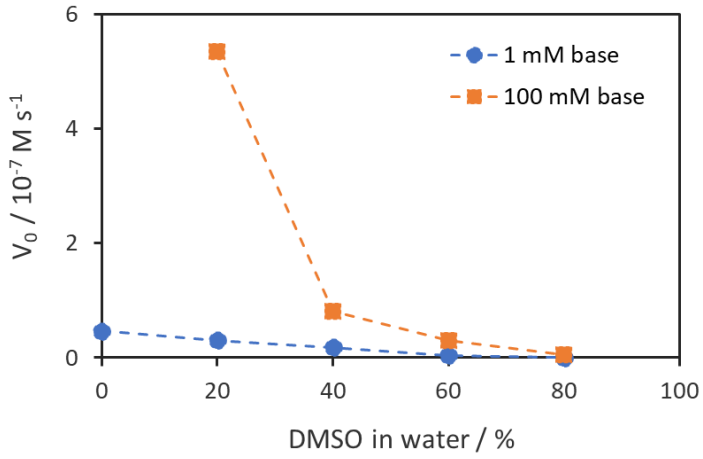

Figure 76. The initial background rate of **HPNPP** cleavage in the presence of 1 mM or 100 mM of DIPEA in absence of any catalysts, [**HPNPP**] = 500 mM at 40 °C.

To investigate how the polarity of the solvent system influenced the rate of **HPNPP** cleavage, we measured the rates of reaction in three representative catalytic systems (only C_{16}Gua **23**, only **20**·Cu^{2+} and 1:1 **20**·Cu^{2+}/C_{16}Gua **23**) in different proportions of DMSO in water and in the presence of 1 mM of DIPEA. From Figure 77, it can be seen that the initial reaction rate with the C_{16}TACN·Cu^{2+} (**20**·Cu^{2+}) system decreased when going from 0% to 10% DMSO in water and remained at a low level when we increased the DMSO percentage up to 80%. The C_{16}Gua **23** catalytic system also demonstrated high catalytic activity at lower concentrations of DMSO, with a rapid decrease in catalytic activity changing from 0 to 40% DMSO in water. What was interesting was that the catalytic activity of the combined system in 10% to 30% DMSO in

water was higher than the sum of catalytic activities of C_{16}Gua **23** and **20**·Cu^{2+} on their own. This was a clear indication of cooperativity between guanidinium and TACN under these reaction conditions. This synergistic effect was seen most strongly in 20% DMSO in water. The catalytic system comprising a 1:1 combination of C_{16}Gua **23** and **20**·Cu^{2+} in this solvent system had a reaction rate that was 4.5 times faster than that in the **20**·Cu^{2+} system and 15 times faster than that in the C_{16}Gua **23** system. The control data shown in Figure 77 (grey dots) represents the background reaction in the absence of any catalysts.

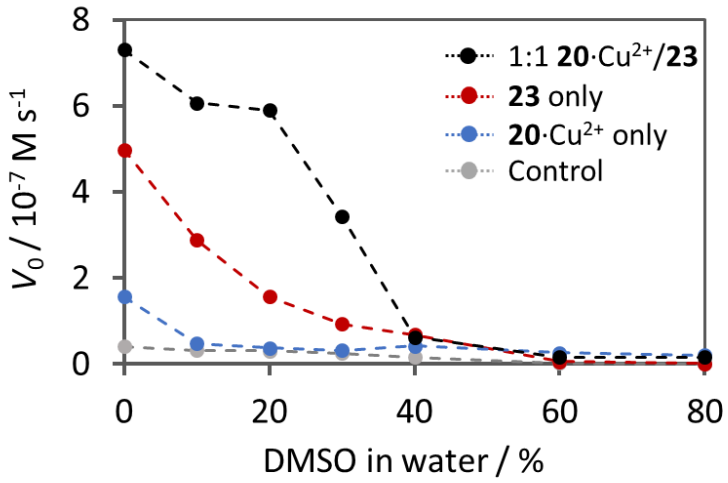

Figure 77. The initial rate of **HPNPP** cleavage of three representative catalytic systems in different proportion of DMSO in water mixtures, [total catalyst] = 200 μM, [**HPNPP**] = 500 mM, [DIPEA] = 1 mM at 40 °C.

It is worth pointing out that the decrease in the reaction rates for all three representative systems at higher proportions DMSO in water may also be due to changes in the self-assembly behaviour of the systems. The increase in hydrophobicity of the solvent environment can lead to disassembly of vesicular structures, as the amphiphiles will be more soluble and there will therefore be less driving force for the hydrophobic chains to be buried within self-assembled structures. This could be another reason why the reaction rates all dropped to a low level in the range from 40% to 80% DMSO in water.

2.2.2 Determination of CAC and structural data of multifunctional catalytic systems in 20% DMSO in water

To determine the CAC of our catalytic system under these new solvent conditions, and to confirm we were working at concentrations above the CAC, we utilised a fluorescence probe. **Nile red** was examined first but it did not give clear changes in fluorescence intensity of wavelength shifts in this 20% DMSO-water system. Several other fluorescence probes were examined, including **coumarin 153**[114] and 1,6-diphenyl-1,3,5-hexatriene (**DPH**),[113] and only **DPH** showed significant changes in fluorescence intensity under these conditions. **DPH** is an apolar fluorescence probe like **Nile red**, which does not fluorescence strongly in polar solvents like water. Its linear structure has made it a popular probe of membrane interiors, as it can be dissolved and oriented parallel to the amphiphilic tails in lipid bilayers.[123]

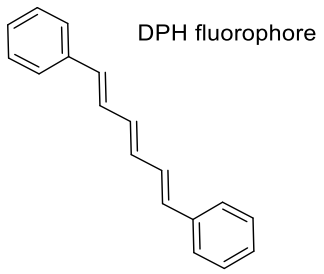

Figure 78. Chemical structure of **DPH** fluorophore

Figure 79 shows a plot of the emission intensity of **DPH** upon the addition of 1:1 C_{16}TACN·Cu^{2+} (**20**·Cu^{2+})/C_{16}Gua **23** in the presence of 500 μM of **model HPNPP**. In this case, **model HPNPP** substrate was used because **HPNPP** would be cleaved too fast in the DMSO system, potentially resulting in a misleading result. Upon addition of small amounts of the catalysts **20**·Cu^{2+}/C_{16}Gua **23** in a 1:1 ratio, there is an initial drop in the emission intensity before the emission stabilizes and steadily increases at increasing concentrations of the amphiphiles. The change in the slope of the fluorescence increase occurs at 130 μM, which indicates a change in the environment surrounding the **DPH** and suggests the formation of aggregates. The CAC

was also measured in the presence of 1000 µM and 1500 µM of **model HPNPP** and determined to be ~100 µM and ~35 µM, respectively. This decrease in CAC at higher substrate concentrations is in line with our previous studies in similar systems[89], and gives confidence to this fluorescence method for CAC determination.

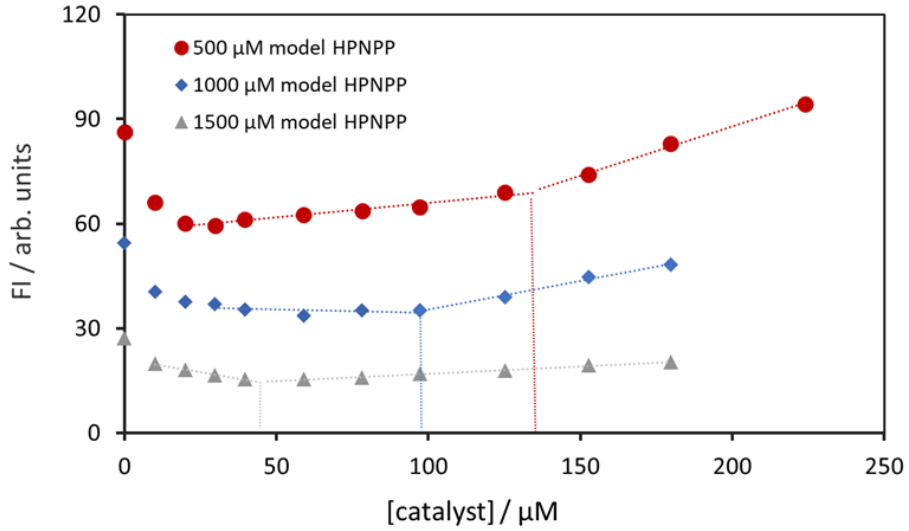

Figure 79. Emission intensity profile of **DPH** (1 µM, λ_{ex} = 350 nm, λ_{em} = 440 nm) at increasing concentration of 1:1 **20**·Cu^{2+}/C_{16}Gua **23** in 20% DMSO in water, [**model HPNPP**] = 500 µM, [DIPEA] = 1 mM at 20 °C.

For further confirmation that we were working above the CAC with our 1:1 **20**·Cu^{2+}/C_{16}Gua **23** system, we examined a 200 µM solution of our 1:1 **20**·Cu^{2+}/C_{16}Gua **23** aggregates by dynamic light scattering (DLS). The average size of the aggregates formed under these conditions was determined to be 50 nm. Moreover, the systems of 1:2 and 1:3 **20**·Cu^{2+}/C_{16}Gua **23** were shown to contain slightly larger structures with an average size of 60 nm and 68 nm, respectively.

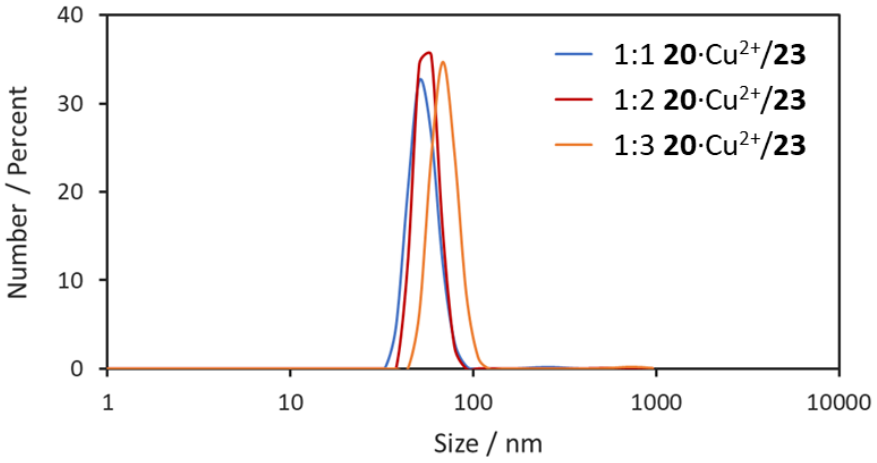

Figure 80. Hydrodynamic diameter of assemblies measured with dynamic light scattering (DLS) in the presence of **model HPNPP** for the combined C_{16}Gua **23** and **20**·Cu^{2+} systems in 20% DMSO in water, [total catalyst] = 200 µM, [**model HPNPP**] = 500 mM and [DIPEA] = 1 mM at 20 °C.

The formation of self-assembled aggregates of combined catalytic systems was also visualized utilising transmission electron microscopy (TEM). In this experiment, the standard **HPNPP** substrate was used due to the short sample preparation time, such that the ongoing hydrolysis of **HPNPP** could be neglected. Uranyl acetate was used to fix the aggregates on the surface of the charged grids right after sample preparation and to provide enhanced contrast. A sample of the 1:2 C_{16}Gua **23**/**20**·Cu^{2+} system in 20% DMSO in water showed hollow black circles with an average size of 60-80 nm, which was in close agreement with the data measured by DLS. The circular hollow structures indicated the presence of vesicles rather than micelles.

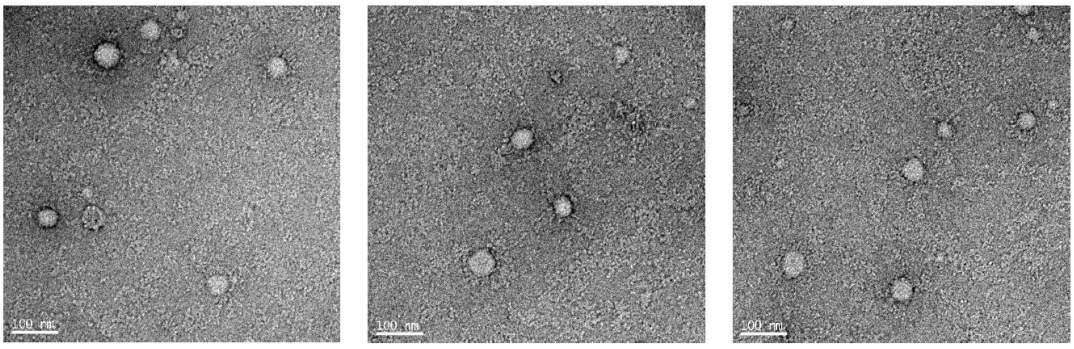

Figure 81. Representive TEM images of the vesicular structures of 1:2 **20**·Cu^{2+}/C_{16}Gua **23** system in 20% DMSO in water mixture, [total catalyst] = 200 μM, [**HPNPP**] = 500 μM and [DIPEA] = 1 mM.

To further investigate the self-assembled structures, we conducted small angle neutron scattering (SANS) experiments in collaboration with Prof. Gregory Warr (University of Sydney) and Dr. Andrew Whitten (instrument scientist, ANSTO) at the Australian Centre for Neutron Scattering. SANS is an experimental technique that investigates the structural data of diverse substances at a mesoscopic scale of around 1–100 nm by using elastic neutron scattering at small scattering angles. The samples were prepared by myself and the data analysed by Prof. Gregory Warr.[107]

The mixed synergistic catalyst **20**·Cu^{2+}/C_{16}Gua **23** in a 1:3 ratio was compared to the control system containing a 1:3 ratio of **20**·Cu^{2+}/C_4Gua **29**. Both experiments were conducted in a mixture of 20% DMSO-d6 in D_2O. The SANS pattern of the sample of 1:3 **20**·Cu^{2+}/C_{16}Gua **23** shows a clear q-2 dependence of the scattered intensity in the low angle range, consistent with the presence of bilayer-like structures, excluding cylindrical micelles, emulsion droplets or other enclosed particles. This data could be satisfactorily modelled as large, unilamellar vesicles with a bilayer thickness of 30 Å and a vesicle radius in the range of 600-2000 Å (broadly consistent with dimensions from DLS), together with a second population of smaller spheres (radius ~30 Å) accounting for the shoulder at higher q. Note that the catalyst concentrations used for these SANS measurements are higher than the concentrations used for catalysis, which was necessary to observe sufficient neutron scattering intensity. However, the data clearly shows that the formation of unilamellar vesicles is possible with a mixture of

20·Cu^{2+}/C_{16}Gua **23** catalysts in 20% DMSO/water.

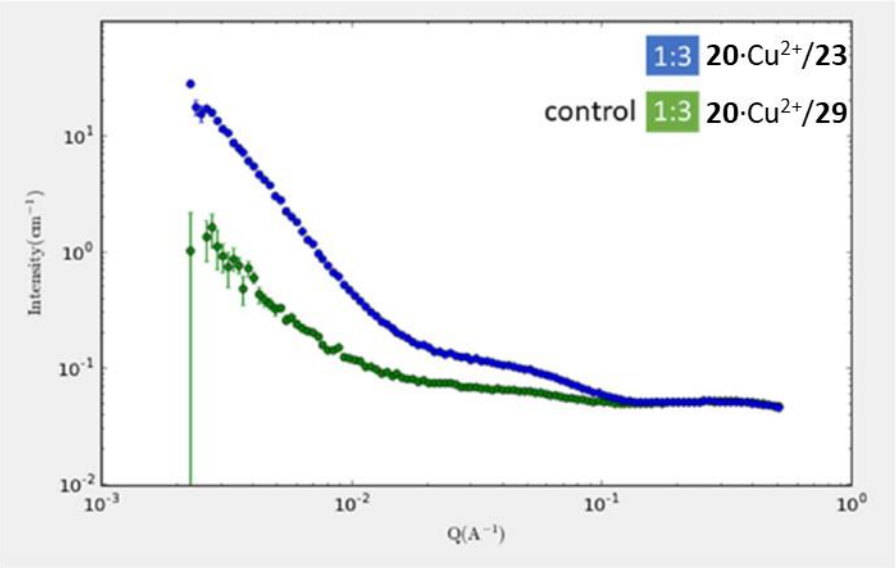

Figure 82. I(q) vs q plot of SANS for the mixed catalyst system **20**·Cu^{2+}/C_{16}Gua **23** (1:3) compared to a control system containing **20**·Cu^{2+}/C_4Gua **29** (1:3).

The data from the control sample of 1:3 **20**·Cu^{2+}/C_4Gua **29** is also consistent with the presence of a much lower concentration of large vesicles (about 20 times less than the main system) plus some small spherical aggregates. Note that both systems contain the common amphiphile **20**·Cu^{2+}, so the presence of some aggregates can be expected. The significantly higher concentrations of vesicles in the main system reinforce the importance of C_{16}Gua **23** for vesicle formation.

2.2.3 Kinetics data for the combined catalytic systems

The catalytic activity of the combined 1:1 **20**·Cu^{2+}/C_{16}Gua **23** system were conducted in 20% DMSO in water with an increasing concentration of 1:1 **20**·Cu^{2+}/C_{16}Gua **23**. In order to reduce the systematic error, we reduced the temperature from 40 °C to 20 °C to slow down the

dramatically fast reaction, so that they may be more easily followed by UV-Visible spectroscopy. Figure 83a shows that the initial reaction rate increased in a slow manner with increase of the concentration of 1:1 **20**·Cu^{2+}/ C_{16}Gua **23** up to 170 μM of total concentration. With a further increase in amphiphilic concentration, the reaction rate was observed to increase in a much more rapid rate. The change in slope was observed at around 170 μM, which was similar to the CAC (130 μM) determined by fluorescence experiments. The catalytic activity of the combined 1:3 **20**·Cu^{2+}/C_{16}Gua **23** system was also measured in 20% DMSO in water. For this system, the change in slope also occurred at around 170 μM (Figure 83b). These results suggested that self-assembly of amphiphiles above CAC was essential for cooperative catalysis, resulting in rate enhancement of **HPNPP** cleavage. Although we did not carefully measure the catalytic activities in all different proportions of C_{16}Gua **23** and **20**·Cu^{2+}, we can expect that aggregates could be formed as we utilize 200 μM of catalyst.

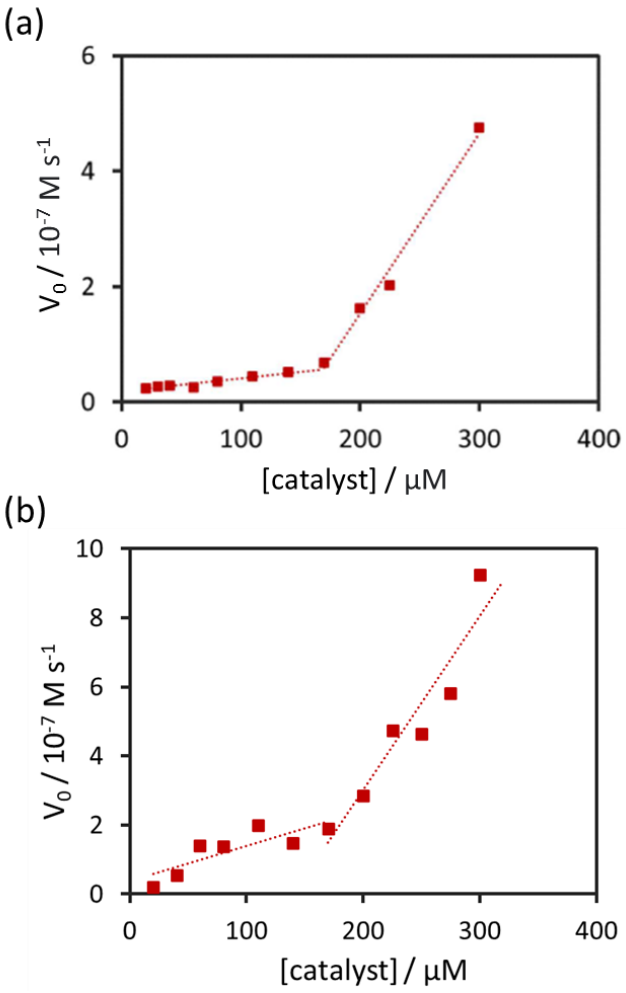

Figure 83. Initial rate of **HPNPP** cleavage with increasing concentration of a) the combined 1:1 **20**·Cu^{2+}/C_{16}Gua **23** and b) the combined 1:3 **20**·Cu^{2+}/C_{16}Gua **23** in 20% DMSO in water, [total catalyst] = 200 µM, [**HPNPP**] = 500 µM, [DIPEA] = 1 mM at 20 °C.

A key objective of this study was to demonstrate the advantage of having a modular system that could provide benefits in terms of catalyst optimisation. Our idea was to examine the catalytic activities of different proportions of our two amphiphiles, to see if different degrees of cooperativity could be observed. This is something that would be very challenging for covalently joined systems, but potentially very straightforward for systems combined using reversible interactions. We therefore measured the catalytic activities of **HPNPP** cleavage at different proportions of C_{16}Gua **23** and **20**·Cu^{2+} in 20% DMSO in a water mixture in the presence of 500 µM of **HPNPP** and 1 mM of DIPEA. This was the condition with the most

synergism between guanidinium and TACN among all the investigations above. Taking the combined 1:1 **20**·Cu^{2+}/C_{16}Gua **23** system as a reference point, the reaction rate decreased steadily with a decreasing proportion of C_{16}Gua **23** to **20**·Cu^{2+} (Figure 84). This reinforced the idea that the cooperativity between guanidinium and TACN is beneficial and that both functional groups are required for catalysis. Interestingly, the catalytic activity was strongly enhanced at increasing proportions of C_{16}Gua **23** to **20**·Cu^{2+} and reached the peak at ~1:3 **20**·Cu^{2+}/ C_{16}Gua **23**, before the catalytic activities dropped at over 80% of C_{16}Gua **23** to **20**·Cu^{2+}. The observed different reaction rates at different proportions of C_{16}Gua **23** and **20**·Cu^{2+} suggested that different catalyst systems with different binding pockets may be being generated.

The same study performed using **20**·Cu^{2+} and the control molecule C_4Gua **29** shows the importance of self-assembly (Figure 84, grey dots). Low catalytic activity was observed with C_4Gua **29**, which has a much shorter alkyl chain which would promote self-assembly to a much lesser degree. This demonstrated the importance of self-assembly for the formation of the active catalyst in this system.

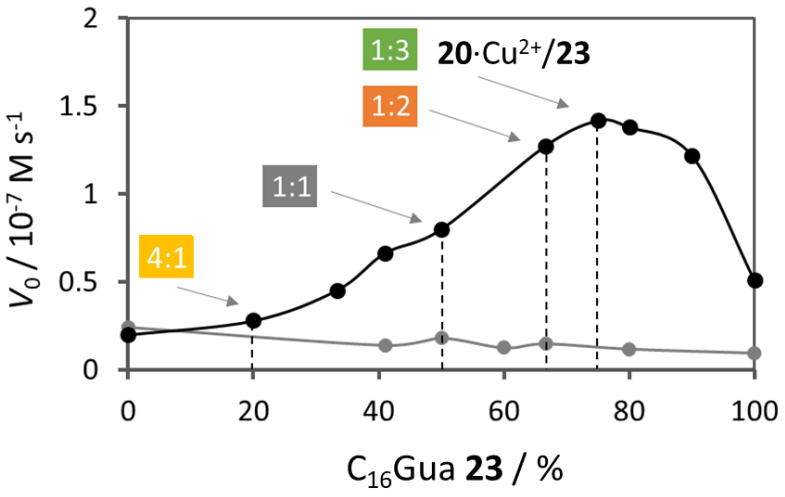

Figure 84. Initial rate of **HPNPP** cleavage with different proportion of C_{16}Gua **23** and **20**·Cu^{2+} in 20% DMSO in water, [total catalyst] = 200 µM, [**HPNPP**] = 500 µM, [DIPEA] = 1 mM at 20 °C. The control reaction was with different proportion of C_4Gua **29** and **20**·Cu^{2+} (grey dots) under the same conditions.

To gain insight into the key differences between the **20**·Cu^{2+}/C_{16}Gua **23** catalytic systems when combined in 1:1, 1:2 and 1:3 proportions, we examined the rates of **HPNPP** cleavage for each of these systems at increasing concentrations of **HPNPP**. The saturation profiles were fitted into the Michaelis-Menten equation, and the K_M and V_{max} of each system were calculated (Figure 85). The K_M value for the 1:3 **20**·Cu^{2+}/C_{16}Gua **23** system was 1.3 ± 0.1 mM, which was almost half of the K_M for the 1:1 and the 1:2 **20**·Cu^{2+}/C_{16}Gua **23** systems, determined to be 2.8 ± 0.3 mM and 2.5 ± 0.6 mM, respectively. The significantly lower K_M for the 1:3 **20**·Cu^{2+}/C_{16}Gua **23** system suggested that the binding between this multifunctional catalyst and the **HPNPP** substrate was the strongest out of the three catalytic systems examined. On the other hand, we observed that the V_{max} value of the 1:2 **20**·Cu^{2+}/C_{16}Gua **23** system was 7.3 ± 1.1 × 10^{-7} mol s^{-1}, which was higher than the 1:1 and the 1:3 **20**·Cu^{2+}/C_{16}Gua **23** systems, determined to be 5.3 ± 0.4 × 10^{-7} mol s^{-1} and 5.2 ± 0.3 × 10^{-7} mol s^{-1}, respectively. The significantly higher V_{max} for the 1:2 **20**·Cu^{2+}/C_{16}Gua **23** system suggested the catalytic pockets generated by this system was intrinsic different, and was able to stabilize the transition state more efficiently than the other two systems examined.

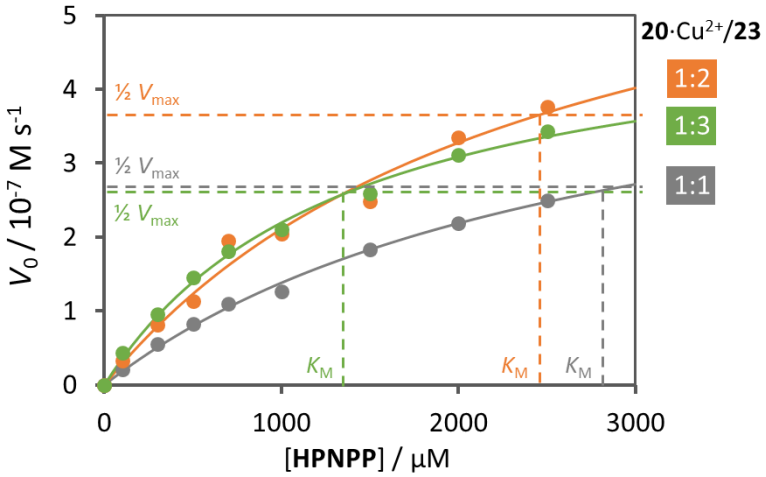

Figure 85. Saturation profiles of catalytic efficiency of three catalytic systems with 1:1 (grey dots), 1:2 (orange dots) and 1:3 (green dots) proportions of **20**·Cu^{2+}/C_{16}Gua **23** at increasing concentration of **HPNPP** in 20% DMSO in water, [total catalyst] = 200 µM, [DIPEA] = 1 mM at 20 °C. The solid lines are fits for a Michaelis-Menten mechanism.

The K_{cat} for the three catalytic systems in the presence of 500 μM of **HPNPP** was determined to be 2.65 ± 0.2 × 10^{-3} s^{-1} (1:1 **20**·Cu^{2+}/C_{16}Gua **23**), 3.65 ± 0.6 × 10^{-3} s^{-1} (1:2 **20**·Cu^{2+}/C_{16}Gua **23**) and 2.60 ± 0.2 × 10^{-3} s^{-1} (1:3 **20**·Cu^{2+}/C_{16}Gua **23**). These values compare well to covalently linked systems reported in the literature, although comparisons are often difficult to perform due to the different reaction conditions used. The majority of artificial phosphodiesterases reported in the literature utilise either 1:1 or 1:2 ratios of guanidinium to TACN·M^{2+}. Salvio and co-workers have designed a number of covalently linked 1:1 TACN·M^{2+} and guanidinium artificial transphosphorylases, with the functional groups attached onto a complex cone-calixarene body[97], and also a simpler xylylene scaffold[120] (Figure 86). A direct comparison with the K_{cat} of our 1:1 **20**·Cu^{2+}/C_{16}Gua **23** system shows that our system is 2 times faster than the related 1:1 calixarene scaffolded catalyst **35** (Figure 86a).[97]

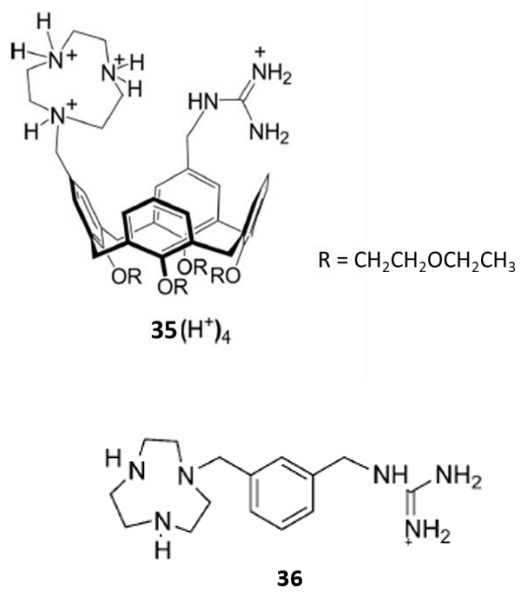

Figure 86. Artificial transphosphorylases containing guanidinium and TACN·M^{2+} functional groups attached to a) a cone-calixarene scaffold[97]; and b) a xylylene scaffold[120]

Systems involving one TACN·M^{2+} cooperating with two guanidinium functionalities are also commonly seen in the literature, especially for RNA cleavage in addition to **HPNPP** cleavage. Figure 87 showed the catalyst **37** reported by Graham and Spiccia (top), who linked one

TACN·M^{2+} and two guanidiniums directly using alkyl spacers.[119] Their K_{cat} is 2 orders of magnitude slower than our self-assembled 1:2 **20**·Cu^{2+}/C_{16}Gua **23** system. Moreover, Anslyn and co-workers reported an example of two guanidinium groups combined with a zinc binding unit for RNA dimer adenylyl(3' → 5')phosphoadenine (**ApA**) cleavage (Figure 87 bottom).[124]

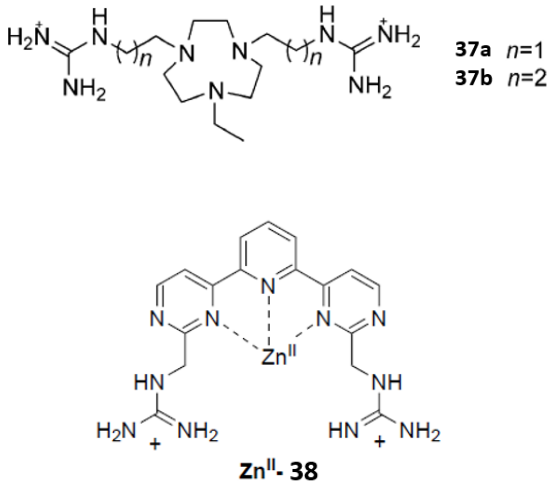

Figure 87. Catalyst structures featuring TACN·M^{2+} in combination with two guanidiniums as reported by Graham[119] and Anslyn[124]

We did not find any examples reporting a 1:3 TACN·M^{2+}/guanidinium system, although in our original screening study (Figure 84), it appeared as if this 1:3 system was the most effective catalyst. However, it is important to note that this early screening study was performed in the presence of 500 μM of **HPNPP**. When comparing this data to the Michaelis-Menten profiles, it can be seen that 500 μM of **HPNPP** is lower than the K_M of the 1:1, 1:2 and 1:3 **20**·Cu^{2+}/C_{16}Gua **23** systems, which sits between 1.3 mM and 2.8 mM (see Figure 88). In the field of enzyme catalysis, excess substrate concentrations imply concentrations larger than the K_M, and therefore, to prevent the misinterpretation of data, we re-examined the catalytic activities of our different catalytic systems in the presence of 3 mM of **HPNPP**. The concentration of DIPEA was also increased to 3 mM to match the concentration of the **HPNPP** substrate. Figure 88 shows the catalytic activities of the 1:2 **20**·Cu^{2+}/C_{16}Gua **23** system with increasing concentrations of **HPNPP** in the presence of 3 mM of DIPEA in 20% DMSO in water.

The data points were fitted into the Michaelis-Menten equation to give V_{max} (1.6 ± 0.3 × 10^{-6} mol s^{-1}) and K_M (1.8 ± 0.7 mM). The K_M value closely matched the K_M of 1:2 **20**·Cu^{2+}/C_{16}Gua **23** system (2.5 ± 0.6 mM) in the presence of 1 mM of DIPEA, while the V_{max} of 1:2 **20**·Cu^{2+}/C_{16}Gua **23** system in 3 mM of DIPEA was almost double that of the V_{max} (7.3 ± 1.1 × 10^{-7} mol s^{-1}) in 1 mM of DIPEA. This suggested that 3 mM of **HPNPP** substrate would be enough to re-examine the catalytic activity of the self-assembled **20**·Cu^{2+} and C_{16}Gua **23** system.

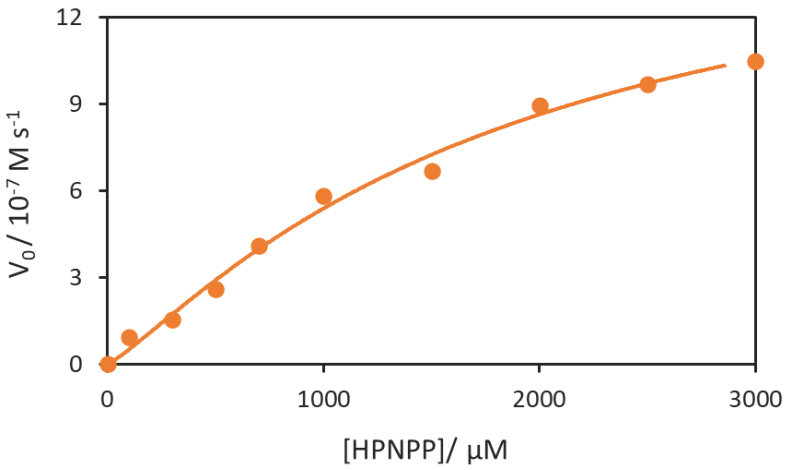

Figure 88. Saturation profiles of catalytic efficiency of the 1:2 **20**·Cu^{2+}/C_{16}Gua **23** at increasing concentration of **HPNPP** in 20% DMSO in water, [total catalyst] = 200 µM, [DIPEA] = 3 mM at 20 °C. The solid lines are the data fits for a Michaelis-Menten mechanism.

Upon re-examination of the kinetics of the reaction under higher substrate concentrations, ([**HPNPP**] = 3 mM, [DIPEA] = 3 mM), we obtained a new optimum ratio of 1:2 **20**·Cu^{2+} to C_{16}Gua **23**. This data is in line with the Michaelis-Menten plots (Figure 89) showing the 1:2 system to have the higher V_{max}.

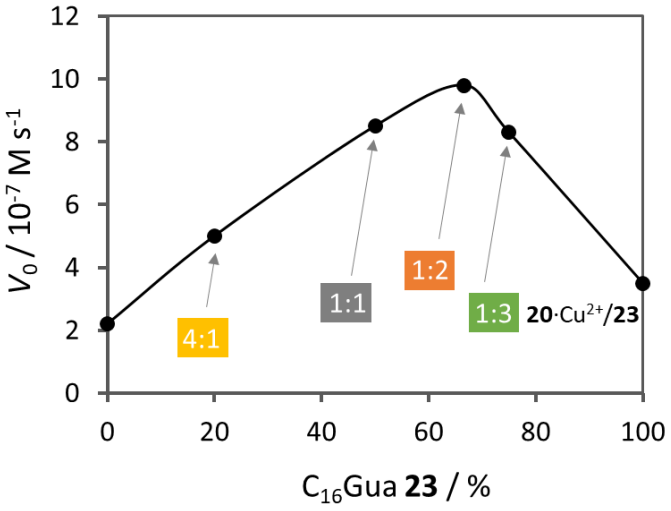

Figure 89. The initial rate of **HPNP**P cleavage with different proportion of C_{16}Gua **23** and **20**·Cu^{2+} in 20% DMSO in water, [total catalyst] = 200 µM, [**HPNPP**] = 3 mM, [DIPEA] = 3 mM at 20 °C.

Next, we wanted to examine the dynamics of the system. As shown in Figure 90a, we first measured the rate of **HPNPP** cleavage in a combined 4:1 **20**·Cu^{2+}/C_{16}Gua **23** system (yellow line) for 4 mins, which showed relatively low catalytic activity. To this reaction mixture, we added enough C_{16}Gua **23** to generate a 1:3 **20**·Cu^{2+}/C_{16}Gua **23** system (green line), which immediately responded by showing a much faster reaction rate. The immediate up-regulation of the **HPNPP** cleavage rate demonstrated that a new catalytic system was generated by fast reorganization of the amphiphiles to form a 1:3 **20**·Cu^{2+}/C_{16}Gua **23** system. In Figure 90a, the ongoing yellow line shows the rate of the unaltered 4:1 **20**·Cu^{2+}/C_{16}Gua **23** system. We were also able to show the reverse of this process. Figure 90b shows us start with measuring the catalytic activity of the 1:3 **20**·Cu^{2+}/C_{16}Gua **23** system (green line) for 3 mins, followed by adding enough **20**·Cu^{2+} amphiphile to generate the 4:1 **20**·Cu^{2+}/C_{16}Gua **23** system (yellow line) in situ. In this case, we observe a down-regulation of catalytic activity. The fast reorganisation and responsiveness of the catalytic system could be only achieved by the reversible self-assembled systems with dynamic and modular nature. To the best of our knowledge, this is the first example that shows a dynamic and modular self-assembled system, which uses weak hydrophobic interaction to induce the cooperativity between multiple functional groups to

create a multifunctional catalyst.

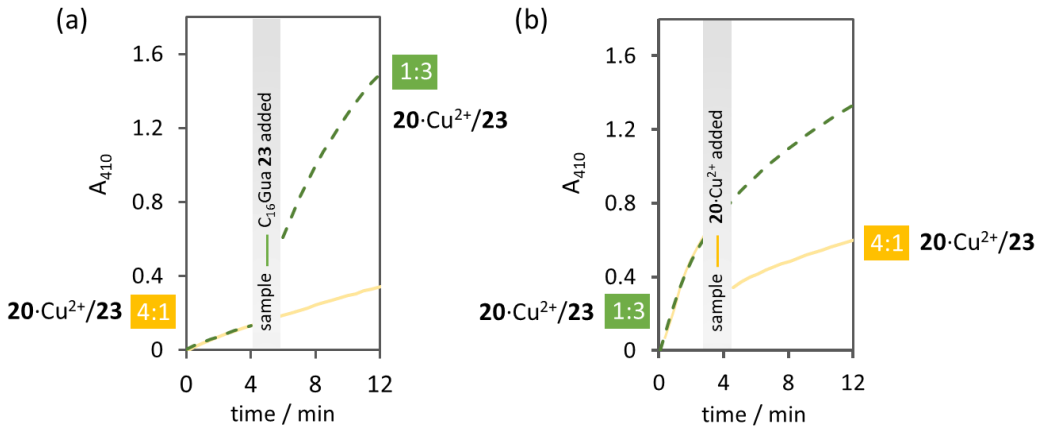

Figure 90. Absorption at 410 nm as a function of time demonstrating the a) up- and b) down-regulation of the combined **20**·Cu^{2+}/C_{16}Gua **23** system, [total catalyst] = 200 µM, [**HPNPP**] = 500 µM, [DIPEA] = 1 mM at 20 °C.

2.3 Conclusions for work on multifunctional catalysis

In this chapter, we have demonstrated the advantages of a self-assembled catalytic system. The modularity of the system allows for the simple mixing of different pre-catalysts and the rapid screening of different proportions of the building blocks to determine the most efficient catalytic system. We have demonstrated this concept by combining two amphiphiles, **20**·Cu^{2+} and C_{16}Gua **23**. Figure 89 shows that these two amphiphiles can be combined to form an efficient transphosphorylase, with the most efficient combination being the 1:2 **20**·Cu^{2+}/C_{16}Gua **23** system. In order for this system, to work there must be synergistic effects between the two amphiphilic building blocks, and we needed to choose specific reaction conditions (20% DMSO in water, and the addition of a base) in order to maximise the cooperative effects. Another interesting observation was that the addition of **HPNPP** induced the formation of the vesicular structures that are catalytically active. This is thus an example of a substrate-induced catalytic system, which has important analogies to out-of-equilibrium

systems, on which we have previously published.[89] The formation of these vesicular structures is important, because it allows cooperativity between the polar headgroups to occur, which is generally not considered possible in micellar systems. The vesicular systems have greater stability and allows the TACN·Cu^{2+} and guanidinium functional groups to be brought in close proximity to work in a synergistic manner for **HPNPP** cleavage. The proposed mechanism is described as a two-point hydrogen bonding via one guanidinium and the general base activation of the copper centre and the other guanidinium.

(Figure 48 was reprinted for clarity)

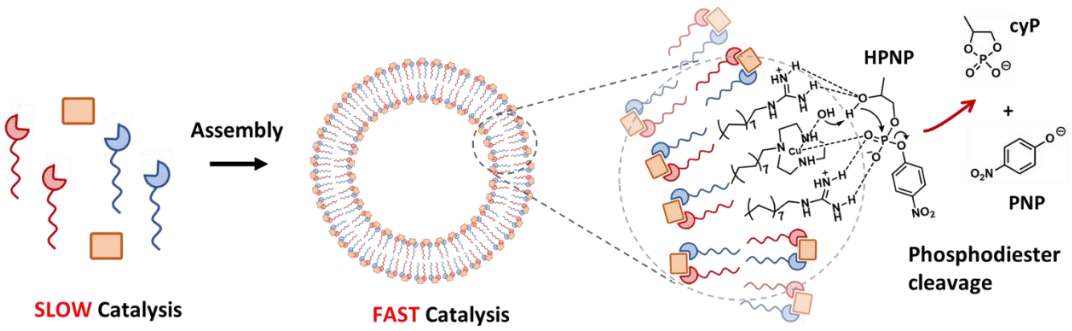

Figure 48. Self-assembly of C_{16}Gua **23** and **20**·Cu^{2+} into vesicular aggregates for **HPNPP** cleavage.

It is worth noting that the catalytic pockets form in our systems are brought together with self-assembly, in contrast to examples reported in the literature, which all involve the formation of pockets within rigid, covalently-linked structures (Table 1). Another important point is that the rates observed with our dynamic system are higher than most of the previously reported examples, though in most cases, this cannot be directly compared due to differences in the reaction conditions used. Although the rigidity of synthetic phosphodiesterases could provide a strong binding with substrates by the specific orientation of functional groups and the entropic trapping of substrates inside the catalytic pockets, there could potentially be issues with product-induced inhibition, where the product could also be trapped in the catalytic pocket, resulting in a lack of turnover. What we can see in Graph 1 (entry 2-12), is that the concentration of the catalyst used was always much higher in concentration (from 2 to 100 times) than the substrates, which suggests that there was limited turnover observed with

these covalently-linked artificial phosphodiesterases. Our self-assembled system appears to overcome this by being highly dynamic. We demonstrated that the catalytic system is able to reorganise itself and demonstrate dynamic up- and down-regulation of catalytic activity. This dynamic nature appears to also overcome any issues with product inhibition, and we are able to employ low catalyst loadings and higher catalyst turnover (Graph 1, entry 1). On the other hand, the dynamic nature of our self-assembled system means that the exact structure of the catalytic pockets formed would be hard to determine, and a dynamic system may not be suitable for real-world applications. The best compromise may be to utilise a dynamic system for screening and optimisation of the catalyst, before constructing an immobilised version to give it greater stability and the possibility of recovery. Work is ongoing by new members of the group, looking at recreating the catalytic triad of an esterase in an artificial self-assembled system, and immobilising them onto Merrifield resin.

Table 1. Summary of reported artificial phosphodiesterases, their catalytic activities and the reaction conditions utilised. (K_{obs} = V_0/[substrate])

Entry	Catalyst	K_{obs} / s^{-1}	[substrate] / mM	[catalyst] / mM	Reaction conditions	Reference
1	1:2 **20**·Cu^{2+}/C_{16}Gua **23** 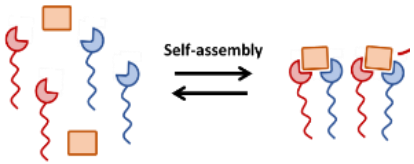	3.3×10^{-4}	3 **HPNPP**	0.2	20% DMSO in water [DIPEA] = 3 mM 20 °C	ref. [107]
2	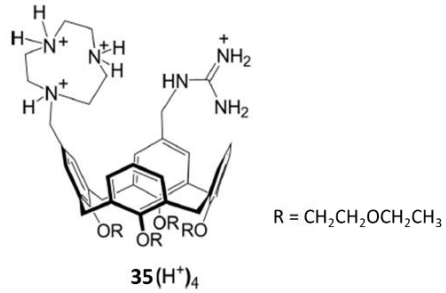 **35**$(H^+)_4$	1.8×10^{-3}	0.2 **HPNPP**	0.5	80% DMSO in water pH 8.9 [DIPEA] = 100 mM [Cu] = 0.5 mM 25 °C	ref. [97]
3	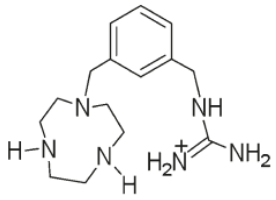 **39**	5.1×10^{-4}	0.2 **HPNPP**	5	80% DMSO in water 0.1 M of DIPEA buffer pH 9.0 25 °C	ref. [120]

4	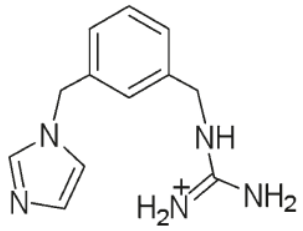 **40**	5.2×10^{-7}	3.0 **HPNPP**	5	80% DMSO in water 0.1 M of **HEPES** buffer pH 7.0 50 °C	ref. [120]
5	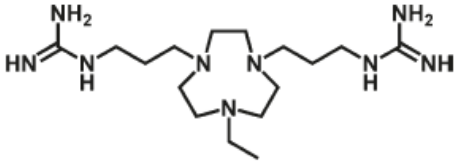 **37b**	$3.2 \pm 0.3 \times 10^{-5}$	0.1 **HPNPP**	2	**HEPES** buffer, pH 7.0 $[CuCl_2]$ = 2 mM $[NaClO_4]$ = 0.15 M 25 °C	ref. [119]
6	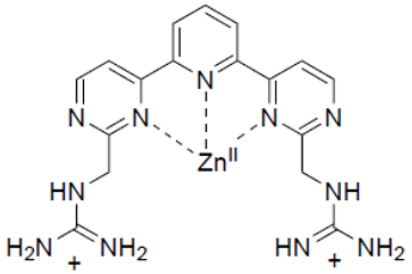 **Zn^{II}- 38**	2.2×10^{-5}	0.05 **ApA**	5	**HEPES** buffer, pH 7.5 37 °C	ref. [124]

7	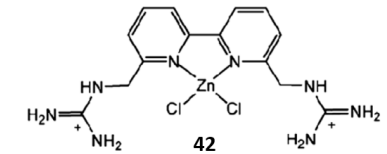 **42** 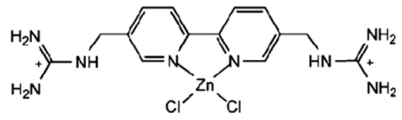 **41**	**41**	3.3×10^{-5}	0.05 **BPNPP**	0.5	50 mM of **Tris** buffer pH = 7.2 25 °C	ref. [125]
		42	6.0×10^{-5}				
8	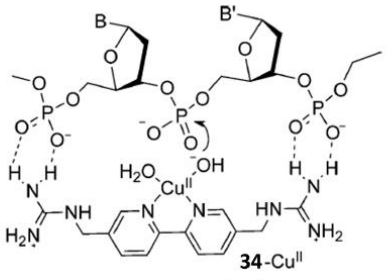 **34**-Cu^{II}	1×10^{-4}		0.038 plasmid pBR322 DNA	0.15	20 mM **HEPES**, pH 7.2 37 °C	ref. [118]
9	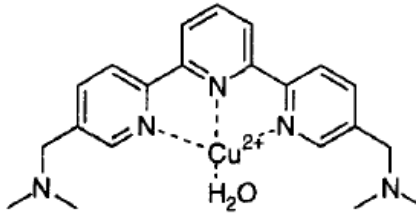 **43**	3.77×10^{-5}		0.2 **HPNPP**	2	50 mM **HEPES**, pH 7.0 25 °C	ref. [126]

10	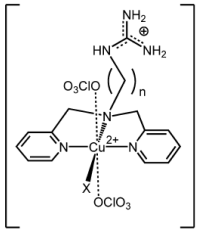 $(ClO_4).xNaClO_4.yH_2O.zMeOH$ **C1**: n = 2, X = H_2O, *x* = 2, *y* = 3, *z* = 0 **C1'**: n = 2, X = MeOH, *x* = 0, *y* = 0, *z* = 1 **C2**: n = 3, X = H_2O, *x* = 2, *y* = 4, *z* = 0 **C2'**: n = 3, X = H_2O, *x* = 0, *y* = 1, *z* = 0 **C3**: n = 4, X = H_2O, *x* = 1, *y* = 0, *z* = 0 **C3'**: n = 4, X = H_2O, *x* = 0, *y* = 1, *z* = 0 **44a-c**	C1	3.05×10^{-7}	0.015 **BPNPP**	0.1	**MOPS** buffer, pH 7.4 0.15 M of $NaClO_4$ 50 °C	ref. [127]
		C2	2.1×10^{-7}					
		C3	4.41×10^{-7}					
		C1	7.2×10^{-3}	0.02 **UpNP**	0.2	**MOPS** buffer, pH 7.4 0.15 M of $NaClO_4$ 37 °C	ref. [127]	
		C2	1.0×10^{-2}					
		C3	1.09×10^{-2}					
11	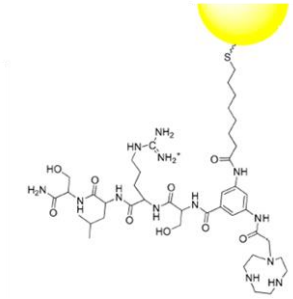 **45**	No K_{obs} data $K_{cat} = 1.4 \times 10^{-2}$ s^{-1}		0.01 **HPNPP**	0.025	10 mM of **EPPS** buffer pH = 7.5 25 °C		ref. [128]
12	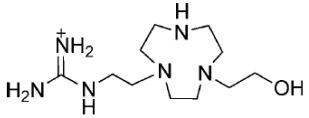 **46**	No Zn^{2+} added	3.6×10^{-5}	0.05 pUC 19 DNA	0.144	50 mM Tris-HCl/10 mM NaCl buffer 37 °C	pH = 7.2	ref. [129]
		1:1 ligand/Zn^{2+}	4.3×10^{-5}				pH = 6.0	

Chapter Three: Fluorescent amphiphiles for sensing applications

3.1 Introduction

During our studies on the self-assembly of amphiphilic molecules to form multifunctional catalytic systems, we realised the difficulty of understanding what was happening at the molecular level upon self-assembly. For our system involving the self-assembly of C_{16}TACN·Cu^{2+} (**20**·Cu^{2+}) and C_{16}Gua **23**, an early problem that we had was understanding whether these two amphiphiles were self-assembling in solution in a heterogenous manner, or whether there was an element of self-sorting to form vesicles composed of a single amphiphile. There could also be elements of both situations, potentially with the formation of clusters, or patches on the surface of the vesicles (see Figure 68). In order to gain insight into the self-assembly of amphiphiles into vesicular structures, we set out to incorporate fluorescent moieties into our catalytically active amphiphiles. The fluorescent groups were chosen for the potential to exhibit fluorescence resonance electron transfer (FRET) interactions, which would be used to give an indication of self-assembly. The fluorescence response would give us information about the identity of the amphiphiles involved in the self-assembled structures and provide insight into clustering or patchiness on the self-assembled surface. In addition, solvatochromic changes to the emission maximum and intensity could be used to give an idea of the polarity of its surrounding environment. An example of this is seen with the **Nile red**-based fluorescence probe **NR18**, used for the investigation of large unilamellar vesicles (LUVs) and giant unilamellar vesicles (GUVs), which was reported by Sessa and co-workers.[130] While **Nile red** itself might not only distribute within the membrane but could also remain deep within the bilayer core, Sessa and co-workers designed an amphiphile with a zwitterionic head group and a long hydrophobic chain which allowed it to be localized selectively within the membrane bilayers. Therefore, the general polarity and other physical states of the phospholipid and cholesterol-containing membranes could be deduced by the changes in fluorescence of **Nile red** due to its solvatochromic effects.

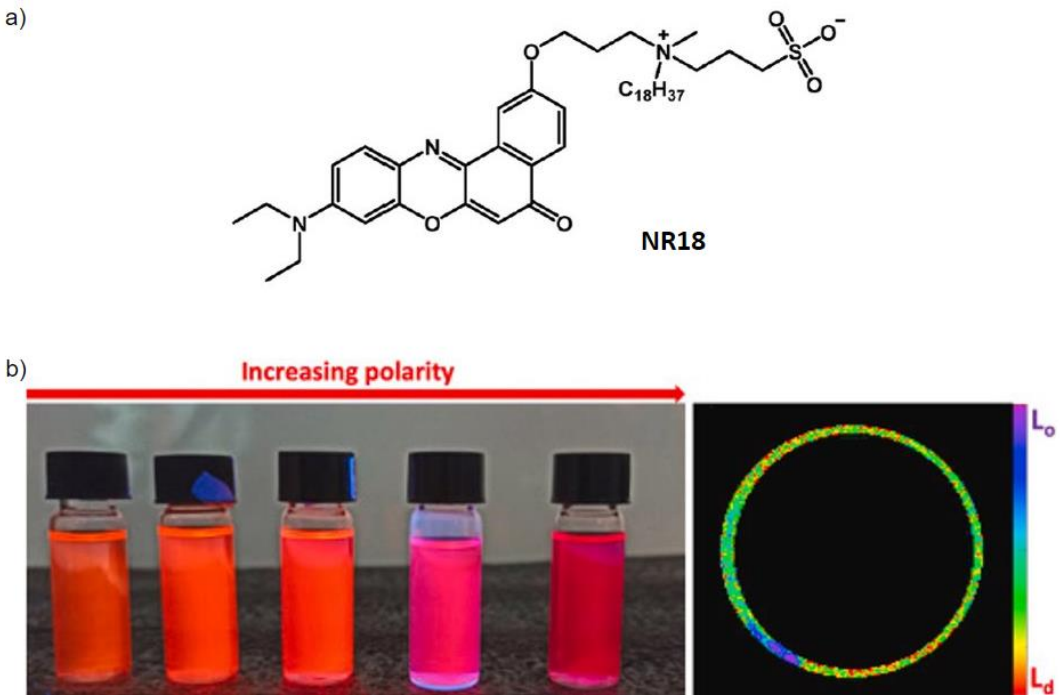

Figure 91. a) Chemical structure of the membrane probe **NR18**; b) the solvatochromic and colorimetric changes of **NR18** in solvents of varying polarity, including dioxane, THF, CH_2Cl_2, acetone, MeOH (from left to right). The fluorescence intensity image of a mixed POPC/sphingomyelin/cholesterol 1:1:1 GUV labelled with **NR18**. Reprinted with permission from ref. 130. Copyright (2021) Elsevier Inc.

3.2 Fluorescence resonance energy transfer (FRET)

Fluorescence is a process of energy release (Figure 92), which starts with energy absorption by substances from light or other electromagnetic radiation. Electrons from the ground state absorb energy and are promoted to an excited energy state. After non-radiative transition to the lowest energy level of the excitation state (internal conversion), the delocalized electron can relax back to the ground state with release of a photon. This energy release process is called fluorescence decay. Fluorophores are chemical compounds that can absorb energy at a specific wavelength and emit photons at a higher wavelength and lower energy.

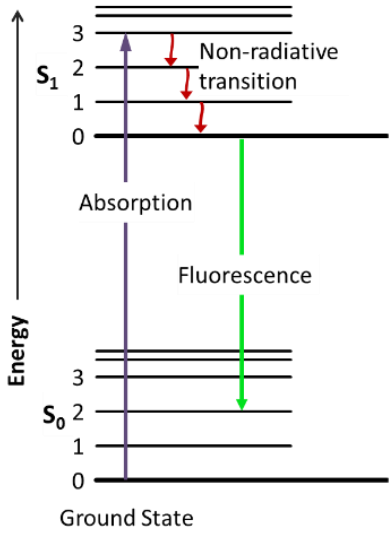

Figure 92. Fluorescence emission from excitation state to the ground state (green arrow)

Fluorescence resonance energy transfer (FRET) occurs when energy transfer occurs between two light-sensitive molecules in close proximity and was first described by Theodor Förster in 1946.[131] FRET occurs between fluorophore pairs (donors/acceptors), when the lowest vibrational energy level in the excited state of the donor matches one of the vibrational energy levels in the excited state of acceptor (Figure 93). The energy transfer starts with energy absorption by the donor, where an electron in the ground energy state is excited to a higher excitation state, followed by non-radiative decay to the lowest vibrational level at the same energy state. It is crucial that the energy from a donor cannot only go through internal conversion by itself but also transfer to an acceptor when the energy of the excited state has a perfect match between a donor and an acceptor. In this way, the energy from a donor can migrate to an acceptor, which dissipates the energy following a traditional fluorescence process.

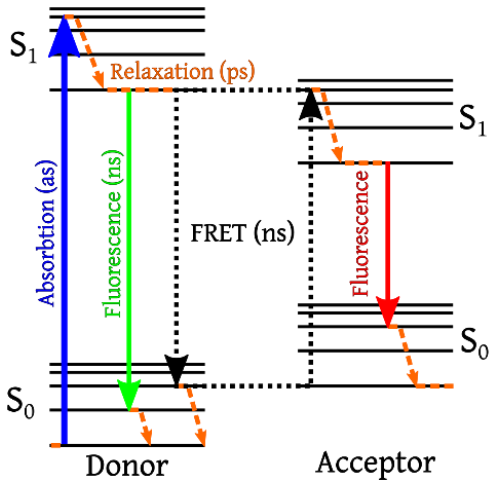

Figure 93. FRET processes between two molecules

For efficient FRET to occur, a significant overlap between the emission spectrum of a donor and the absorption spectrum of an acceptor is required (Figure 94a).[132] Usually, a minimum of 30% spectral overlap is required, and the FRET process results in a decrease in donor emission and an increase in acceptor emission when there is excitation at the maximum absorption of the donor. Another essential criterion affecting FRET is the distance between the donors and acceptors. FRET is extremely sensitive to small changes in distance with a relationship that is inversely proportional to the sixth power of the distance between the FRET pair. Energy can only transfer efficiently from donors to proximal acceptors if they are within the Förster distance R_0 (normally from 1 nm to 10 nm). The Förster distance R_0 is a constant for a given combination of fluorescence pairs. In Figure 94b, the sigmoidal relationship between FRET efficiency and Förster distance reveals that the distance between fluorescence pairs is crucial for high FRET efficiency. This makes FRET a useful tool in many research fields (e.g. biology, chemistry) for obtaining information about distance.

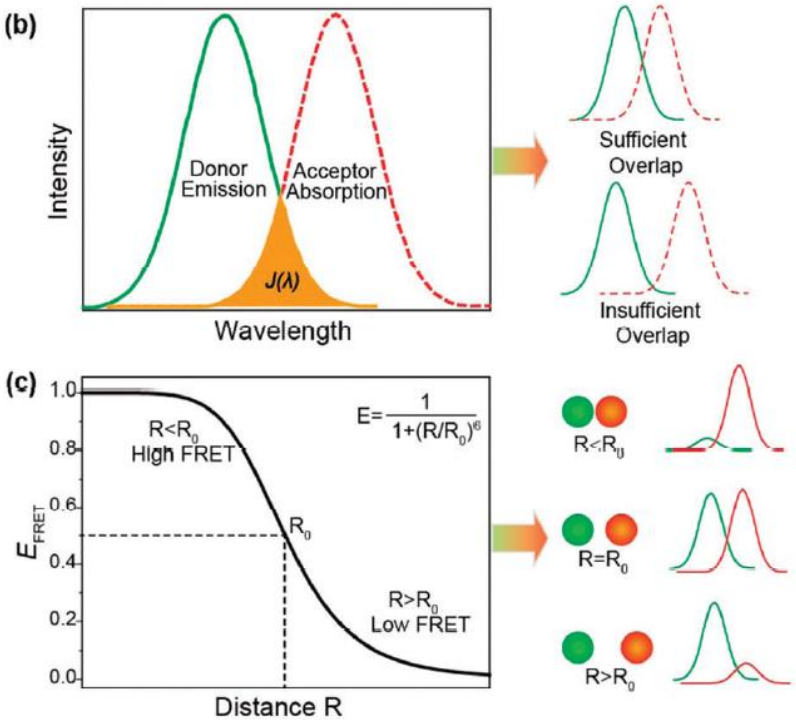

Figure 94. a) Graphical representation of spectral overlap between the emission of donors and excitation of acceptors. b) FRET efficiency with the function of Förster distance R_0 between fluorescence pairs. Adapted with permission from ref. 132. Copyright (2018) Royal Society of Chemistry.

3.2.1 Current applications of FRET

Taking advantage of the high sensitivity and distance dependence properties, FRET has been widely utilised in detection and sensing applications in numerous biomedical and experimental fields. Famous examples include the utilisation of FRET for the detection of protein folding,[133] lipid mixing assays in membrane fusion[134] and the detection of signal transduction.[135]

Figure 95 shows an example of FRET used in the study of membrane fusion. Amphiphiles labelled with either fluorescence donors or acceptors were co-assembled with phospholipids

to form liposomes where FRET could be observed. When these liposomes are combined with an unlabelled liposome, FRET is diminished as this expands the size of the resulting liposome, causing spatial separation between fluorescence donors and acceptors. The sensitivity of FRET to the distance between donors and acceptors can be used to qualitatively detect even small changes in the size of liposomes. Moreover, the reverse method, where two liposomes, one labelled with fluorescence donors and the other labelled with fluorescence acceptors, is also possible. With fusion, fluorophore pairs are brought closer resulting in an increase in FRET.

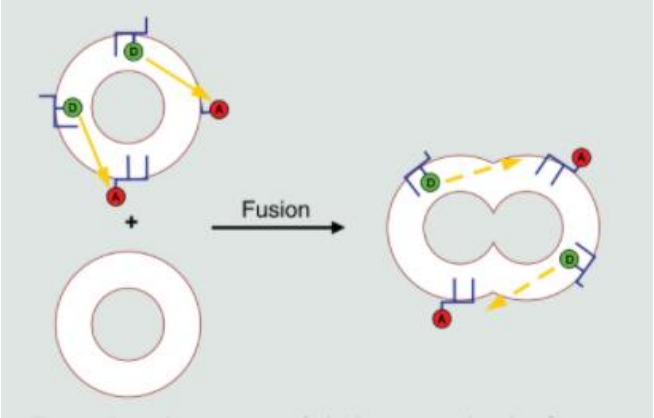

Figure 95. A graphical illustration of membrane fusion resulting in changes in the spatial distance between fluorescence donors and acceptors.

Furthermore, Bernitzki and Schrader reported an artificial system for messenger-induced transmembrane signalling.[135] Two unsymmetric cholesterol-based transmembrane units **47** and **48** were constructed with bisphosphonate dianions at one end for recognition of polycationic signals, and fluorophore dyes (tryptophan and dansyl) at the other end for FRET output. After the two functionalized transmembrane units were co-assembled with dipalmitoylphosphatidylcholine (DPPC) to form synthetic liposomes, the addition of polycationic diethylenetriammonium (DET) as primary messengers induced the complexation of heterodimeric transmembrane units via strong ion interactions. As a result, the internal fluorophores tryptophan and dansyl were brought into proximity and give a strong FRET signal under light irradiation. This example of messenger transduction through impermeable

membranes was of great importance for the imitation of transmembrane signalling in living cells utilizing FRET as a readable signal.

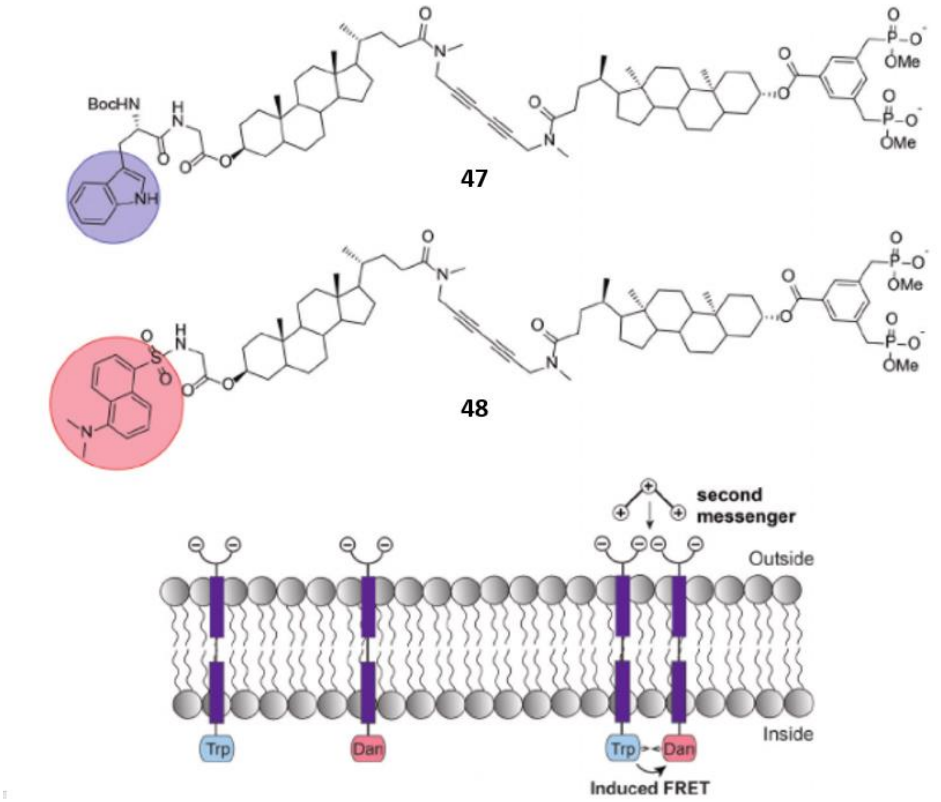

Figure 96. Signal transduction through a membrane bilayer using FRET to generate an output. Reprinted with permission from ref. 34. Copyright (2021) Wiley-VCH GmbH, Weinheim.

König and co-workers reported the peptide-induced recruitment of amphiphilic receptors embedded with artificial membranes.[136] The binding affinity between peptides and amphiphilic receptors was first studied using membranes composed of 1,2-dioleoyl-sn-glycero-3-phosphocholine (DOPC), embedded with 1 mol% of each of the amphiphilic receptors Zn-3,5-bis[(bispyridin-2-ylmethylamino)methyl]-4-hydroxyphenyl (**Zn-DPA**; green) and Cu-nitrilotriacetic acid (**Cu-NTA**; blue). As these receptors have been previously shown to bind strongly with phosphates and imidazole rings, the peptide **P1** were designed to contain both phosphates and imidazole rings for provide multipoint interactions with the receptor amphiphiles. The peptide **P1** was also labelled with a fluorophore carboxylfluorescein (FAM;

yellow star) to detect the successful binding of peptide **P1** to both receptor amphiphiles on the surface of synthetic membranes. The authors were able to show that peptide **P1** induced the fusion of the two receptor amphiphiles in membranes due to its ability to form strong multivalent interactions.

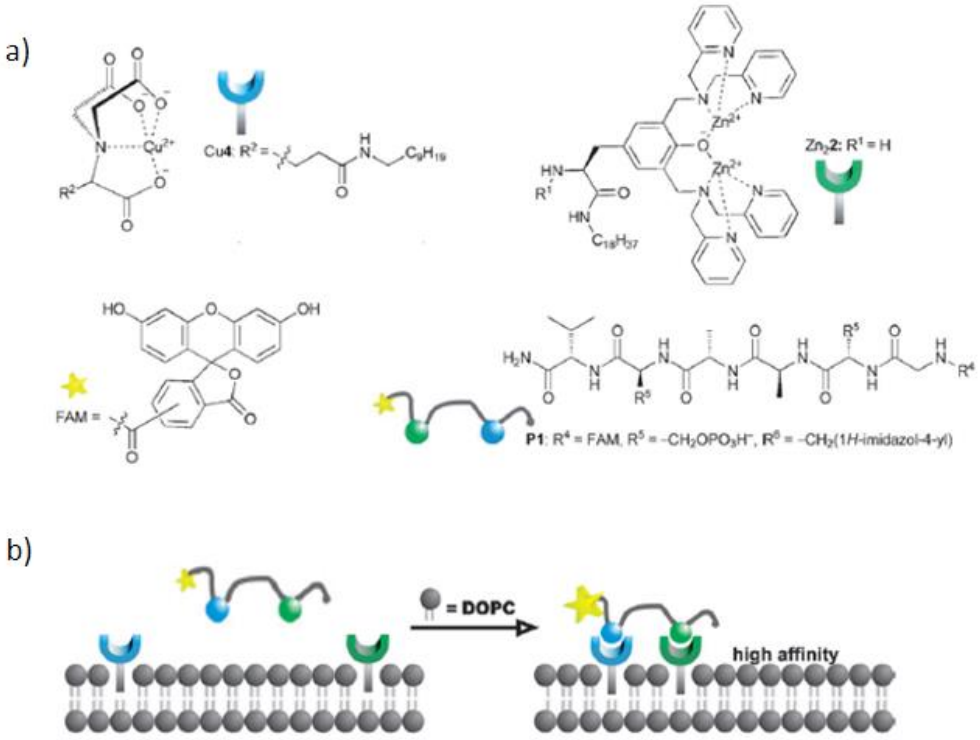

Figure 97. a) Chemical structures of receptor amphiphiles and the peptide **P1**; b) A graphical illustration of the fusion of receptor amphiphiles induced by peptides **P1**. Adapted with permission from ref. 136. Copyright (2020) Wiley-VCH GmbH, Weinheim.

The binding between peptides and the two amphiphilic receptors could also be detected by two fluorophore pairs. The peptide **P2** was modified from **P1** by removing the fluorophore FAM, and both receptors were labelled with one of a fluorescence donar-acceptor pair. The **Zn-DPA** amphiphile was labelled with FAM to form **Zn-DPA-FAM**, and the **Cu-NTA** amphiphile was labelled with rhodamine (TMR) to form **Cu-NTA-TMR**.

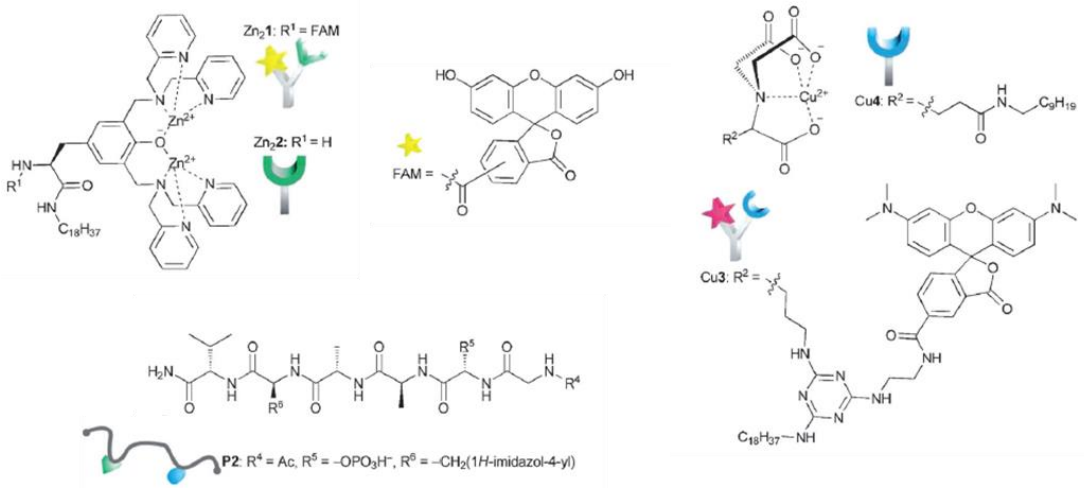

Figure 98. Chemical structures of two amphiphilic receptors and peptide **P2**. Reprinted with permission from ref. 136. Copyright (2020) Wiley-VCH GmbH, Weinheim.

The divalent binding of peptide **P2** induced the dimerization of **Zn-DPA-FAM** amphiphiles and **Cu-NTA-TMR** amphiphiles in the DOPC membranes, where the two fluorescent pairs (yellow and pink stars in Figure 99a) were brought into close proximity within the Förster distance of 5.5 nm. The spatial arrangement of **Zn-DPA-FAM** amphiphiles and **Cu-NTA-TMR** amphiphiles, which was driven by the strong binding affinity of **P2**, gave FRET output with a decrease in the emission of the donor FAM (λ_{em} = 490 nm) and an increase in the emission of the acceptor TMR (λ_{em} = 580 nm), as shown in Figure 99b. The control study using monovalent peptides had no significant effect on the observed emission spectra. Depending on the spatial arrangement of multiple fluorophores in the membrane, a particular spectroscopic output can be used to provide information on the specific binding of targets and their receptors, as well as providing spatial information.

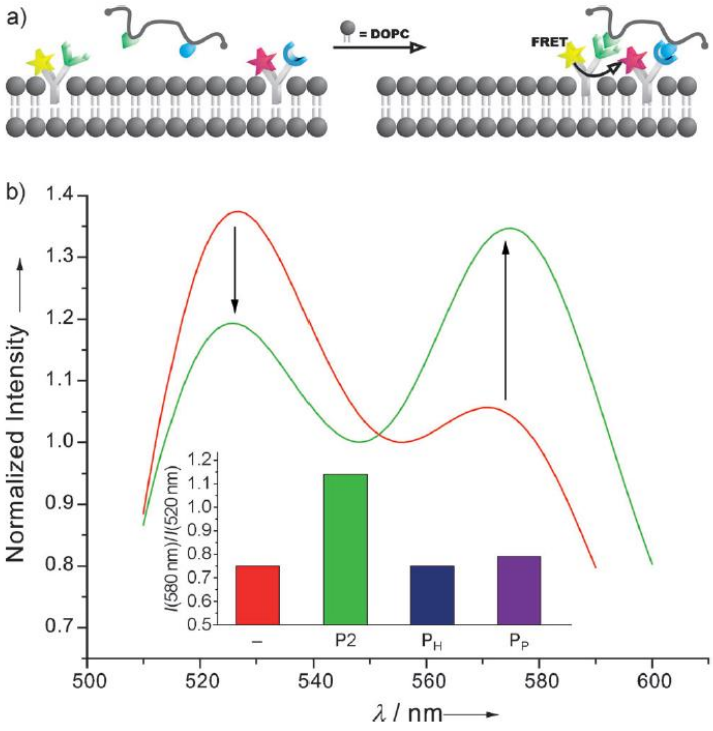

Figure 99. a) A graphical illustration of the fusion of labelled membrane receptors induced by peptides resulting in a FRET output; b) Fluorescence spectra of DOPC vesicles containing labelled receptors **Zn-DPA-FAM** amphiphiles and **Cu-NTA-TMR** amphiphiles (0.5 mol% each) in the absence (red) and presence (green) of peptide **P2**. Relative FRET emission ratio ($I_{580\ nm}/I_{520\ nm}$) of **P2** and monovalent $\mathbf{P_H}$ and $\mathbf{P_P}$ as control (inset). Reprinted with permission from ref. 136. Copyright (2020) Wiley-VCH GmbH, Weinheim.

3.2.2 Using FRET to detect self-assembly

Inspired by the above literature examples, we wanted to use FRET to investigate the aggregation properties of our self-assembled vesicular systems. We wanted to investigate the use of FRET to determine whether self-sorted homogenous or heterogenous assembly takes place when mixing two or more pre-catalyst ligands. To achieve this, we aimed to make fluorescent analogues of numerous catalyst ligands containing different polar head groups. We expected that if single amphiphiles aggregated with themselves to form homogeneous

aggregates (Figure 68b), then the donor or acceptor fluorescent pairs would be present in separate aggregates and would be too far apart for FRET to be observed. However, if heterogeneous self-assembly occurs (Figure 68a), the fluorescent donor-acceptor pairs should be close enough for FRET to occur. Our aim was to investigate if this concept was possible, and whether FRET could be used to estimate the degree of heterogenous mixing.

(Figure 68 was reprinted for clarity)

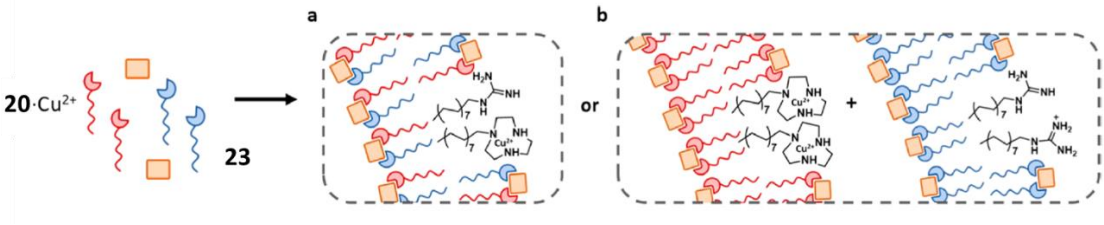

Figure 68. Graphical illustration of the possibility of homogeneous or heterogeneous self-assembly when mixing two different amphiphiles. Reprinted with permission from ref. 107. Copyright (2020) American Chemical Society.

These fluorescent amphiphiles could also be used to determine the most efficient binding between a substrate (or transition-state analogue) with an array of pre-catalyst ligands in solution, allowing rapid screening of potential catalyst combination. These concepts will be discussed in more detail later on in this chapter.

3.2.3 Fluorophores and their properties

Our goal was to use fluorescent compounds capable of exhibiting FRET as a probe to investigate the self-organisation of amphiphiles. The commencement of this study was to choose suitable fluorophore donor-acceptor pairs, which should not only have enough spectral overlap for energy transfer but would also have to have suitable synthetic handles for conversion into catalytically active amphiphiles.

Fluorophores are fluorescent substances that can re-emit light upon light irradiation. They exist not only as small organic molecules but also as fluorescence proteins[137] and even fluorescence nanoparticles,[138] such as gold nanoparticles and quantum dots. In this project, our goal was to use small organic molecules due to their small size, and the ability to easily modify their chemical structures to attach a catalytic head and a hydrophobic tail.[139-140]

Small organic fluorescent molecules are normally made up of several extended aromatic groups, or planar and cyclic moieties with several π bonds, which allows for extensive delocalisation of electrons. Commonly used fluorophores are summarized in Figure 100, showing an abundant of choice in the UV-Vis region from 200 nm to 800 nm.

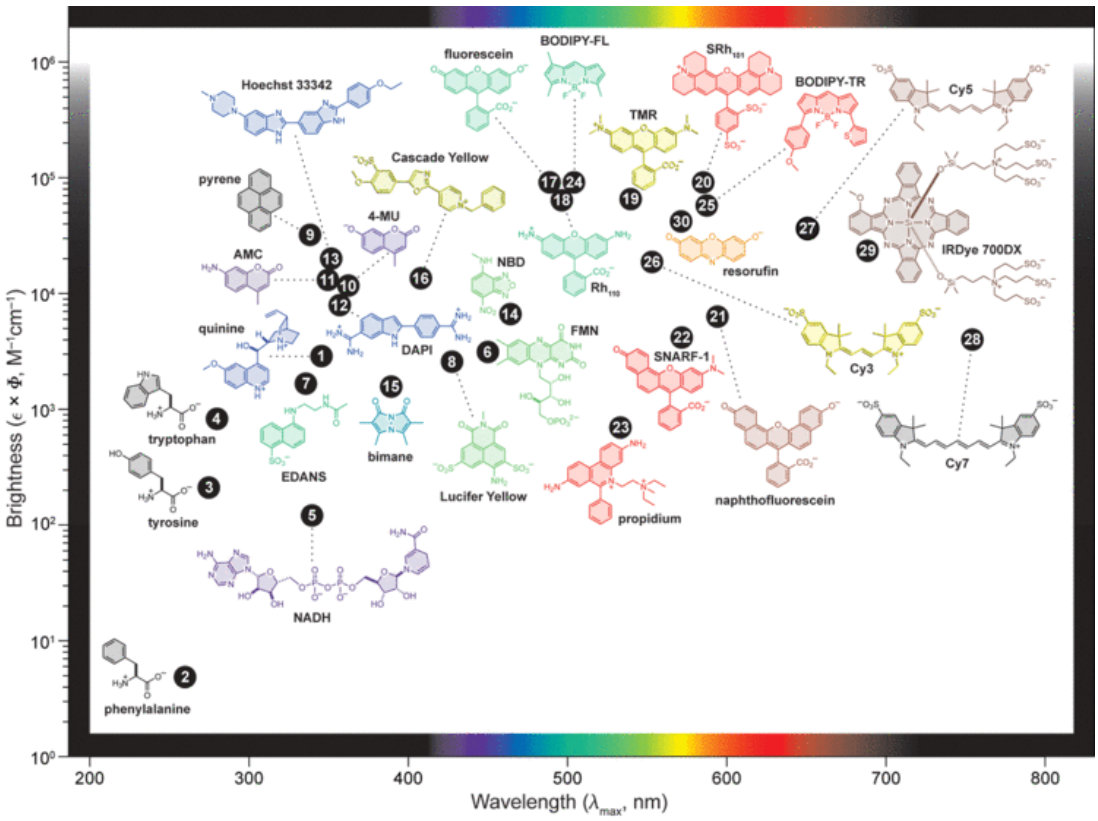

Figure 100. Summary of commonly used fluorophores arranged according to their brightness and absorption maximum.

Regarding the choice of fluorophore donor-acceptor pairs, the basic criteria used were the spectral overlap as well as the FRET efficiency, including a higher quantum yield of fluorophore donors and a lower extinction coefficient of fluorophore acceptors. We began by utilising tryptophan as one of the fluorophores and searched for other fluorophores with significant spectral overlap.

Pushina and co-workers reported a dual-chromophore FRET-based sensor for the identification of chiral analytes (amines, amino alcohols, diols and hydroxy acids) and determination of their enantiomeric excess (Figure 101).[141] The chromophores that they used were tryptophanol (FRET donor) and a dihydroxycoumarin (FRET acceptor). The fluorophore displacement studies were initially conducted to confirm that a diol or a hydroxy acid analyte could displace the diol fluorophore **FL2**. Prior to the addition of diol and hydroxyl acid, the initial ensemble of tryptophanol, dihydroxycoumarin and 2-formylphenylboronic acid core showed an intramolecular FRET signal with fluorescence quenching of tryptophanol (donor) and fluorescence amplification of coumarin (acceptor). However, after the addition of a diol or a hydroxy acid, the coumarin fluorophore (**FL2**) was released. This resulted in unsuccessful FRET with an increase of tryptophanol emission and decrease of coumarin emission as the distance between the fluorescence pairs were no longer close enough for energy transfer. The degree of fluorescence amplification and quenching of the donor-acceptor pair was used to differentiate between the enantiomers of the analytes due to their different affinity to the central boronic acid.

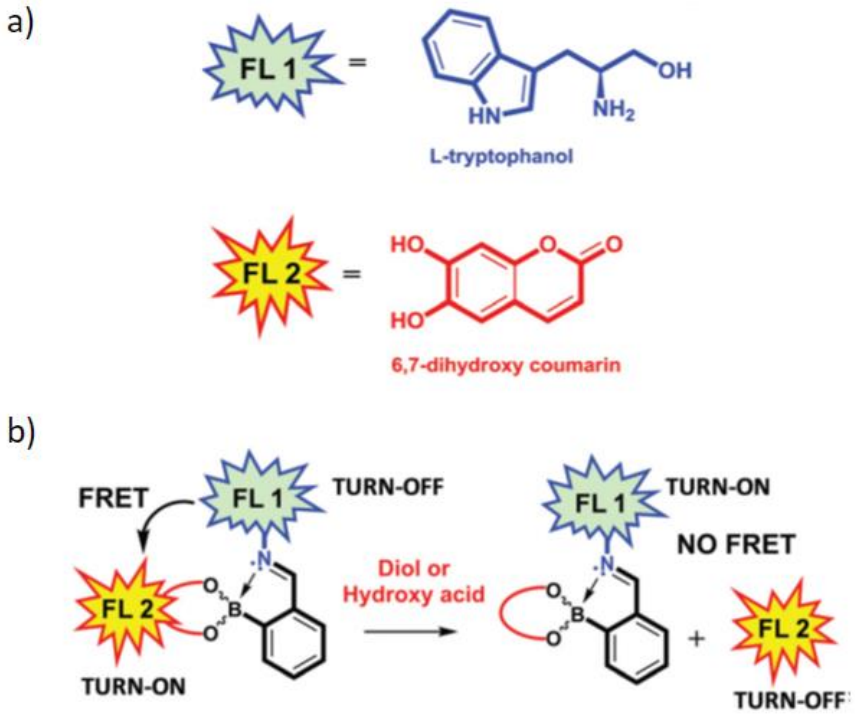

Figure 101. a) Chemical structures of fluorophore pair **FL1** and **FL2**; b) schematic representation of the FRET-based assays. Reprinted with permission from ref. 141. Copyright (2019) Royal Society of Chemistry.

Numerous different fluorophore donor-acceptor pairs have been reported in the literature for a variety of different applications. For example, the fluorophore pair of coumarin and naphthalimide have been commonly employed in ratiometric sensing systems for hydrogen sulfides,[142] thiophenols[143] and the measurement of pH.[144-145] Dong and co-workers reported a dual chromophore ratiometric fluorescent sensing system based on a ICT-PET-FRET mechanism for the measurement of pH in the range 5.0-7.2 within the endoplasmic reticulum (ER).[144] This dual-site ratiometric probe **49** consists of a fluorescence donor-acceptor pair (coumarin and naphthalimide), two pH sensitive groups (morpholine and phenol) and an endoplasmic reticulum targeting group. Under weakly acidic conditions, form 1 of **49** predominates, and the protonation of morpholine prevents PET processes, resulting in successful FRET from the coumarin moiety to the naphthalimide, resulting in green fluorescence. With an increasing pH, deprotonation of morpholine results in form 2

dominating, so that the electrons in morpholine is transferred to naphthalimide and FRET is inhibited by photo-induced electron transfer (PET). The sensor therefore fluoresces faint blue from coumarin itself. Under basic conditions, the sensor loses the proton on the phenol group of the coumarin, giving form 3, which promotes an efficient intramolecular charge transfer (ICT) process involving the phenoxide anion, resulting is strong blue emission. The authors hypothesized that the sensitive response of **49** towards pH change was simultaneously based on the mechanisms of ICT, PET and FRET.

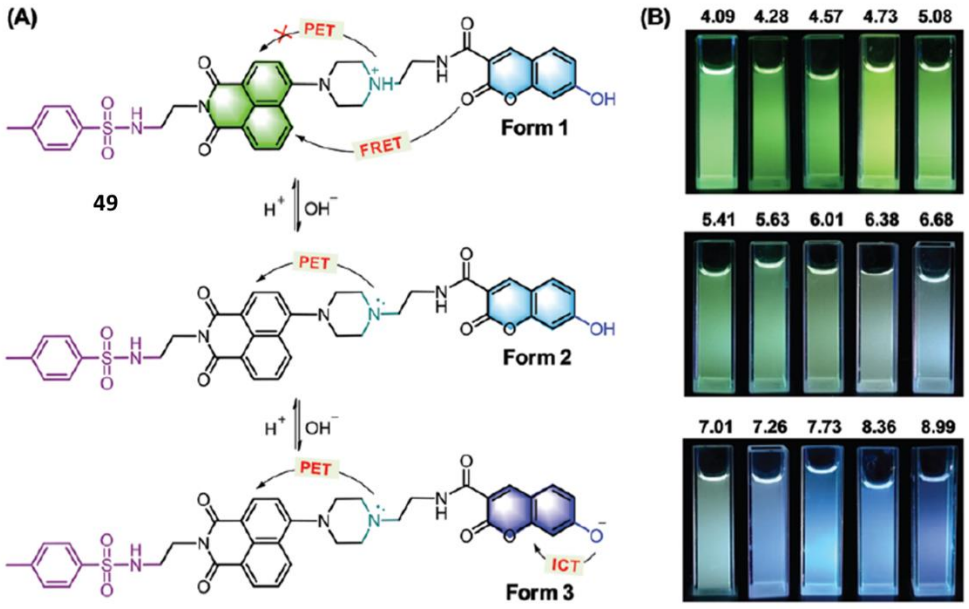

Figure 102. Schematic representation of the three forms of **49** and the effects of PET, FRET and ICT at different pH values. Reprinted with permission from ref. 144. Copyright (2019) Royal Society of Chemistry.

Due to the abundance of literature examples demonstrating successful FRET between tryptophan and coumarin as well as coumarin and naphthalimide, we decided to perform our investigations using these two fluorophore pairs. We began our studies by measuring the excitation and emission spectra of tryptophan **50**, coumarin derivative **51** and naphthalimide **52** in 20% DMSO in water. This solvent system was chosen for better solubility and also because it matches the conditions under which self-assembled multifunctional catalysis was earlier

performed in our group.[107] The maximum excitation and emission of L-tryptophan **50** (λ_{ex} = 278 nm, λ_{em} = 354 nm), coumarin **51** (λ_{ex} = 388 nm, λ_{em} = 477 nm) and naphthalimide **52** (λ_{ex} = 460 nm, λ_{em} = 550 nm) are shown in Figure 103. Looking at the fluorophore pair of tryptophan **50** and coumarin **51**, there is an excellent degree of spectral overlap between the emission spectrum of tryptophan **50** and the excitation spectrum of coumarin **51**. The overlap was over 90%, from which we could expect high efficiency of energy transfer. Furthermore, the stronger intensity of excitation and emission of tryptophan **50** compared to coumarin **51** suggested that tryptophan **50** possessed a higher quantum yield, which fits the summary data in Figure 103 with the higher expected brightness of tryptophan **50**. The high quantum yield of tryptophan **50** was of great importance for transferring more energy to the acceptor, giving better chance for a successful and efficient FRET processes. With regards to the fluorophore pair of coumarin and naphthalimide, the emission of coumarin **51** and the excitation of naphthalimide **52** also showed a good degree of spectral overlap. Therefore, we confirmed that the tryptophan/coumarin and coumarin/naphthalimide pairs could be suitable fluorophore for further investigation.

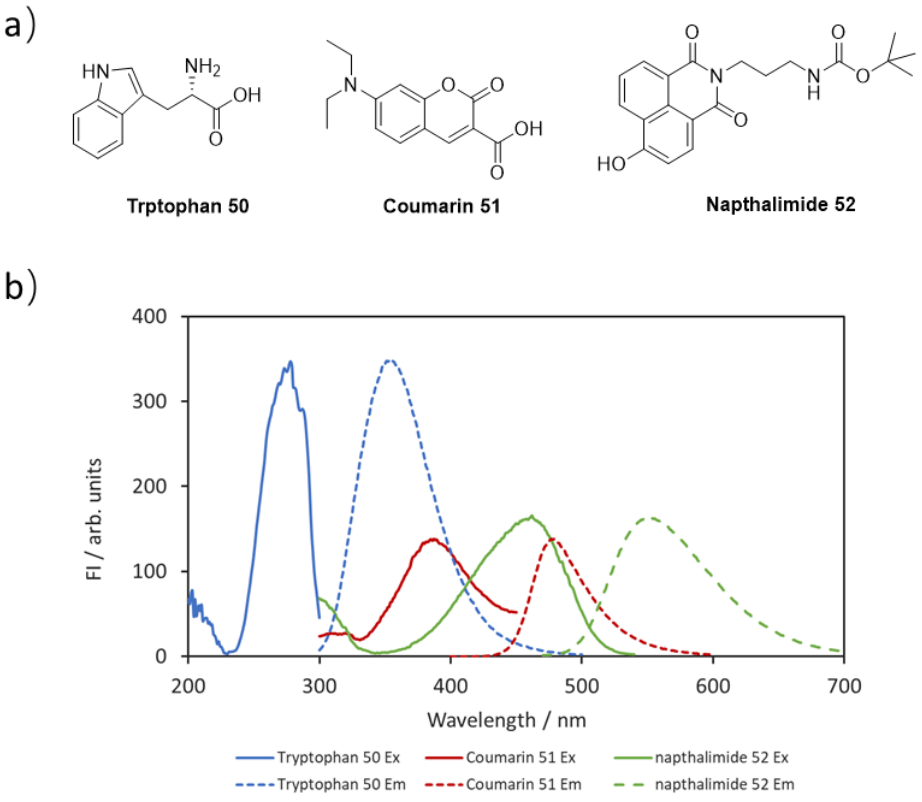

Figure 103. a) The chemical structures of L-tryptophan **50**, coumarin derivative **51** and naphthalimide **52**; b) fluorescence excitation and emission spectra for 50 μM of tryptophan **50**, coumarin **51** and naphthalimide **52** in 20% DMSO in water, slit 2.5/5.

3.3 Design, synthesis and properties of the fluorescent amphiphiles

Our aim was to design and synthesise fluorescent analogues of the C_{16}TACN **20** and C_{16}Gua **23** amphiphiles that we have shown to effectively self-assemble into vesicular structures and perform catalysis. The fluorescent amphiphiles would contain a catalytic polar head (TACN or guanidinium group) that allows for **HPNPP** cleavage via a cooperative mechanism, a fluorophore (tryptophan, coumarin or naphthalimide) for FRET, and a hydrophobic alkyl chain for inducing self-assembly in aqueous solution. Our goal was to use these amphiphiles to gain insight into the self-assembled structures formed by these cooperative catalysis and to probe dynamic changes in its structure in real time.

3.3.1 Overall design of the fluorescent amphiphiles

One design we investigated, was a simple linear structure similar to the catalytic amphiphiles of C_{16}TACN **20** and C_{16}Gua **23**, and with the fluorophores inserted into the hydrophobic chains as shown in Figure 104. The amphiphiles synthesised were C_{12}-I-Trp-TACN **53**, C_{12}-I-Coum-TACN **54** and C_{12}-I-Naph-Gua **55**. These amphiphiles have packing parameters close to one, with a cone-like shape what we envisaged would be favoured to assemble into bilayer and vesicular structures.

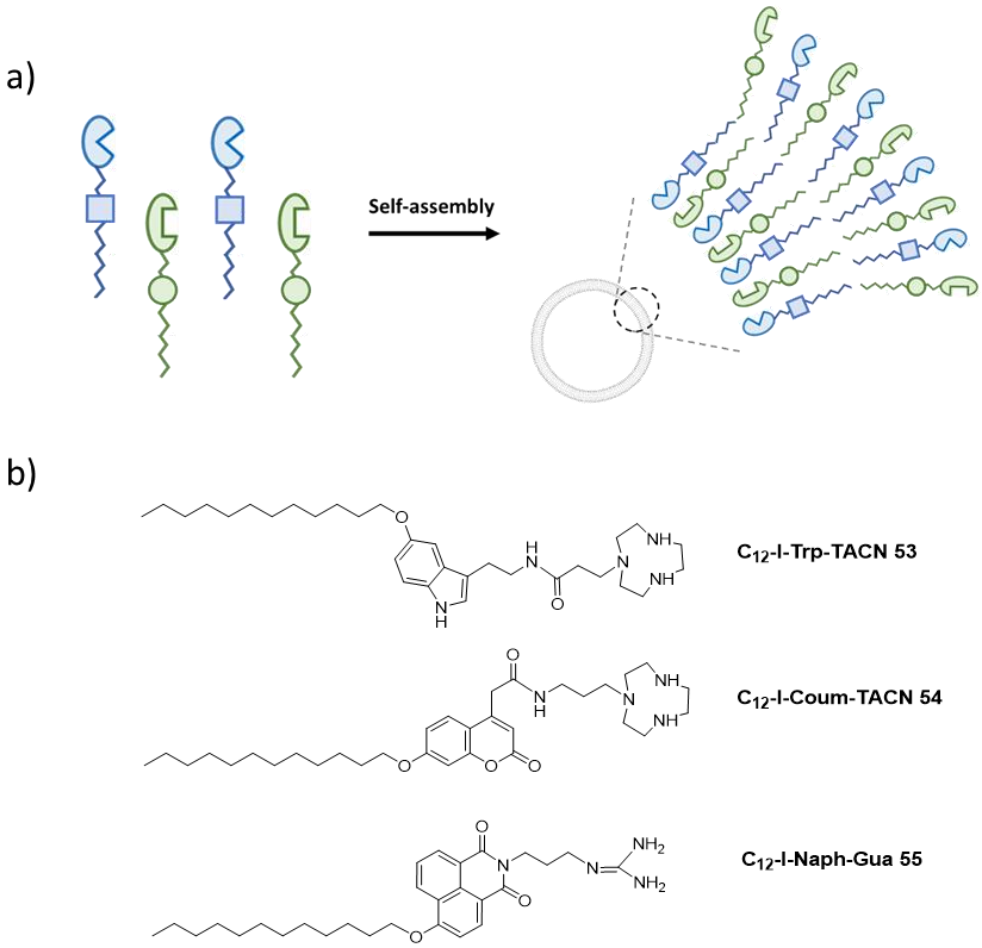

Figure 104. a) Graphic representation of the linear shape (I-shaped) amphiphiles containing fluorophores (blue squares and green circles) inserted in the hydrophobic chains and catalytic head groups towards a bulky solution and b) the chemical structures of the C_{12}-I-Trp-TACN **53**, C_{12}-I-Coum-TACN **54** and C_{12}-I-Naph-Gua **55** amphiphiles.

We also investigated the use of a Y-shaped design for the amphiphiles, where the catalytic polar head and the fluorophore would branch out from the hydrophobic chain (Figure 105). This would give these Y-shaped amphiphiles a bulky head group and a relatively low packing parameter with its overall shape being a cone or a truncated cone. With this critical packing shape, self-assemble into micellar structure rather than vesicles is predicted. If micelles are formed, the amphiphilic molecules would experience a much faster exchange between the self-assembled structures and the bulk, resulting in poor catalysis as well as inefficient FRET processes. We were thus also interested in these molecules to investigate if we could use

changes in fluorescence to probe these ideas.

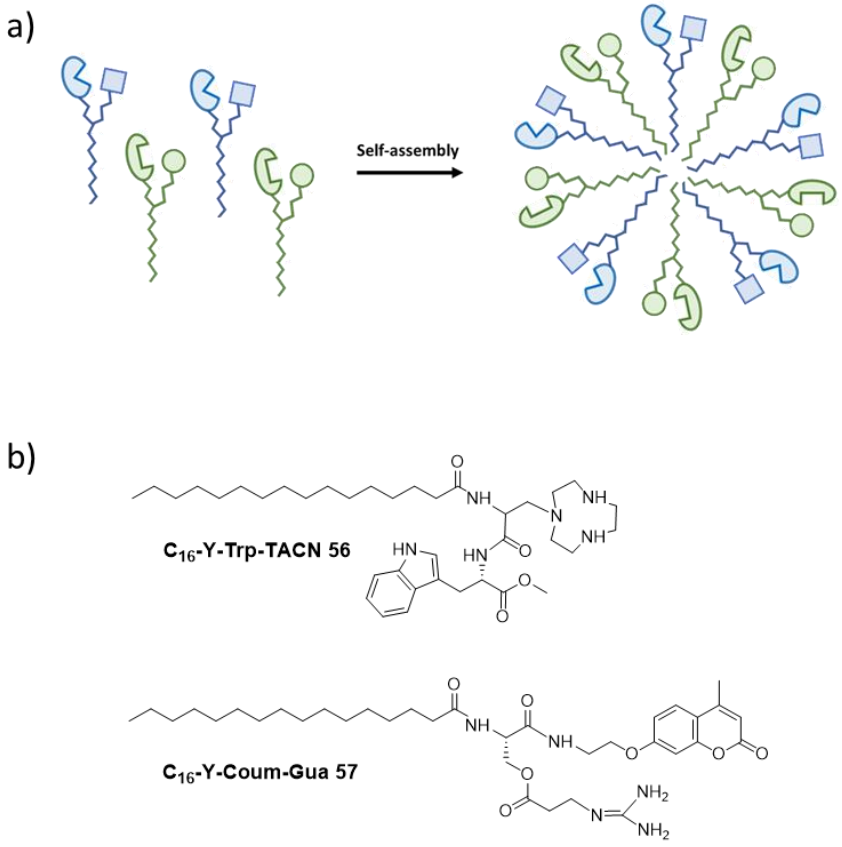

Figure 105. a) Graphic representation of the Y-shaped amphiphiles containing fluorophores (blue squares and green circles) and b) the chemical structures of the C_{16}-Y-Trp-TACN **56** and C_{16}-Y-Coum-Gua **57** amphiphile.

3.3.1.1 Design and synthesis of C_{12}-I-Trp-TACN 53

The synthesis of tryptophan ligand **53** was first attempted through a straightforward route (Scheme 7), which combines TACN **59** and a tryptophan fluorophore **60** to afford building block **61**. This was followed by the attachment of a hydrophobic chain to produce the protected tryptophan ligand **62**. The alkylation of 1-bromododecane on the building block **61**, however, gave a lower yield (7%) than expected, which would waste the important building block **61**. We believe the reason for this is the poor nucleophilicity of the phenol group on the

tryptophan, which is required to act as a nucleophile in the S_N2 reaction. The electron density of the hydroxyl group on tryptophan **61** can be delocalised into the aromatic ring of the tryptophan, which greatly decreases its nucleophilicity. Due to the difficulties observed with this step, we attempted an alternative synthetic route.

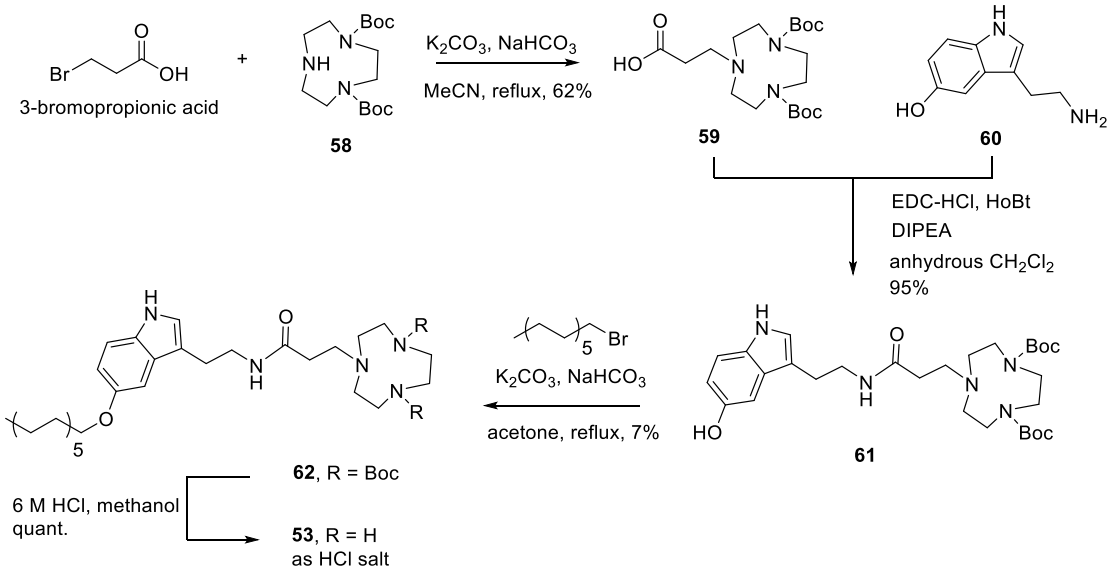

Scheme 7. The synthetic route of a tryptophan ligand **53**

The modified synthetic route is shown below in Scheme 8. A similar example in the literature by Jose and co-workers suggested that the protection of the pendant amine in compound **60** by a Boc protecting group was essential to prevent amine alkylation and to minimize interactions between the pendant amine and the intramolecular hydroxyl group of tryptophan **60**.[146] Therefore, the synthesis of tryptophan began with protection of the amino group in tryptophan **60** with di-*tert*-butyl dicarbonate (Boc anhydride) to afford crude tryptophan **63**, followed by alkylation of a long hydrocarbon chain to produce tryptophan **64** through an S_N2 mechanism in overall 53% yield. Removing the Boc protecting group by treatment with 6 M HCl would release the amino group on tryptophan **65** quantitatively for further modification. In parallel, the alkylation of spacer **66** onto TACN·diBoc **58** via an S_N2 mechanism produced TACN **59** in 62% yield. The combination of building block **59** and tryptophan **65** was achieved by esterification in the presence of coupling reagents *N*,*N*-diisopropylethylamine

hydrochloride (EDC·HCl) and hydroxybenzotriazole (HOBt), which afforded pre-catalyst **62** in over 97% yield. Deprotection of the Boc protecting group in tryptophan **62** with 6 M HCl afforded a tryptophan-TACN ligand **53** as a hydrochloride salt quantitatively.

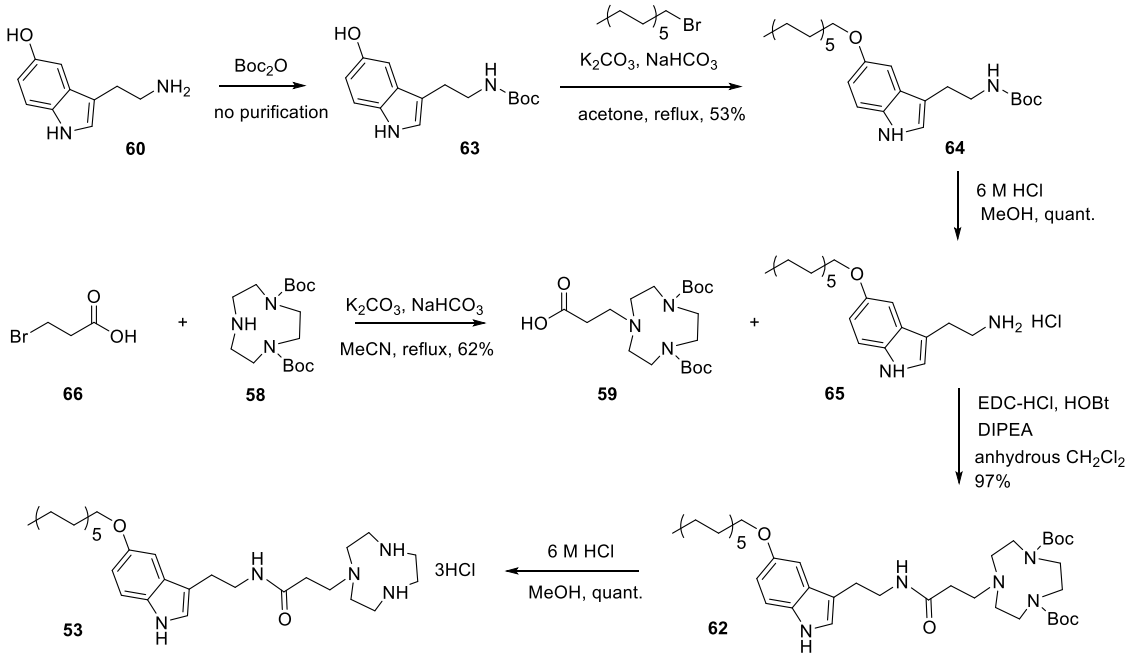

Scheme 8. The final synthetic route of tryptophan ligand **53**

However, the tryptophan-TACN ligand **53** was not stable as the hydrochloride salt, which turned from faint pink to dark blue over time. There was no change in the NMR spectrum except for the loss of aromatic signals as seen in Figure 106. This suggested that the indole was reacting with acid in the reaction mixture. We believe that the instability is due to protonation of the indole amine whose pK_a is around 16, which could lead to the formation of a positively-charged species, stabilised with chloride ions through simple electrostatic attraction, for which there is some literature precedent (Figure 107).[147]

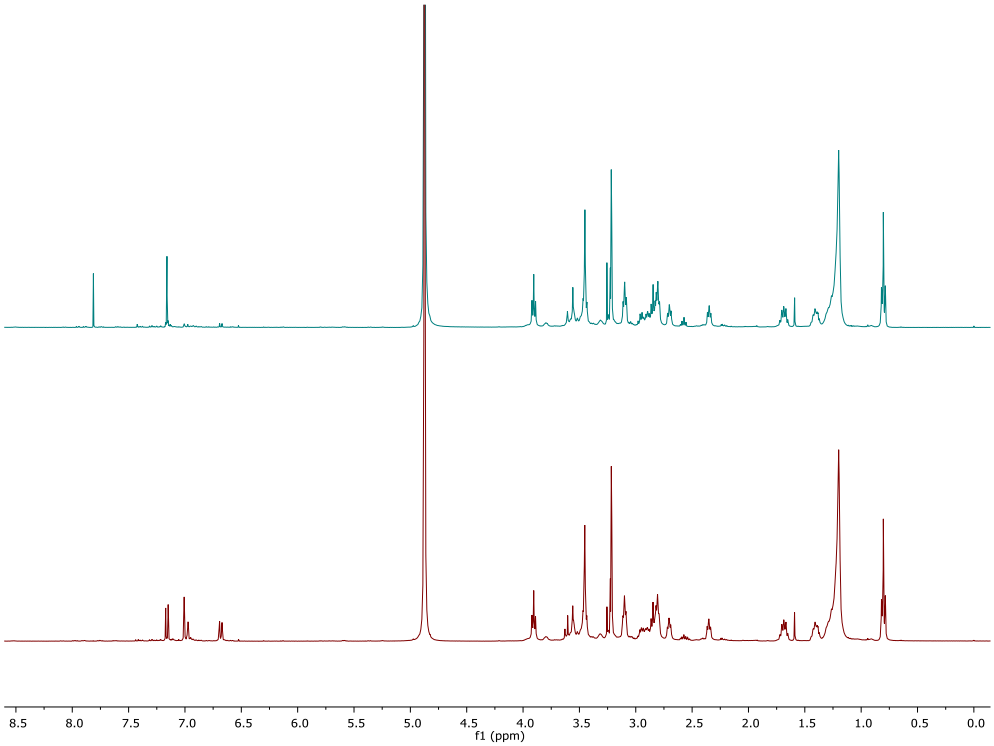

Figure 106. The NMR comparison of tryptophan **53** (bottom) and its chloride complex (top)

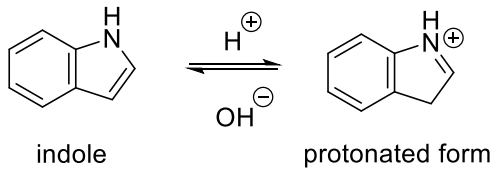

Figure 107. Protonation and deprotonation of an indole

When 1 M NaOH was added to neutralize the above solution, the colour changed from dark blue to paint pink. We believed that deprotonation of the indole, allowed for decomposition of the chloride-indole complex. This colour change was reversible with changes in pH. However, the loss of the aromatic protons in indole was not reversible. Therefore, this last step (Boc deprotection) of the reaction sequence was optimised so that tryptophan **62** was only exposed to strong acid for a very short period of time (20 mins instead of three hours), followed by immediate neutralization with 1 M NaOH to pH ~7. The solvent was removed under reduced pressure by a rotary evaporator with precipitation of NaCl salt. Tryptophan **53** could be washed

off from the NaCl salt with methanol and the product could be confirmed by NMR. To prepare a stock solution of C_{12}-I-tryptophan-TACN **53** of known concentration, the solution needed to be calibrated by the addition of an internal standard (C_{12}-I-Coum-TACN **54**), since small amounts of NaCl remained with tryptophan **53**. Unfortunately, this stock solution still turned dark blue over time, and we think this was due to trace amounts of acid, which was reacting with the tryptophan. As the presence of the blue colour could affect the absorption or fluorescence behaviour for this ligand, we decided to focus on the other fluorophore pairs planned earlier involving the coumarin and naphthalimide linkers.

3.3.1.2 Design and synthesis of C_{12}-I-Coum-TACN 54

The C_{12}-I-Coum-TACN **54** was synthesized over a 5-step sequence (Scheme 9). The synthesis began with the alkylation of TACN·diBoc **58** with the phthalimide protected C_3 spacer **67**. This reaction occurred via a simple S_N2 mechanism and was followed by the deprotection of the phthalimide group with hydrazine to afford amine **69** in an overall 81% yield. Next, the fluorophore coumarin derivative **70** was coupled with amine **69** in the presence of amide coupling reagents EDC·HCl and HOBt to produce amide **71** in 89% yield. Alkylation of the phenol of coumarin **71** with a long hydrophobic chain was achieved by nucleophilic substitution to afford coumarin **72** in 58% yield. This was followed by deprotection of the Boc groups by the treatment of acid, to produce coumarin ligand **54** as a hydrochloric salt, in quantitative yield.

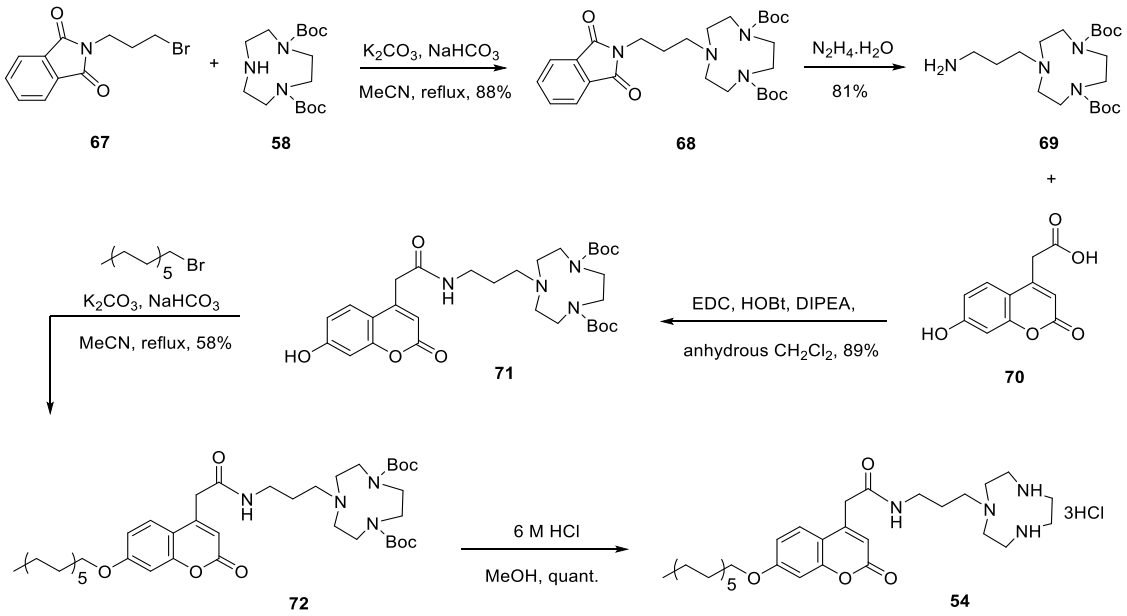

Scheme 9. The synthetic route to access coumarin ligand **54**

3.3.1.2A Synthesis of amine 69

Following alkylation of TACN·diBoc **58** with bromide **67**, the liberation of the amino group in TACN **68** was achieved by treatment with hydrazine. This is a common strategy for the removal of phthalimides and is commonly used in the Gabriel synthesis of primary amines.[148] The mechanism of cleavage begins with nucleophilic attack of the hydrazine onto the carbonyl in phthalimide **68**, resulting in the formation of a tetrahedral intermediate **72**. Reformation of the carbonyl then results opening of the phthalimide ring. Following proton transfer in intermediate **73**, intramolecular nucleophilic attack by the free amine group in hydrazine **74** results in liberation of amine **69** and the formation of phthalhydrazide **76** as a side product.[149]

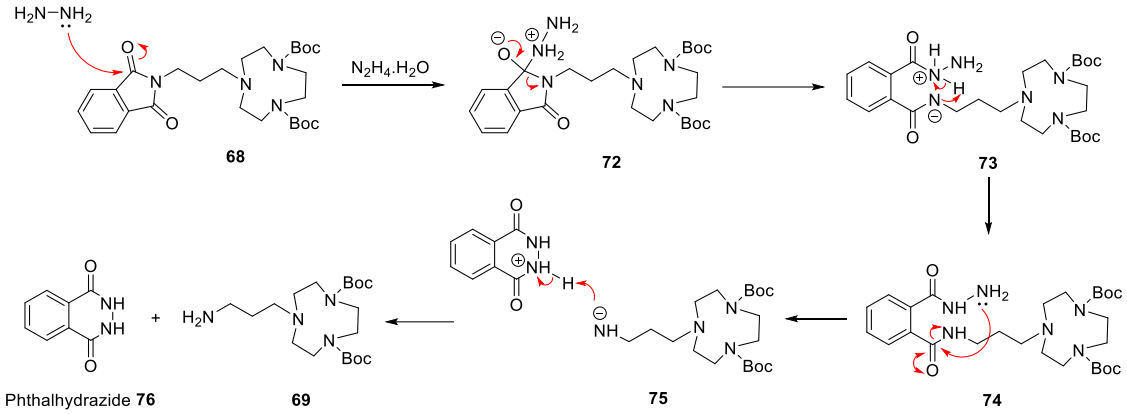

Scheme 10. Proposed mechanism for the synthesis of amine **69**

3.3.1.2B Synthesis of amide 71

The formation of amide **71** was achieved in the presence of the commonly used amide coupling agents, EDC·HCl and HOBt. EDC is an example of a carbodiimide and is now more commonly used than the related and older dicyclohexylcarbodiimide (DCC) coupling agent. The mechanism of this reaction begins with deprotonation of the carboxylic acid in **70** by NEt_3. The resulting carboxylate formed is nucleophilic and able to attack the carbodiimide functional group in EDC·HCl to form intermediate **77**. The addition of EDC·HCl was important because the strong electron withdrawing groups introduced by EDC helps to activate the hydroxyl group on the carboxylic acid and allows it to become a leaving group. This allows intermediate **77** to be attacked by HOBt, which acts as a nucleophile, activating the carbonyl group for attack by primary amine **69**. This results in formation of the ester product **71** in up to 89% yield, and a urea **78** as a side product. In this case, because EDC is used, the urea side product **78** is water soluble and can be removed easily by extraction. This is in contrast with the use of DCC, which results in a urea side product that is commonly difficult to remove from the desired product.

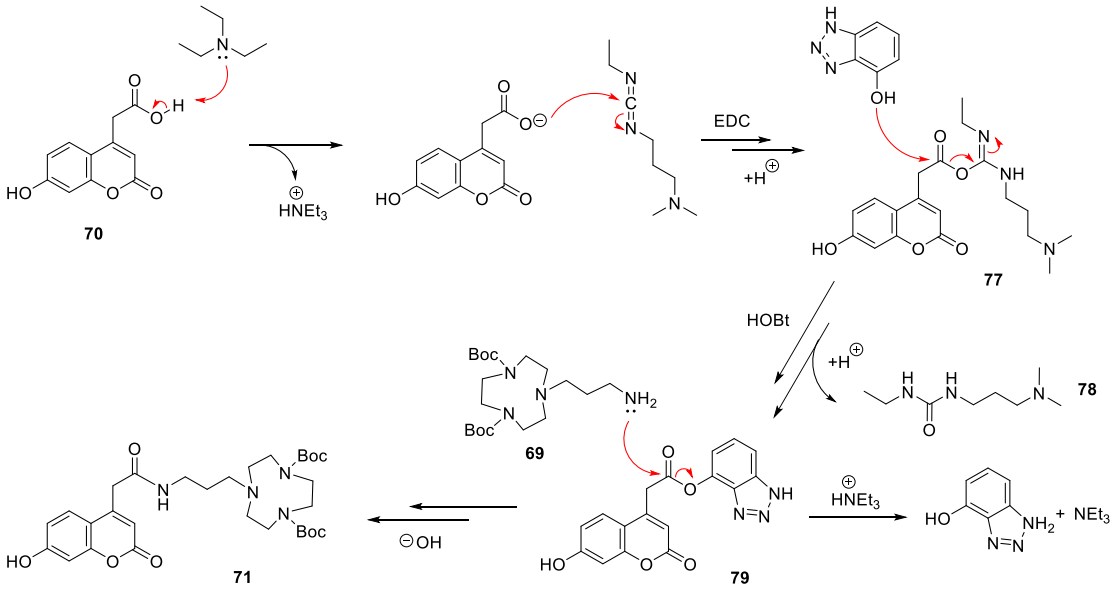

Scheme 11. Proposed mechanism for the synthesis of coumarin **71**

3.3.1.2C Synthesis of coumarin 72 and C_{12}-I-Coum-TACN 54

The alkylation of coumarin **71** with a hydrocarbon chain occurred in the presence of K_2CO_3. This weak base is strong enough to deprotonate the phenol due to the relatively high acidity of phenols (pKa ~10). The phenoxide is a good nucleophile and reacts with 1-bromohexadecane under an S_N2 mechanism, to afford coumarin **72**. After deprotection of the Boc protecting groups in coumarin **72** using standard acidic conditions, the desired C_{12}-I-Coum-TACN ligand **54** was formed.

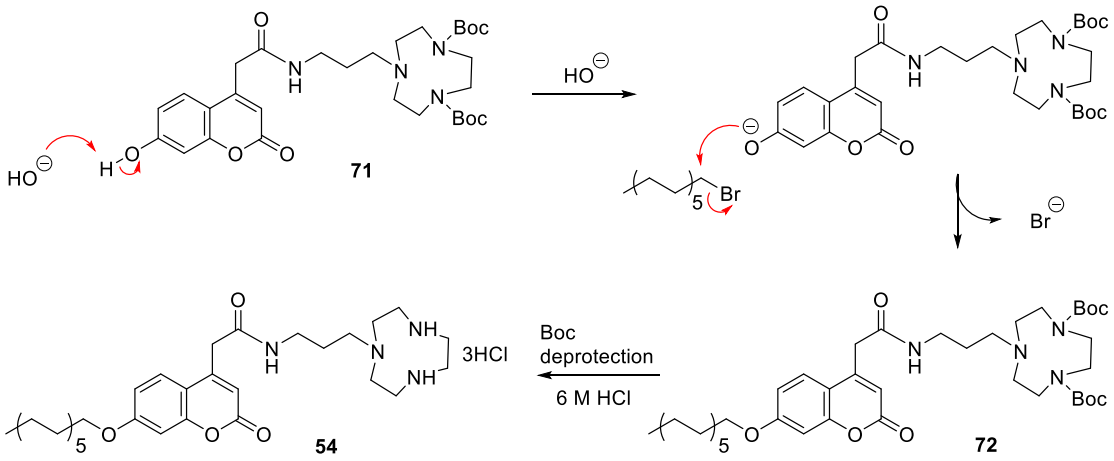

Scheme 12. Mechanism for synthesis of coumarin **72** and C_{12}-I-Coum-TACN **54**

3.3.1.3 Design and synthesis of C_{12}-I-Naph-Gua 55

The synthesis of C_{12}-I-Naph-Gua **55** began with 4-bromo-1,8-naphthalic anhydride **80**, which was converted to its 4-hydroxy analogue **81** over 4 steps in an overall yield of 66% (Scheme 14). To form C_{12}-I-Naph-Gua ligand **55**, we needed a linker that possessed a primary amine on either terminus, one to join up with the 4-hydroxy-1,8-naphthalic anhydride **81**, and the other to introduce the guanidinium functional group. The alkylation of spacer **82** onto naphthalimide **81** afforded the desired product **83** in 46% yield, and this was followed by Boc deprotection to free the amino group in naphthalimide **84**. The guanidinium functional group was introduced by the addition of 1,3-di-Boc-2-(trifluoromethylsulfonyl)guanidine **26** to form phenol **85**. Alkylation of the phenol with a C_{16} chain was achieved in 27% yield, and finally Boc deprotection allowed access to the desired guanidinium **55** quantitatively as the hydrochloride salt.

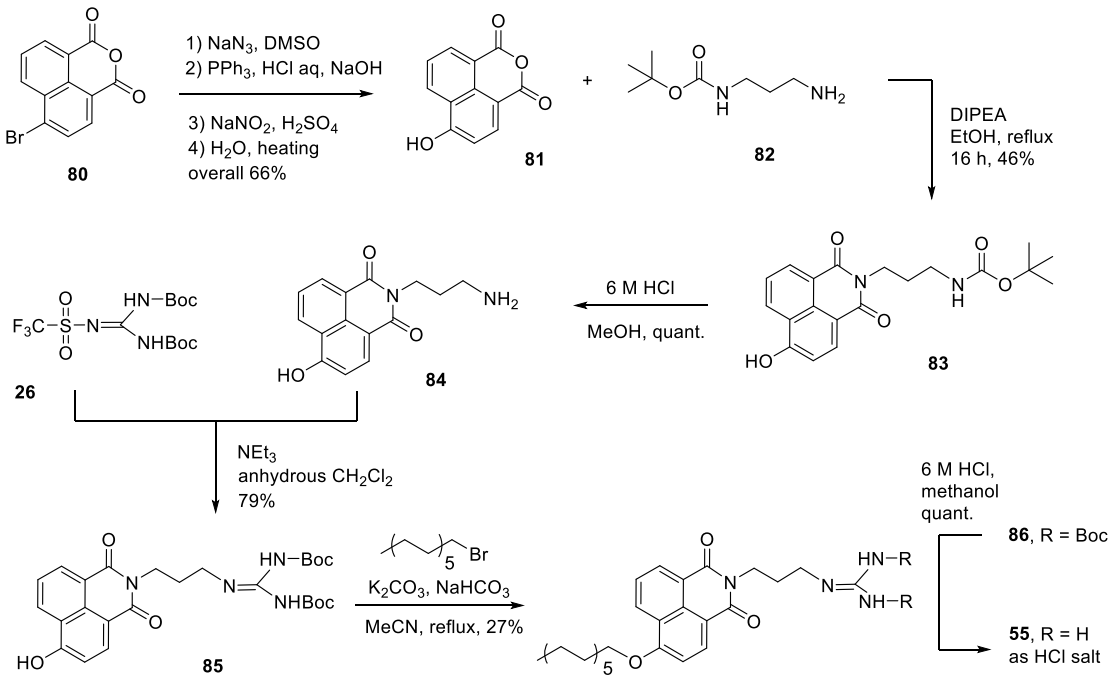

Scheme 13. The synthetic route to C_{12}-I-Naph-Gua ligand **55**

3.3.1.3A Synthesis of 6-hydroxy-1H,3H-benzo[de]isochromene-1,3-dione 81

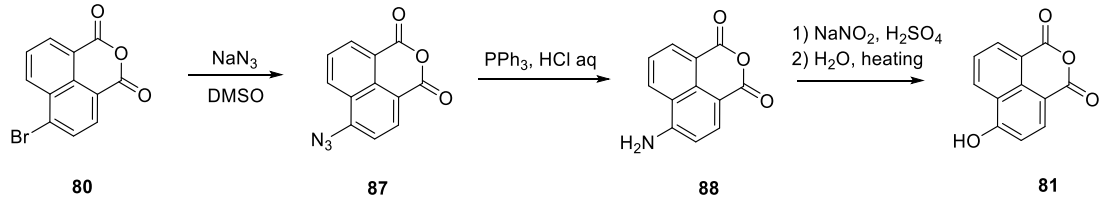

Scheme 14. The formation of hydroxyl-substituted naphthalic anhydride **81** from bromo-substituted naphthalic anhydride **80**

The conversion of 4-bromo-1,8-naphthalic anhydride **80** to its 4-hydroxyl analogue **81** can be broken down to four steps as shown in Scheme 14. The azide functional group was first introduced via an S_NAr reaction between azide and 4-bromo-1,8-naphthalic anhydride **80**. The azide ion acts as a nucleophile to attack carbon 4 on the naphthalimide ring, which is possible because of the presence of an electron withdrawing group in the para position. This allows the elections to be pushed into the carbonyl of the anhydride group. The electrons can then be

pushed back, to reform the aromatic ring and push out the bromine as a leaving group. This conversion usually takes place in polar aprotic solvents, for example, DMSO or acetonitrile.

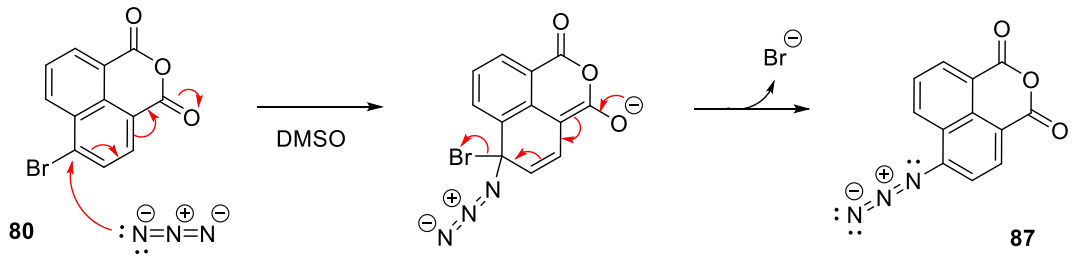

Scheme 15. Mechanism for the conversion of bromide **80** to azide **87**

The Staudinger reaction used to reduce the azide group in naphthalimide **87** to the amino-substituted naphthalimide **88** as shown in Scheme 16. The Staudinger reaction is famous for transforming azides into primary amines under mild conditions, which is often favoured over reductions under harsh reductions, for example using $LiAlH_4$. A lone pair of electrons in triphenylphosphine attacks the nitrogen of the azide leading to the rearrangement of electrons in the azide functional group. Then the electrons on the terminal nitrogen of the azide attacks the positively-charged phosphine to cyclize and form a four-member ring in intermediate **89**, followed by facile decomposition due to the high bond strain to afford phosphine imine **90** and the release of nitrogen gas. The next stage of the Staudinger reaction involves hydrolysis of the intermediate phosphine imine **90** by a water molecule. The desired amine **88** is formed in addition to the formation of phosphine oxide as a side product.

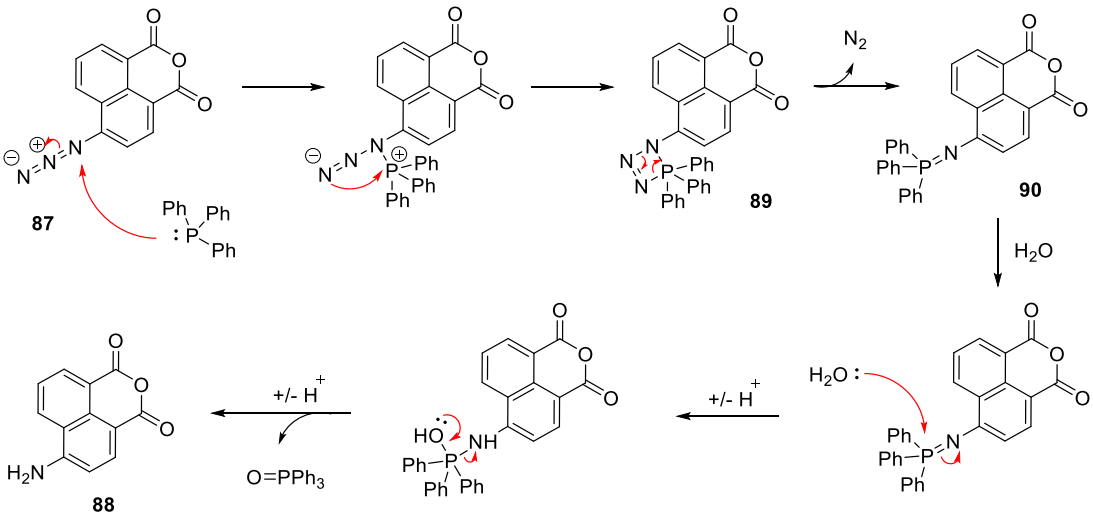

Scheme 16. The reduction of azide **87** by a Staudinger reaction to form amine **88**

The final steps are the substitution of the amino group of naphthalimide **88** to form the corresponding hydroxyl-substituted **81**. The mechanism proceeds with the reaction of the amino group in **88** with sodium azide to form a diazonium intermediate, which can be easily substituted with other nucleophiles, for example, hydroxyl groups to afford the hydroxyl-substituted **81**. The reaction started with the decomposition of sodium nitrite, which is a stable source of nitrous acid, which then forms the strongly electrophilic nitrosonium ion in acidic conditions. Once the nitrosonium ions were formed, they are able to react with amine **88**, leading to the formation of more nitrosonium ions.

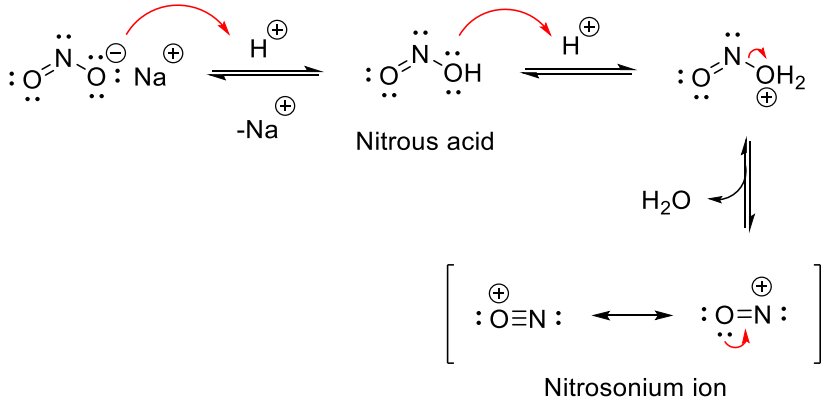

Scheme 17. The mechanism for the formation of nitrosonium ions

Next, the diazotization of amine **88** occurs with nucleophilic attack of the amino group in **88** onto a nitrosonium ion. After several steps involving proton exchange, followed by the loss of water, aryl diazonium **91** is formed as a key intermediate.

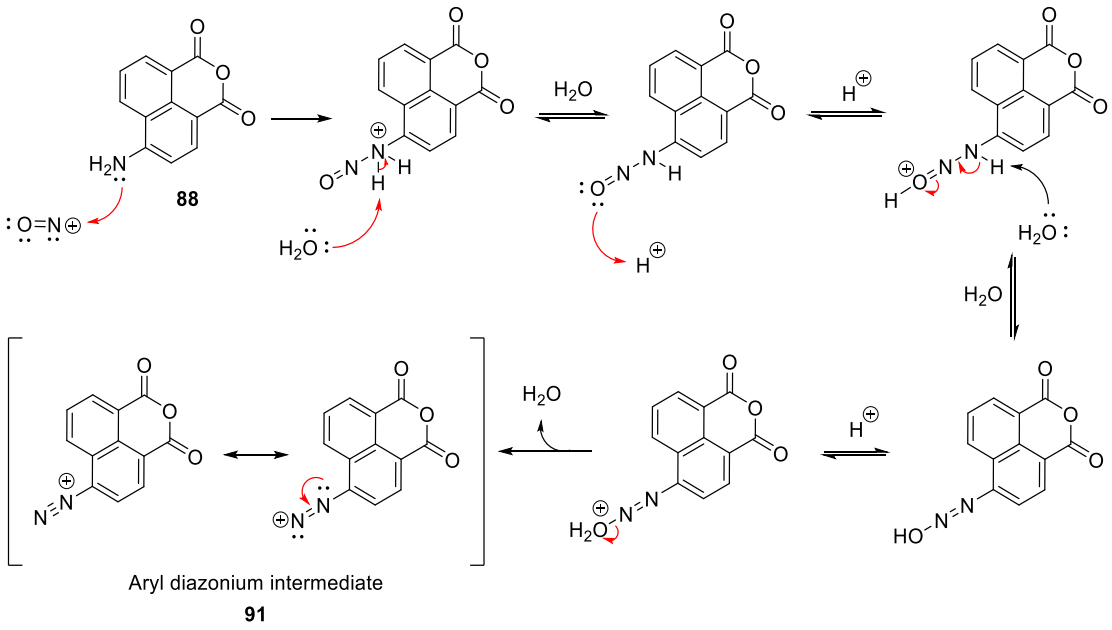

Scheme 18. Proposed mechanism for the synthesis of aryl diazonium intermediate **91**

It is important to note that the formation of the aryl diazonium intermediate is an extremely useful strategy for the synthesis of aromatic compounds which are not easy to make following normal substitution rules (Figure 108). The aryl diazonium functional group can easily leave to produce a variety of substitution compounds through different mechanisms, mainly aromatic nucleophilic substitution mechanisms (Ar-S_N) that involve either an aryl cation intermediate or an aryl radical intermediate.

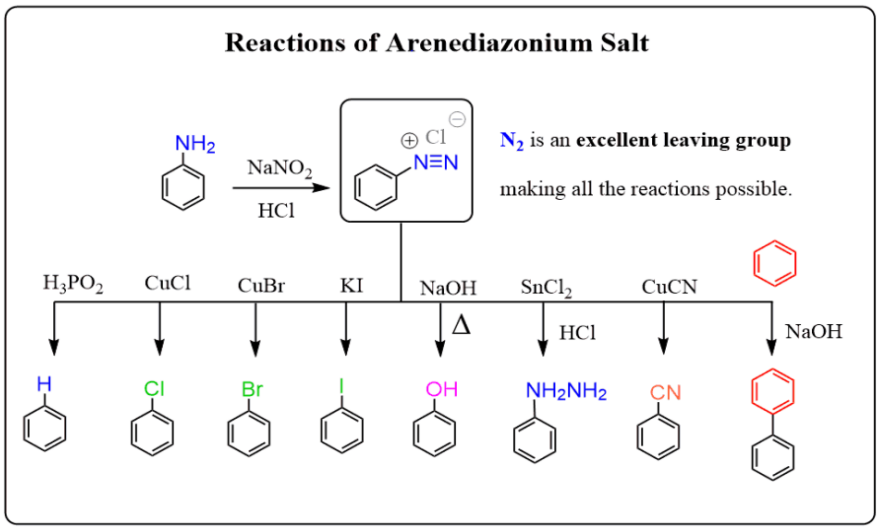

Figure 108. A variety of functional compounds can be formed from aryl diazonium intermediates

In our case, it is predicted that under heating, the diazo group leaves the naphthalic anhydride core and nitrogen is lost to produce the naphthalic cation **92**. The naphthalic cation **92** is reasonably stable due to a number of possible resonance states, where the positive charge can be repositioned around the naphthalic ring. The naphthalic cation is readily trapped by a water molecule, which forms naphthalic anhydride **81** following deprotonation.

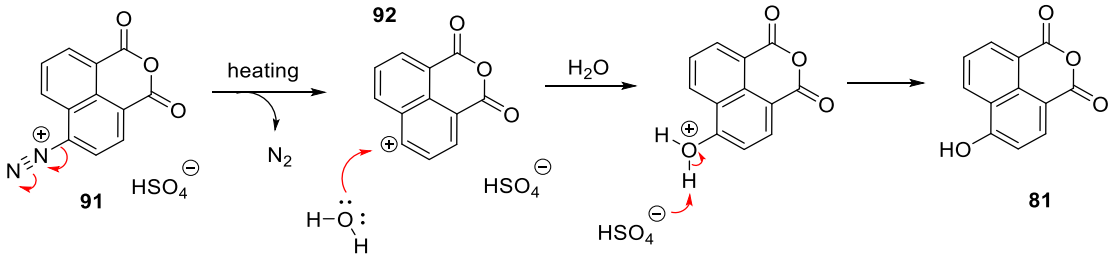

Scheme 19. Proposed mechanism for the synthesis of hydroxyl substituted **81**

3.3.1.3B Synthesis of amine 84

The imidation of naphthalic anhydride **81** to form naphthalimide **83** begins with attack of primary amine **82** onto the anhydride functional group. This results in opening of the

anhydride ring and the formation of an amide bond. The nitrogen of the amine next attacks the newly formed carboxylic acid, resulting in the formation of the ring. Finally, loss of water allows formation of the naphthalimide ring.[150]

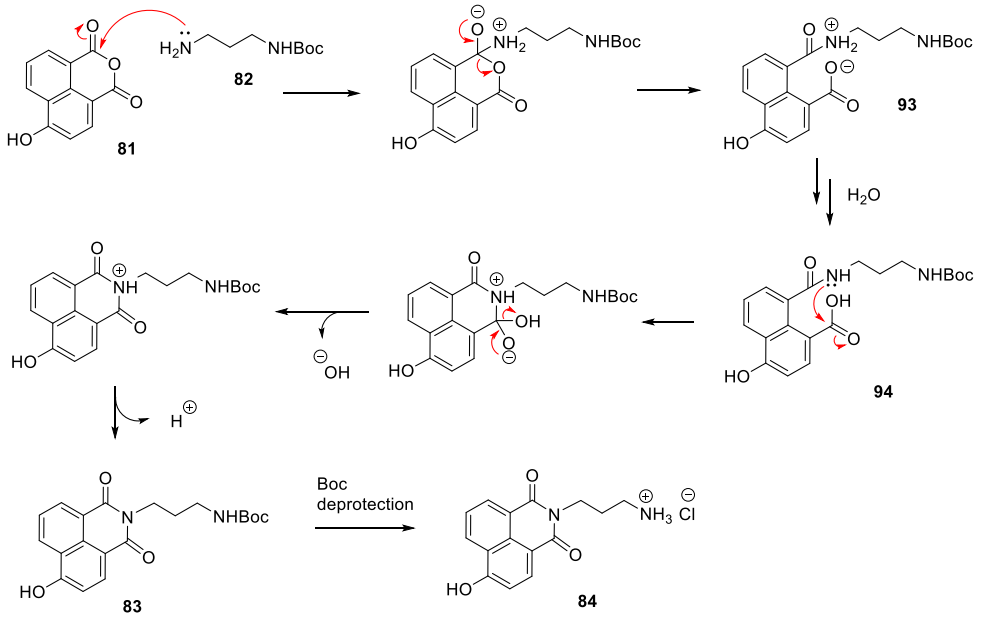

Scheme 20. Proposed mechanism for the synthesis of naphthalimide **84**

Following treatment of naphthalimide **83** with acid, the Boc protecting group was removed to afford naphthalimide **84** as the HCl salt.

3.3.1.3C Synthesis of naphthalimide 85

The coupling of naphthalimide **84** and 1,3-di-Boc-2-(trifluoromethylsulfonyl)guanidine **26** is shown in Scheme 21, where nucleophilic attack of the amino group in naphthalimide **84** occurs at the sp^2 carbon of guanidine **26**. The guanidium functional group is very stable group due to its chemical structure, for which several resonance forms can be drawn (Scheme 22). The presence of the trifluorosulfonyl group is therefore very important, as it is a strong electron withdrawing group and polarises the bond to make the sp^2 carbon electrophilic. Its presence also allows trifluoromethanesulfonamide to leave as a leaving group and increases the efficiency of this step.

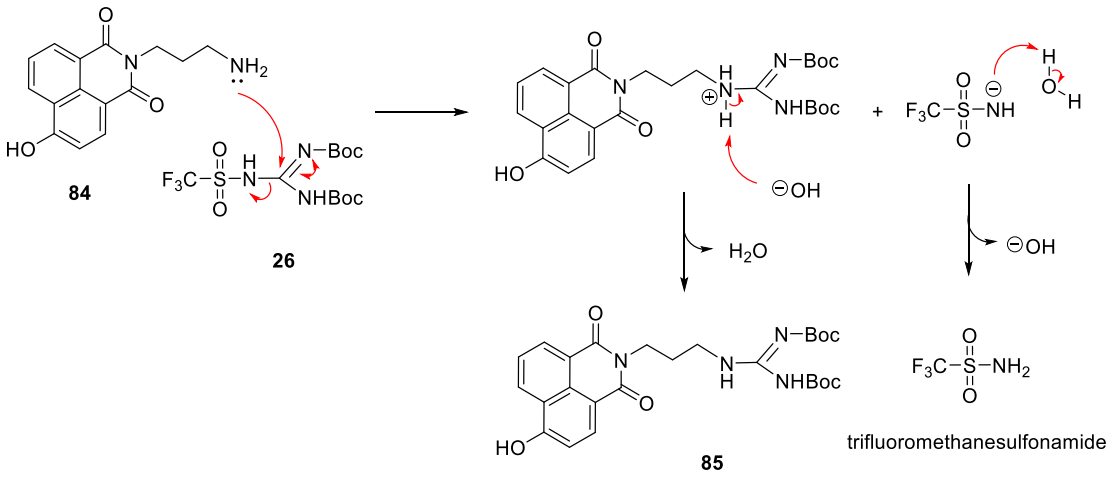

Scheme 21. Proposed mechanism for the synthesis of naphthalimide **85**

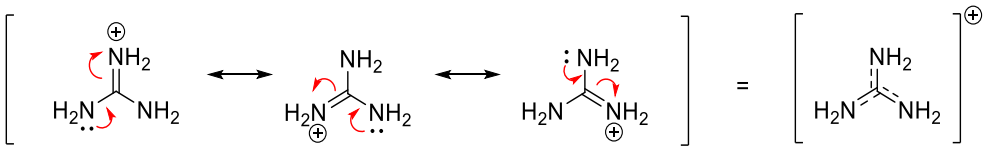

Scheme 22. Three resonance contributors for the guanidinium ion, and its resonance hybrid structure.

3.3.1.3D Synthesis of C_{12}-I-Naph-Gua 55

The alkylation of naphthalimide **85** with a long hydrocarbon chain occurs in the presence of K_2CO_3 as described earlier. Deprotection of the Boc protecting groups on the guanidinium was performed under acidic conditions as described previously.

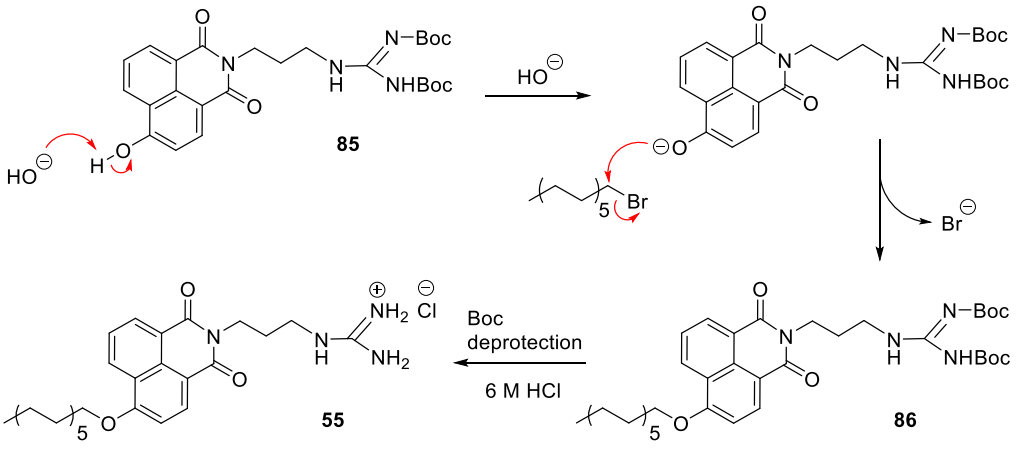

Scheme 23. Mechanism for the synthesis of C_{12}-I-Naph-Gua **55**

3.4 Initial FRET investigations

3.4.1 UV-Vis studies

After successfully synthesizing the two fluorescent amphiphiles, C_{12}-I-Naph-Gua **55** and C_{12}-I-Coum-TACN **54**, their absorption spectra were measured to determine their maximum absorbance. Considering the experimental conditions of the previous catalysis work, the spectra were measured in both CHES buffered aqueous solution (pH 9.1) and in 20% DMSO in water with 1 mM DIPEA. Figure 109a shows the absorption spectra of C_{12}-I-Naph-Gua **55** and C_{12}-I-Coum-TACN **54** in CHES buffered solution (pH 9.1). The absorption maximum of C_{12}-I-Coum-TACN **54** and C_{12}-I-Naph-Gua **55** were at 343 nm and 375 nm, respectively. Changing the solvent system to 20% DMSO in water did not affect the absorption maximum or the absorption intensity (Figure 109b). However, in both the solvent systems, the absorption spectra of both amphiphiles have a certain degree of overlap, which is not desirable for FRET. This means that attempts to irradiate C_{12}-I-Coum-TACN **54** could also lead to the irradiation of the C_{12}-I-Naph-Gua **55** and could lead to fluorescence from both molecules which would complicate data interpretation. In any case, we proceeded to investigate the fluorescence properties of these two molecules.

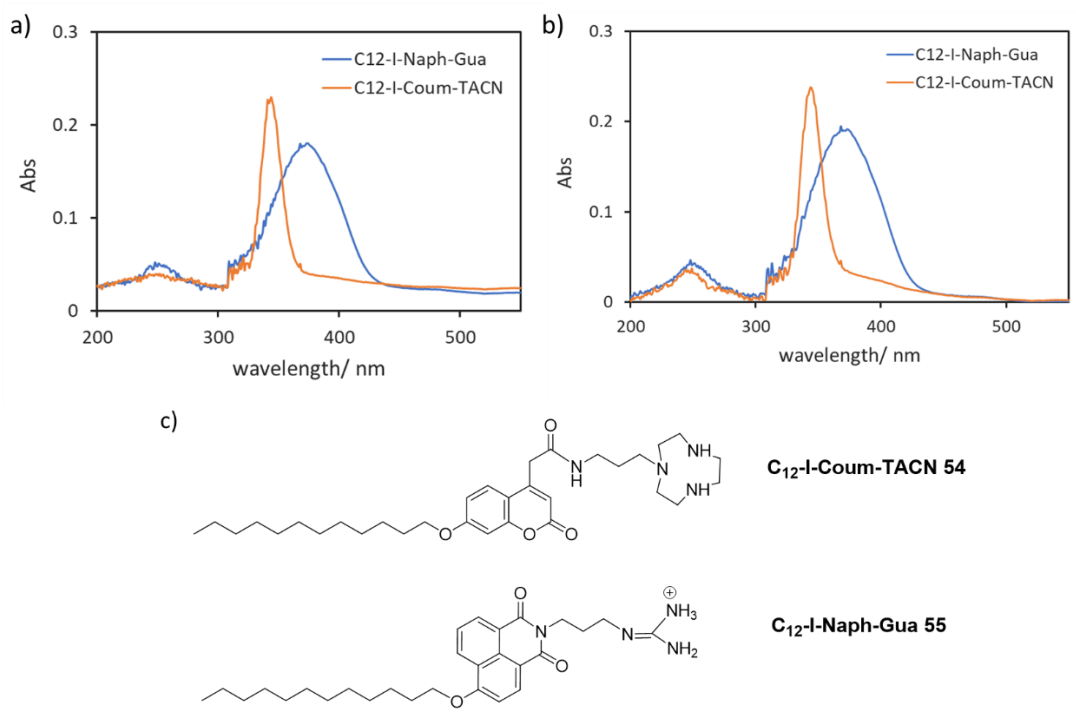

Figure 109. The absorption spectra of C_{12}-I-Coum-TACN **54** (50 μM) and C_{12}-I-Naph-Gua **55** (50 μM) in a) CHES buffered solution (5 mM, pH = 9.1); and b) 20% DMSO in water and 1 mM DIPEA. C) The chemical structures of C_{12}-I-Coum-TACN **54** and C_{12}-I-Naph-Gua **55**.

3.4.2 Fluorescence studies

Following the initial UV absorption studies, the fluorescence emission and excitation spectra were measured for C_{12}-I-Coum-TACN **54** (λ_{ex} = 325 nm, λ_{em} = 400 nm) and C_{12}-I-Naph-Gua **55** (λ_{ex} = 375 nm, λ_{em} = 470 nm) in a CHES buffered solution (Figure 110). Both C_{12}-I-Coum-TACN **54** and C_{12}-I-Naph-Gua **55** have similar fluorescence intensities and a good degree of spectral overlap was seen between the emission of C_{12}-I-Coum-TACN **54** and the excitation of C_{12}-I-Naph-Gua **55**, suggesting there was potential for successful FRET.

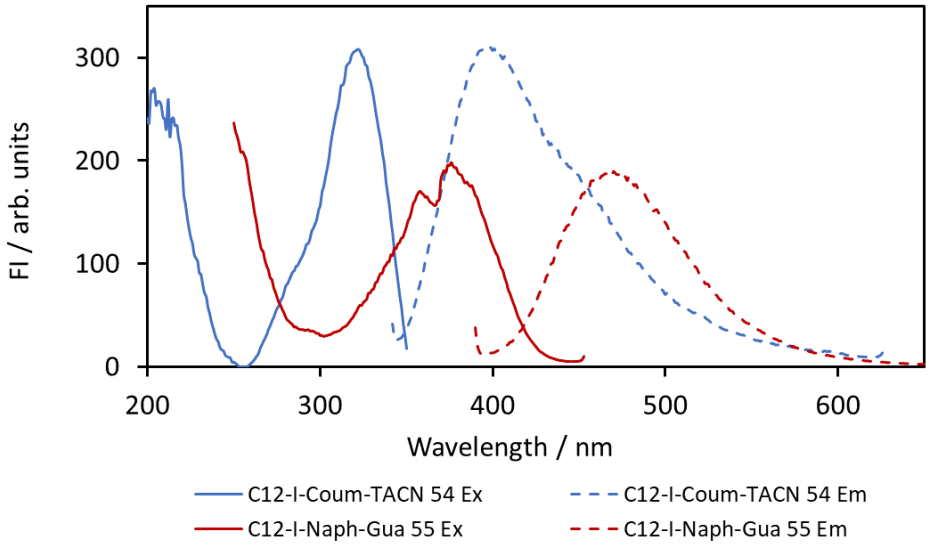

Figure 110. Fluorescence spectra for C_{12}-I-Coum-TACN **54** (50 μM) and C_{12}-I-Naph-Gua **55** (50 μM) in CHES buffered solution (5 mM, pH at 9.1), slit 10/10.

The maximum excitation and emission of C_{12}-I-Coum-TACN **54** (λ_{ex} = 325/260 nm, λ_{em} = 400 nm) and C_{12}-I-Naph-Gua **55** (λ_{ex} = 375 nm, λ_{em} = 470 nm) was also measured in 20% DMSO in water (Figure 111), as these were the conditions that we had previously used for our catalysis studies. Although their excitation and emission wavelength did not shift, the fluorescence intensity (FI) of C_{12}-I-Naph-Gua **55** was much higher in the 20% DMSO than in the aqueous buffer, whereas the FI of C_{12}-I-Coum-TACN **54** remained at the same level. The FI of C_{12}-I-Coum-TACN **54** (FRET donor) was lower than C_{12}-I-Naph-Gua **55** (FRET acceptor), which suggests that there will be a less efficient FRET process due to the weak quantum yield generated by C_{12}-I-Coum-TACN **54**.

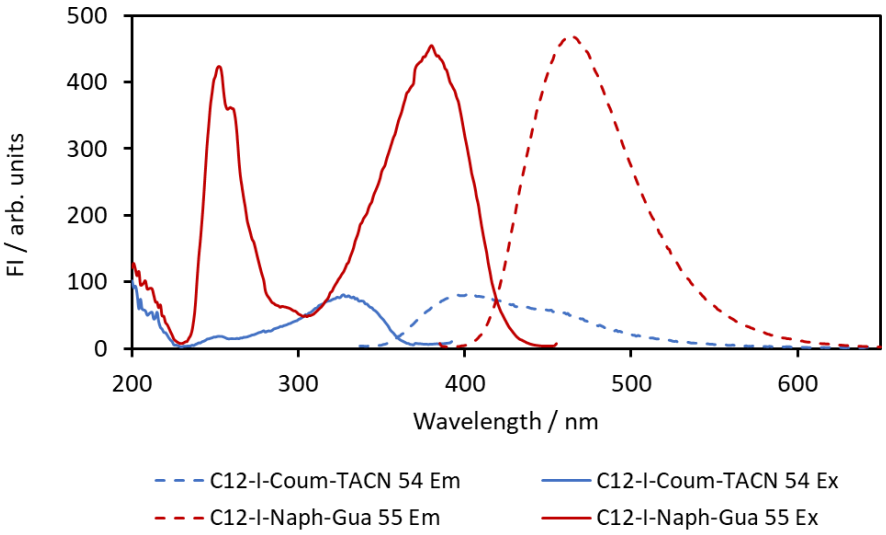

Figure 111. Fluorescence spectrum of 50 μM of C_{12}-I-Coum-TACN **54** (blue) and C_{12}-I-Naph-Gua **55** (red) in 20% DMSO in water and in the presence of 1 mM of DIPEA, slit 5/5.

The efficiency of the FRET process was first examined using C_{12}-I-Coum-TACN **54** and C_{12}-I-Naph-Gua **55** in the absence of the phosphate substrate. This was to exclude any unknown interactions between the amphiphiles and phosphate since FRET processes are known to be sensitive to the surrounding environment. Furthermore, the metal ions usually associated with TACN were also not added to exclude effects due to chelation. Figure 112 shows the emission spectra obtained when C_{12}-I-Coum-TACN **54** (50 μM) and C_{12}-I-Naph-Gua **55** (50 μM) were each excited individually at 325 nm (Figure 112, orange and grey curves), which is the excitation maximum for C_{12}-I-Coum-TACN **54**. The emission maxima observed for C_{12}-I-Coum-TACN **54** and C_{12}-I-Naph-Gua **55** were at 400 nm (FI = 140 a.u.) and 480 nm (FI = 147 a.u.), respectively. The is not desirable as we were hoping that C_{12}-I-Naph-Gua **55** would not produce significant emission at the excitation wavelength of C_{12}-I-Coum-TACN **54**.

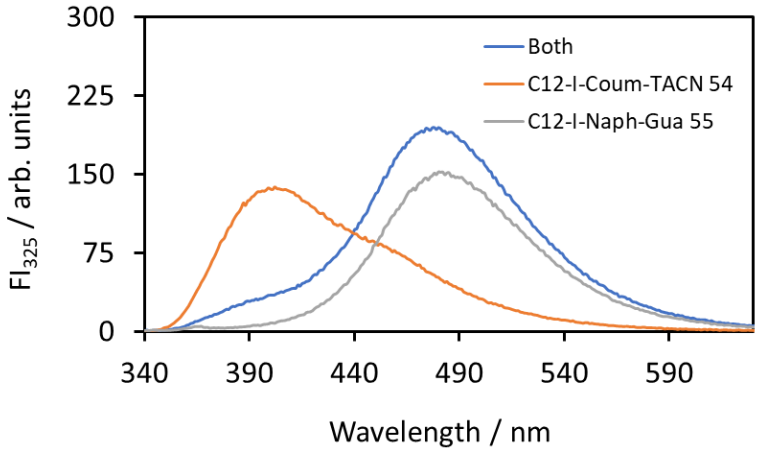

Figure 112. Fluorescence spectra of C_{12}-I-Coum-TACN **54** (50 μM), C_{12}-I-Naph-Gua **55** (50 μM) and 1:1 ratio of C_{12}-I-Coum-TACN **54** and C_{12}-I-Naph-Gua **55** (50 μM each) excited at 325 nm in CHES buffered solution (5 mM, pH = 9.1), slit 5/5.

In any case, we continued to explore any indication of FRET by preparing a solution containing a 1:1 ratio of C_{12}-I-Coum-TACN **54** and C_{12}-I-Naph-Gua **55** ligands (50 μM each) in aqueous buffer. When this mixture was excited at 325 nm, two fluorescence emissions were observed at 400 and 480 nm with FI of 33 a.u. and 193 a.u., respectively. These results show that the emission of C_{12}-I-Coum-TACN **54** (at 400 nm) was absorbed by the C_{12}-I-Naph-Gua **55**, resulting in significantly lower emission (at 400 nm), with a reduction of around 75% in the presence of C_{12}-I-Naph-Gua **55.** The emission of C_{12}-I-Naph-Gua **55** (at 480 nm) in this mixed system appeared to increase, but upon closer examination, the maximum fluorescence intensity was roughly equal to the sum of the emissions (at 480 nm) of C_{12}-I-Coum-TACN **54** and C_{12}-I-Naph-Gua **55** (each 50 μM) measured separately. This suggested that there was efficient absorption of the coumarin emission by the naphthalimide functional group in C_{12}-I-Naph-Gua **55**, but unfortunately no enhancement of fluorescence emission. We also attempted to excite the mixed system at 305 nm in order to minimise the direct emission of C_{12}-I-Naph-Gua **55**, but we still did not find strong evidence for successful FRET.

In order to increase the possibility of successful FRET, the ratio of C_{12}-I-Coum-TACN **54** and C_{12}-I-Naph-Gua **55** was increased to 2:1 in an attempt to enhance the energy transfer from C_{12}-I-

Coum-TACN **54** to C_{12}-I-Naph-Gua **55**. The emission spectra of C_{12}-I-Coum-TACN **54** (66 μM) and C_{12}-I-Naph-Gua **55** (33 μM) was first determined with excitation at 325 nm. This gave emission of C_{12}-I-Coum-TACN **54** at 400 nm (FI = 137 a.u.) and emission of C_{12}-I-Naph-Gua **55** at 480 nm (FI = 100 a.u.) (Figure 113, orange and grey curves). When a mixture of 2:1 C_{12}-I-Coum-TACN **54** to C_{12}-I-Naph-Gua **55** was excited at 327 nm, there was a decrease in coumarin emission at 400 nm (FI = 51 a.u.) and an increase of naphthalimide emission at 470 nm (FI = 215 a.u.). However, the increase of naphthalimide emission was roughly equal to the sum of the emission of C_{12}-I-Coum-TACN **54** and C_{12}-I-Naph-Gua **55** separately at 470 nm in the control fluorescence spectrum. Unfortunately, these results also suggested a non-successful FRET in the 2:1 C_{12}-I-Coum-TACN **54** and C_{12}-I-Naph-Gua **55** system.

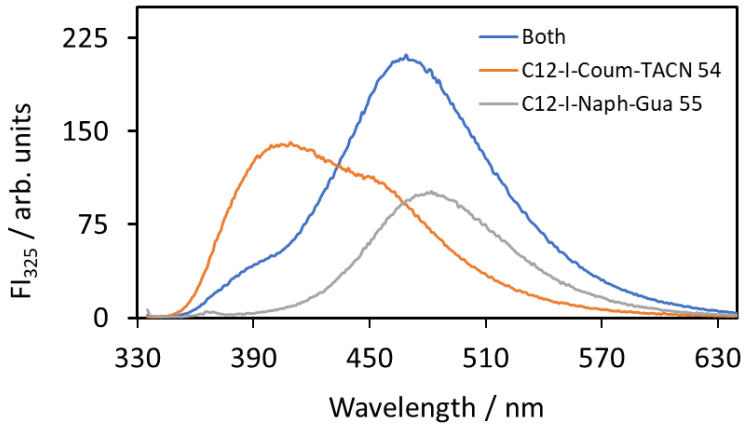

Figure 113. Fluorescence spectrum of C_{12}-I-Coum-TACN **54** (67 μM), C_{12}-I-Naph-Gua **55** (33 μM) and 2:1 ratio of C_{12}-I-Coum-TACN **54** and C_{12}-I-Naph-Gua **55** (total 100 μM) in CHES buffered solution (5 mM, pH = 9.1), slit 5/5.

A report by Zhou and co-workers showed a ratiometric chemosensor **95** consisting of a coumarin moiety (FRET donor) and an amino-naphthalimide moiety (FRET acceptor) for sensing changes in pH.[145, 151] Under basic conditions, the electron pair in the amino group of the piperazine moiety quenched the fluorescence of amino-naphthalimide by photo-induced electron transfer (PET). This prevented the FRET processes from occurring, and only coumarin

fluorescence was observed. However, in acidic conditions, the piperazine moiety was protonated, which prevented the PET process, resulting in the restoration of naphthalimide fluorescence via FRET mechanisms. Therefore, the ratiometric fluorescence of coumarin and naphthalimide could be used for sensing different pH's. (The FRET mechanism was explained in Chapter 3.2, and the PET mechanism will be explained in Chapter 3.5.6.)

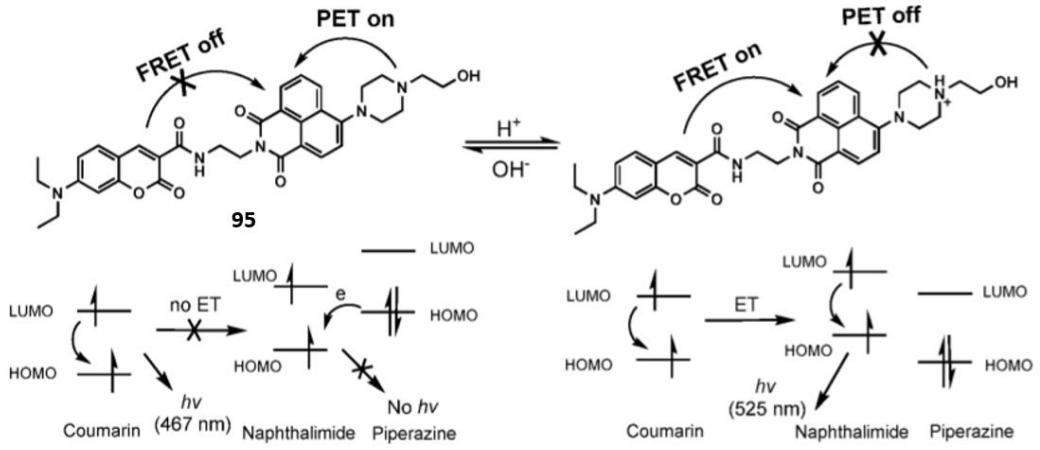

Figure 114. A PET-FRET based chemosensor **95** (top) and a schematic illustration of frontier orbital energy changes (bottom). Reprinted with permission from ref. 151. Copyright (2016) Royal Society of Chemistry.

Examining our mixed C_{12}-I-Coum-TACN **54**/C_{12}-I-Naph-Gua **55** system in light of the above report, it is possible that a PET process was occurring which was preventing FRET. At pH 9.1, the guanidinium functional group would be partially in its neutral non-protonated form, and would allow PET between the naphthalimide and guanidine groups, preventing FRET enhancement. More could have been done to investigate whether this was the case, for example, performing these experiments at a lower pH, to see if protonation of the guanidium to form guanidinium could result in removal of the PET effect. However, because we knew that a higher pH, and the availability of the guanidine groups in the non-ionic form was important for catalysis, we proceeded to investigate conditions that were closer to what we had

previously used for **HPNPP** catalysis.

The lack of significant FRET observed in these initial experiments could be due to the presence of PET effects like we described above, or due to the lack of self-assembly between the C_{12}-I-Coum-TACN **54** and C_{12}-I-Naph-Gua **55** amphiphiles, meaning they are not close enough in proximity for FRET to occur. This latter explanation is plausible because we performed the above experiments in the absence of the metal ions and the **HPNPP** substrate. We have previously shown that the presence of the **HPNPP** substrate induces self-assembly of the amphiphiles to form vesicular structures.[89] The metal ion is also essential for the strong binding between the amphiphile and the **HPNPP**, and the formation of vesicles. We therefore performed FRET experiments next in the presence of all reaction components, namely in the presence of the phosphates and Zn^{2+} ions.

For the experiments, we could not use **HPNPP** or **model HPNPP** as the phosphate substrate as both compounds absorb strongly at 405 nm due to the presence of the nitrophenyl moiety. Adding these substrates would have a marked effect on the excitation and emission of C_{12}-I-Coum-TACN **54** and C_{12}-I-Naph-Gua **55**. Therefore, we added dimethylphosphate (DMP), which we have previously shown can also induce the formation of vesicles. DMP would not affect the fluorescence properties of coumarin and naphthalimide as it lacks a nitrophenyl moiety. DMP (500 μM) was first added to a solution containing a 2:1 ratio of C_{12}-I-Coum-TACN·Zn^{2+} (**54**·Zn^{2+}) and C_{12}-I-Naph-Gua **55**. A large increase in the emission of C_{12}-I-Coum-TACN·Zn^{2+} (**54**·Zn^{2+}) was observed, whereas the emission of C_{12}-I-Naph-Gua **55** remained at the same level, suggesting the complete absence of FRET. To reduce the FI of C_{12}-I-Coum-TACN·Zn^{2+} (**54**·Zn^{2+}), the concentration of **54**·Zn^{2+} was reduced to 33 μM, which gave a final ratio of 1:2 **54**·Zn^{2+} to C_{12}-I-Naph-Gua **55**, which is the same ratio of amphiphiles used for the catalysis experiments in Chapter 2, Figure 48 was reprinted for clarity). Lastly, the concentration of DMP was reduced by 50%. From Figure 115, we see that under irradiation at 325 nm, relatively high emission from **54**·Zn^{2+} is seen compared to the emission from C_{12}-I-Naph-Gua **55** in the presence of 250 μM of DMP. The 1:2 combined system showed a much-decreased emission due to the

coumarin fluorophores from roughly 90 a.u. to 40 a.u. Furthermore, the slight increase in emission from the naphthalimide fluorophore from 10 a.u. to 30 a.u. was slightly higher than the sum of FI of both 2:1 **54**·Zn^{2+} and C_{12}-I-Naph-Gua **55** individually. It showed some sign of FRET, though not as pronounced as we had hoped for.

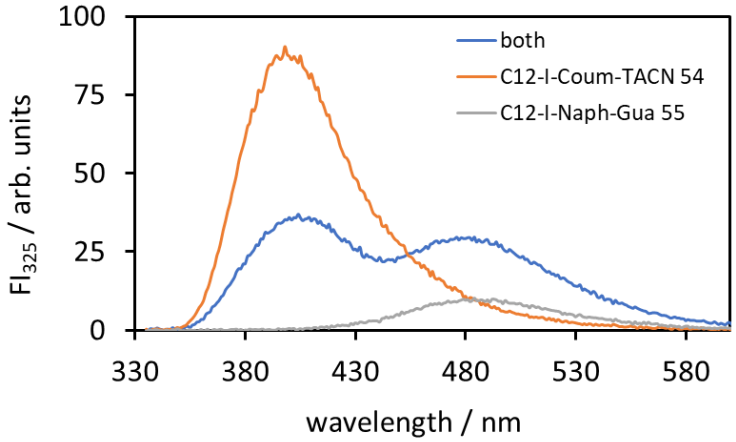

Figure 115. Fluorescence spectrum of C_{12}-I-Coum-TACN·Zn^{2+} (**54**·Zn^{2+}) (33 μM), C_{12}-I-Naph-Gua **55** (67 μM) and 1:2 ratio of C_{12}-I-Coum-TACN **54** and C_{12}-I-Naph-Gua **55** (total 100 μM) in the presence of 250 μM of DMP in CHES buffered solution (5 mM, pH = 9.1), slit 2.5/2.5.

(Figure 48 was reprinted for clarity)

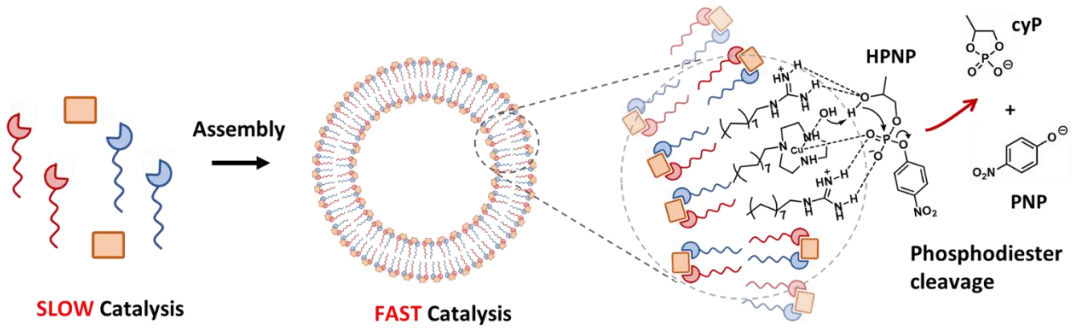

Figure 48. Self-assembly of C_{16}Gua **23** and **20**·Cu^{2+} into vesicular aggregates for **HPNPP** cleavage.

The fluorescence properties of C_{12}-I-Coum-TACN **54** and C_{12}-I-Naph-Gua **55** were also conducted in the absence and presence of DMP in 20% DMSO in water. The total concentration

of amphiphiles was increased 200 μM to ensure we were working above the CAC. Under these conditions, in the absence of DMP, we observed no indication of FRET with all ratios of C_{12}-I-Coum-TACN **54** and C_{12}-I-Naph-Gua **55** examined (1:1, 1:2 or 2:1). However, when we added DMP (500 μM) and Zn^{2+} into the system (2:1 C_{12}-I-Coum-TACN **54** and C_{12}-I-Naph-Gua **55**, total concentration of 200 μM), a significant jump in the emission intensity (FI = 270 a.u.) was observed for C_{12}-I-Coum-TACN **54** and a slight increase (FI = 60 a.u.) was observed for C_{12}-I-Naph-Gua **55** (FI under slit 2.5/2.5 would be roughly 25 times less than under slit 5/5). The FI of C_{12}-I-Coum-TACN **54** in the presence of DMP and Zn^{2+} was significantly higher than its initial FI in the absence of DMP and Zn^{2+} in Figure 111. This unique behaviour of C_{12}-I-Coum-TACN **54** was studied in further detail and will be discussed in the following sections. Although the emission of C_{12}-I-Coum-TACN **54** was significant, there was no strong indication of FRET transfer to C_{12}-I-Naph-Gua **55**.

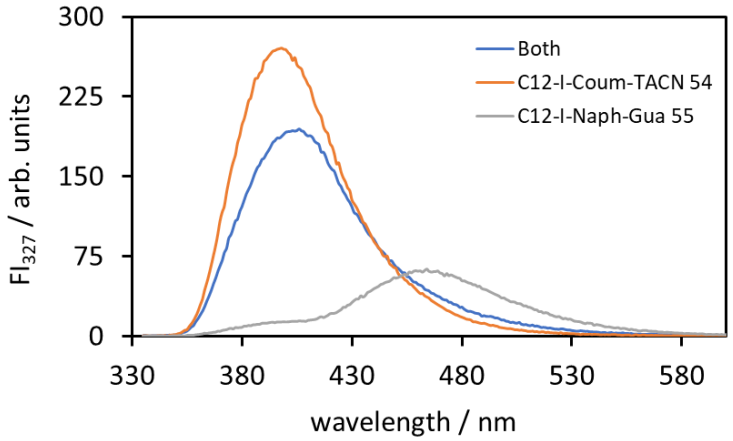

Figure 116. Fluorescence spectrum of C_{12}-I-Coum-TACN·Zn^{2+} (**54**·Zn^{2+}) (133 μM), C_{12}-I-Naph-Gua **55** (67 μM) and 2:1 ratio of C_{12}-I-Coum-TACN **54** and C_{12}-I-Naph-Gua **55** (total 200 μM) in the presence of 500 μM of DMP in 20% DMSO in water, slit 2.5/2.5.

To summarise, while there were indications of FRET between the C_{12}-I-Coum-TACN **54** and C_{12}-I-Naph-Gua **55** amphiphiles under some specific conditions, the results were not strong enough to convince us to further pursue this idea at this stage. Due to the high sensitivity of FRET to small changes in the surrounding environment, it became evident that the complexity

of the system meant that more work was needed to determine the effects of the Zn^{2+} ions and phosphate on the fluorescence behaviour of these two amphiphiles. We were drawn particularly to the behaviour of C_{12}-I-Coum-TACN **54**, which appeared to exhibit enhancement of fluorescence in the presence of DMP. The effects of different metal ions and different phosphates on the fluorescence behaviour of C_{12}-I-Coum-TACN **54** will be discussed in the following sections.

3.5 The fluorescence behaviour of C_{12}-I-Coum-TACN 54

The unique fluorescence properties of C_{12}-I-Coum-TACN **54** were examined in CHES buffer and 20% DMSO in water, with the sequential addition of Zn^{2+} and dimethylphosphate. To a solution of C_{12}-I-Coum-TACN ligand **54** (50 μM) in CHES buffer (pH 9.1), 50 μM of Zn^{2+} and 500 μM of dimethyl phosphate (DMP) was added sequentially (see Figure 117, blue bars). The initial emission intensity of C_{12}-I-Coum-TACN **54** in CHES buffer is reasonable low (25 a.u.) when excited at 325 nm (slit 2.5/5). Following the sequential addition of Zn^{2+} and DMP, the fluorescence intensity increased moderately to 111 a.u. and 205 a.u., respectively.

The C_{12}-I-Coum-TACN ligand **54** was also examined in a 20% DMSO in the water system, where a higher concentration of C_{12}-I-Coum-TACN **54** (100 μM) was used due to the higher CAC expected in 20% DMSO/water. The initial fluorescence intensity of C_{12}-I-Coum-TACN **54** was 15 a.u., which increased to 43 a.u. following the addition of 100 μM of Zn^{2+}. Interestingly, addition of 500 μM of dimethyl phosphate induced a dramatic jump in the fluorescence intensity to 800 a.u. (see Figure 117, orange bars, slit 2.5/5).

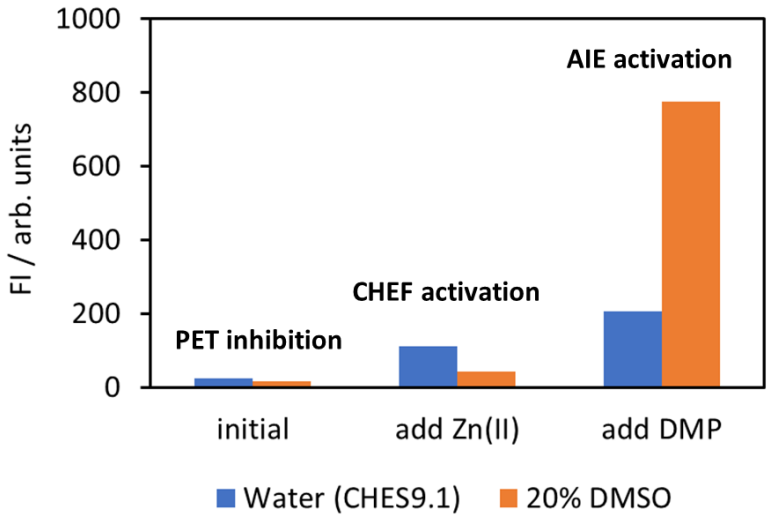

Figure 117. Fluorescence profile of 50 μM of C_{12}-I-Coum-TACN **54** (blue bars) excited at 325 nm, slit 2.5/5, following the addition of 50 μM of Zn^{2+} and 500 μM of DMP in CHES buffer solution (5 mM, pH 9.1). And fluorescence profile of 100 μM of C_{12}-I-Coum-TACN **54** (orange bars) excited at 325 nm, slit 2.5/5, following the addition of 100 μM of Zn^{2+} and 500 μM of DMP in 20% DMSO in water and 1 mM of DIPEA.

To provide insight into the mechanism of this dramatic fluorescence enhancement, we examined the UV spectra of C_{12}-I-Coum-TACN **54** in the absence and presence of 100 μM zinc ions and 500 μM DMP (Figure 118a). The initial UV spectrum showed that the maximum absorption of the C_{12}-I-Coum-TACN **54** only reached 0.37 a.u., and there is no significant change, following the addition of 100 μM of Zn^{2+} ions and the subsequent addition of 500 μM of DMP substrates. Absorbance spectra were also measured at a higher concentration of C_{12}-I-Coum-TACN **54** (250 μM). The absorption intensity of only C_{12}-I-Coum-TACN **54** was observed to be higher (0.8 a.u.), as expected due to the higher concentration of the coumarin fluorophore. However, there was negligible change in the absorption of C_{12}-I-Coum-TACN **54** following the addition of 250 μM Zn^{2+} and 500 μM DMP. This suggests that the changes in fluorescence behaviour was not due to changes in the absorption properties of C_{12}-I-Coum-TACN **54**. The unique fluorescence phenomena should therefore be due to changes in the emission of light, which can be affected by interactions of our molecule with metal ions and phosphates in solution.

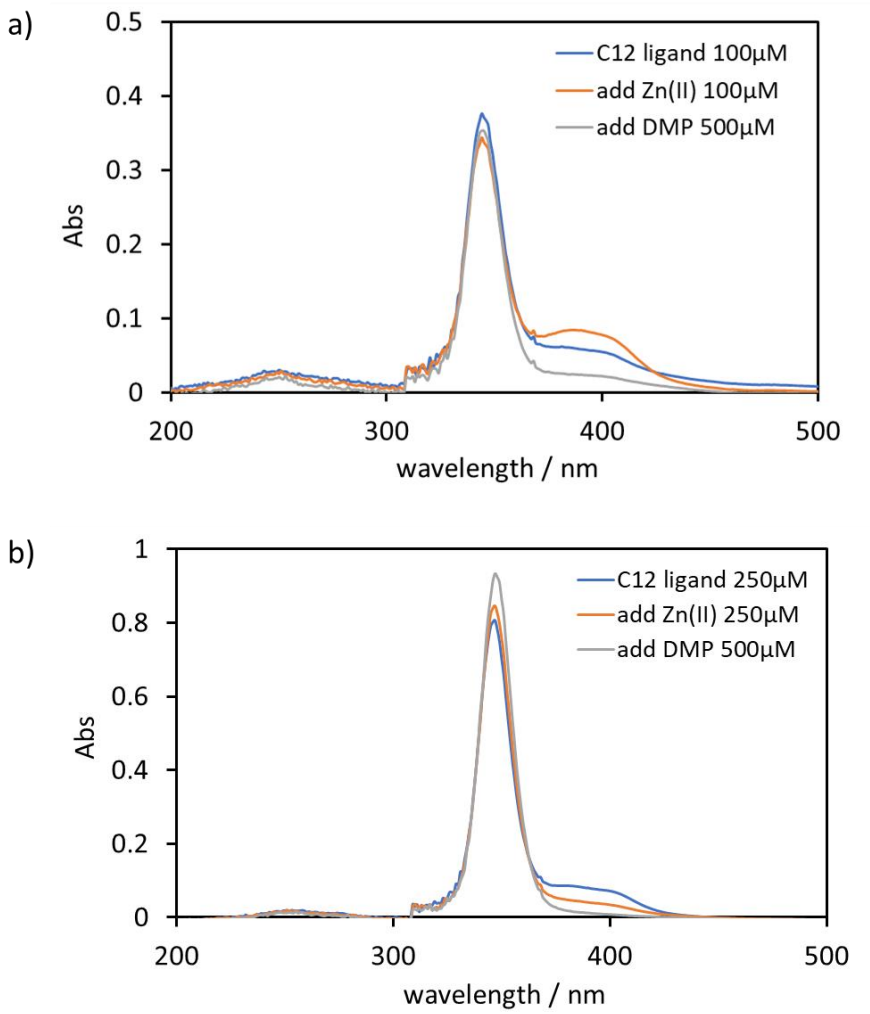

Figure 118. UV-Visible profile of a) 100 µM of C_{12}-I-Coum-TACN **54** (blue curve), with the addition of 100 µM of Zn^{2+} ions (orange curve) and with the further addition of either 500 µM of DMP (grey curve); b) 250 µM of C_{12}-I-Coum-TACN **54** (blue curve), with the addition of 250 µM of Zn^{2+} ions (orange curve) and with the further addition of either 500 µM of DMP (grey curve) in 20% DMSO in water and in the presence of 1 mM of DIPEA.

3.5.1 Our hypothesis

Fluorescence behaviours can be split generally into fluorescence quenching and fluorescence enhancement processes. The mechanisms for quenching and enhancement are diverse, with the main categories being self-quenching, photo-induced electron transfer (PET),

intramolecular charge transfer (ICT) effects, twisted intramolecular charge transfer (TICT), fluorescence resonance energy transfer (FRET), aggregation induced emission enhancement (AIE), and aggregation caused quenching (ACQ). It is common to see dual or triple interplaying mechanisms in a single fluorescent system.[151] However, few such fluorescence mechanisms can be easily predicted, due to the extreme sensitivity of different fluorophores toward its chemical environment.

Our hypothesis for the unusual fluorescence behaviour of C_{12}-I-Coum-TACN **54** is shown in Figure 119. The initial fluorescence emission for C_{12}-I-Coum-TACN **54** was reasonably low, potentially due to photo-induced electron transfer (PET) resulting in fluorescence quenching. Under basic conditions, the lone pairs of electrons on the TACN can donate electron density to the coumarin, with help of tautomerisation of the amide bond (PET will normally occur over a 3-carbon distance[152]). Upon addition of metal ions such as Zn^{2+}, chelation with the TACN head groups will inhibit PET quenching and result in an increase in fluorescence due to chelation enhanced fluorescence (CHEF). Further fluorescence enhancement is observed in the presence of the phosphate substrate, which could be related to the self-assembly of C_{12}-I-Coum-TACN **54** and be described as an aggregation induced effect (AIE), where the CAC of C_{12}-I-Coum-TACN **54** is greatly decreased due to strong interactions with phosphate in solution. The effects of different metal ions and phosphates on the fluorescence behaviour of C_{12}-I-Coum-TACN **54** is described in the subsequent sections.

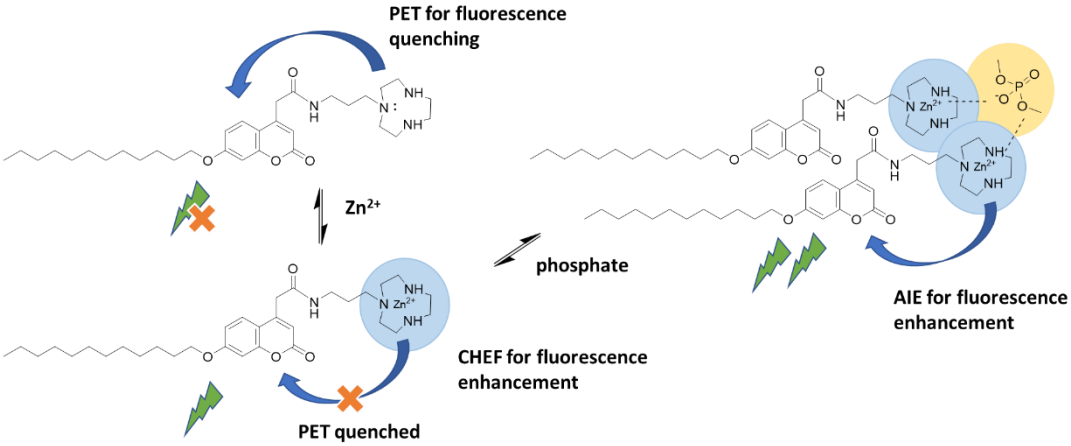

Figure 119. Proposed PET, CHEF and AIE mechanisms for the unique fluorescence increase observed with C_{12}-I-Coum-TACN **54** in the presence of Zn^{2+} and DMP.

3.5.2 Investigating the effect of self-assembly

Therefore, two control molecules were synthesised, one with a much shorter C_4-alkyl chain, and the other without an alkyl chain on the phenol of the coumarin (Figure 120). C_0-I-Coum-TACN **96** was obtained directly from the deprotection of intermediate **72**, while the synthesis of C_4-I-Coum-TACN **97** utilised the same procedure as for C_{12}-I-Coum-TACN **54**, but utilising alkylation with a shorter C_4-alkyl chain (Scheme 9).

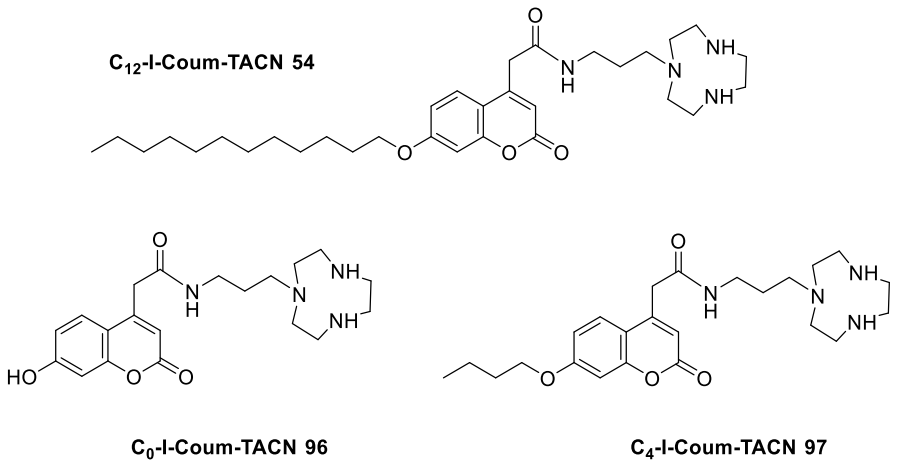

Figure 120. The chemical structure of C_{12}-I-Coum-TACN **54** and the control molecules, C_0-I-Coum-TACN **96** and C_4-I-Coum-TACN **97**.

The UV spectra of C_0-I-Coum-TACN **96**, C_4-I-Coum-TACN **97** and C_{12}-I-Coum-TACN **54** were first measured, and this is shown in Figure 121. C_4-I-Coum-TACN **97** and C_{12}-I-Coum-TACN ligand **54** had the same absorption maximum (345 nm), while the absorption intensity of C_4-I-Coum-TACN **97** at this wavelength was 1.6 times higher than for C_{12}-I-Coum-TACN **54**. This could be due to self-quenching effects as more hydrophobic molecules would have a greater propensity to self-assemble in aqueous solution to minimise interactions with water. The control molecule C_0-I-Coum-TACN **96** had an absorption maximum at 375 nm and a much higher absorption intensity of 1.6 a.u.. This can be attributed to the free hydroxyl group in the 4-coumarin position which has a strong electron donation effect, resulting in significant red shift of its absorption and enhanced absorption intensity.

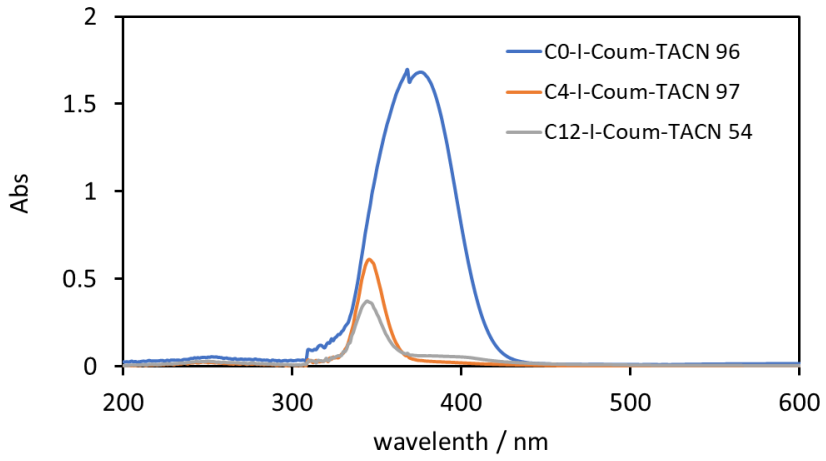

Figure 121. UV-Visible spectrum of 100 µM of C_0-I-Coum-TACN **96**, the C_4-I-Coum-TACN **97** and the C_{12}-I-Coum-TACN ligand **54** in 20% DMSO in water and 1 mM of DIPEA.

The changes in fluorescence emission upon addition of Zn^{2+} and DMP was investigated for the three ligands C_0-I-Coum-TACN **96**, C_4-I-Coum-TACN **97** and C_{12}-I-Coum-TACN **54** (Figure 122). Different slit widths were applied to adjust their fluorescence intensity, due to the significant difference in absorption intensity observed with the C_0-I-Coum-TACN **96**. The data is still comparable as we were concerned about the relative changes in intensity upon addition of Zn^{2+} and DMP rather than the absolute intensity. From Figure 122, it can be seen that the fluorescence intensity of 100 µM of C_{12} ligand **54** (λ_{ex} 327 nm/ λ_{em} 377 nm) increased three times from FI = 14 a.u. to 48 a.u. following addition of 100 µM of Zn^{2+}. Subsequent addition of DMP results in a 18 times increase in FI intensity, reaching 878 a.u.. On the other hand, addition of Zn^{2+} to a solution of 100 µM of C_4 ligand **97** (λ_{ex} 327 nm/ λ_{em} 377 nm) resulted in a five times increase in emission from 73 a.u. to 349 a.u.. Importantly, there was no significant jump of FI following the addition of DMP. These results support the hypothesis that the addition of Zn^{2+} allowed for chelation to TACN, resulting in a decrease of PET quenching and activation of CHEF enhancement. Addition of DMP then induces the aggregation of C_{12} ligand **54** giving another significant FI increase. The C_4 ligand **97**, however, could chelate with metal ions for PET inhibition and CHEF activation, but it could not self-assemble due to the much lower hydrophobic effect from the C_4 alkyl chains. This suggests that the self-assembly of the ligands was essential for the dramatic fluorescence increase. For the C_0 ligand **96**, no

fluorescence intensity change was observed following the addition of either Zn^{2+} ions or DMP when excited at 344 nm. This is likely due to the presence of the 7-hydroxyl group on the coumarin structure, which would be in its phenoxide form under these basic conditions, and the strong electron donating effect due to this may have prevented quenching of fluorescence emission by PET.

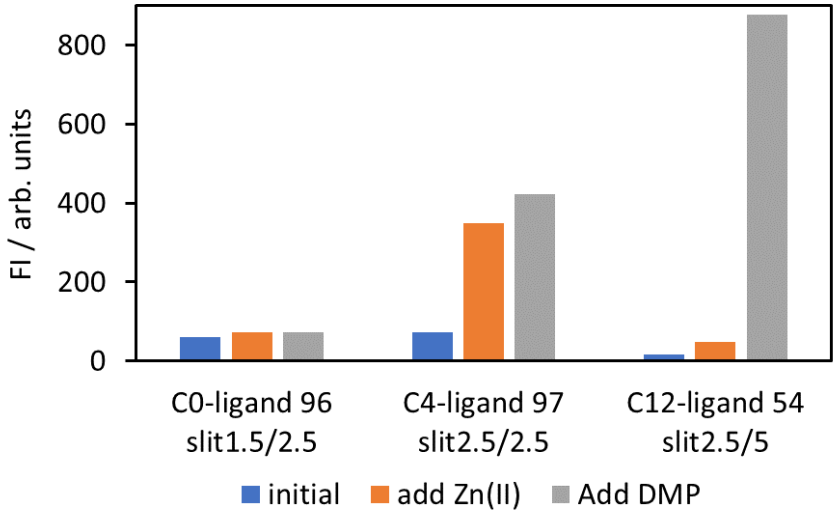

Figure 122. The fluorescence intensity of 100 µM of each C_0-I-Coum-TACN **96**, C_4-I-Coum-TACN **97** and C_{12}-I-Coum-TACN ligand **54** (blue bar), with the addition of 100 µM of Zn^{2+} ions (orange bar) and 500 µM of DMP substrates (grey bar) subsequently in 20% DMSO in water and 1 mM of DIPEA.

To confirm the role of Zn^{2+} in the self-assembly of the C_{12}-I-Coum-TACN amphiphile **54**, the above experiment was repeated but swapping the sequence of the addition of Zn^{2+} and DMP (Figure 123). For all three ligands, there was no dramatic increase in fluorescence after the addition of DMP (orange bars). This suggests that the binding interaction between the TACN sites of the ligands and DMP is weak without the assistance of Zn^{2+} ions. Upon addition of Zn^{2+} to each of the systems, there was no increase in fluorescence intensity for the C_0 **96** system, a small increase with the C_4 ligand **97** and a significant jump in intensity for the C_{12} ligand **54** system. This result reinforced the importance of both Zn^{2+} and DMP for the self-assembly of C_{12}-I-Coum-TACN amphiphile **54** and the resulting fluorescence enhancement.

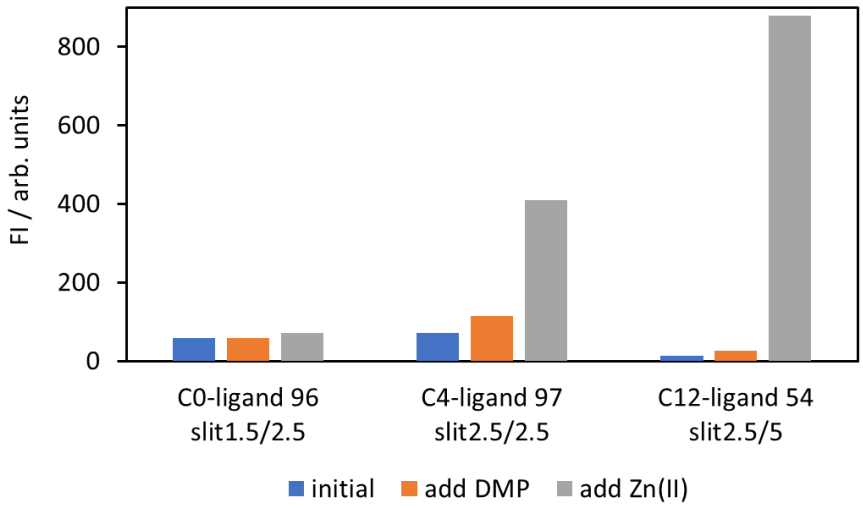

Figure 123. The fluorescence intensity of 100 μM of each C_0-I-Coum-TACN **96** (λ_{ex} = 344 nm), C_4-I-Coum-TACN **97** (λ_{ex} = 327 nm) and C_{12}-I-Coum-TACN ligand **54** (λ_{ex} = 327 nm) (blue bar), with the addition of 500 μM of DMP (orange bar) and 100 μM of Zn^{2+}(grey bar) subsequently in 20% DMSO in water and in the presence of 1 mM of DIPEA.

3.5.3 Self-quenching effects

From our above experiments, we noticed that the addition of a longer chain to the coumarin resulted in a decrease in the initial fluorescence emission of the molecule on its own. This suggests that there may also be some form of self-quenching occurring, given the greater propensity for these more hydrophobic molecules to self-assemble and form supramolecular structures. Fluorescence quenching is one of the most common phenomena in fluorescent systems, and can be caused by changes in the surrounding environment (for example, changes in pH and temperature), electron transfer, energy transfer, complex formation (formation of coordination compounds that are not fluorescent), and others.[153-156] Self-quenching is a special type of fluorescence quenching where fluorophores and their quenchers are identical. Particularly, self-quenching of fluorophores in highly concentrated solutions is particularly common and occurs due to the close proximity of fluorophores.[157] Therefore, it is essential to study the self-quenching properties of C_{12}-I-Coum-TACN ligands **54** and to see how this affects

their fluorescence behaviour in comparison to the control compounds.

The change in fluorescence intensity with different concentrations of C_0-I-Coum-TACN **96**, C_4-I-Coum-TACN **97** and C_{12}-I-Coum-TACN **54** is shown in Figure 124. Increasing the concentration of C_0-I-Coum-TACN **96** (λ_{ex} = 344 nm/ λ_{em} = 460 nm) resulted in a steady increase in the fluorescence intensity from 0 a.u. up to around 300 a.u., followed by evidence of quenching after the concentration of C_0-I-Coum-TACN **96** reached 30 µM. At even higher concentrations, this quenching effect becomes more evident, resulting in an overall decrease in the fluorescence intensity. The self-quenching behaviour for both the C_4-I-Coum-TACN **97** and C_{12}-I-Coum-TACN **54** ligands (λ_{ex} = 327 nm/ λ_{em} = 400 nm) were similar but less pronounced, and signs of self-quenching for all three of the C_X-I-Coum-TACN ligands (x = 0, 4, 12) started to appear in the region of 10-30 µM.

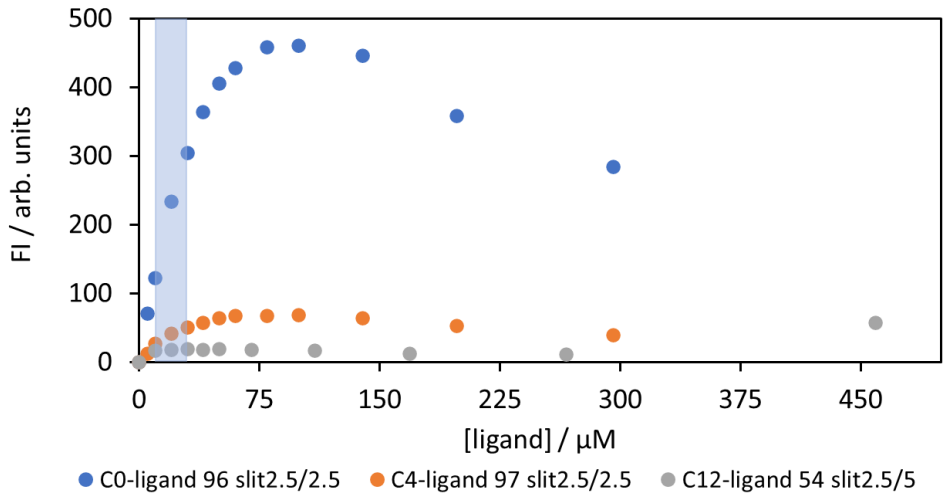

Figure 124. Fluorescence profile of C_0-I-Coum-TACN **96** (λ_{ex} = 344 nm), C_4-I-Coum-TACN **97** (λ_{ex} = 327 nm) and C_{12}-I-Coum-TACN **54** (λ_{ex} = 327 nm) in 20% DMSO in water and in the presence of 1 mM of DIPEA at 25 °C.

The same self-quenching experiments were performed for each of the ligands C_X-I-Coum-TACN (x = 0, 4, 12) in the presence of Zn^{2+}. Although the FI intensity of each ligand was stronger due to the metal chelation effect, the self-quenching properties did not significantly change, and

for all three ligands, the self-quenching became evident in the region of 10-30 µM. Different slits were applied with each C_X-I-Coum-TACN·Zn^{2+} system to get a clearer comparison. However, one unexpected observation was that the FI of C_{12}-I-Coum-TACN·Zn^{2+} jumped significantly up to 800 a.u. at 200 µM, which did not follow the trend of quenching observed with C_4-I-Coum-TACN·Zn^{2+} (**97**·Zn^{2+}) and C_0-I-Coum-TACN·Zn^{2+} (**96**·Zn^{2+}). This observation will be elaborated on in the next section.

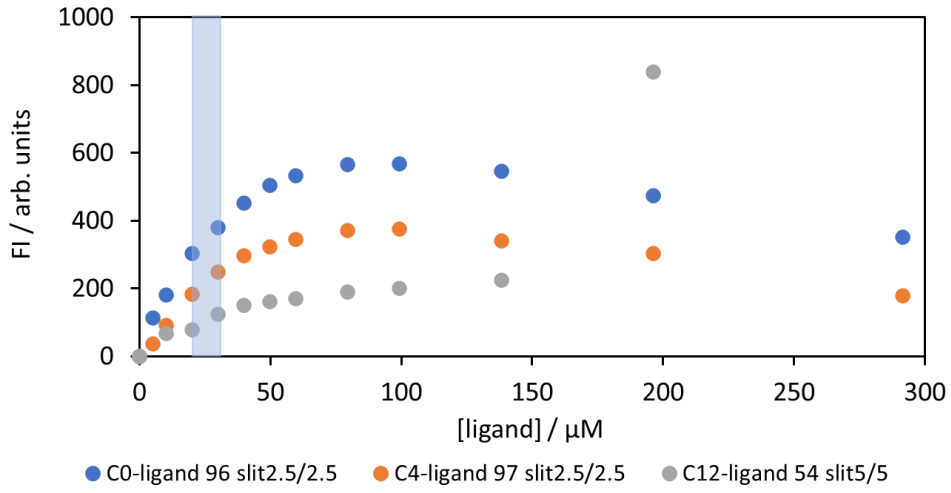

Figure 125. Fluorescence profile of C_0-I-Coum-TACN·Zn^{2+} (**96**·Zn^{2+}, λ_{ex} = 344 nm), C_4-I-Coum-TACN·Zn^{2+} (**97**·Zn^{2+}, λ_{ex} = 327 nm) and C_{12}-I-Coum-TACN·Zn^{2+} (**54**·Zn^{2+}, λ_{ex} = 327 nm) in 20% DMSO in water and in presence of 1 mM of DIPEA at 25 °C.

The previous experiments showed that each of the C_X-I-Coum-TACN and C_X-I-Coum-TACN·Zn^{2+} compounds all began to exhibit self-quenching phenomena below a concentration of 30 µM. The fact that the length of the hydrophobic chain on the ligand had no bearing on the concentration at which self-quenching occurs, suggests that the self-quenching behaviour is not due to the formation of self-assembled structures. Several common scenarios could result in fluorescence self-quenching. Firstly, the H aggregation (π-π stacking) of dyes is one common reason due to the presence of flat π-conjugated structures, resulting in aggregation caused quenching (ACQ).[157-158] However, the literature reported by Iyer and co-workers states that the presence of long alkyl chains providing hydrophobic interactions effectively abolishes strong

π-stacks of fluorophores in an aqueous medium.[159] As we do not observe any differences in the concentrations at which quenching occurs for our three ligands with different length alkyl chains, it is unlikely that self-quenching observed for our system is due to ACQ.

A second fluorescence self-quenching scenario is related to homo-FRET, in which the energy migrates between identical fluorophores.[157] This is also called an energy trap, resulting in no energy loss. However, homo-FRET would only occur when there is some extent of overlap between the excitation and emission spectra of the identical fluorophore. Therefore, there is a low chance that this is the self-quenching mechanism for the C_{12}-I-Coum-TACN **54** system due to the lack of excitation and emission spectrum overlap as seen in previous studies (Figure 111).

Lastly, a high concentration of fluorophore resulting in an inner filter effect (IFE) could be another reason for fluorescence quenching, suggesting that the fluorophores are too concentrated in solution. Under primary IFE, highly concentrated fluorophores strongly absorbs and attenuates the excitation beam so that only the front part of the cuvette facing the excitation beam fluoresces strongly (Figure 126, middle).[160] Therefore, less excitation intensity remains to be absorbed by the rest of the fluorophores in the detection area of the cuvette, resulting in distortion and loss of a certain amount of emission signal.[161] In addition, the reabsorption of emission by the ground-state fluorophores causes secondary IFE, even though in our case, the requirement of excitation and emission spectrum overlap is not met with the C_X-I-Coum-TACN system. It appears most likely that fluorescence quenching in our system is due to primary IFE, and that in any case, the ability of the molecule to self-assemble does not affect the self-quenching properties.

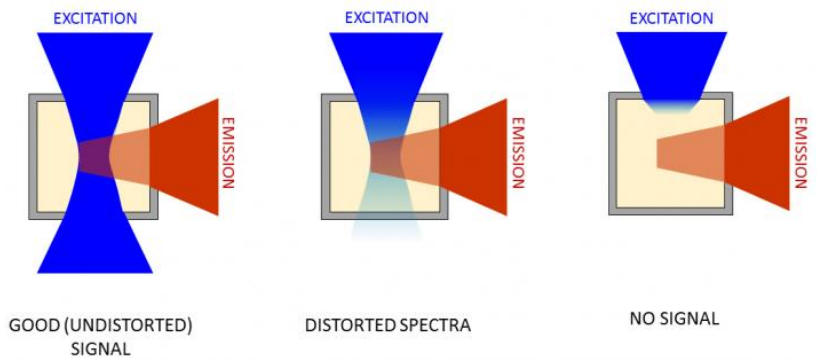

Figure 126. Schematic diagram of the inner filter effect in fluorescent system. The yellow square represents the solution in a cuvette, the blue area represents the excitation beam, and the red area represents the emission output.

To further investigate the jump in fluorescence intensity observed with C_{12}-I-Coum-TACN **54** as shown in Figure 127, we proceeded to measure the change in fluorescence at even higher concentrations of the ligand. In order to see the whole titration within the same plot, we reduced the slit to 2.5/2.5 to prevent the saturation of the detector and the data going out of range. From Figure 127, we can observe an even bigger jump in fluorescence intensity when going from 200 µM of C_{12}-I-Coum-TACN·Zn^{2+} (**54**·Zn^{2+}) to 250 µM, followed by a gradual plateau upon further addition of **54**·Zn^{2+}. Interestingly, there was no shift in the emission maximum across all concentrations of **54**·Zn^{2+} observed. Our hypothesis is that this jump in fluorescence intensity is due to the formation of self-assembled structures, and that the subsequent plateau in fluorescence is due to further IFE.

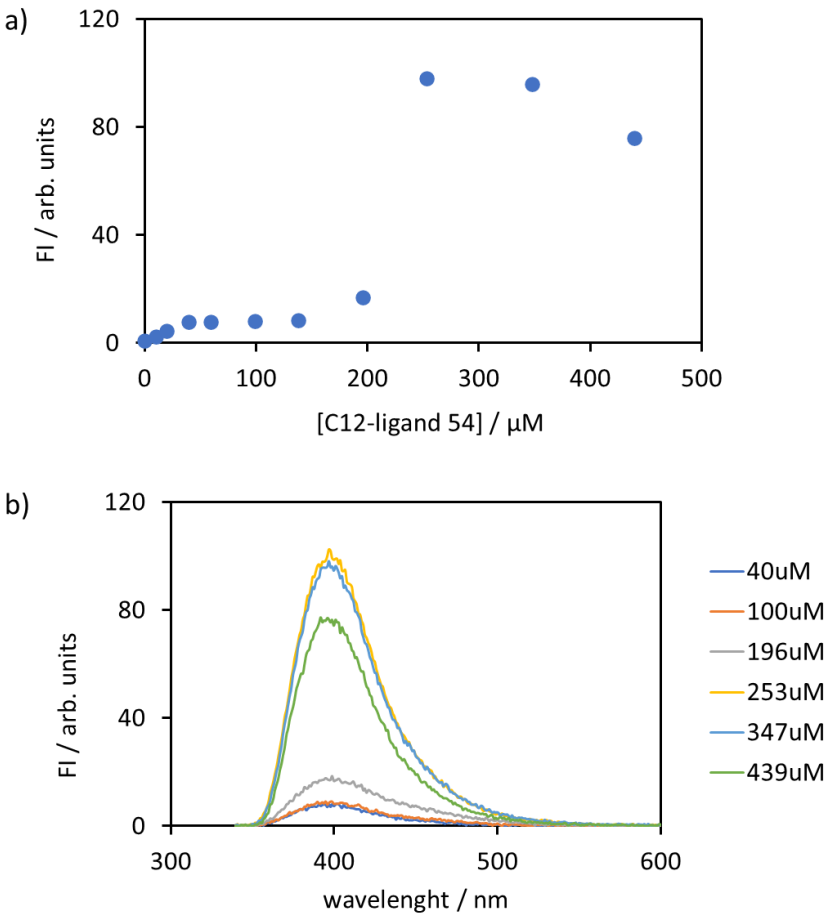

Figure 127. a) Fluorescence profile and b) emission spectrum of C_{12}-I-Coum-TACN **54**·Zn^{2+} in 20% DMSO in water. Experimental conditions: varying of [C_{12}-I-Coum-TACN **54**] = [Zn^{2+}], [DIPEA] = 1 mM in 20% DMSO in water, 25 °C, excited at 327 nm, slit 2.5/2.5.

3.5.4 Self-assembly and CAC data

Although our C_x-I-Coum-TACN ligands contain a coumarin fluorophore within their chemical structures, it was not ideal to be directly used as a probe to determine their self-assembly properties. This is because of the self-quenching of C_x-I-Coum-TACN as discussed above, which would result in concentration-dependent effects independent of changes in the self-assembly of the amphiphiles. Therefore, the CAC value of this amphiphile was determined using an external fluorescence probe, **Nile red** (λ_{ex} 600 nm/ λ_{em} 660 nm), which has a much higher excitation and emission compared to coumarin and therefore does not interfere with

fluorescence of the C_X-I-Coum-TACN ligands.

We titrated increasing amounts of C_{12}-I-Coum-TACN into the solvent media in the presence of 1 mM of DIPEA and 3 µM of **Nile red**. We did not observe a clear change in fluorescence intensity, but we did see a clear shift in the emission maximum of **Nile red** with increasing concentrations of the amphiphile. Figure 128 shows that the emission maximum of **Nile red** initially decreased with increasing concentration of C_{12}-I-Coum-TACN up to a concentration of 260 µM, after which the emission maximum increased upon further addition of C_{12}-I-Coum-TACN. The sensitivity of **Nile red** toward the polarity of its surrounding environment is commonly used to determine the CAC of amphiphiles, and in this case indicates that the CAC of C_{12}-I-Coum-TACN under these conditions is approximately 260 µM. This data closely matches the concentration at which an immense jump in the fluorescence of C_{12}-I-Coum-TACN·Zn^{2+} is observed, which occurs at 250 µM. These observations support the hypothesis that the strong fluorescence jump observed is due to phosphate-induced self-assembly of C_{12}-I-Coum-TACN·Zn^{2+} amphiphiles.

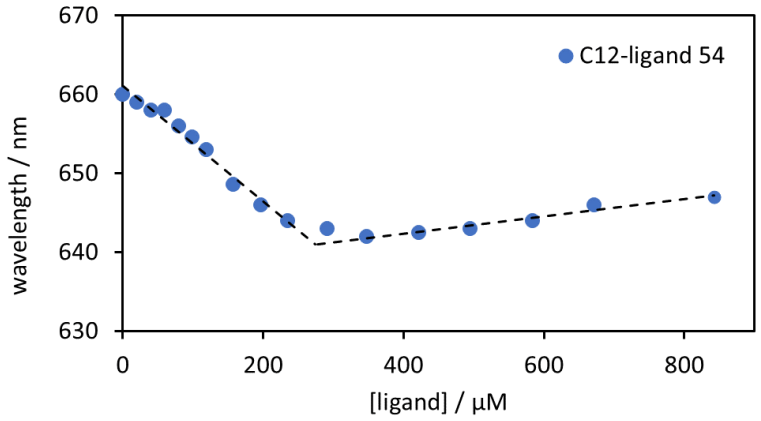

Figure 128. Shift in $\lambda_{max(em)}$ of **Nile red** (3 µM, λ_{ex} = 600 nm) at increasing concentrations of C_{12}-I-Coum-TACN **54** in 20% DMSO in water and 1 mM of DIPEA.

These fluorescence titrations were repeated in the presence of zinc ions, for the in-situ formation of C_x-I-Coum-TACN·Zn^{2+} systems. There is a prominent shift in the emission

maximum of Nile red at 200 µM for the C_{12}-I-Coum-TACN **54**·Zn^{2+} system, with another shift above 400 µM which suggests the formation of another supramolecular structure. These results match the large significant fluorescence jump observed with C_{12}-I-Coum-TACN **54**·Zn^{2+} at 250 µM (Figure 125), and it again reinforces the importance of self-assembly. There were no significant changes in the fluorescence of **Nile red** upon addition of increasing concentrations of the control molecules C_0-I-Coum-TACN **96**·Zn^{2+} and C_4-I-Coum-TACN **97**·Zn^{2+}, with no observed shift in the emission of **Nile red** under the concentration range we studied (Figure 129).

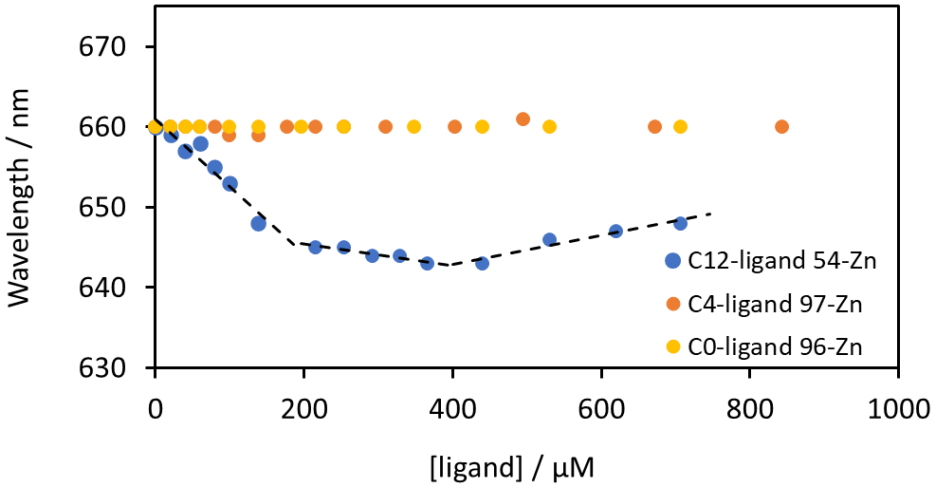

Figure 129. Shift in $\lambda_{max(em)}$ of Nile red (3 µM, λ_{ex} = 600 nm) at increasing concentrations of C_X-I-Coum-TACN·Zn^{2+} in 20% DMSO in water and 1 mM of DIPEA.

Finally, we determined the CAC of C_{12}-I-Coum-TACN **54**·Zn^{2+} in the presence of 500 µM of dimethylphosphate (DMP) and pyrophosphate (**PPi**). As previously observed in similar systems, the CAC of C_{12}-I-Coum-TACN **54**·Zn^{2+} was dramatically reduced in the presence of phosphates, due to their binding with Zn^{2+} and their ability to induce aggregation. In the presence of 500 µM of DMP, we observed a reduction of CAC to 100 µM, where there was an obvious shift in the emission maximum of **Nile red**. A similar effect was observed in the presence of 500 µM of **PPi**, with an estimated CAC of 100 µM, which suggested that 100 µM of C_{12}-I-Coum-TACN **54**·Zn^{2+} was a suitable concentration for these studies.

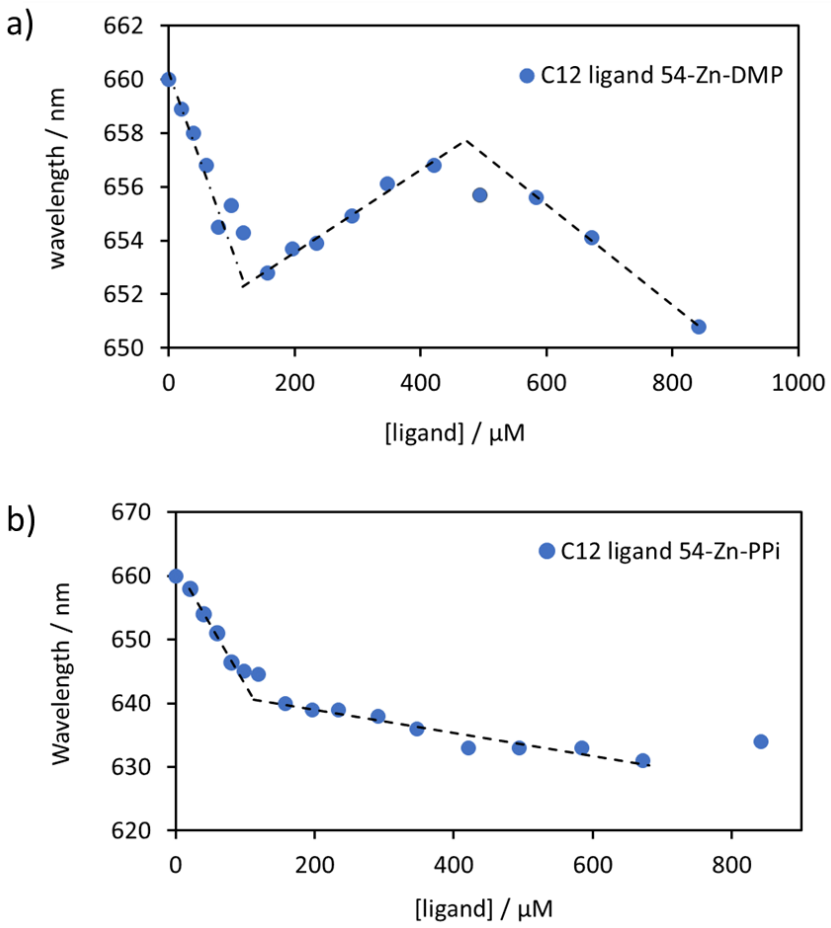

Figure 130. Shift in $\lambda_{max(em)}$ of **Nile red** (3 µM, λ_{ex} = 600 nm) at increasing concentrations of C_{12}-I-Coum-TACN·Zn^{2+} (**54**·Zn^{2+}) in the presence of 500 µM of a) DMP or b) **Ppi** in 20% DMSO in water.

3.5.5 TEM and DLS Studies

To provide further support for the self-assembly of C_{12}-I-Coum-TACN·Zn^{2+} (**54**·Zn^{2+}) to form supramolecular structures, we examined these systems using TEM and DLS. We initially examined a solution of 250 µM of **54**·Zn^{2+} in 20% DMSO, which is above the calculated CAC of ~200 µM. Dynamic light scattering measurements indicated the formation of structures in the range of 22 nm in the absence of DMP (Figure 131).

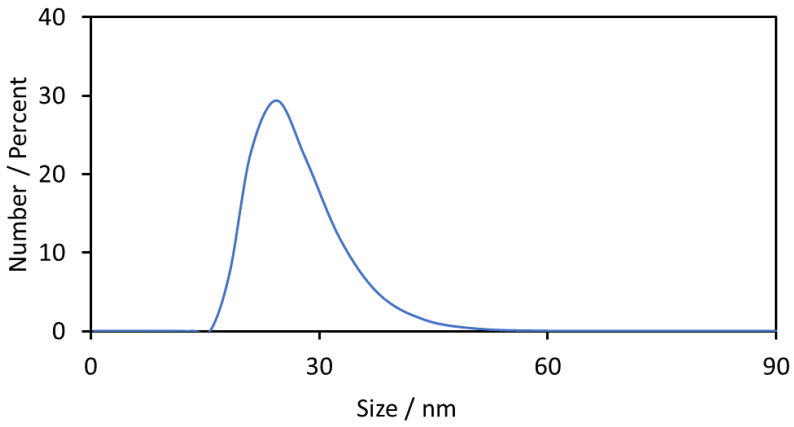

Figure 131. Hydrodynamic diameter of assemblies measured with dynamic light scattering (DLS) in the presence of **54**·Zn^{2+} in 20% DMSO in water, [C_{12}-I-Coum-TACN **54**] = [Zn^{2+}] = 250 μM, [DIPEA] = 1 mM in 20% DMSO in water at 25 °C.

The formation of self-assembled aggregates in a sample of 250 μM of C_{12}-I-Coum-TACN·Zn^{2+} (**54**·Zn^{2+}) in 20% DMSO in water was also visible using transmission electron microscopy (TEM). The samples were fixed onto charged grids with uranyl acetate to allow for greater contrast. The black hollow circles observed suggests a morphology that is consistent with vesicular structures. The structures formed had an average size of ~20-30 nm, which was in close agreement of the data measured by DLS.

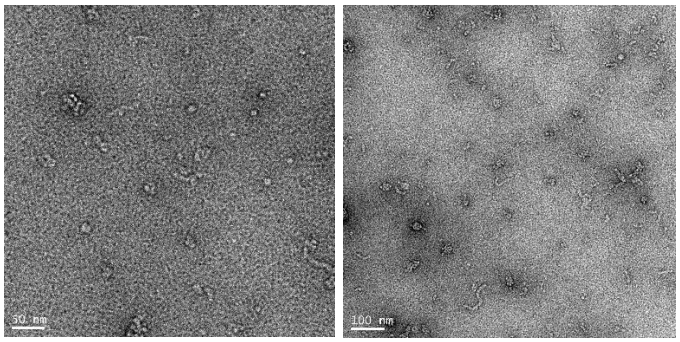

Figure 132. Representative TEM images of the vesicular structures of 250 μM of C_{12}-I-Coum-TACN **54**·Zn^{2+} in 20% DMSO in water and 5 mM of DIPEA.

TEM images of C_{12}-I-Coum-TACN **54**·Zn^{2+} (100 μM) in the presence of DMP (500 μM) also showed distinct black hollow circles with morphology highly indicative of the formation of

vesicular structures. In the presence of DMP, these structures had an average size of ~50-60 nm, which clearly indicated the formation of vesicles rather than micelles. TEM imaging of the control samples C_4-I-Coum-TACN **97** and C_0-I-Coum-TACN **96** revealed no obvious structures either in the presence or absence of DMP.

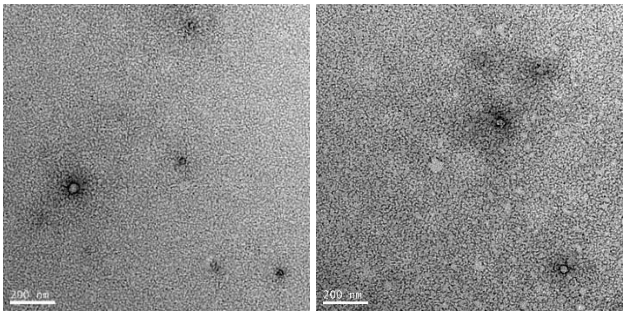

Figure 133. Representative TEM images of the vesicular structures of 100 μM of C_{12}-I-Coum-TACN **54**·Zn^{2+} in the presence of 500 μM of DMP in 20% DMSO in water, [C_{12}-I-Coum-TACN **54**] = [Zn^{2+}] = 100 μM, [DMP] = 500 μM, [DIPEA] = 1 mM in 20% DMSO in water at 25 °C.

3.5.6 Exploiting PET and CHEF effects to obtain a sensor for metal ions

The PET effect describes the mechanism by which a lone pair of electrons is able to quench the fluorescence emission of a fluorophore. In this mechanism, a lone pair of electrons that is part of a free receptor, which has higher energy than the highest occupied molecular orbital (HOMO) of a fluorophore, would have a chance to donate an electron into a partially filled HOMO, and thus prevent the relaxation of an excited electron back to the HOMO (Figure 134).[162] In such processes, upon excitation of an electron of a fluorophore into the excited state, the original partially occupied HOMO state can be filled quicker by the adjacent electron in the free receptor. This blocks the ability of the excited electron to relax back into the HOMO, and leads to fluorescence quenching.

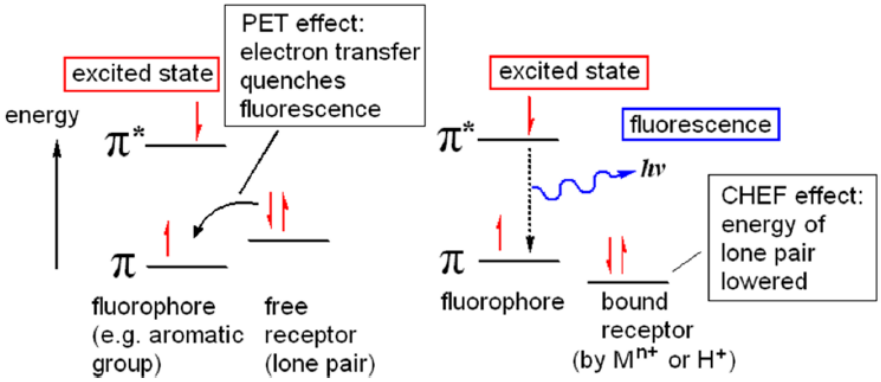

Figure 134. Schematic illustration of photoinduced energy transfer effect (left) and chelation enhanced fluorescence effect (right). Reprinted with permission from ref. 162. Copyright (2013) American Association for the Advancement of Science.

However, the pair of electrons on the free receptor can be stabilized by chelation with metal ions, for example, Zn^{2+} and Ca^{2+}. If the energy level of the chelated receptor is lower than the HOMO of the fluorophore, electron transfer from bound receptor to the HOMO of fluorophores will be prevented. Therefore, radiative relaxation from LUMO to HOMO of fluorophores can occur, resulting in the normal fluorescence process. This is called the CHEF effect and allows for enhancement of fluorescence (Figure 134, right).

The incorporation of PET and CHEF effects is commonly observed in the design of fluorescent sensors for metal ions.[152, 162-164] De Silva and co-workers reported the well-known PET chemosensor **98**, which contains a di-2-picolylamine (DPA) and an anthracene fluorophore (Figure 135).[163] The electrons in the aliphatic amine of DPA were able to transfer through the methylene group to the excited anthracene, resulting in PET quenching. However, the addition of Zn^{2+} resulted in formation of a complex with DPA which limited the PET process via the CHEF effect, and dramatically increased the fluorescence.

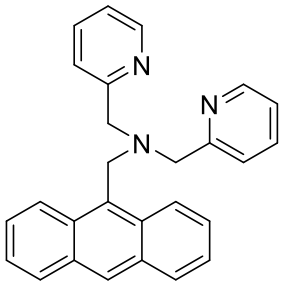

98

Figure 135. Chemical structure of the PET chemosensor **98** reported by Silva and co-workers.[163]

The distance between fluorophores and lone-pair containing receptors is usually kept within the length of a three-carbon linker to ensure strong and efficient PET. However, exceptions can occur via binding to functional groups attached to the fluorophore. Xu and co-workers reported an amide-containing DPA receptor **99** for Zn^{2+} sensing where the quenching of naphthalimide fluorescence could be released by zinc chelation to the DPA receptor via an amide bond.[152, 165] This is another example of PET deactivation and CHEF activation. They also confirmed good selectivity of DPA to Zn^{2+} over other heavy metals, for example, Fe^{2+}, Co^{2+}, Ni^{2+}, Cu^{2+}, Cd^{2+}, and Hg^{2+}. In Figure 136, the tautomerisation of the amide spacer into an imidic acid form allowed chelation with Zn^{2+} to inhibit the PET effect and activate the CHEF, resulting in fluorescence enhancement of naphthalimide.

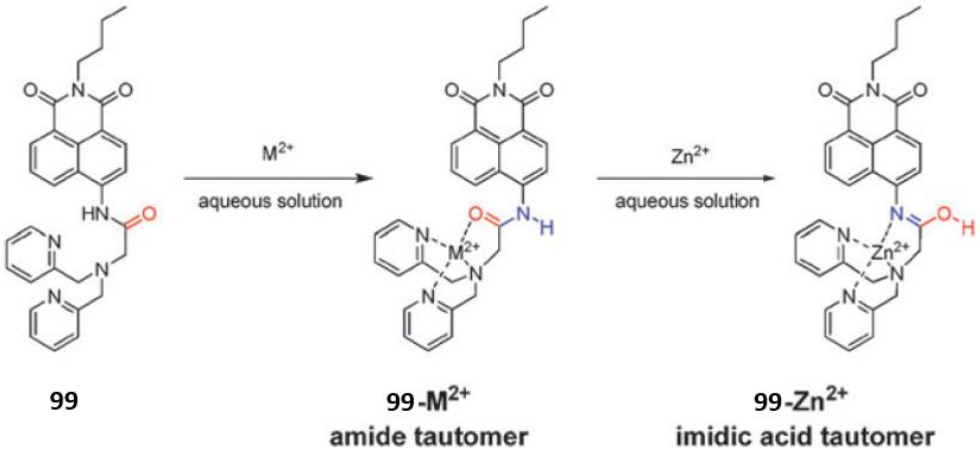

Figure 136. Proposed mechanisms of the binding with heavy transition metals using Xu's fluorescence sensor **99**. Reprinted with permission from ref. 152. Copyright (2010) Royal Society of Chemistry.

Our self-assembled system is based on amphiphilic C_{12}-I-Coum-TACN **54**, which contains terminal TACN receptors for zinc binding, that is linked to the coumarin fluorophore via an amide bond and a propyl chain (Figure 137). In basic conditions, the tertiary nitrogen on the TACN head group remains deprotonated, and the lone pairs of electrons is able to migrate to the coumarin fluorophore potentially by binding to the amide bridge or by direct binding with carbonyl group of the coumarin core. This PET process would result in fluorescence quenching. However, upon the addition of Zn^{2+}, complexation with TACN would occur very quickly due to its high binding affinity with Zn^{2+}. This would allow for reversal of the PET process and CHEF fluorescence enhancement.

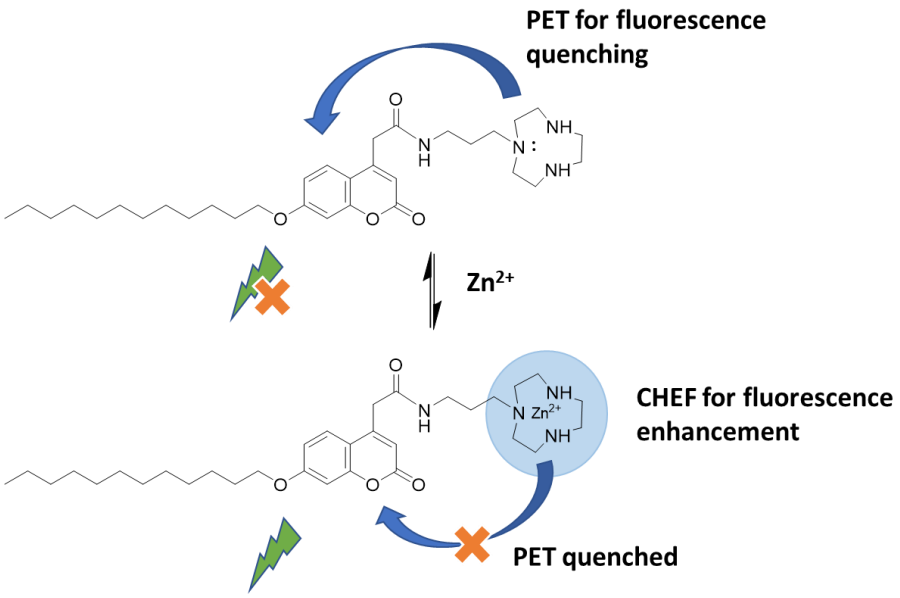

Figure 137. Schematic representation of the interplay between PET and CHEF effects on the fluorescence properties of the C_{12}-I-Coum-TACN amphiphile **54** upon addition of Zn^{2+}.

In order to investigate the viability of our system to act as a fluorescent sensor for metal ions, the fluorescence behaviour of C_{12}-I-Coum-TACN **54**, C_4-I-Coum-TACN **97** and C_0-I-Coum-TACN **96** was determined upon the addition of Zn^{2+} (Figure 138). Different slit widths were applied for clearer and more direct comparisons between the different samples. With 100 µM of the catalyst in 20% DMSO in water, five and three times fluorescence enhancement was observed upon the addition of 100 µM of Zn^{2+} to C_4-I-Coum-TACN **97** and C_{12}-I-Coum-TACN **54**, respectively. There was no significant fluorescence enhancement in the C_0-I-Coum-TACN **96** system due to the strong electron donating effect of the hydroxyl group attached to the coumarin ring. While some CHES enhancement was observed for these samples, the enhancement was not pronounced enough to be used as a sensor, and therefore we explored a range of different experimental conditions in order to find a greater difference between the 'on' and 'off' states.

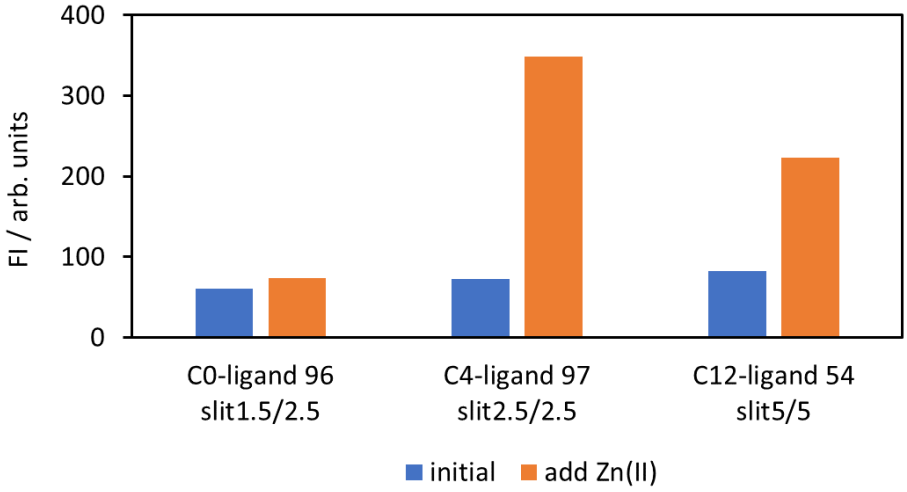

Figure 138. Fluorescence intensity of 100 μM of each of C_0-I-Coum-TACN **96** (λ_{ex} = 344 nm), C_4-I-Coum-TACN **97** (λ_{ex} = 327 nm) and C_{12}-I-Coum-TACN **54** ligand (λ_{ex} = 327 nm) (blue bar) and with the addition of 100 μM of Zn^{2+} (orange bars) in 20% DMSO in water and 1 mM of DIPEA at 25 °C.

Given the known solvatochromic properties of coumarin, we decided to screen a number of different solvent conditions as well as ligand concentrations. The solvent conditions examined were aqueous buffer solutions (either HEPES solution at pH 7.0 or CHES solution at pH 9.1) and a range of different 20% DMSO in water solutions, including samples where the water was buffered at different pH's. Each solvent condition was screened with three concentrations of C_{12}-I-Coum-TACN **54**·Zn^{2+} (50 μM, 100 μM and 250 μM) and these results are summarised in Figure 139. Some degree of CHEF enhancement was observed at all concentrations and all conditions except for 20% DMSO in water. Encouraging results were observed in water buffered at pH 7, where the solutions containing 50 μM and 100 μM C_{12}-I-Coum-TACN **54**·Zn^{2+} (**54**·Zn^{2+}) showed good response upon addition of Zn^{2+}. However, the most interesting result was for the 20% DMSO & DIPEA solutions, where relatively low fluorescence was observed when 50 μM or 100 μM C_{12}-I-Coum-TACN **54**·Zn^{2+} was used, but a dramatic enhancement was observed at 250 μM.

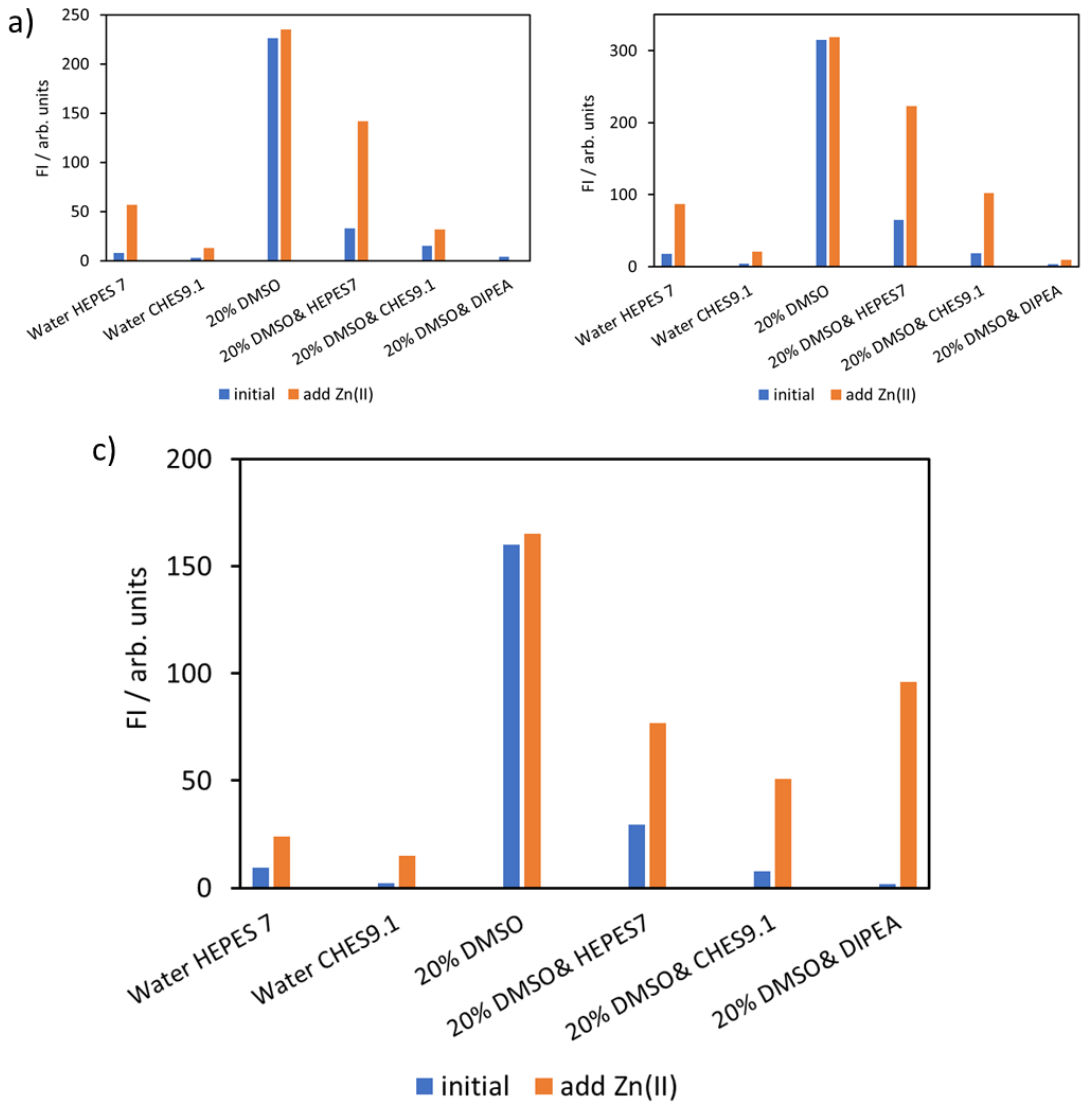

Figure 139. Fluorescence intensity of a) 50 μM, b) 100 μM and c) 250 μM of C_{12}-I-Coum-TACN **54** ligands (blue bar) and with the addition of the same equivalent of Zn^{2+} (orange bar) in different conditions, excited at 327 nm, slit 2.5/2.5 at 25 °C.

For clearer comparison of the CHEF enhancement of C_{12}-I-Coum-TACN·Zn^{2+} (**54**·Zn^{2+}) in each of the screened conditions, we extracted the relative CHEF ratio between the FI of **54**·Zn^{2+} in the presence of Zn^{2+} ions and their initial FI in the absence of Zn^{2+} ions (CHEF ratio = $FI_{addition\ of\ Zn}$/ $FI_{initial}$). These results are summarised in Figure 140, where moderate CHEF ratios can be seen with the majority of solutions, and sit in the region of a 1 to 7-fold increase. However, a 55-fold CHEF enhancement was observed with 250 μM of **54**·Zn^{2+} in 20% DMSO & DIPEA

(green dots). The fact that this degree of enhancement was only seen with the highest concentration of **54**·Zn^{2+} indicates that this fluorescence enhancement also benefited from the self-assembly of the C_{12}-I-Coum-TACN **54**·Zn^{2+} amphiphiles.

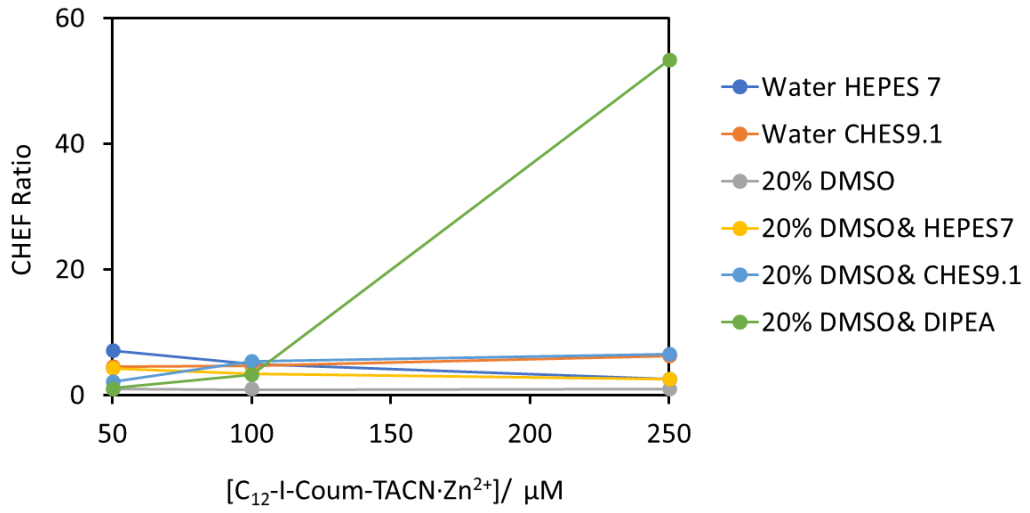

Figure 140. Fluorescence CHEF ratio of 50 µM, 100 µM and 250 µM of C_{12}-I-Coum-TACN·Zn^{2+} (**54**·Zn^{2+}) in a range of solvent conditions, excited at 327 nm, slit 2.5/2.5 at 25 °C.

To investigate how this potential sensor responds to different Zn^{2+} concentrations, the fluorescence response of C_{12}-I-Coum-TACN **54** (250 µM) was measured while titrating with increasing concentrations of Zn^{2+} in a 20% DMSO + DIPEA solution. Figure 141 shows a plot of the observed $FI_{327\ nm}$ against increasing concentrations of Zn^{2+}. At low concentrations of Zn^{2+}, there is no significant increase in the FI of C_{12}-I-Coum-TACN **54** until the [Zn^{2+}] reaches 125 µM. Strong fluorescence enhancement is observed from 200 µM, and this continues up to 300 µM, after which the FI begins to plateau. This behaviour may be rationalised by assuming that at low concentrations of Zn^{2+}, the interaction between the Zn^{2+} ions and TACN was not strong enough to overcome the PET effect. Some CHEF enhancement is observed from about 125 µM of Zn^{2+}, however, the CHEF effect is very small compared to the aggregation-induced fluorescence enhancement observed from 200 µM of Zn^{2+} onwards. Further increase of [Zn^{2+}] above 300 µM results only in smaller increases in FI as the TACN moieties become gradually saturated with Zn^{2+}. The point at which there is a sudden increase in FI matches the CAC data

and reinforces that fact that self-assembly plays an important role in fluorescence enhancement. The non-linear increase in fluorescence with respect to Zn^{2+} concentration suggests that this indicator would not be useful for the accurate quantification of Zn^{2+} in unknown solutions. However, the on/off behaviour of this ligand, and especially the lack of fluorescence at low concentrations of Zn^{2+}, suggests that this ligand could be useful for imaging applications involving Zn^{2+}, the second most abundant transition metal in biology that is involved in numerous biochemical processes, especially in the brain.[166]

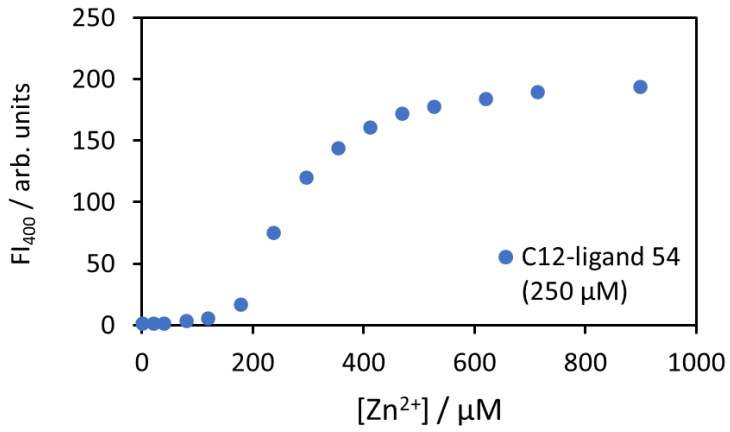

Figure 141. Fluorescence intensity of 250 µM of C_{12}-I-Coum-TACN **54** with increasing concentration of Zn^{2+} in 20% DMSO in water and 1 mM of DIPEA, excited at 327 nm, slit 2.5/2.5 at 25 °C

In contrast, C_4-I-Coum-TACN **97** did not show a sigmoidal pattern of FI increase with the addition of zinc ions (Figure 142). The FI began above zero, and increased with gradually increasing zinc concentration up to 250 µM, following which, a plateau was reached with further increase of Zn^{2+} ions. This plot clearly showed 1:1 binding between the TACN moiety of C_4-I-Coum-TACN **97** and Zn^{2+} ions. No fluorescence enhancement was observed for the other control molecule C_0-I-Coum-TACN **96**.

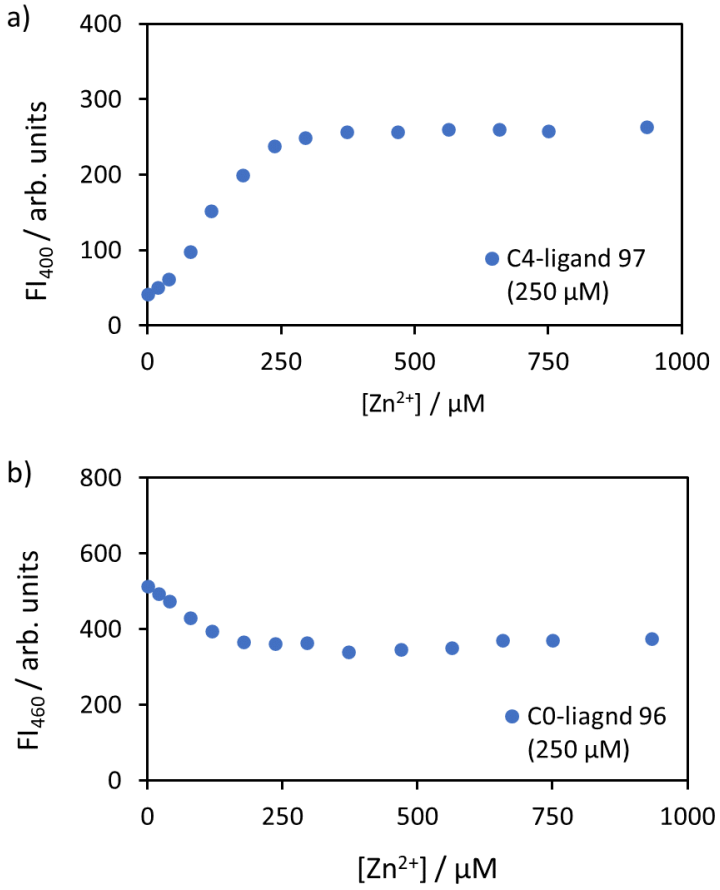

Figure 142. Fluorescence intensity of 250 µM of a) C_4-I-Coum-TACN **97** and b) C_0-I-Coum-TACN **96** with increasing concentration of Zn^{2+} ions in 20% DMSO in water and 1 mM of DIPEA, excited at 327 nm for C_4 ligand and 344 nm for C_0 ligand **96**, slit 2.5/2.5 at 25 °C

In the above studies, we investigated the ability of C_{12}-I-Coum-TACN **54** to act as a sensor for Zn^{2+} ions. However, indicators featuring cyclic polyamines, di-2-picolylamine (DPA), iminodiacetic acid, bipyridine, quinoline, and Schiff-bases have been well-studied in the literature, and often suffer from interference from heavy and transition metal ions such as Fe^{2+}, Co^{2+}, Ni^{2+}, Cu^{2+}, and Hg^{2+}.[152, 167] Consequently, it is important for us to also investigate the selectivity of C_{12}-I-Coum-TACN **54** fluorescence towards different metal ions. We therefore performed a comparative study using a series of 17 metal ions. These included eight main group metal ions (Li^{2+}, Mg^{2+}, Na^{+}, Cs^{2+}, Ba^{2+}, Al^{3+}, Pb^{2+} and Ca^{2+}) and nine transition metal ions (Ag^{2+}, Mn^{2+}, Fe^{2+}, Fe^{3+}, Co^{2+}, Ni^{2+}, Cu^{2+}, Zn^{2+} and Cd^{2+}), which are currently known or thought to

be required for normal biological functions in humans. From Figure 143, we can see that a significant increase in FI was observed in the presence of Zn^{2+}, Fe^{3+}, Al^{3+} and Pd^{2+}, and a weaker signal was observed for Fe^{2+}, Ni^{2+} and Cd^{2+}. The success of ion differentiation of C_{12}-I-Coum-TACN **54** is related to the strength of coordination between the TACN receptors and metal ions.[168]

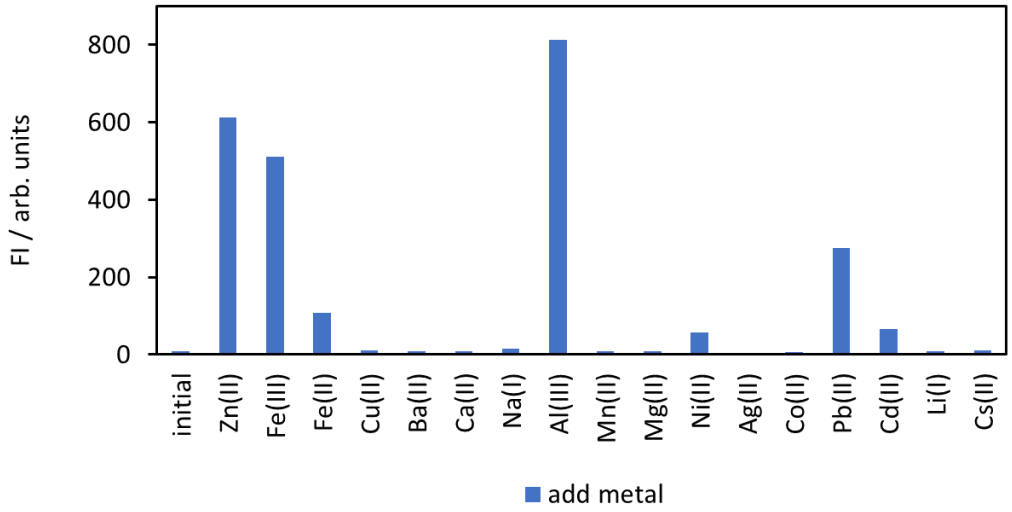

Figure 143. Fluorescence response of C_{12}-I-Coum-TACN to various metal ions in 20% DMSO in water. Experimental conditions: [C_{12}-I-Coum-TACN] = [metal ions] = 250 μM, [DIPEA] = 1 mM in 20% DMSO in water, excited at 327 nm, slit 2.5/5 at 25 °C.

Four of the most active metals (Zn^{2+}, Al^{2+}, Fe^{3+} and Pb^{2+}) and four non-active metals (Cu^{2+}, Ca^{2+}, Na^{+} and Mg^{2+}) were chosen to investigate their ability to elicit a response with our control ligands. C_4-I-Coum-TACN **97** responded similarly to the C_{12}-I-Coum-TACN **54** system, in that the strongest response was observed with Zn^{2+}, Al^{2+}, Fe^{3+} and Pb^{2+} and no increase in fluorescence was observed with Cu^{2+}, Ca^{2+}, Na^{+} and Mg^{2+}. However, due to the fact that there is significant starting fluorescence, it is clear that C_4-I-Coum-TACN **97** would not be an effective sensor for metal ions. For the C_0-I-Coum-TACN **96** system, there was no clear change in fluorescence with the majority of the metal salts examined. The clear differences observed with our C_{12}-I-Coum-TACN ligand **54** compared to these two control compounds demonstrates the importance of

self-assembly for the effectiveness of this potential metal-ion sensor.

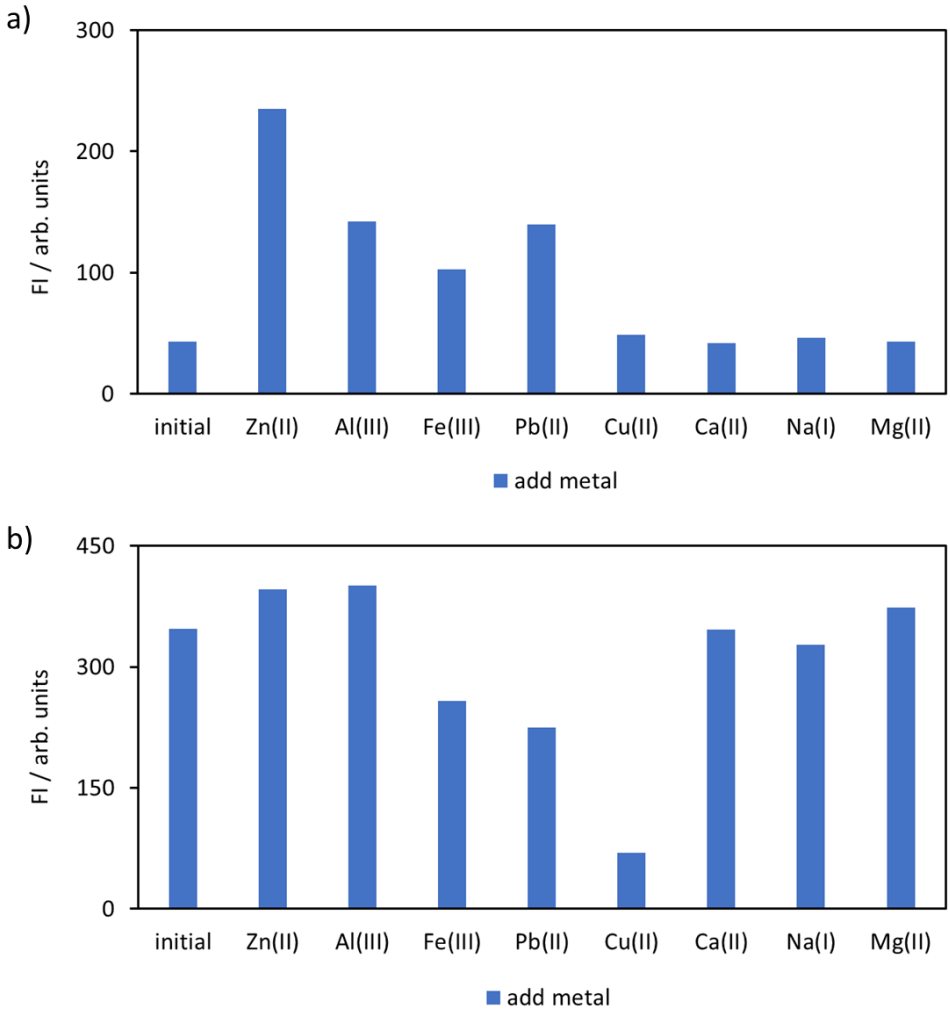

Figure 144. Fluorescence response of a) C_4-I-Coum-TACN **97** and b) C_0-I-Coum-TACN **96** to various metal ions in 20% DMSO in water and 1 mM of DIPEA. Experimental conditions: [C_x-I-Coum-TACN] = [metal ions] = 250 µM, [DIPEA] = 1 mM in 20% DMSO in water, excited at 327 nm for C_4 ligand **97** or 344 nm for C_0 ligand **96**, slit 2.5/2.5 at 25 °C.

3.5.7 Exploiting AIE activation to obtain a dialkylphosphate sensor

We next examined the potential for C_{12}-I-Coum-TACN **54** to be used as a sensor for phosphates. We had observed a considerable increase in fluorescence upon the addition of dimethyl

phosphate to a solution of 100 μM of C_{12}-I-Coum-TACN·Zn^{2+} (**54**·Zn^{2+}) in DMSO/water (Figure 117). These properties were observed only when this ligand possessed a long hydrophobic chain, suggesting that the ability for these amphiphiles to self-assemble had an important role to play in the fluorescence enhancement.

(Figure 117 was reprinted for clarity.)

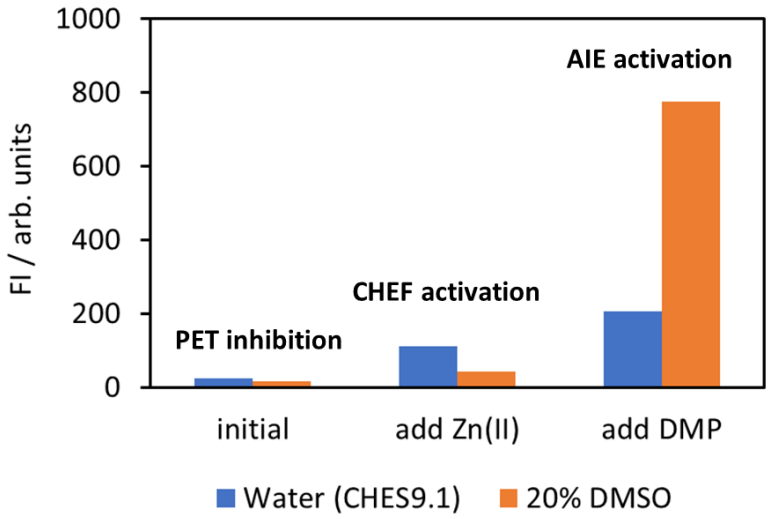

Figure 117. Fluorescence profile of 50 μM of C_{12}-I-Coum-TACN **54** (blue bars) excited at 325 nm, slit 2.5/5, following the addition of 50 μM of Zn^{2+} and 500 μM of DMP in CHES buffer solution (5 mM, pH 9.1). And fluorescence profile of 100 μM of C_{12}-I-Coum-TACN **54** (orange bars) excited at 325 nm, slit 2.5/5, following the addition of 100 μM of Zn^{2+} and 500 μM of DMP in 20% DMSO in water and 1 mM of DIPEA.

Based on observations from our previous studies, we hypothesise that the addition of phosphates induces the self-assembly of **54**·Zn^{2+} due to the formation of ion-ion interactions that neutralise the cationic headgroups of **54**·Zn^{2+}, resulting in a reduction in CAC and inducing the formation of supramolecular aggregates such as vesicles. The substrate-induced formation of self-assembled systems was reported recently by our research group[89] and discussed in Chapter 1.3.1. We hypothesise that these self-assembled structures produced fluorescence enhancement that can be referred to as aggregation induced enhancement (AIE, Figure 145).

In this section, I will focus on a systematic investigation of the AIE effect.

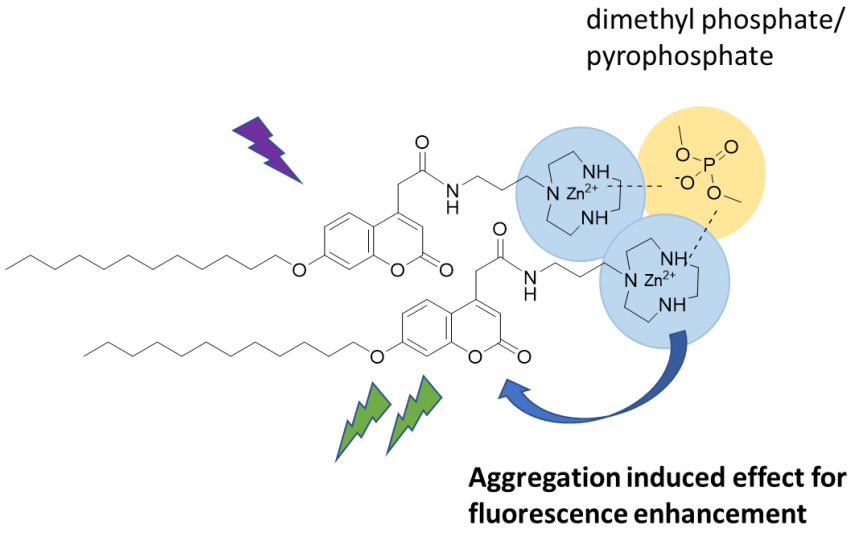

Figure 145. Schematic representation of AIE with **54**·Zn^{2+} in the presence of dimethylphosphate

Literature showing aggregation-induced fluorescence changes can be broadly classified into two types: aggregation caused quenching (ACQ) and aggregation induced emission (AIE). ACQ fluorophores are only emissive in dilute solutions and non-emissive in concentrated solutions or the solid state. One well-known example is perylene, shown in Figure 146. The planar structure of perylene favours aggregation through π-π stacking at high concentrations or in the solid state, leading to fluorescence quenching via non-radiative decay.[169]

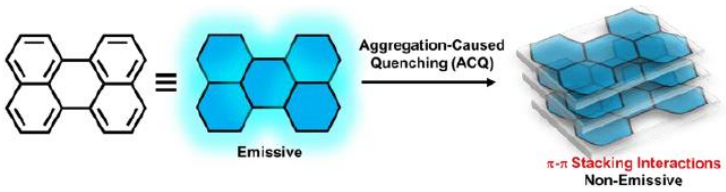

Figure 146. Schematic illustration of aggregation caused quenching (ACQ) in perylene. Adapted with permission from ref. 169. Copyright (2019) MDPI.

Then in 2001, a new phenomenon termed the AIE effect was described by Tang and co-workers

which showed fluorescence properties that were opposite to ACQ.[170-173] The fluorophores were not fluorescent in dilute solution but became brightly emissive in the aggregated and solid states where there was restriction of intramolecular motion. For example, the propeller-like tetraphenylethene (**TPE**) consists of four phenyl groups linked to a central ethene rod through single bonds. The free rotation of the four phenyl rings allows for non-radiative decay of the excited states, resulting in the absence of fluorescence when TPE is excited in a dilute solution. However, intramolecular rotation is restricted when TPE aggregates in viscous solutions, resulting in suppression of the non-radiative transitions and the observation of fluorescence. Similarly, in 10,10′,11,11′-tetrahydro-5,5′-bidibenzo[*a,d*][7]annulenylidene (**THBA**), two non-coplanar scallop shape sections of the molecule are in an anti-conformation. Under dilute conditions, the two phenyl rings on each side of the molecule dynamically bend and vibrate to give a relaxation pathway for non-radiative decay, while under concentrated conditions, the restriction of intramolecular vibration allows AIE of fluorescence.

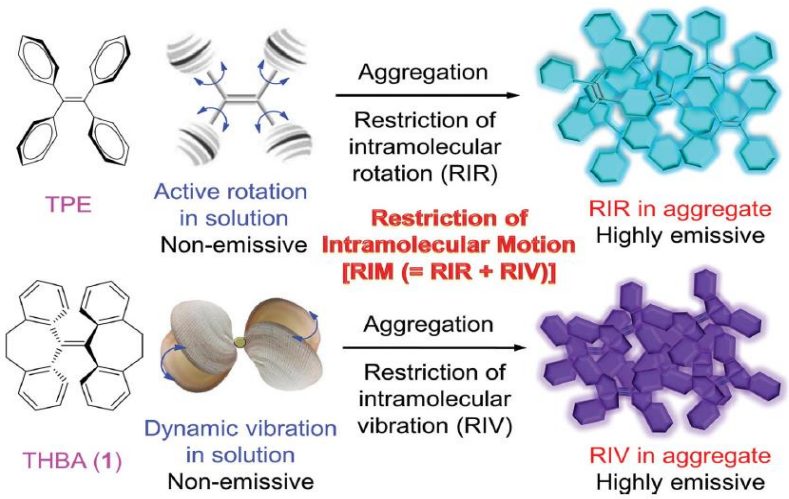

Figure 147. Schematic illustration of aggregation induced emission (AIE) due to restriction of intramolecular motion. Reprinted with permission from ref. 173. Copyright (2014) Wiley-VCH GmbH, Weinheim.

The amphiphile C_{12}-I-Coum-TACN **54** does not have a rotatable functional group to trigger the typical AIE mechanisms mentioned above, which occur via the restriction of motion. However,

we clearly see an increase in fluorescence emission upon the formation of aggregates, and this effect is not observed when using the control molecule C_4-I-Coum-TACN, which differs only in the length of the hydrophobic chain on the molecule. We therefore have two suggested explanations for the AIE observed for C_{12}-I-Coum-TACN **54**, with one hypothesis being that aggregation causes changes in the polarity of the local environment surrounding the coumarin fluorophore, which is known to be highly solvatochromic. In this scenario, the formation of self-assembled structures buries the coumarin moiety deep inside the hydrophobic bilayer, which makes the environment much less polar.

An alternative hypothesis is the presence of through-space conjugation effects, which was described recently as a new mechanism by which fluorescence can be activated.[174] Sturala reported the intramolecular and intermolecular through-space effect can descride the unusual AIE appearance reasonably.[175] Figure 148a demonstrates that as the water content in DMF increases, so does the luminescence intensity and wavelength of syn-heptaphenylcycloheptatriene (Ph_7C_7H). In nanoaggregates of Ph_7C_7H in 70 %-90 % H_2O in DMF, the parallel stacking of the benzene rings from two molecules causes the delocalization of the electron cloud, leading to a through-space conjugation effect. In an intramolecular fashion, the face-to-face contact between phenyl rings in Ph_7C_7H (Figure 148b) also allow the through space π system to interact, leading to a relaxed exciton and a red-shifted emission.

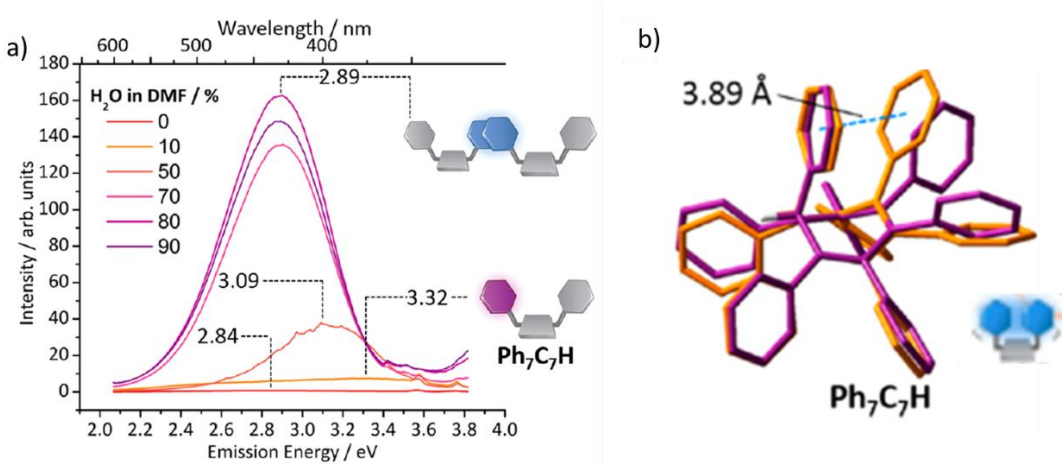

Figure 148. a) Steady-state photoluminescence spectra of Ph_7C_7H suspensions in difference proportion of H_2O in DMF and b) DFT minimum energy geometries calculated for the S_0 (purple) and S_1 (orange) of Ph_7C_7H. Adapted with permission from ref. 175. Copyright (2017) American Chemical Society.

To confirm that the observed fluorescence enhancement was due to the self-assembling properties of C_{12}-I-Coum-TACN **54**, the fluorescence emission of C_{12}-I-Coum-TACN **54** at four different concentrations (50 μM, 100 μM, 150 μM or 250 μM), both below and above the CAC, were measured. From Figure 149, we can see that the fluorescence intensity of 50 μM of C_{12}-I-Coum-TACN **54** is very low and increases slightly following both the addition of Zn^{2+} (50 μM) and the addition of DMP (500 μM). Overall, the FI is still very low due to negligible AIE. With 100 μM of C_{12}-I-Coum-TACN **54**, the FI increased by 3 times following the addition of Zn^{2+} (100 μM) because of the CHEF effect, while a massive FI increase was observed after the addition of DMP (500 μM), which was able to effectively induce the formation of supramolecular aggregates. The formation of self-assembled structures at 100 μM of **54**·Zn^{2+} in the presence of 500 μM of DMP was confirmed by CAC fluorescence titrations (Figure 130a) as described in Chapter 3.5.4. This same pattern of fluorescence increases was observed with 150 μM of **54**·Zn^{2+} in the presence of 500 μM of DMP. Interestingly, at 250 μM of C_{12}-I-Coum-TACN **54**, a large FI jump could be observed following the addition of only Zn^{2+} (250 μM). The low FI at 250 μM of C_{12}-I-Coum-TACN **54** was due to PET inhibition in the absence of Zn^{2+}, and no self-assembly of C_{12}-I-Coum-TACN **54** as it was at a concentration lower than its CAC (~260 μM, see Figure 128). With the addition of Zn^{2+} (250 μM), the CAC was reached as Zn^{2+} facilitates

coordination and decreases the CAC. This is confirmed by CAC fluorescence titrations (see Figure 129). Therefore, the significant FI enhancement (orange bar, Figure 149a) was due to both the CHEF effect and the AIE effect, as self-assembly also occurs at these concentrations. Subsequently, a second FI increase following the addition of DMP occurs, which can likely be attributed to tighter binding between the **54**·Zn^{2+} amphiphiles due to coordination to DMP.

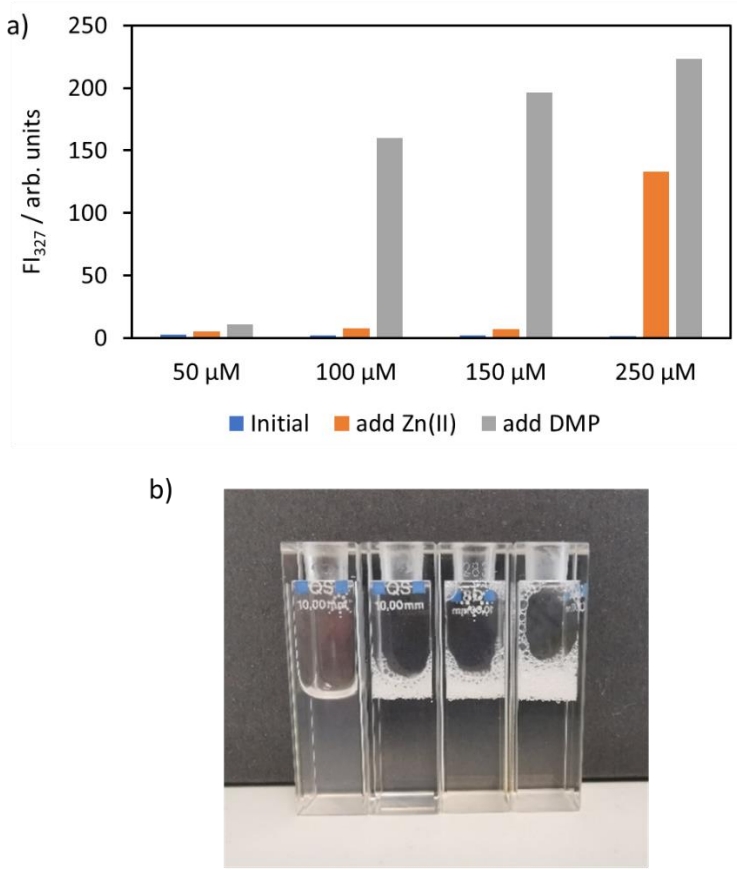

Figure 149. a) Fluorescence profile of different concentrations of C_{12}-I-Coum-TACN·Zn^{2+} in the presence of 500 µM of DMP; b) Amphiphilic solution of C_{12}-I-Coum-TACN·Zn^{2+} at 50 µM, 100 µM, 150 µM and 250 µM in the presence of 500 µM of DMP in quartz cuvettes. Experimental condition: [C_{12}-I-Coum-TACN **54**] = [Zn^{2+}] = 50 µM, 100 µM, 150 µM or 250 µM, [DMP] = 500 µM, [DIPEA] = 1 mM in 20% DMSO in water, slit 2.5/2.5, excited at 327 nm, 25 °C.

To better understand the interactions between C_X-I-Coum-TACN·Zn^{2+} and DMP in the self-assembled system, the FI of 100 µM of C_X-I-Coum-TACN·Zn^{2+} was measured in the presence of

increasing concentration of DMP. As shown in Figure 150, a sigmoidal curve was observed where the initial FI of C_{12}-I-Coum-TACN·Zn^{2+} (**54**·Zn^{2+}) barely increased with the addition of DMP up until 200 µM. Upon further addition of DMP, the FI of C_{12}-I-Coum-TACN·Zn^{2+} significantly increased up to 300 a.u., and reached a plateau following the addition of roughly 500 µM of DMP. This could be because no self-assembled structures are formed at low concentrations, but self-organisation of **54**·Zn^{2+} occurs after the addition of 200 µM of DMP, resulting in aggregation induced emission. Upon addition of increasing amounts of DMP, the FI initially increases, likely due to the formation of more supramolecular structures, and then plateaus, likely because there are no more **54**·Zn^{2+} amphiphiles to be recruited into the assembly. Importantly, there are no significant changes in FI when using the two control molecules C_4-I-Coum-TACN·Zn^{2+} (**97**·Zn^{2+}) and C_0-I-Coum-TACN·Zn^{2+} (**96**·Zn^{2+}) following addition of 15 equivalents of DMP, which suggested that no self-assembled structures formed at the concentrations that were studied. These experiments demonstrated the importance of the long hydrophobic chain in the amphiphile, and the importance of self-assembly for the observed increase in fluorescence emission.

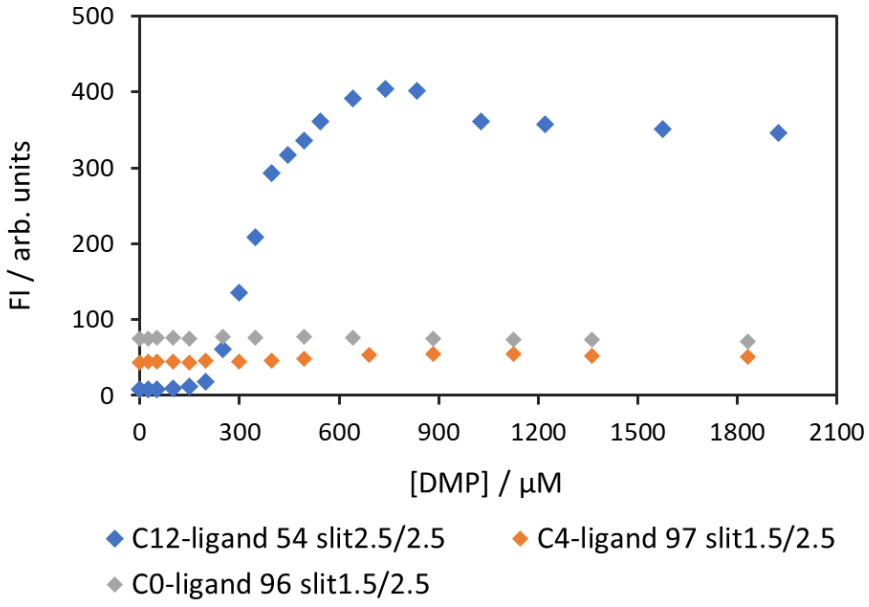

Figure 150. Fluorescence emission profile of 100 µM of C_X-I-Coum-TACN amphiphile (n = 0, 4, 12) at increasing concentrations of DMP in the presence of 100 µM of Zn^{2+} in 20% DMSO/water and 1 mM of DIPEA at 25 °C.

A subsequent titration was performed in the presence of 500 μM of DMP and the addition of increasing amounts of C_{12}-I-Coum-TACN **54**, in the presence and absence of Zn^{2+}. Figure 151 shows a steady increase in FI as the concentration of C_{12}-I-Coum-TACN **54** is increased, due to the organisation of C_{12}-I-Coum-TACN **54** assisted by the DMP in the system. In the presence of Zn^{2+}, The maximum FI was reached following the addition of around 80 μM of C_{12}-I-Coum-TACN **54**, after which the fluorescence intensity decreases due likely to concentration-related quenching effects. This peak in FI roughly matched the CAC value (~100 μM) under such conditions. On the other hand, the FI of C_{12}-I-Coum-TACN **54** in the absence of Zn^{2+} peaked at a higher concentration of **54** (~180 μM). This suggested that the CAC for C_{12}-I-Coum-TACN **54** is higher in the absence of Zn^{2+}, and this is likely due to the much weaker binding between the C_{12}-I-Coum-TACN **54** amphiphiles and DMP substrates without the assistance of Zn^{2+}, which is known to bind strongly to both TACN and phosphates, and has been previously shown to facilitate the self-assembly of similar amphiphiles.

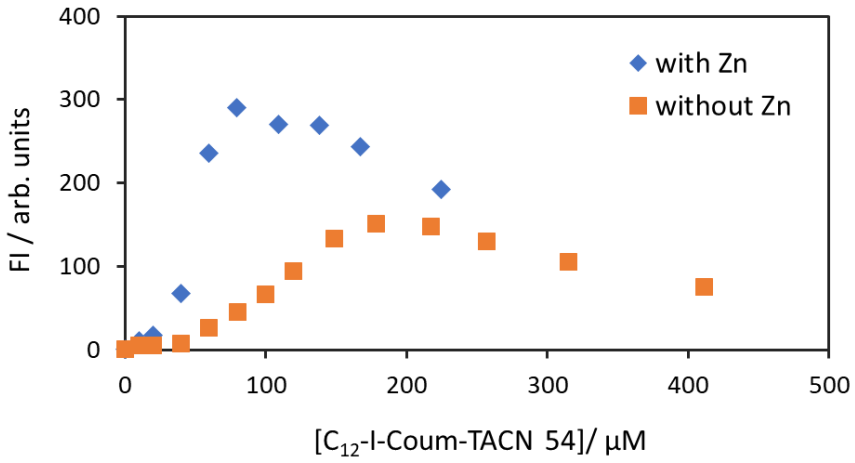

Figure 151. Fluorescence emission profile of C_{12}-I-Coum-TACN **54** amphiphiles in the presence of 500 μM of dimethyl phosphate in 20% DMSO in water mixture, [C_{12}-I-Coum-TACN] = [Zn^{2+}], [DIPEA] = 1 mM, slit 2.5/2.5 at 25 °C.

To investigate the possibility of using C_{12}-I-Coum-TACN·Zn^{2+} **54** as a phosphate sensor, we studied the responsiveness of this system to pyrophosphate (PPi). PPi is the simplest inorganic

diphosphate and has very high charge density. Several supramolecular sensors have been developed that are selective for binding to PPi, including important studies by Jolliffe et al.[176-179] The changes in FI of 100 μM of C_{12}-I-Coum-TACN **54** was measured after the sequential addition of 100 μM of Zn^{2+} and 500 μM of PPi. Compared to Figure 122 (with DMP as the substrate), similar results were obtained, in terms of the CHEF effect following the addition of Zn^{2+}, and another jump in FI following the addition of PPi, which we attribute to an AIE effect. However, this effect is much weaker with PPi as the substrate, with the observed FI being around 5 times less than what was observed with DMP. With the control molecule C_0-I-Coum-TACN **96**, no CHEF effect nor AIE effect was observed, while with C_4-I-Coum-TACN **97**, a moderate CHEF effect was observed, but no AIE effect. These controls reaffirm the importance of long hydrophobic chain on the amphiphilic molecule.

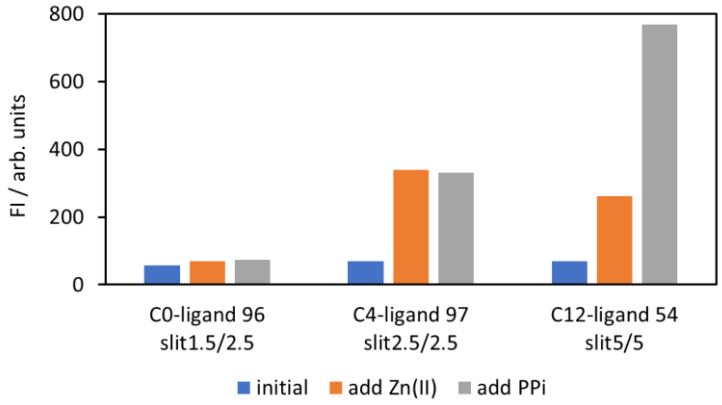

Figure 152. The fluorescence intensity of 100 μM of each of C_0-I-Coum-TACN **96**, C_4-I-Coum-TACN **97** and C_{12}-I-Coum-TACN ligand **54** (blue bars), with the addition of 100 μM of Zn^{2+} (orange bars) and 500 μM of PPi substrates (grey bars) in 20% DMSO in water.

These experiments were also performed using a different order for the addition of PPi and Zn^{2+}. In the presence of only C_x-I-Coum-TACN and PPi, no increase in FI was observed, in line with what was observed in the presence of DMP. However, once Zn^{2+} was added, a significant increase in the FI was observed for both the C_4-I-Coum-TACN **97** and C_{12}-I-Coum-TACN **54** systems, with the latter showing more significant AIE activation.

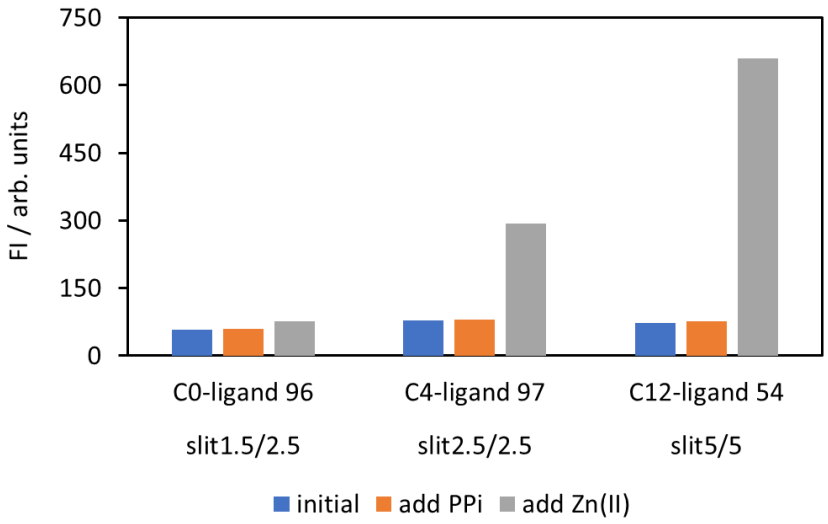

Figure 153. The fluorescence intensity of 100 μM of each of C_0-I-Coum-TACN **96**, C_4-I-Coum-TACN **97** and C_{12}-I-Coum-TACN ligand **54** (blue bars), with the addition of 500 μM of **PPi** (orange bars) and 100 μM of Zn^{2+} ions (grey bars) in 20% DMSO in water and 1 mM of DIPEA.

However, the fluorescence behaviour of C_{12}-I-Coum-TACN·Zn^{2+} (**54**·Zn^{2+}) in the presence of increasing concentrations of **PPi** was quite different compared to that with DMP. As shown in Figure 154, the FI of 100 μM of **54**·Zn^{2+} steadily increased upon the addition of **PPi** up to approximately 200 μM, after which it quickly plateaued. This behaviour is significantly different to the changes in FI that occurs with the addition of DMP (Figure 150). The addition of DMP does not induce a significant change in FI at low concentrations, but reaches much higher FI (up to 400 a.u.) under the same conditions. The change in fluorescence behaviour with PPi suggests that the addition of Zn is binding strongly to cause self-assembly, but upon binding of all the amphiphiles, this effect tails off, resulting in a plateauing of the FI. By plotting a line-of-best-fit for the first four data points and determining the intersection with the line-of-best-fit for the last 5 data points, we were able to determine that saturation of binding occurred at 250 μM of PPi, which suggested a binding ratio of 2:5 **54**·Zn^{2+} : PPi. Interestingly, no FI increase for C_{12}-I-Coum-TACN **54** was observed in the absence of Zn^{2+} ions even up to a concentration of PPi over 2000 μM. This reinforces our assumption that the Zn^{2+} ion is crucial for the self-assembly of this three-component system, by acting as an important link between the amphiphile and the PPi. Another important point to note is that no changes in the emission

profile was observed during the course of the titration, and no changes in the Vmax of the emission spectrum were observed.

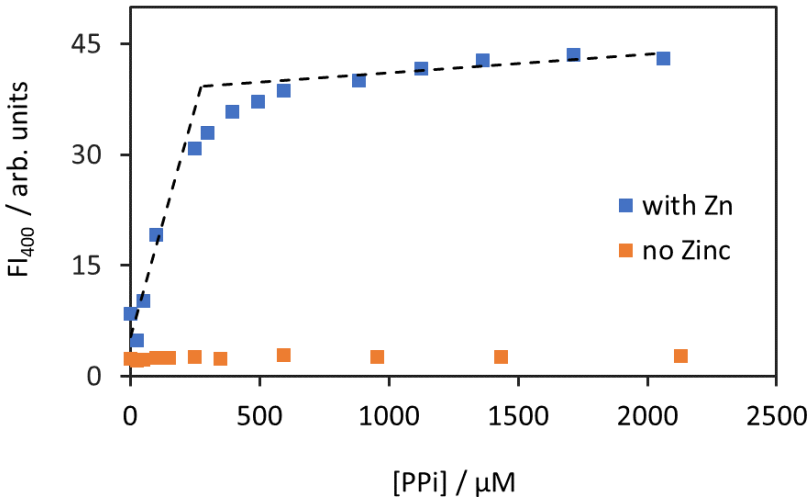

Figure 154. Fluorescence emission profile of 100 µM of C_{12}-I-Coum-TACN **54** amphiphile at increasing concentration of pyrophosphate in the a) presence of 100 µM of Zn^{2+} and b) absence of Zn^{2+} in 20% DMSO in water mixture, [C_{12}-I-Coum-TACN **54**] = 100 µM, [DIPEA] = 100 µM, slit 2.5/2.5 at 25 °C.

The fluorescence response of the **54**·Zn^{2+} system towards various phosphates was measured as shown in Figure 155. The **54**·Zn^{2+} system was found to respond most strongly to DMP, followed by PPi, with other phosphates such as ATP, ADP and AMP showing even weaker fluorescence. The response to citrate was also measured as citrate is known to be a strong chelator for Zn^{2+} ions. The fact that this **54**·Zn^{2+} system is selective for DMP is a unique discovery, as there are several reported supramolecular sensors that are selective for phosphates such as PPi[176-177, 179] and ATP[180-181], but we have not found any that are selective for DMP over PPi or ATP. This fills a research gap which we are keen to further explore in the near future.

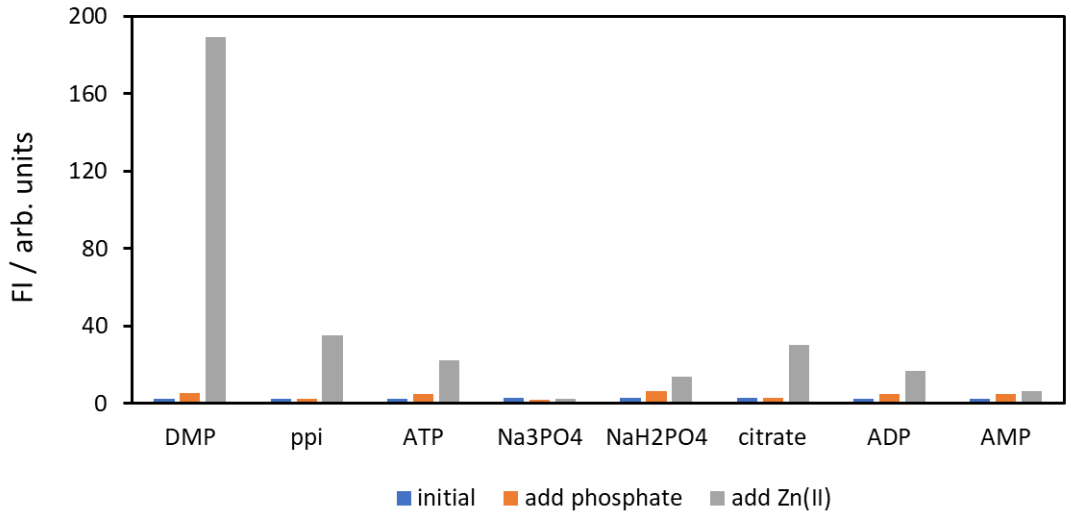

Figure 155. Fluorescence profile of 100 μM of **54**·Zn^{2+} in the presence of various of phosphates in 20% DMSO in water. [C_{12}-I-Coum-TACN **54**] = [Zn^{2+}] = 100 μM, [phosphate] = 500 μM, [DIPEA] = 1 mM, excited at 327 nm, slit 2.5/2.5 at 25 °C.

DMP is an important compound to detect because it is one of the degradation products of organophosphates, which are commonly used as herbicides, pesticides and chemical warfare agents.[182] The widespread overuse of organophosphates in agriculture has caused negative effects on animals and aquatic plants, with flow-on effects on humans due to consumption of contaminated food. This can cause severe adverse health effects, namely acute and neurodevelopmental toxicity.[182-183] It has become an important objective to identify and quantify organophosphates and their metabolites.[184-185] Although there are many commonly used organophosphates, approximately 75% of them can be metabolized and degraded into six dialkyl phosphates (DAPs) in vivo and in the environment. These include diethyl dithiophosphate (**DEDTP**), diethyl thiophosphate (**DETP**), diethyl phosphate (**DEP**), dimethyl dithiophosphate (**DMDTP**), dimethyl thiophosphate (**DMTP**) and dimethyl phosphate (DMP).[182-183, 185] The concentrations of DAPs in human urine are often used as biomarkers for exposure to organophosphates but the low concentration of urinary DAPs can hinder epidemiological studies. In the future, we aim to investigate the effectiveness of our fluorescence "turn-on" sensor **54**·Zn^{2+} for the detection of and differentiation of different DAPs,

as currently there is a lack of methods that are able to easily and specifically detect dialkyl phosphates.

3.6 Conclusions for the chapter

In summary, we have designed and synthesised two amphiphilic ligands, namely C_{12}-I-Coum-TACN **54** and C_{12}-I-Naph-Gua **55**. Both were designed to utilise hydrophobic interactions to induce the formation of supramolecular assemblies, with the initial goal being to induce FRET between the two amphiphiles and to use FRET to probe proximity, and to ultimately use these amphiphiles to investigate self-assembly processes. During these studies, we were able to observe evidence of FRET between these two amphiphiles, although the concentration of the coumarin-based amphiphile needed to be increased in order to observe significant FRET. At this point it was decided to pivot our studies and to examine in more detail on the unique fluorescent properties of C_{12}-I-Coum-TACN **54** (see below). A decision was made that in the future, we would design and synthesise new amphiphiles that will hopefully exhibit more efficient FRET (see future work, next chapter).

During the FRET investigations, we discovered that the C_{12}-I-Coum-TACN **54** amphiphile possessed some very unique fluorescence properties. Significant fluorescence enhancement was observed upon the addition of Zn^{2+} ions, when **54** was in 20% DMSO and DIPEA. This was attributed to a reduction in PET inhibition upon binding of the TACN moiety to Zn^{2+}, which can also be described as CHEF activation upon chelation of the metal ion. We explored the magnitude of CHEF activation with a range of different metal ions and found selectivity for Zn^{2+}, Fe^{3+}, Al^{3+} and Pb^{2+} over Fe^{2+}, Cu^{2+}, Ba^{2+}, Ca^{2+}, Mn^{2+}, Mg^{2+}, Ni^{2+}, Ag^{2+}, Co^{2+}, Cd^{2+}, Li^{2+}, Cs^{2+}. Further work needs to be performed to determine the potential for C_{12}-I-Coum-TACN **54** to be used as a fluorescence-ON cation sensor.

A much more pronounced fluorescence enhancement was observed upon the addition of dimethylphosphate (DMP) to C_{12}-I-Coum-TACN **54**·Zn^{2+}. Studies were performed to confirm the importance of having a long hydrophobic chain on the molecule, which supported the hypothesis that the fluorescence enhancement was due to the formation of supramolecular assemblies in solution. This represents a novel example of aggregation-induced emission (AIE), for which there are not a great number of examples in the literature. The AIE was most pronounced in the presence of DMP, which is unusual as we were not able to find examples of supramolecular sensors that could respond to DMP in preference to highly charged anions such as PPi and ATP. Further work needs to be performed to determine the usefulness of C_{12}-I-Coum-TACN **54**·Zn^{2+} as a sensor for dialkylphosphates, which are known biomarkers for herbicides and pesticides that have been metabolised in body. Suggestions for the next steps to take are described in chapter 5.

Chapter Four: Conclusions and Future Work

4.1 Self-selection of catalysts from a dynamic combinatory library

In the first section of this thesis, we described the formation of multifunctional catalysts formed by the self-assembly of C_{16}TACN **20**·Cu^{2+} and C_{16}Gua **23** amphiphiles into vesicular structures. Self-assembly brought the headgroups of these amphiphilic molecules together, which allowed the formation of cooperative catalytic pockets on the surface of the vesicles. This system benefited from the modularity of the self-assembled catalyst, which allowed one to easily screen different functional groups to investigate their catalytic activity, and to also modify the proportions of these pre-catalysts during catalyst optimisation. This opens up the potential to use this strategy for the screening of libraries amphiphilic molecules for the development of novel multifunctional catalysts.

As future work, we plan to synthesise a library of amphiphilic pre-catalysts that contain a range of different functional groups. For example, the different amphiphiles can contain functional groups that are commonly found in the active site of enzymes, such as histidines, guanidines, phenols, carboxylic acids, and metal-binding centres. These amphiphiles could then be mixed in different combinations and screened for catalytic activity for a number of different chemical reactions. A related and interesting example by Nothling *et al.* shows a bioinspired cosurfactant micellar system used to mimic the protease alpha-chymotrypsin, which contains a Ser-His-Asp catalytic triad for ester hydrolysis (Figure 156).[39] They combined the hydroxyl, imidazole and carboxylate functionalities of the catalytic triad into the head group of an amphiphile and co-assembled it with an amphiphile containing a C16 chain and a guanidinium polar head. The guanidnium functional group acted as an oxyanion hole for transition-state stabilization, and this combination of intramolecular and intermolecular cooperativity resulted in a dramatic rate enhancement in ester hydrolysis.

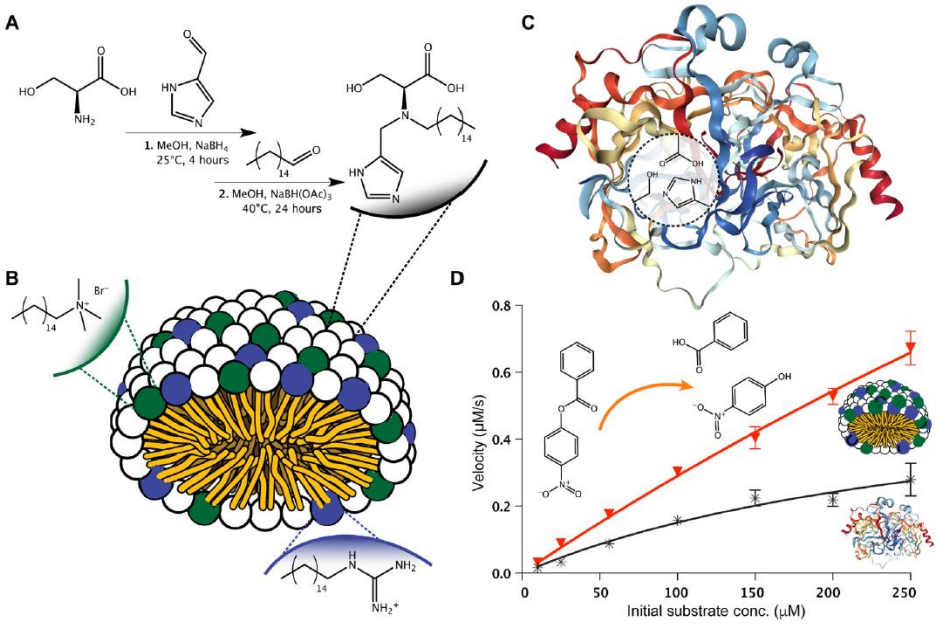

Figure 156. A hydrolase-inspired cosurfactant catalyst system. Reprinted with permission from ref. 39. Copyright (2020) American Association for the Advancement of Science.

Another concept that we would like to explore in the future is the self-selection of the catalyst system from a library of amphiphilic molecules. The amphiphiles containing a range of different functional head groups can be considered a dynamic combinatorial library (DCL), where there each of the amphiphiles represent building blocks that are able to self-assemble via reversible intermolecular interactions driven by the hydrophobic effect.

Our aim would be to investigate whether the addition of transition state analogues (TSA) would be able to affect the specific amphiphiles to self-assemble in preference to other amphiphiles. Our hypothesis is that two amphiphiles which bind best to the transition state analogues would in effect form an amphiphiles with two tails, which would have a higher propensity to aggregate than an amphiphile with a single hydrophobic tail. Separation of the assembled aggregates and analysis of their composition would then allow for rapid determination of the best combination of amphiphiles for a specific catalyst.

Wulff and co-workers have demonstrated that imprinted polymers can be formed using TSA

by the templated assembly of monomers and the cross-linking of the monomers to form highly specific catalytic cavities (Figure 157).[186] Following removal of the TSA, a polymeric pocket is formed that is a perfect fit for the substrate of the reaction.

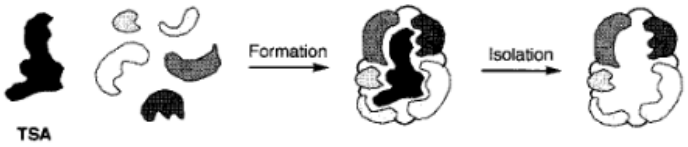

Figure 157. A general representation for generating receptors or catalytic cavities capable of recognition and catalysis. Reprinted with permission from ref. 186. Copyright (1997) Wiley-VCH GmbH, Weinheim.

Otto and co-workers reported a dynamic combinatorial library of interconverting building blocks where the most effective catalyst was selected by exposure to a transition state analogue (Figure 158).[187] Their DCL was formed from three dithiol building blocks **100**, **101** and **102**, which can form a variety of macrocycles through interconverting dithiol bonds. They investigated the ability of the system to catalyse the Diels-Alder reaction and the product **103** was used as the TSA due to its high similarity to the transition state of the reaction. The addition of **103** was shown to result in a shift of the equilibrium in favour of the formation of the macrocycles **104** and **105**, which made up 79% of the DCL. Interestingly, the two macrocycles would only constitute 12% of the DCL in the absence of the TSA. The two macrocycles **104** and **105** were then individually synthesised to investigate their catalytic properties. The macrocycle **104** was shown to exhibit stronger binding to the starting material **103** rather than the product, and was therefore found to be catalytically inactive. On the other hand, macrocycle **105** was found to successfully catalyse the targeted reaction. This demonstration of the use of a TSA to aid in the selection of the best catalyst system from a DCL is what inspires us to attempt a similar idea using the self-assembly of our amphiphilic pre-catalysts.

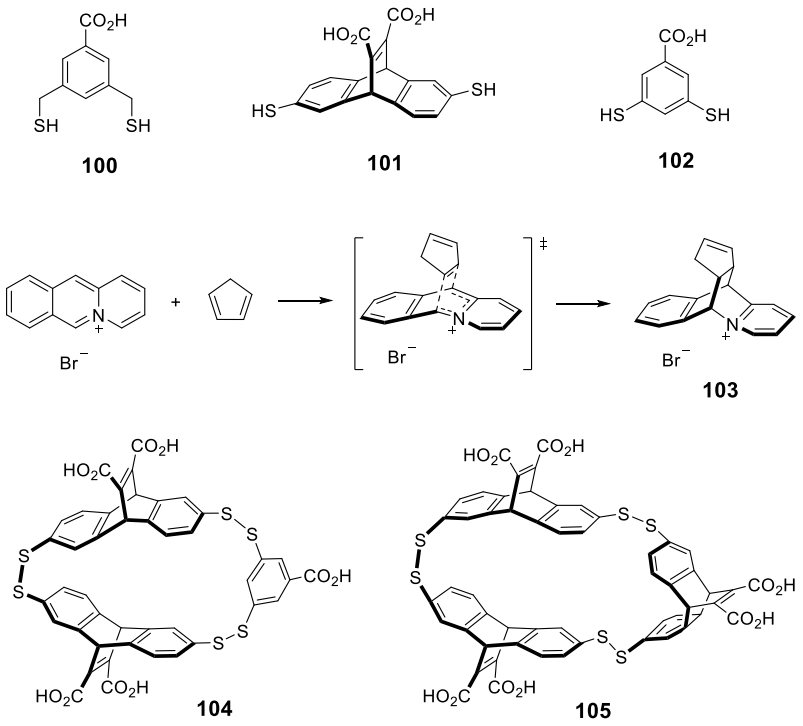

Figure 158. The chemical structures of the dithiol precursors **100**, **101** and **102** used for the DCL. The Diels-Alder reaction of interest, and product **103**, which was used as the TSA for the selection of macrocycles **104** and **105** from the DCL. Adapted with permission from ref. 187. Copyright (2003) Wiley-VCH GmbH, Weinheim.

In our vesicular system, the overall hypothesis is summarised in Figure 159. We will use our preliminary studies in the TACN and guanidinium vesicular system as a foundation and combine with other amphiphiles to form a DCL. We will work at a concentration where the DCL of the catalyst precursors would not self-assemble (in the absence of a TSA), working below the CAC. With the addition of the TSA, the amphiphiles that have the strongest binding affinity with the TSA will be selected from DCL. The TSA-amphiphile(s) complex would have greater propensity to self-assemble into organised aggregates due to stronger hydrophobic interactions, compared to those free amphiphilic monomers who do not bind to the TSA. If we can separate the self-assembled structures from the free catalyst precursors, we will be able to know which functional groups are required for catalysis and also the ratio at which they are required. This selection approach cuts down the cost and time required for screening and it provide us with a quick method to obtain the lead structures for further optimisation. In future

work, we will need to investigate the design and synthesis of the TSA and the separation of self-assembled structures from the catalyst library, which are all challenges that needs to be overcome.

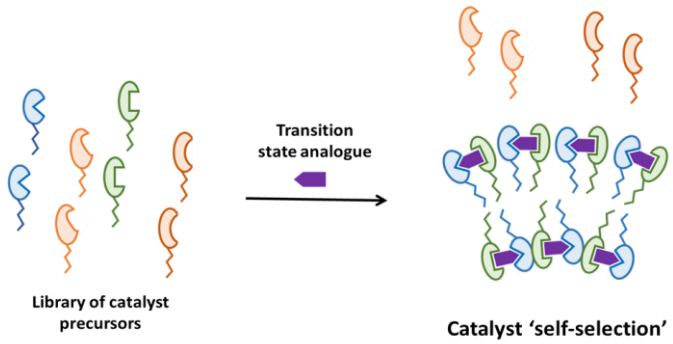

Figure 159. Representation of the self-selection of catalysts from a DCL upon addition of a TSA

4.2 A method to probe the self-selection of catalysts

With regards to the self-selection of amphiphiles from a library of compounds, the identification of the amphiphiles that are 'selected' from the pre-catalyst library will be a key challenge to overcome. In Chapter Three, we introduced the idea of using FRET to probe the assembly and proximity of amphiphilic molecules within supramolecular assemblies. FRET is highly dependent on the distance between two fluorophores and their spectral overlap. Any red or blue shifts in the absorption spectrum of the fluorophore acceptors could affect FRET intensity, as well any changes in the distance between the fluorophore pairs (Figure 160).[132] In the future, one objective would be to design new amphiphiles that are optimised for FRET, to be used for probing the assembly of the amphiphiles.

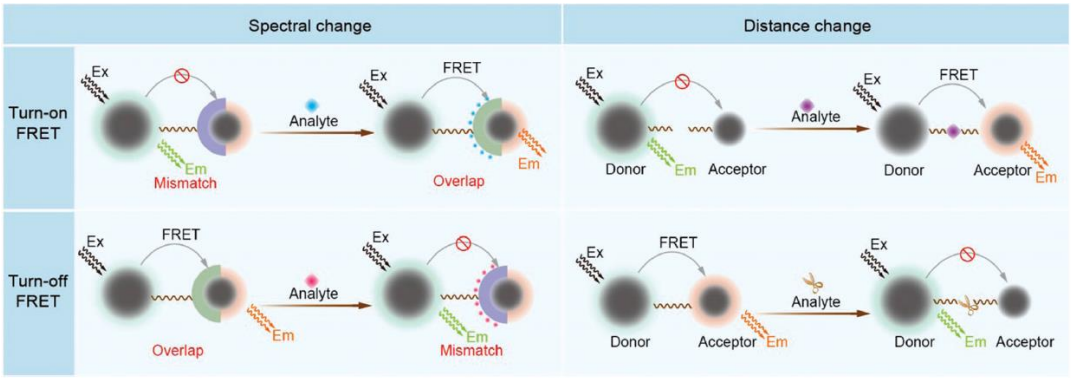

Figure 160. Graphical representation of how FRET is affected by spectral changes and distance changes. Reprinted with permission from ref. 132. Copyright (2018) Royal Society of Chemistry.

We plan to design and synthesise Y-shaped fluorescent amphiphiles where one arm of the "Y" will contain the catalytic moiety while the other arm of the "Y" will contain the fluorophore (Figure 161, bottom). The fluorophore will no longer be embedded into the hydrophobic chain of the amphiphile and will now have the possibility to move into more polar or non-polar regions and exhibit solvatochromic effects that provide information on its surrounding environment. These Y-shaped molecules were chosen also because the majority of examples of successful FRET between amphiphiles that we have found in the literature have had the fluorophore at the end of the amphiphile, rather than being embedded within the core of the amphiphile.[135, 188]

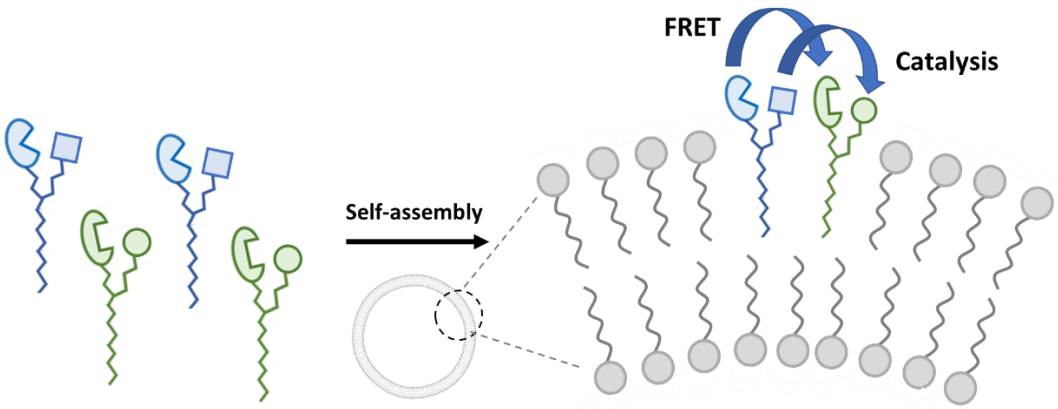

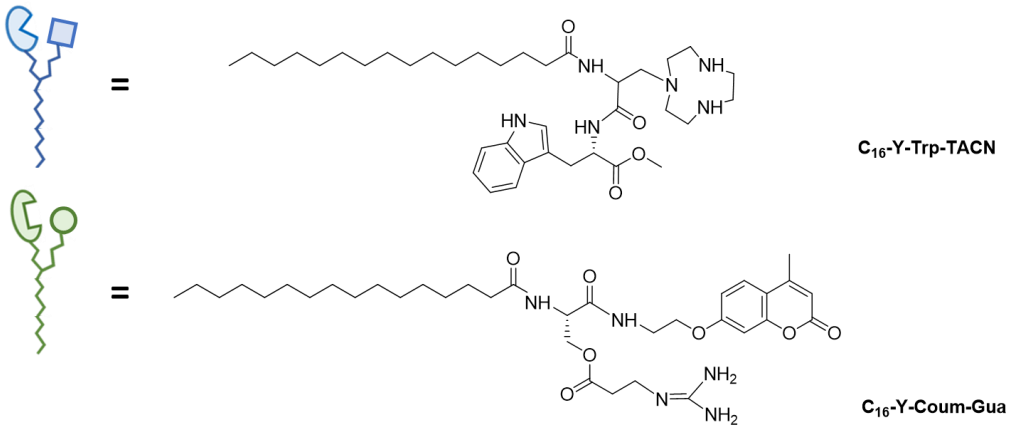

Figure 161. a) Graphical representation of FRET between two Y-shaped amphiphilic molecules. b) Chemical structure of C_{16}-Y-Trp-TACN **56** and C_{16}-Y-Coum-Gua **57**.

4.3 Sensing arrays for phosphate recognition

In this thesis, we have shown that our C_{12}-I-Coum-TACN **54**·Zn^{2+} amphiphile acts as a fluorescence-ON sensor with high selectivity to DMP. This system also responded moderately to other phosphates and the metal-free amphiphile C_{12}-I-Coum-TACN also possessed a fluorescence-ON effect with different metal ions. In the future, we aim to investigate the utility of these systems for the non-selective but differential sensing of metal ions and phosphates using a pattern-based approach for sensing.

In the past decade, numerous research groups have shifted their attention from studying selective receptors towards pattern-based analysis using an array of sensors.[189-190] This mimics the function of mammalian noses and tongues for sensing chemical analytes. The specificity of pattern-based analysis is not obtained from a specific signal from a single receptor but from the recognition of a response pattern generated by a large number of sensor units.[191] A large number of sensor components with varying degrees of interaction combine to generate a pattern distinct to a particular analyte. Such pattern recognition approaches may be powerful enough to match the capabilities of analyte-specific sensors, which are difficult to produce. An individual sensor can also be subjected to pattern-based analysis if the different analytes

produce a distinct spectral pattern.[192] In contrast to the many measurements necessary for analyte-specific sensors, pattern-based sensing generally produces a single spectrum as the data for further analysis (Figure 162).

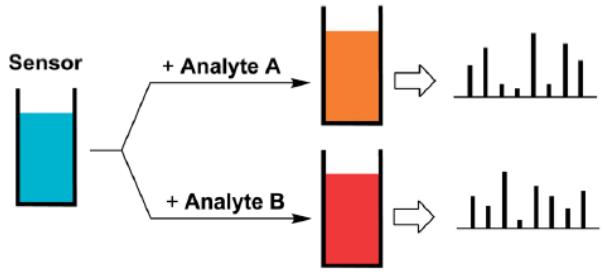

Figure 162. Schematic illustration of a pattern-based approach to sensing. Reprinted with permission from ref. 192. Copyright (2014) Royal Society of Chemistry.

A colorimetric sensing array was reported by Katrina Jolliffe and co-workers for the determination of mono-, di- and tri-phosphates.[193] The array elements contained the novel bis[Zn(II)DPA] cyclic peptide **106** and an equimolar amount of one of six colorimetric fluorescence indicators, namely pyrocatechol violet (PV), pyrogallol red (PGR), chromeazurol S (CAS), eriochrome cyanine R (ECR), bromopyrogallol red (BPG), and xylenol orange (XO). The addition of phosphates having different binding affinities to the ligands displaced the fluorescence indicators to different extents so that their fingerprint fluorescence responses could be used through both principal component analysis (PCA) and linear discriminant analysis (LDA) to discriminate different phosphates as either mono-, di-, tri- or pyro-phosphate (PPi). The classification of phosphates was also been reported utilising the sensing arrays of supramolecular structures,[194] quantum dots,[195] and MOFs.[196] In these examples, the PCA and LDA methods were used to analyse the fingerprint responses in a statistical way to allow for recognition of the analytes.

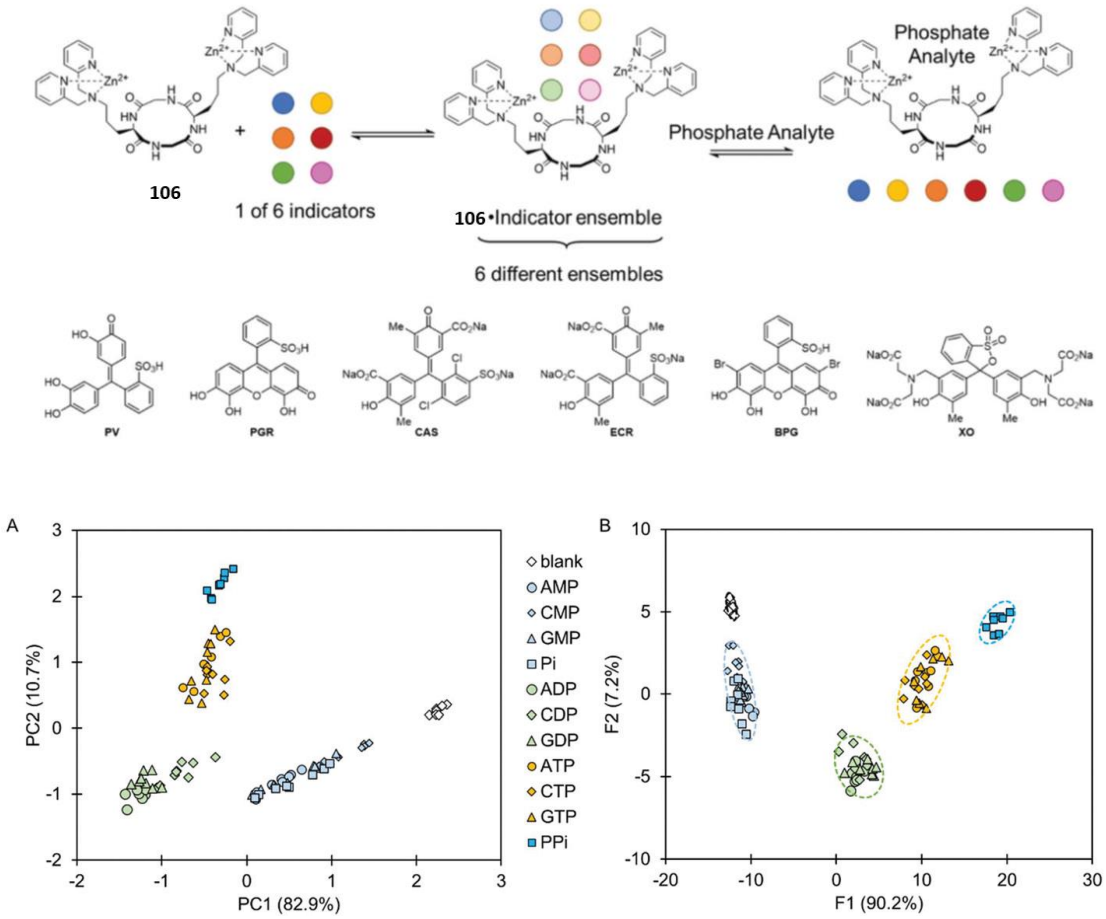

Figure 163. a) Schematic representation of the indicator displacement assay-based array and the chemical structures of the indicators; b) Two dimensional PCA plot and LDA score plot generated from the colorimetric array data. Reprinted with permission from ref. 193. Copyright (2021) Royal Society of Chemistry.

Pattern-based recognition of nucleotides has been reported by Pezzato and co-workers who utilised the functionalized gold nanoparticles **Au MPC·M^{2+}**.[197] These gold nanoparticles were covered with a positively charged monolayer containing TACN·M^{2+}, which could bind with small anionic molecules, for example, peptides and nucleotides. In the system, three fluorescent indicators were used to not only bind with **Au MPC·M^{2+}** with different binding affinities, but also excite and emit at different wavelengths. The initial fluorescence of the three indicators is quenched while bound to the surface of the gold nanoparticles. With the addition of each of the 8 nucleotides, the displacement of the fluorophore indicators on the surface of the gold nanoparticles took place. As each fluorescent indicator was displaced to

different extents with each analyte, the discrimination of the eight nucleotides was possible following PCA and LDA analysis.

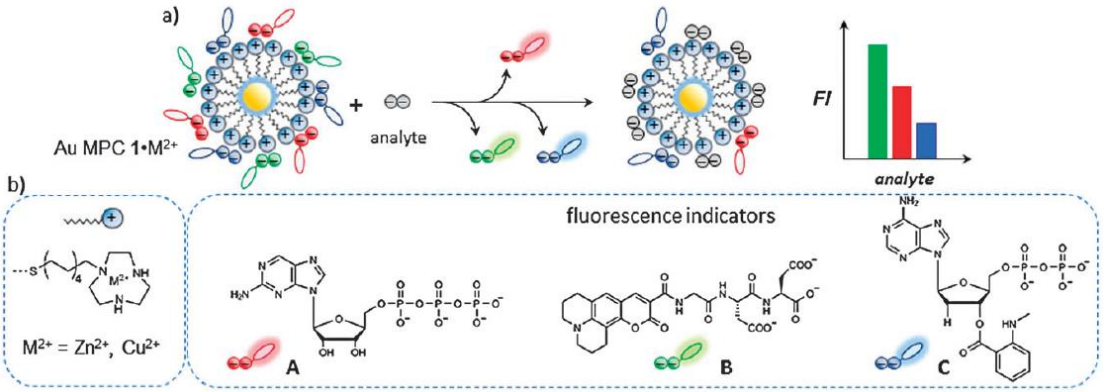

Figure 164. a) Schematic representation of the displacement of multiple fluorescent indicators from the surface of **Au MPC·M^{2+}** upon the addition of an analyte. b) Molecular structures of the monolayer and fluorescence indicators. Reprinted with permission from ref. 197. Copyright (2013) Royal Society of Chemistry.

Preliminary data suggest that our C_{12}-I-Coum-TACN **54** system could be utilised as a non-selective but differential sensor for phosphates. The following graph shows the fluorescence response of C_{12}-I-Coum-TACN **54** following the addition of each phosphate and following the addition of Zn^{2+} (Figure 165, the response following the addition of DMP has been omitted for clarity). It is interesting to observe that the distinctive patterns observed with each phosphate is not seen when the same experiments are conducted with the control molecule C_0-I-Coum-TACN **96**·Zn^{2+} (Figure 165b).

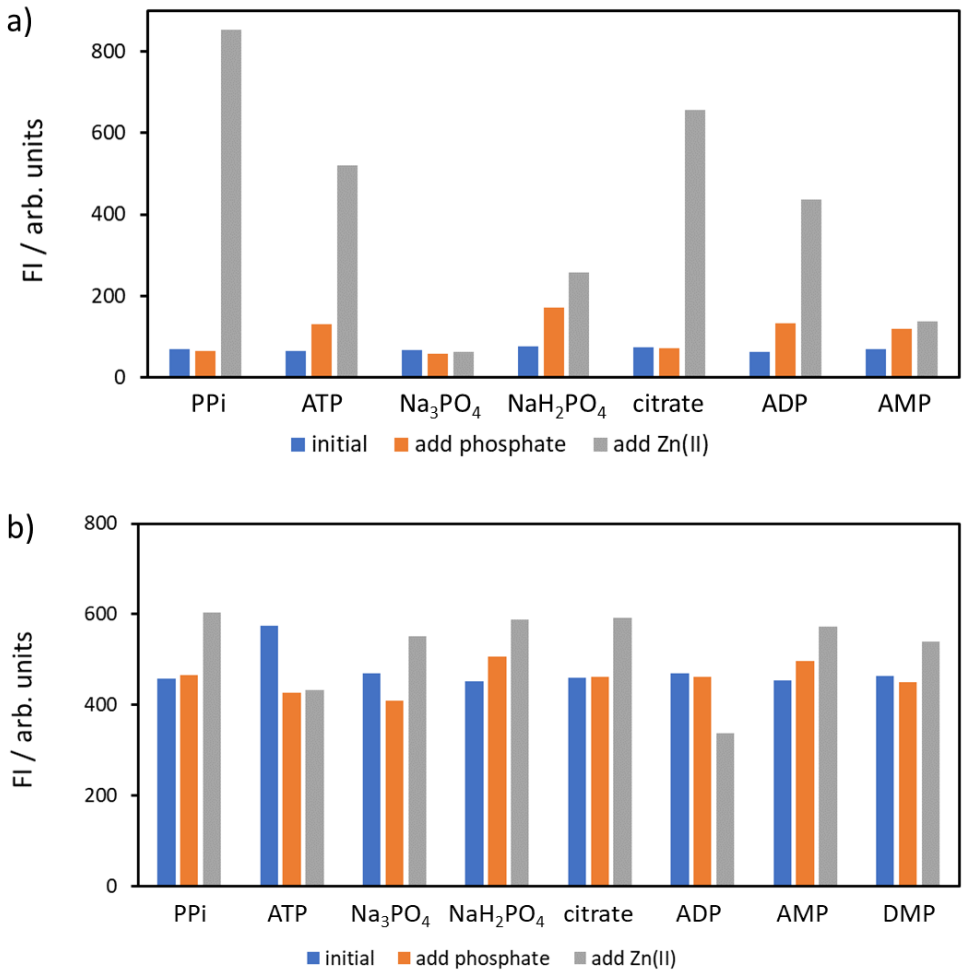

Figure 165. Fluorescence response of 100 μM of a) C_{12}-I-Coum-TACN **54**·Zn^{2+} (excited at 327 nm, slit 5/5) and b) C_0-I-Coum-TACN **96**·Zn^{2+} (excited at 344 nm, slit 2.5/2.5) in the presence of various of phosphates in 20% DMSO in water, [C_X-I-Coum-TACN] = [Zn^{2+}] = 100 μM, [phosphate] = 500 μM, [DIPEA] = 1 mM in 20% DMSO in water at 25 °C.

To obtain a sufficient array of data that would allow for differentiation of the analytes using PCA and LDA analysis, we performed some preliminary experiments combining C_{12}-I-Coum-TACN **54** with a range of different metal ions to create an array of sensors. Figure 166 summarises the fingerprint fluorescence response of the C_{12}-I-Coum-TACN **54**·M^{2+} system towards eight phosphates. Only 1 (Figure 166a) or 2.5 (Figure 166b) molar equivalents of phosphates was used due to the high fluorescence sensitivity of the sensing system. From the different fluorescence responses of the C_{12}-I-Coum-TACN **54**·M^{2+} ligand towards the

phosphates examined, it appears promising that the fingerprint responses could provide sufficient information for statistical discrimination using the principal component analysis and linear discrimination analysis. This will be further explored in the future with the objective of developing a fluorescent sensing system for the discrimination of a range of biologically relevant phosphates.

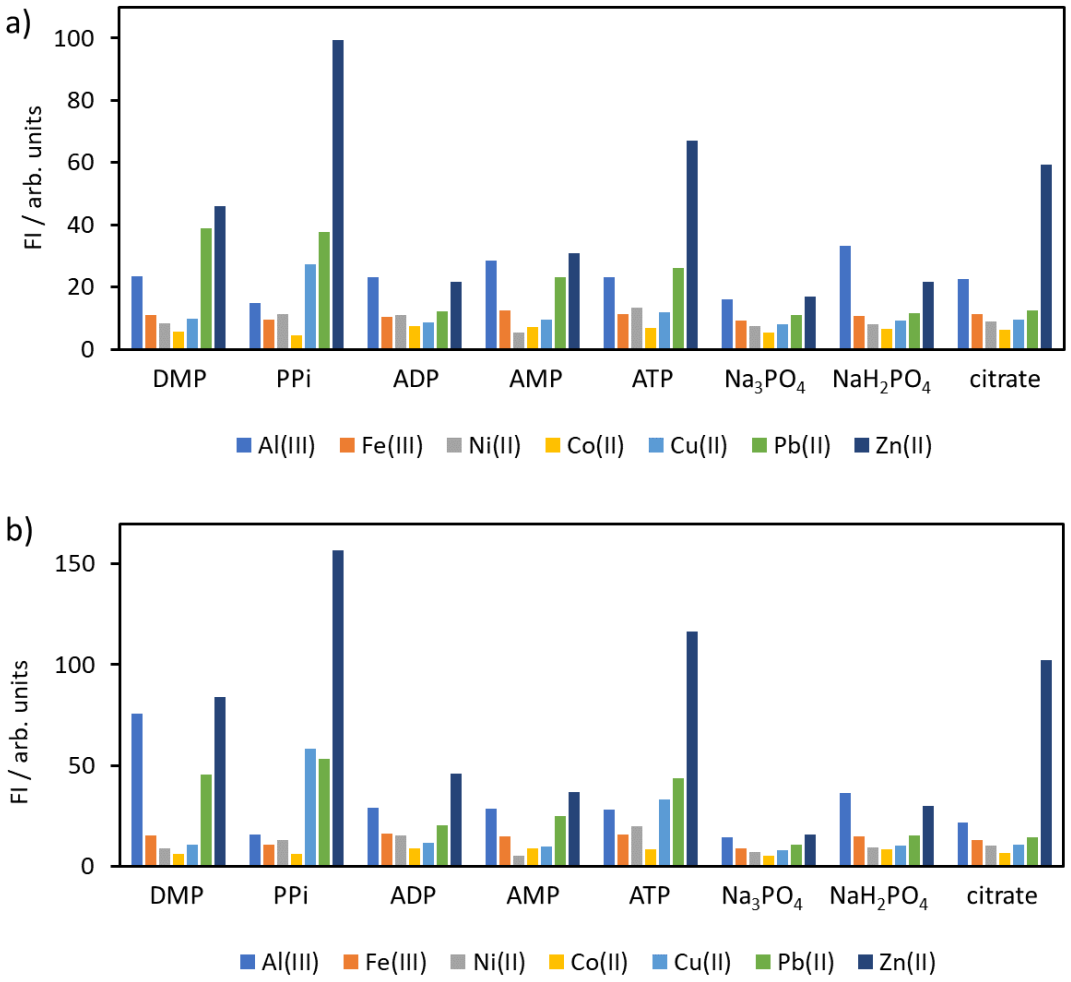

Figure 166. A C_{12}-I-Coum-TACN **54**·M^{2+} sensing array for phosphate pattern recognition. [C_{12}-I-Coum-TACN **54**] = [metal] = 100 μM, [phosphates] = 100 μM (a) or 250 μM (b), [DIPEA] = 1 mM in 20% DMSO in water at 25 °C, slit 2.5/5.

Chapter Five: Experimental

5.1 General details

All fine chemicals were sourced from commercial suppliers, including Sigma-Aldrich and AK Scientific, and were used directly without purification unless mentioned. Compounds lacking experimental details were prepared according to the literature as cited and are in agreement with published spectra.

NMR solvents including CD_3OD, $CDCl_3$ and $(CD_3)_2SO$ were purchased from Eurisotop. Acetone and hexanes (analytical grade) were purchased from ECP chemicals along with dichloromethane and ethyl acetate of laboratory quality. Hydrochloric acid 37% and methanol were purchased from Thermo Fisher Scientific. Celite® 545 was purchased from Sigma-Aldrich. Anhydrous magnesium sulfate was purchased from ECP chemicals.

Organic compounds were synthesised and characterised by ^{1}H, ^{13}C NMR, IR and HRMS(ESI) and the data compared to literature values where available. Flash column chromatography was performed using silica gel 60 (Aldrich) and a suitable eluent. Analytical TLC was performed on aluminium backed plates pre-coated (0.25 mm) with Merck Silica Gel 60 F254 with a suitable solvent system and was visualised using UV fluorescence (254 nm) and/or developed with ninhydrin, phosphomolybdic acid (PMA) or potassium permanganate.

4-(2-Hydroxyethyl)-1-piperazineethanesulfonic acid (**HEPES**) was purchased from AK Scientific and *N*-cyclohexyl-2-aminoethanesulfonic acid (**CHES**) and 2-(*N*-morpholino)ethanesulfonic acid hydrate (**MES** hydrate) were purchased from Sigma-Aldrich and used without further purification. The pH of buffer solutions was determined at room temperature using a Metrohm-632 pH-meter equipped with a Ag/AgCl/KCl reference electrode. In all cases, stock solutions were prepared using deionised water filtered with a MilliQ-water-purifier (Millipore) and stored at 4 °C unless stated otherwise. $Zn(NO_3)_2$ and $Cu(NO_3)_2$ were analytical grade

products and the concentration of stock solutions were determined by atomic absorption spectroscopy. Stock solutions of the **HPNPP** and model **HPNPP** substrate were prepared by weight and their concentrations were confirmed by UV spectroscopy and adjusted if necessary.

^{1}H and ^{13}C NMR spectra were recorded using a Bruker Ascend 400 NMR spectrometer operating at 400 MHz for ^{1}H nuclei and 100 MHz for ^{13}C nuclei. Chemical shifts (δ) are quoted in parts per million (ppm) and coupling constants (J) are in Hertz (Hz). Residual solvent peaks were used as the internal reference for ^{1}H and ^{13}C NMR. Abbreviations for multiplicity are as follows: s = singlet, br s = broad singlet, d = doublet, t = triplet, q = quartet, m = multiplet, dd = doublet of doublet, etc.).

Infrared (IR) spectra were recorded using a Nicolet iS10 spectrometer (Thermo Fisher Scientific Inc.) with the absorption peaks expressed in wavenumbers (cm^{-1}) and recorded from 450 to 4000 cm^{-1}. IR spectra were analysed using OMNIC 9.2.86. High resolution electrospray ionisation mass spectrometry (HRESIMS) measurements were obtained using a VG-70SE spectrometer at a nominal resolution of 5000 to 10000 as appropriate.

UV-visible spectroscopy was conducted using a Cary 100 UV-visible spectrophotometer (Agilent Technologies, model number: G9821A), equipped with a Cary temperature controller (Agilent Technologies, model number: G9844A). UV-visible spectra were recorded using Cary WinUV 4.20(468). Fluorescence measurements were recorded on a Varian Cary Eclipse Fluorescence spectrophotometer equipped with a thermostatted cell holder. Nile red was added from a concentrated solution in EtOH (typically 1 µL of a 1 mM solution was present in a 1 mL solution).

Standard TEM images were recorded on a FEI Tecnai FEG20 or a FEI Tecnai 12 with Gatan cold stages and a Gatan Ultrascan 100 4 Mpixel digital camera. DLS analysis was performed on a Malvern Zetasizer Nano-S instrument using filtered milli-Q water and a filtered buffer solution.

Curve fitting (Michealis-Menten curve) was performed using Origin fitting tools.

Small-angle neutron scattering experiments were performed on the BILBY[198] time-of flight instrument at the Australian Centre for Neutron Scattering at Lucas Heights (ANSTO). This work benefited from the use of the SasView application (http://www.sasview.org/), originally developed under NSF award DMR-0520547. SasView contains code developed with funding from the European Union's Horizon 2020 research and innovation program under the SINE2020 project, grant agreement No 654000.

5.2 Synthesis of amphiphiles for multifunctional catalysts

5.2.1 Synthesis of guanidinium amphiphiles

_N_,_N_'-Bis(_tert_-butoxycarbonyl)-_N_''-hexadecylguanidine 27

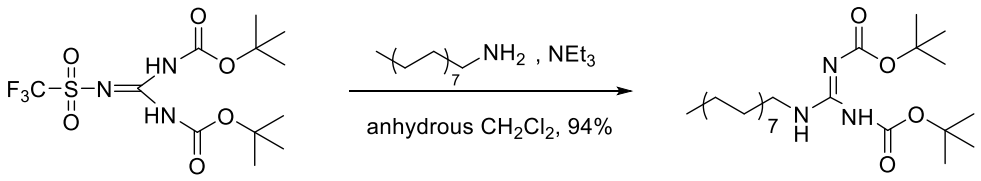

26 **27**

To a solution of 1,3-di-Boc-2-(trifluoromethylsulfonyl)guanidine **26** (100 mg, 0.26 mmol, 1.2 eq.) in anhydrous CH_2Cl_2 (20 mL) was added hexadecylamine (51 mg, 0.21 mmol, 1.0 eq.) and triethylamine (30 µL, 0.21 mmol, 1.0 eq.). The reaction mixture was stirred at RT for 16 h, followed by the addition of water (25 mL) and vigorous stirring for a further 30 min. The aqueous layer was then separated and extracted with CH_2Cl_2 (2 x 20 mL). The organic layer was collected, dried over anhydrous Na_2SO_4 and the solvent evaporated under reduced pressure. The crude product was purified by flash column chromatography (1:9 ethyl acetate/hexane) to yield the *title compound* (97 mg, 94 %) as a faint yellow oil.

^{1}H NMR (400 MHz, $CDCl_3$) δ (ppm) 11.41 (s, 1H), 8.22 (s, 1H), 3.35-3.29 (m, 2H), 1.55-1.46 (m, 2H), 1.44 (s, 9H), 1.42 (s, 9H), 1.33-1.08 (m, 26H), 0.81 (t, J = 6.8 Hz, 3H). **^{13}C NMR** (100 MHz, $CDCl_3$) δ (ppm) 162.7, 155.1, 152.3, 81.9, 78.1, 40.0, 30.9, 28.7, 28.7, 28.6, 28.6, 28.6, 28.5, 28.4, 28.3, 28.0, 27.3, 27.1, 25.8, 21.7, 13.1. **IR** ν_{max}(film)/cm^{-1}: 2914, 2849, 1725, 1638, 1615, 1572, 1422, 1365, 1328, 1169, 1131, 1051. **HRMS** found (ESI): MH$^+$, 484.4120, $C_{27}H_{54}N_3O_4$ requires 484.4109. This compound is a novel compound, although the spectroscopic data has been compared to and is comparable to an analogous compound reported in the literature containing a C_{18} carbon chain.[199]

1-Hexadecylguanidinium chloride 23

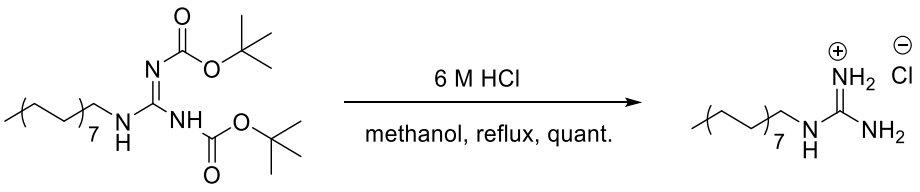

27 **23**

To a solution of guanidinium **27** (24.1 mg, 0.05 mmol, 1.0 eq.) in methanol (2 mL) was added 6 M HCl (9 mL). The reaction mixture was heated at reflux for 3h. The solvent was evaporated under reduced pressure and the deprotected product was obtained without further purification. The *title compound* (16 mg, 0.05 mmol) was obtained as a white solid.

^{1}H NMR (400 MHz, CD_3OD) δ (ppm) 3.21 (m, 1H), 3.07 (t, J = 7.1 Hz, 2H), 1.56-1.41 (m, 2H), 1.36-1.10 (m, 24H), 0.80 (t, J = 6.9 Hz, 3H). **^{13}C NMR** (100 MHz, CD_3OD) δ (ppm) 157.2, 41.2, 31.7, 29.4, 29.4, 29.3, 29.3, 29.1, 29.0, 28.6, 26.4, 22.3, 13.1. **IR** ν_{max}(film)/cm^{-1}: 3394, 3131, 2954, 2918, 2848, 1669, 1638, 1606, 1466. **HRMS** found (ESI): MH$^+$, 284.3062, $C_{17}H_{38}N_3$ requires 284.3066. This compound is a novel compound, although the spectroscopic data has been compared to and closely matches an analogous compound reported in the literature containing a C_{18} carbon chain.[199]

N,*N*'-Bis(*tert*-butoxycarbonyl)-*N*''-butylguanidine 28

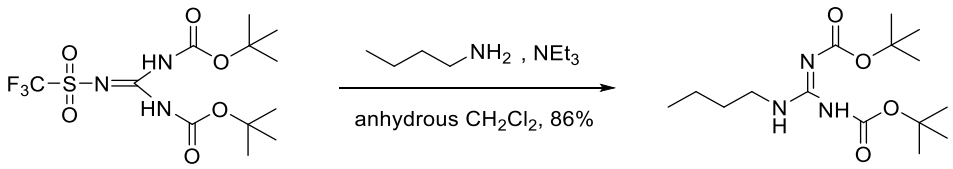

26 **28**

To a solution of 1,3-di-Boc-2-(trifluoromethylsulfonyl)guanidine **26** (100 mg, 0.26 mmol, 1.2 eq.) in anhydrous CH_2Cl_2 (20 mL) was added *n*-butylamine (15.6 mg, 0.21 mmol, 1.0 eq.) and triethylamine (30 µL, 0.21 mmol, 1.0 eq.). The reaction mixture was stirred at RT for 16 h, followed by the addition of water (25 mL) and vigorous stirring for a further 30 min. The aqueous layer was then separated and extracted with CH_2Cl_2 (2 x 20 mL). The organic layer was collected, dried over anhydrous Na_2SO_4 and the solvent evaporated under reduced pressure. The crude product was purified by flash column chromatography (1:9 ethyl acetate/hexane) to yield the *title compound* (58.2 mg, 86 %) as a faint yellow oil.

^{1}H NMR (400 MHz, $CDCl_3$) δ (ppm) 11.44 (s, 1H), 8.31 (s, 1H), 3.34 (m, 2H), 1.53-1.46 (m, 2H), 1.44 (s, 9H), 1.42 (s, 9H), 1.31 (m, 2H), 0.87 (t, J = 7.3 Hz, 3H). **^{13}C NMR** (100 MHz, $CDCl_3$) δ (ppm) 163.7, 156.1, 153.3, 83.0, 79.2, 40.7, 31.1, 28.3, 28.1, 20.1, 13.8. **IR** ν_{max}(film)/cm^{-1}: 3343, 2976, 2930, 1714, 1612, 1568, 1414, 1366, 1326, 1252, 1282, 1227, 1124, 1052, 1026, 810, 771. **HRMS** found (ESI): MNa^+, 338.2075, $C_{15}H_{29}N_3NaO_4$ requires 338.2050. This compound is a novel compound, although the spectroscopic data has been compared to and is similar to an analogous compound reported in the literature containing a C_6 carbon chain.[200]

1-Butylguanidinium chloride 29

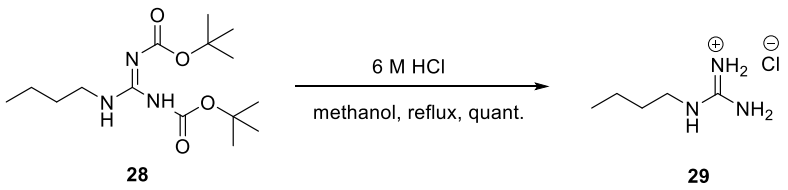

To a solution of guanidinium **28** (58.2 mg, 0.18 mmol, 1.0 eq.) in methanol (2 mL) was added 6 M HCl (9 mL). The reaction mixture was heated at reflux for 3 h. The solvent was evaporated under reduced pressure and the deprotected product was obtained without further purification. The *title compound* (27 mg, 0.18) was obtained as a faint pink oil.

^{1}H NMR (400 MHz, CD_3OD) δ (ppm) 3.22 (m, 1H), 3.09 (t, J = 7.0 Hz, 2H), 1.54-1.41 (m, 2H), 1.39-1.24 (m, 2H), 0.87 (t, J = 7.3 Hz, 3H). **^{13}C NMR** (100 MHz, CD_3OD) δ (ppm) 157.2, 40.9, 30.6, 19.5, 12.6. **IR** ν_{max}(film)/cm^{-1}: 3325, 3164, 2960, 2934, 2874, 1622, 1465. **HRMS** found (ESI): MH^+, 116.1186, $C_5H_{14}N_3$ requires 116.1182.

5.2.2 Synthesis of HPNPP and model HPNPP substrates

2-Hydroxypropyl *p*-nitrophenyl phosphate (HPNPP)

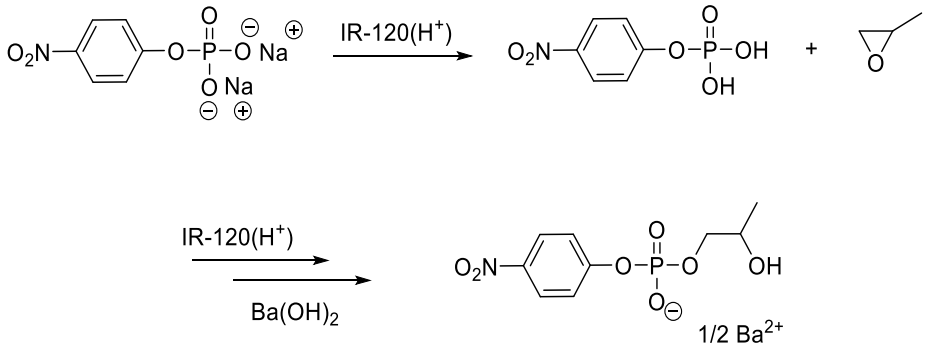

Disodium p-nitrophenyl phosphate (1.0 g, 2.69 mmol) was dissolved in water (5 mL), and the

aqueous solution was passed down a column of IR-120 (H^+) resin to wash off sodium ions replaced by hydrogen ions. Then the pH of the acidic eluent was adjusted to pH ~8 with aqueous ammonia, and the solution was concentrated to 15 mL. 1,2-Epoxypropane (10 mL) was added, and the reaction mixture was stirred at 35°C for 40 h.

The unreacted epoxide (bp. 34°C) was evaporated under reduced pressure, and the crude material was passed down a column of IR-120 (H^+) resin. The solution was neutralized no higher than pH ~7 with barium hydroxide solution (carbonate-free) and condensed to 20 mL by rotary evaporator under reduced pressure at RT. Ethanol (2 vol.) was added, and uncharged p-nitrophenyl phosphate was precipitated, followed by filtration to remove the solid. The filtrate was condensed into a small volume by rotary evaporation under reduced pressure at RT. To a solution of 10% ethanol in acetone (200 mL) was added the corresponding filtrate with vigorous stirring. The white precipitate of barium p-nitrophenyl 2-hydroxypropyl phosphate (**HPNPP**) was filtered off, followed by drying under high vacuum to give the titled compound (247 mg, 0.72 mmol, 27% yield).

^{1}H NMR (400 MHz, D_2O) δ 8.29 (d, J = 9.2, 2H), 7.38 (d, J = 9.2, 2H), 4.11 – 3.89 (m, 2H), 3.89 – 3.75 (m, 1H), 1.16 (d, J = 6.5 Hz, 3H). **^{13}C NMR** (100 MHz, D_2O) δ 157.4, 125.8, 120.5, 120.4, 71.0, 66.5, 17.7. The spectroscopic data were in agreement with literature values.[201]

4-Nitrophenyl propyl hydrogen phosphate (model HPNPP)

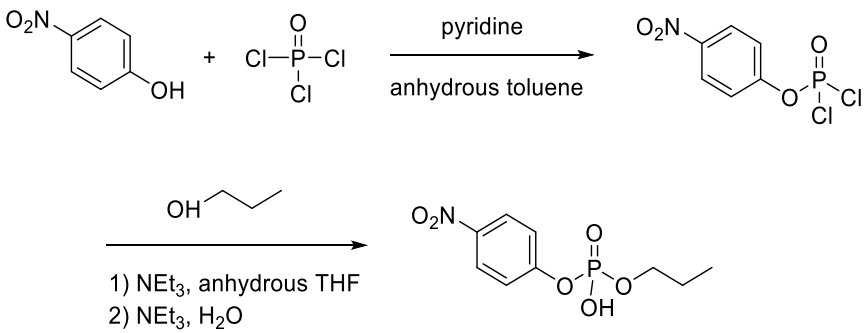

To a suspension of *p*-nitrophenol (648 mg, 4.7 mmol, 1 eq.) in anhydrous toluene (27 mL) was added phosphorus oxychloride (1 mL, 10.7 mmol, 2.3 eq.). The reaction mixture was heated to 95 °C, and pyridine (380 µL, 4.7 mmol, 1 eq.) was added dropwise over a period of 15 mins. The reaction mixture was refluxed at 110 °C for further 15 mins. The salts were removed by filtration, and the filtrate was condensed under reduced pressure by a rotary evaporator. The crude product was obtained as a yellow oil and was directly used in the next step without purification.

Anhydrous THF (10 mL) was added to the crude mixture and the solution was placed under an inert atmosphere of N_2 at 0 °C. A solution of propan-1-ol (347 µL, 4.6 mmol, 1 eq.) and triethylamine (643 µL, 4.7 mmol, 1 eq.) in anhydrous THF (10 mL) was added via a dropping funnel over a period of 1 h. After the addition was completed, the reaction mixture was allowed to stir at RT overnight. A solution of 20% v/v NEt_3 in H_2O (8.75 mL) was added to hydrolyse the intermediate monochloride, and the reaction mixture was stirred for a further 30 mins followed by the evaporation of THF under reduced pressure. The aqueous phase was washed with CH_2Cl_2 (3 x 30 mL). The aqueous phase was collected, and the solvent was evaporated under reduced pressure. The crude product was purified by flash column chromatography (10% MeOH in $CHCl_3$) to yield the title compound (128 mg, 0.49 mmol, 10%) as a white solid.

^{1}H NMR (400 MHz, D_2O) δ 8.3 (d, J = 9.1 Hz, 2H), 7.38 (d, J = 9.1 Hz, 2H), 3.98 (dd, J = 13.5, 6.6 Hz, 2H), 1.73 – 1.58 (m, 2H), 0.92 (t, J = 7.4 Hz, 3H). **^{13}C NMR** (101 MHz, D_2O) δ 157.53, 125.86, 120.48, 120.43, 68.86, 23.16, 9.48.

5.3 Synthesis of FRET amphiphiles

5.3.1 Synthesis of C_{12}-I-Coum-TACN 54

di-tert-Butyl 1,4,7-triazonane-1,4-dicarboxylate 58

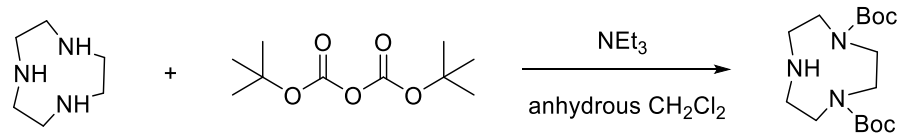

58

To a solution of 1,4,7-triazacyclononane trihydrochloride (TACN·3HCl, 400 mg, 1.68 mmol, 1.0 eq.) in anhydrous CH_2Cl_2 (10 mL) was added 1,8-diazacyclo[5.4.0]undec-7-ene (DBU, 1.73 mL, 11.42 mmol, 6.8 eq.). The reaction mixture was cooled to 0°C and stirred for 10 min. Then to the reaction mixture was added a solution of di-*tert*-butyl decarbonate (730 mg, 3.36 mmol, 2.1 eq.) in anhydrous CH_2Cl_2 (5 mL) drop wise over 15 mins. The reaction mixture was allowed to warm to RT and stirred for 16 h. After the reaction was quenched by adding saturated $NaHCO_3$ aq. (20 mL), the organic layer was separated and washed with brine (2 × 20 mL). Then the solvent was evaporated under reduced pressure and the crude product was purified by flash column chromatography (5% MeOH in CH_2Cl_2) to yield the title compound (242 mg, 0.73 mmol, yield 44%) as a colourless oil.

^{1}H NMR (400 MHz, $CDCl_3$) δ 3.42 – 3.28 (m, 4H), 3.23 – 3.08 (m, 4H), 2.90 – 2.76 (br s, 4H), 2.30 (s, 1H), 1.37 (s, 18H). **^{13}C NMR** (100 MHz, $CDCl_3$) δ 155.9, 155.6, 79.7, 79.6, 52.6, 51.9, 50.3, 49.4, 47.9, 47.5, 28.4. **IR** ν_{max}(film)/cm^{-1}: 3369, 2974, 2930, 1681, 1460, 1408, 1364, 1245, 1165, 1131, 752. **HRMS** found (ESI): MNa^+, 352.2207; $C_{16}H_{31}N_3NaO_4$ requires 325.2212. The spectroscopic data were in agreement with literature values.[62]

di-tert-Butyl 7-(3-(1,3-dioxoisoindolin-2-yl)propyl)-1,4,7-triazonane-1,4-dicarboxylate 68

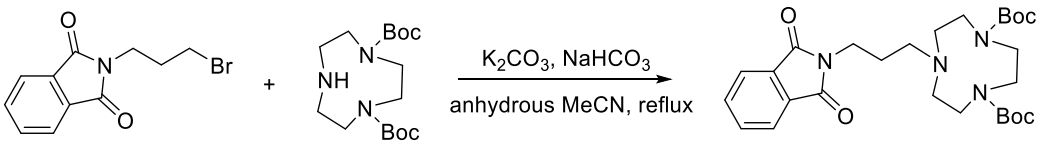

67 **58** **68**

To a solution of TACN·diBoc **58** (100 mg, 0.30 mmol, 1.0 eq.) in anhydrous MeCN (3 mL) was added N-(3-bromopropyl)phthalimide **67** (98 mg, 0.36 mmol, 1.2 eq.), K_2CO_3 (55 mg, 0.40 mmol, 1.3 eq.) and $NaHCO_3$ (33 mg, 0.40 mmol, 1.3 eq.). The reaction mixture was refluxed for 16 h. The solvent was evaporated under reduced pressure and the crude product was purified by flash column chromatography (EtOAc/hexane 1:2) to yield the title compound (138 mg, 0.27 mmol, 88%) as a faint yellow oil.

^{1}H NMR (400 MHz, $CDCl_3$) δ 7.85 – 7.74 (m, 2H), 7.73 – 7.61 (m, 2H), 3.71 (t, J = 7.4 Hz, 2H), 3.56 – 3.37 (m, 4H), 3.37 – 3.12 (m, 4H), 2.71 – 2.47 (m, 6H), 1.87 – 1.63 (m, 2H), 1.42 (s, 9H), 1.40 (s, 9H). **^{13}C NMR** (100 MHz, $CDCl_3$) δ 168.4, 168.4, 155.5, 155.4, 133.8, 133.8, 132.2, 132.1, 123.2, 123.1, 79.4, 77.3, 54.2, 54.1, 53.9, 53.7, 50.6, 49.7, 49.4, 36.2, 28.5, 28.5. **IR** ν_{max}(film)/cm^{-1}: 2972, 2932, 1684, 1461, 1394, 1364, 1244, 1143, 1030, 720. **HRMS** found (ESI): MH^+, 517.3021; $C_{27}H_{41}N_4O_6$ requires 517.3026. The spectroscopic data were in agreement with literature values.[202]

di-tert-Butyl 7-(3-aminopropyl)-1,4,7-triazonane-1,4-dicarboxylate 69

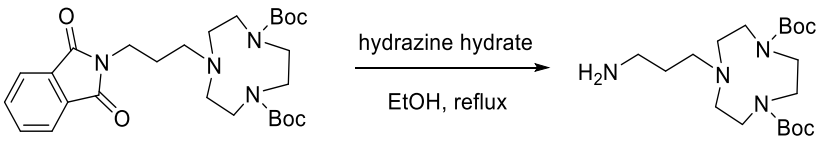

68 **69**

To the corresponding TACN **68** (94 mg, 0.18 mmol, 1.0 eq.) in EtOH (5 mL) was added hydrazine monohydrate (92 mg, 1.8 mmol, 10 eq.) drop wise. The reaction mixture was refluxed for 16 h. Then the reaction mixture was filtered through Celite and washed with diethyl ether (10 mL). The filtrate was combined, and the solvent was evaporated under reduced pressure. The crude product was purified by flash column chromatography (10% MeOH in CH_2Cl_2, 1% NH_4OH) to yield the title compound (52 mg, 0.14 mmol, 81%) as a colourless oil.

^{1}H NMR (400 MHz, $CDCl_3$) δ 3.53 – 3.36 (m, 4H), 3.34 – 3.18 (m, 4H), 2.78 (t, *J* = 6.4 Hz, 2H), 2.66 – 2.60 (m, 4H), 2.57 (t, *J* = 6.4 Hz, 2H), 1.70 – 1.58 (m, 2H), 1.47 (s, 18H). **^{13}C NMR** (100 MHz, $CDCl_3$) δ 155.9, 155.6, 79.6, 54.7, 54.2, 53.4, 52.0, 50.6, 49.7, 49.2, 39.9, 30.4, 28.6. **IR** ν_{max}(film)/cm^{-1}: 2973, 2931, 1682, 1460, 1412, 1364, 1245, 1142, 750. **HRMS** found (ESI): MH^+, 387.2955; $C_{19}H_{39}N_4O_4$ requires 387.2971. The spectroscopic data were in agreement with literature values.[202]

di-tert-Butyl 7-(3-(2-(7-hydroxy-2-oxo-2H-chromen-4-yl)acetamido)propyl)-1,4,7-triazonane-1,4-dicarboxylate 71

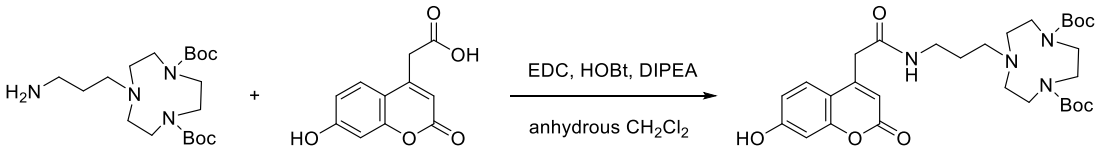

69 70 71

To a solution of TACN **69** (62 mg, 0.16 mmol, 1.0 eq.) in anhydrous CH_2Cl_2 (5 mL) was added 7-hydroxycoumarinyl-4-acetic acid **70** (53 mg, 0.24 mmol, 1.5 eq.). EDC-HCl (62 mg, 0.32 mmol, 2 eq.), HOBt (44 mg, 0.32 mmol, 2.0 eq.) and *N*,*N*-diisopropylethylamine (DIPEA, 42 mg, 0.32 mmol, 2.0 eq.) was added to the reaction mixture and the reaction mixture was stirred for 16 h at RT The solvent was evaporated under reduced pressure and the crude product was purified by flash column chromatography (5% MeOH in $CHCl_3$) to yield the *title compound* (84 mg, 0.14 mmol, 89%) as a white solid.

^{1}H NMR (400 MHz, $CDCl_3$) δ 8.42 – 8.19 (br s, 1H), 7.55 (d, *J* = 8.9 Hz, 1H), 6.75 (d, *J* = 8.9 Hz, 1H), 6.66 (s, 1H), 6.28 (s, 1H), 3.76 (s, 2H), 3.59 – 3.25 (m, 6H), 3.25 – 3.07 (m, 4H), 2.58 – 2.43 (m, 4H), 2.42 – 2.29 (m, 2H), 1.71 – 1.57 (m, 2H), 1.48 (s, 9H), 1.46 (s, 9H). **^{13}C NMR** (100 MHz, $CDCl_3$) δ 169.4, 161.7, 161.1, 156.9, 156.0, 155.4, 149.7, 126.0, 113.5, 113.3, 112.1, 103.5, 80.2, 58.4, 55.7, 52.7, 51.6, 50.6, 48.1, 40.2, 36.1, 28.5, 26.0, 18.3. **IR** ν_{max}(film)/cm^{-1}: 3273, 2973, 2933, 1655, 1607, 1565, 1467, 1392, 1365, 1246, 1137. **HRMS** found (ESI): MH^+, 589.3232; $C_{30}H_{45}N_4O_8$ requires 589.3237.

di-tert-Butyl 7-(3-(2-(7-(dodecyloxy)-2-oxo-2H-chromen-4-yl)acetamido)propyl)-1,4,7-triazonane-1,4-dicarboxylate 72

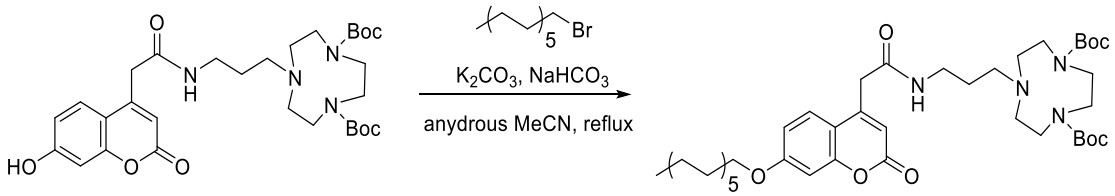

71 72

To a solution of coumarin **71** (57 mg, 0.097 mmol, 1.0 eq.) in anhydrous MeCN (4 mL) was added 1-bromododecane (32 mg, 0.13 mmol, 1.3 eq.), K_2CO_3 (18 mg, 0.13 mmol, 1.3 eq.) and $NaHCO_3$ (11 mg, 0.13 mmol, 1.3 eq.). The reaction mixture was refluxed for 16 h. The solvent was evaporated under reduced pressure and the crude product was purified by flash column chromatography (5% MeOH in $CHCl_3$) to yield the *title compound* (43 mg, 0.057 mmol, 58%) as a colourless oil.

^{1}H NMR (400 MHz, $CDCl_3$) δ 8.05 – 7.90 (br s, 1H), 7.68 (dd, *J* = 8.8, 4.2 Hz, 1H), 6.81 (dd, *J* = 8.8, 2.3 Hz, 1H), 6.77 (d, *J* = 2.3 Hz, 1H), 6.32 (s, 1H), 3.98 (t, *J* = 6.6 Hz, 2H), 3.69 (s, 2H), 3.52 – 3.17 (m, 6H), 3.17 – 2.86 (m, 4H), 2.54 – 2.33 (m, 4H), 2.31 – 2.14 (m, 2H), 1.87 – 1.73 (m, 2H), 1.64 – 1.50 (m, 2H), 1.44 (s, 9H), 1.41 (s, 9H), 1.30 – 1.19 (m, 18H), 0.86 (t, *J* = 7.0 Hz, 3H). **^{13}C NMR** (100 MHz, $CDCl_3$) δ 168.3, 162.3, 161.2, 156.8, 155.8, 155.4, 149.6, 126.2, 113.8,

112.6, 101.4, 79.9, 68.6, 55.9, 55.3, 52.6, 51.5, 50.7, 50.4, 48.0, 45.8, 40.6, 35.7, 31.9, 29.6, 29.6, 29.6, 29.5, 29.3, 29.0, 28.5, 25.9, 22.7, 14.1. **IR** ν_{max}(film)/cm^{-1}: 3308, 2924, 2854, 1667, 1611, 1462, 1365, 1247, 1140, 751. **HRMS** found (ESI): MH$^+$, 757.5110; $C_{42}H_{69}N_4O_8$ requires 757.5115.

di-tert-Butyl 7-(3-(2-(7-(dodecyloxy)-2-oxo-2H-chromen-4-yl)acetamido)propyl)-1,4,7-triazonane-1,4-dicarboxylate 54

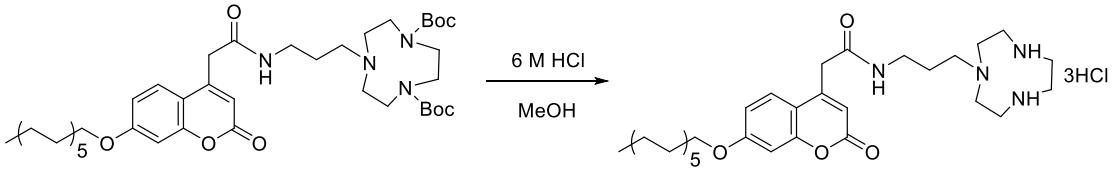

72 **54**

To a solution of coumarin **72** (18 mg, 0.024 mmol, 1.0 eq.) in methanol (3 mL) was added 6 M HCl (10 mL). The reaction mixture was stirred for 3 h at 60 °C. The solvent was evaporated under reduced pressure and the deprotected product was obtained without further purification to yield the *title compound* (13 mg, quant.) as a white solid.

^{1}H NMR (400 MHz, CD_3OD) δ 7.62 (d, J = 8.8 Hz, 1H), 6.87 (d, J = 8.8 Hz, 1H), 6.81 (s, 1H), 6.17 (s, 1H), 3.98 (t, J = 6.6 Hz, 2H), 3.70 (s, 2H), 3.61 – 3.45 (m, 4H), 3.28 – 3.07 (m, 6H), 2.97 – 2.83 (m, 4H), 2.76 – 2.61 (m, 2H), 1.79 – 1.63 (m, 4H), 1.44 – 1.34 (m, 2H), 1.32 – 1.11 (m, 16H), 0.79 (t, J = 7.1 Hz, 3H). **^{13}C NMR** (100 MHz, CD_3OD) δ 169.9, 162.8, 161.8, 155.4, 151.1, 126.1, 112.8, 112.5, 112.3, 101.1, 68.5, 53.1, 48.4, 43.9, 42.4, 38.8, 37.3, 31.7, 29.4, 29.3, 29.3, 29.1, 28.8, 25.7, 25.0, 22.3, 13.0. **IR** ν_{max}(film)/cm^{-1}: 3335, 2921, 2852, 2653, 1708, 1610, 1555, 1391, 1267, 1142. **HRMS** found (ESI): MH$^+$, 557.4061; $C_{32}H_{53}N_4O_4$ requires 557.4067.

N-(3-(1,4,7-Triazonan-1-yl)propyl)-2-(7-(dodecyloxy)-2-oxo-2H-chromen-4-yl)acetamide trihydrochloride 97

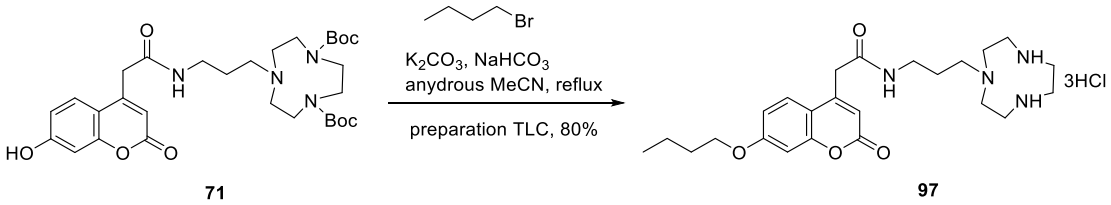

71 97

To a solution of coumarin **71** (75 mg, 0.13 mmol, 1.0 eq.) in anhydrous MeCN (4 mL) was added 1-bromobutane (23 mg, 0.17 mmol, 1.3 eq.), K_2CO_3 (26 mg, 0.17 mmol, 1.5 eq.) and $NaHCO_3$ (16 mg, 0.17 mmol, 1.5 eq.). The reaction mixture was refluxed for 16 h. The solvent was evaporated under reduced pressure and the crude product was purified by preparation TLC (5% MeOH in $CHCl_3$), the two Boc protecting groups were also removed under these conditions to afford the *title compound* (56 mg, 0.10 mmol, 80%) as a faint yellow solid.

^{1}H NMR (400 MHz, D_2O) δ 7.44 (d, J = 8.9 Hz, 1H), 6.74 (d, J = 8.9 Hz, 1H), 6.52 (s, 1H), 6.14 (s, 1H), 3.85 (t, J = 7.3 Hz, 2H), 3.67 (s, 2H), 3.62 – 3.49 (m, 4H), 3.37 – 3.24 (m, 4H), 3.19 (t, J = 7.6 Hz, 2H), 3.06 – 2.87 (m, 4H), 2.72 (t, J = 7.6 Hz, 2H), 1.80 – 1.72 (m, 2H), 1.64 (quint., J = 7.3 Hz, 2H), 1.39 (quint., J = 7.3 Hz, 2H), 0.89 (t, J = 7.3 Hz, 3H). **^{13}C NMR** (100 MHz, D_2O) δ 170.6, 163.4, 162.0, 154.4, 151.6, 125.9, 113.1, 112.3, 112.1, 101.3, 68.7, 52.4, 47.4, 43.3, 41.9, 38.8, 37.6, 30.4, 24.0, 18.7, 13.2. **IR** ν_{max}(film)/cm^{-1}: 3304, 2958, 2872, 2621, 1707, 1609, 1554, 1390, 1265, 1140. **HRMS** found (ESI): MH^+, 445.2809; $C_{24}H_{37}N_4O_4$ requires 445.2815.

_N_-(3-(1,4,7-Triazonan-1-yl)propyl)-2-(7-hydroxy-2-oxo-2H-chromen-4-yl)acetamide trihydrochloride 96

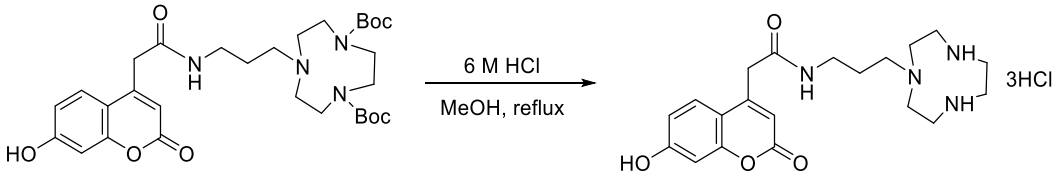

71 96

To a solution of coumarin **71** (45 mg, 0.076 mmol, 1.0 eq.) in methanol (3 mL) was added 6 M HCl (10 mL). The reaction mixture was stirred for 3 h at 60 °C. The solvent was evaporated under reduced pressure and the deprotected product was obtained without further purification to yield the *title compound* (38 mg, quant.) as a faint yellow solid.

^{1}H NMR (400 MHz, D_2O) δ 7.39 (d, J = 8.8 Hz, 1H), 6.72 (dd, J = 8.8, 2.4 Hz, 1H), 6.54 (d, J = 2.4 Hz, 1H), 6.10 (s, 1H), 3.65 (s, 2H), 3.52 (m, 4H), 3.23 (m, 4H), 3.16 (t, J = 6.9 Hz, 2H), 2.92 (m, 4H), 2.64 (t, J = 6.9 Hz, 2H), 1.75 – 1.68 (m, 2H). **^{13}C NMR** (100 MHz, D_2O) δ 171.0, 163.8, 160.1, 154.5, 151.6, 126.2, 113.6, 111.9, 111.9, 102.8, 52.4, 47.4, 43.1, 41.8, 38.9, 37.4, 23.9. **IR** ν_{max}(film)/cm^{-1}: 3308, 2983, 2645, 1693, 1602, 1563, 1444, 1394, 1316, 1268, 1137. **HRMS** found (ESI): MH$^+$, 389.2183; $C_{20}H_{29}N_4O_4$ requires 389.2189.

5.3.2 Synthesis of C_{12}-I-Naph-Gua 55

6-Hydroxy-1H,3H-benzo[de]isochromene-1,3-dione 81

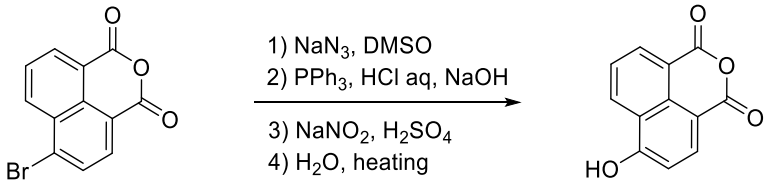

80 81

To a solution of 4-bromo-1,8-napthalic anhydride **80** (1.38 g, 5.0 mmol, 1.0 eq.) in DMSO (20 mL) was added sodium azide (0.488 g, 7.5 mmol, 1.5 eq.). The reaction mixture was stirred at 60 °C for 4 h. The resulting mixture was poured into water. The solid was precipitated out, collected by filtration, and washed with water (3 × 10 mL). The obtained solid was suspended in a mixture of THF (75 mL) and 0.5 M HCl aq. (15 mL). Then triphenylphosphine was added slowly, and the reaction mixture was stirred for 30 min. The mixture was basified with 2M NaOH aq. (5 mL), and the organic solvent was removed. The reaction mixture was diluted with EtOAc (20 mL). The solid precipitated from solution and washed with EtOAc (2 × 10 mL) and water (2 × 10 mL). The solvent was evaporated under reduced pressure to afford the crude intermediate as an orange solid (~ 1 g).

To a suspension of the above intermediate was added water (5 mL) followed by the slow addition of conc. sulfuric acid (8 mL) at 0 °C. A solution of sodium nitrite (0.395 g, 5.7 mmol, 1.1 eq.) in water (3 mL) was added dropwise at 0 °C for 30 min. The reaction mixture was stirred at 0 °C for 30 min. Then the reaction mixture was allowed to warm to RT and stirred for 1 h. The reaction was quenched with a solution of urea in water (40 mL) and refluxed for 30 min. Then the mixture was cooled to RT and diluted with water (50 mL). The solid was formed and collected by filtration, followed by washing with water (3 × 10 mL). The solvent was evaporated under reduced pressure and the product was obtained without further purification to yield the title compound (0.70 g, 3.3 mmol, 66% over four steps) as an orange-brown solid.

^{1}H NMR (400 MHz, DMSO-d_6) δ 12.27 (s, 1H), 8.59 (dd, J = 8.2, 1.2 Hz, 1H), 8.49 (dd, J = 7.2, 1.2 Hz, 1H), 8.38 (d, J = 8.2 Hz, 1H), 7.84 – 7.74 (m, 1H), 7.18 (d, J = 8.2 Hz, 1H). **^{13}C NMR** (100 MHz, DMSO-d_6) δ 161.9, 161.9, 160.8, 136.2, 133.6, 132.3, 130.7, 126.5, 123.0, 119.1, 111.0, 109.0. **IR** ν_{max}(film)/cm^{-1}: 3267, 1764, 1714, 1589, 1574, 1399, 1224, 1013, 977, 774. **HRMS** found (ESI): MNa^+, 237.0158; $C_{12}H_6NaO_4$ requires 237.0164. The spectroscopic data were in agreement with literature values.[203]

tert-Butyl (3-(6-hydroxy-1,3-dioxo-1H-benzo[de]isoquinolin-2(3H)-yl)propyl)carbamate 83

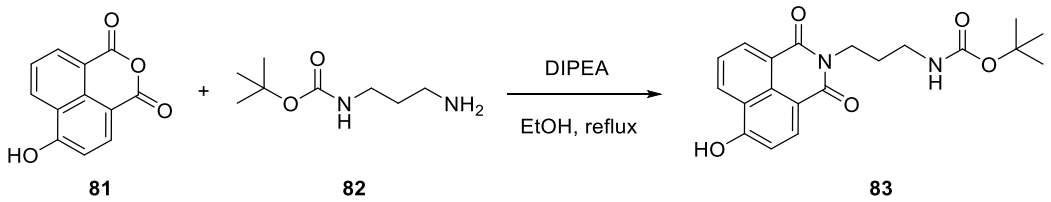

81 82 83

To a solution of naphthalimide **81** (150 mg, 0.70 mmol, 1.0 eq.) in EtOH (5 mL) was added N-Boc-1,3-propanediamine **82** (183 mg, 1.0 mmol, 1.5 eq.). The reaction mixture was refluxed at 80 °C for 16 h. Then the solvent was evaporated under reduced pressure and the crude product was purified by flash column chromatography (5% MeOH in $CHCl_3$) to yield the *title compound* (120 mg, 0.32 mmol, 46%) as a dark orange oil which solidified over time.

^{1}H NMR (400 MHz, CD_3OD) δ 8.50 (dd, J = 8.2, 1.2 Hz, 1H), 8.44 (dd, J = 7.2, 1.2 Hz, 1H), 8.31 (d, J = 8.2 Hz, 1H), 7.63 – 7.54 (m, 1H), 7.47 (s, 1H), 6.97 (d, J = 8.2 Hz, 1H), 4.15 (t, J = 6.7 Hz, 2H), 3.10 (t, J = 6.4 Hz, 2H), 1.85 (quint., J = 6.7 Hz, 2H), 1.39 (s, 9H). **^{13}C NMR** (100 MHz, CD_3OD) δ 165.2, 164.6, 160.9, 156.7, 134.1, 131.7, 129.7, 129.6, 125.2, 122.8, 121.6, 112.8, 109.6, 79.2, 37.6, 37.5, 28.2, 28.1. **IR** ν_{max}(film)/cm^{-1}: 3374, 3153, 2970, 1764, 1703, 1584, 1524, 1389, 1346, 1239, 1162, 725.

2-(3-Aminopropyl)-6-hydroxy-1H-benzo[de]isoquinoline-1,3(2H)-dione hydrochloride 84

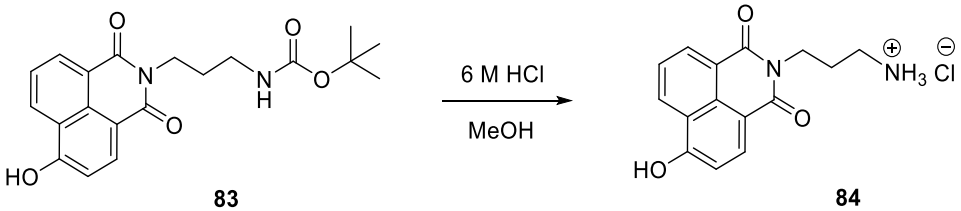

83 84

To a solution of naphthalimide **83** (120 mg, 0.32 mmol, 1.0 eq.) in methanol (5 mL) was added 6 M HCl (20 mL). The reaction mixture was stirred for 3 h at 60 °C. The solvent was evaporated under reduced pressure and the deprotected product was obtained without further purification to yield the *title compound* (99 mg, 0.32 mmol, quant.) as an orange solid.

^{1}H NMR (400 MHz, D_2O) δ 7.86 (d, *J* = 8.2 Hz, 1H), 7.83 (d, *J* = 7.2 Hz, 1H), 7.62 (d, *J* = 8.2 Hz, 1H), 7.32 – 7.22 (m, 1H), 6.39 (d, *J* = 8.2 Hz, 1H), 3.91 (t, *J* = 7.5 Hz, 2H), 3.14 (t, *J* = 7.5 Hz, 2H), 2.09 – 1.95 (m, 2H). **^{13}C NMR** (100 MHz, D_2O) δ 165.0, 164.12, 159.7, 133.7, 131.5, 129.3, 127.7, 125.2, 121.0, 119.3, 111.0, 109.8, 37.2, 37.1, 25.4. **IR** ν_{max}(film)/cm^{-1}: 2924, 1692, 1646, 1589, 1512, 1391, 1356, 1263, 1238, 1091, 783. **HRMS** found (ESI): MH^+, 271.1077; $C_{15}H_{15}N_2O_3$ requires 271.1083.

Naphthalimide 85

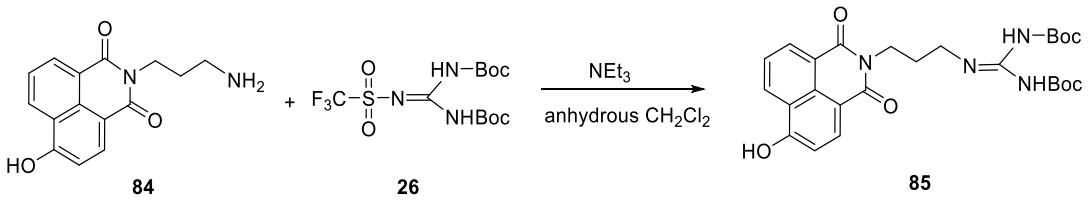

To a solution of naphthalimide **84** (137 mg, 0.45 mmol, 1.0 eq.) in anhydrous CH_2Cl_2 (5 mL) was added 1,3-di-Boc-2-(trifluoromethylsulfonyl) guanidine **26** (210 mg, 0.54 mmol. 1.2 eq.) and triethylamine (90 mg, 0.89 mmol, 2.0 eq.). The reaction mixture was stirred under N_2 at RT for 16 h. Then the solvent was evaporated under reduced pressure and the crude product was purified by flash column chromatography (10% MeOH in $CHCl_3$) to yield the *title compound* (180 mg, 0.35 mmol, 79%) as a brown oil.

^{1}H NMR (400 MHz, $CDCl_3$) δ 11.55 (s, 1H), 8.93 (s, 1H), 8.40 (d, *J* = 7.3 Hz, 1H), 8.36 (d, *J* = 8.3 Hz, 1H), 8.08 (d, *J* = 8.3 Hz, 1H), 7.48 – 7.38 (m, 1H), 6.98 (d, *J* = 8.3 Hz, 1H), 4.20 (t, *J* = 6.1 Hz, 2H), 3.68 – 3.49 (m, 2H), 2.17 – 1.93 (m, 2H), 1.48 (s, 9H), 1.23 (s, 9H). **^{13}C NMR** (100 MHz,

$CDCl_3$) δ 165.1, 164.4, 162.2, 160.5, 156.3, 153.0, 133.6, 131.4, 129.4, 129.4, 125.0, 122.7, 121.6, 112.7, 110.6, 83.8, 80.4, 39.4, 37.6, 28.5, 28.0, 28.0. **IR** ν_{max}(film)/cm^{-1}: 3280, 2979, 1643, 1615, 1577, 1358, 1340, 1227, 1130, 748. **HRMS** found (ESI): MH^+, 513.2344; $C_{26}H_{33}N_4O_7$ requires 513.2349.

Naphthalimide 86

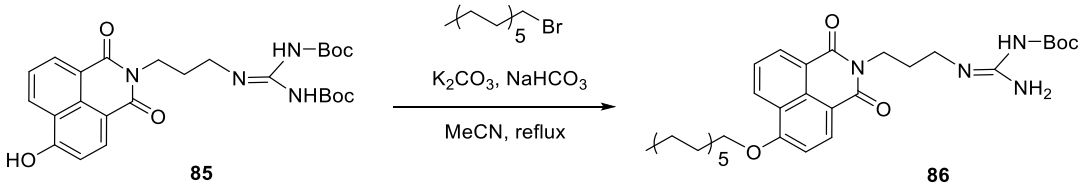

To a solution of naphthalimide **85** (100 mg, 0.20 mmol, 1.0 eq.) in anhydrous MeCN (5 mL) was added 1-bromododecane (63 mg, 0.25 mmol, 1.3 eq.), K_2CO_3 (40 mg, 0.29 mmol, 1.5 eq.) and $NaHCO_3$ (25 mg, 0.29 mmol, 1.5 eq.). The reaction mixture was refluxed for 16 h under N_2. Then the solvent was evaporated under reduced pressure and the crude product was purified by flash column chromatography (7% MeOH in CH_2Cl_2) to yield the *title compound* (31 mg, 0.053 mmol, 27%) as a yellow oil which solidified over time.

^{1}H NMR (400 MHz, $CDCl_3$) δ 9.47 – 9.30 (br s, 1H), 8.47 (d, *J* = 7.3 Hz, 1H), 8.44 (d, *J* = 8.4 Hz, 1H), 8.41 (d, *J* = 8.4 Hz, 1H), 7.65 – 7.50 (m, 1H), 6.92 (d, *J* = 8.4 Hz, 1H), 4.29 – 4.14 (m, 4H), 3.55 – 3.42 (m, 2H), 2.17 – 1.08 (m, 2H), 2.00 – 1.89 (m, 2H), 1.61 – 1.49 (m, 2H), 1.47 (s, 9H), 1.46 – 1.36 (m, 2H), 1.35 – 1.20 (m, 14H), 0.86 (t, *J* = 7.0 Hz, 3H). **^{13}C NMR** (100 MHz, $CDCl_3$) δ 164.8, 164.3, 160.6, 154.8, 152.6, 134.0, 131.7, 129.3, 129.0, 125.8, 123.4, 121.8, 114.1, 105.9, 84.8, 69.2, 40.0, 37.4, 31.9, 29.7, 29.6, 29.6, 29.6, 29.4, 29.3, 29.0, 28.2, 27.9, 26.1, 22.7, 14.1. **IR** ν_{max}(film)/cm^{-1}: 3302, 3107, 2976, 2853, 1689, 1656, 1591, 1390, 1353, 1249, 1147, 1085, 777. **HRMS** found (ESI): MH^+, 581.3697; $C_{33}H_{49}N_4O_5$ requires 581.3703.

2-(3-(6-(Dodecyloxy)-1,3-dioxo-1H-benzo[de]isoquinolin-2(3H)-yl)propyl)guanidine dihydrochloride 55

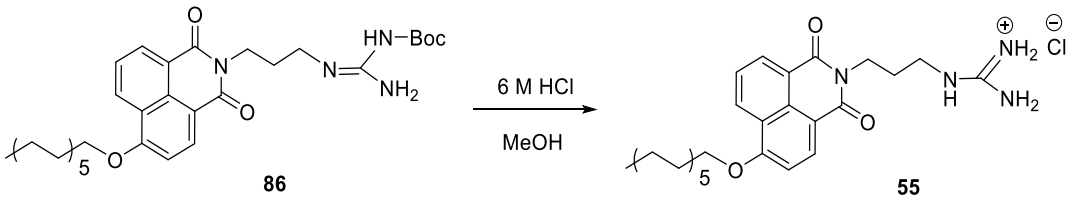

To a solution of naphthalimide **86** (22 mg, 0.037 mmol, 1.0 eq.) in methanol (3 mL) was added 6 M HCl (10 mL). The reaction mixture was stirred for 3 h at 60 °C. The solvent was evaporated under reduced pressure and the deprotected product was obtained without further purification to yield the *title compound* (20 mg, quant.) as a yellow solid.

^{1}H NMR (400 MHz, CD_3OD) δ 8.51 – 8.41 (m, 2H), 8.39 (d, J = 8.0 Hz, 1H), 7.72 – 7.60 (m, 1H), 7.11 (d, J = 8.0 Hz, 1H), 4.28 (t, J = 5.9 Hz, 2H), 4.17 (t, J = 6.6 Hz, 2H), 3.30 – 3.24 (m, 2H), 2.04 – 1.92 (m, 2H), 1.63 – 1.54 (m, 2H), 1.49 – 1.40 (m, 2H), 1.36 – 1.14 (m, 16H), 0.86 (t, J = 6.8 Hz, 3H). **^{13}C NMR** (100 MHz, CD_3OD) δ 164.6, 164.0, 160.6, 157.3, 133.6, 131.1, 129.0, 128.6, 125.6, 123.3, 121.7, 113.8, 106.1, 69.2, 38.9, 37.0, 31.7, 29.4, 29.3, 29.1, 28.7, 27.4, 25.9, 22.3, 13.1. **IR** ν_{max}(film)/cm^{-1}: 3336, 3137, 2921, 2852, 1617, 1591, 1393, 1355, 1267, 1237, 1087, 776. **HRMS** found (ESI): MH^+, 481.3156; $C_{28}H_{41}N_4O_3$ requires 481.3179.

References

1. Leigh, D. A., Genesis of the Nanomachines: The 2016 Nobel Prize in Chemistry. *Angew. Chem. Int. Ed.* **2016,** *55* (47), 14506-14508.
2. Noorden, R. V.; Castelvecchi, D., Chemistry Nobel for nanomachines. *Nature* **2016,** *538*, 152.
3. Hobza, P.; Rezac, J., Introduction: Noncovalent Interactions. *Chem. Rev.* **2016,** *116* (9), 4911-2.
4. Latimer, W. M.; Rodebush, W. H., Polarity and ionization from the standpoint of the Lewis theory of valence. *J. Am. Chem. Soc* **1920,** *42* (7), 1419-1433.
5. Chandler, D., Interfaces and the driving force of hydrophobic assembly. *Nature* **2005,** *437* (7059), 640-7.
6. Kauzmann, W., Some factors in the interpretation of protein denaturation. *Adv. Protein Chem.* **1959,** *14*, 1-63.
7. Pedersen, C. J., The discovery of crown ethers. *Science* **1988,** *241* (4865), 536-40.
8. B.Dietrich; J.M.Lehn; J.P.Sauvage, Les Cryptates. *Tetrahedron Lett.* **1969,** *10*, 2889-2892.
9. Lehn, J.-M., Cryptates: The Chemistry of Macropolycyclic Inclusion Complexes. *Acc. Chem. Res.* **1978,** *11*, 48-57.
10. Cram, D. J., The design of molecular hosts, guests, and their complexes. *Science* **1988,** *240*, 760-767.
11. Livoreil, A.; Dietrich-Buchecker, C. O.; Sauvage, J.-P., Electrochemically Triggerred Swinging of a [2]-Catenate. *J. Am. Chem. Soc.* **1994,** *116*, 9399-9400.
12. Collin, J. P.; Dietrich-Buchecker, C.; Gavina, P.; Jimenez-Molero, M. C.; Sauvage, J. P., Shuttles and muscles: linear molecular machines based on transition metals. *Acc. Chem. Res.* **2001,** *34* (6), 477-87.
13. Aricó, F.; Badjic, J. D.; Cantrill, S. J.; Flood, A. H.; Leung, K. C.-F.; Liu, Y.; Stoddart, J. F., Templated Synthesis of Interlocked Molecules. *Top. Curr. Chem.* **2005,** *249*, 203-259.
14. Bissell, R. A.; Cordova, E.; Kaifer, A. E.; Stoddart, J. F., A chemically and electrochemically switchable molecular shuttle. *Nautre* **1994,** *369*, 133-137.
15. Badjic, J. D.; Balzani, V.; Credi, A.; Silvi, S.; Stoddart, J. F., A molecular elevator. *Science* **2004,** *303* (5665), 1845-9.
16. Bruns, C. J.; Stoddart, J. F., Rotaxane-based molecular muscles. *Acc. Chem. Res.* **2014,** *47* (7), 2186-99.
17. Koumura, N.; Zijlstra, R. W.; van Delden, R. A.; Harada, N.; Feringa, B. L., Light-driven monodirectional molecular rotor. *Nature* **1999,** *401* (6749), 152-5.
18. Qu, D. H.; Wang, Q. C.; Zhang, Q. W.; Ma, X.; Tian, H., Photoresponsive Host-Guest Functional Systems. *Chem. Rev.* **2015,** *115* (15), 7543-88.
19. Yu, G.; Han, C.; Zhang, Z.; Chen, J.; Yan, X.; Zheng, B.; Liu, S.; Huang, F., Pillar[6]arene-based photoresponsive host-guest complexation. *J. Am. Chem. Soc.* **2012,** *134* (20), 8711-7.
20. Pray, L. A., Discovery of DNA Structure and Function: Watson and Crick. *Nature Education* **2008,** *1*, 100.
21. Trickett, C. A.; Osborn Popp, T. M.; Su, J.; Yan, C.; Weisberg, J.; Huq, A.; Urban, P.; Jiang, J.;

Kalmutzki, M. J.; Liu, Q.; Baek, J.; Head-Gordon, M. P.; Somorjai, G. A.; Reimer, J. A.; Yaghi, O. M., Identification of the strong Bronsted acid site in a metal-organic framework solid acid catalyst. *Nat. Chem.* **2019,** *11* (2), 170-176.

22. Fan, W.; Liu, X.; Wang, X.; Li, Y.; Xing, C.; Wang, Y.; Guo, W.; Zhang, L.; Sun, D., A fluorine-functionalized microporous In-MOF with high physicochemical stability for light hydrocarbon storage and separation. *Inorg. Chem. Front.* **2018,** *5*, 2445-2449.
23. Ma, N.; Li, F.; Li, S.; Chu, S.; Han, L.; Liu, S.; Yan, T.; Tian, R.; Luo, Q.; Liu, J., A remote optically controlled hydrolase model based on supramolecular assembly and disassembly of its enzyme-like active site. *Nanoscale* **2019,** *11* (8), 3521-3526.
24. Biedermann, F.; Schneider, H. J., Experimental Binding Energies in Supramolecular Complexes. *Chem Rev* **2016,** *116* (9), 5216-300.
25. Hartgerink, J. D.; Beniash, E.; Stupp, S. I., Self-assembly and mineralization of peptide-amphiphile nanofibers. *Science* **2001,** *294* (5547), 1684-8.
26. Fujita, D.; Ueda, Y.; Sato, S.; Mizuno, N.; Kumasaka, T.; Fujita, M., Self-assembly of tetravalent Goldberg polyhedra from 144 small components. *Nature* **2016,** *540* (7634), 563-566.
27. Fenniri, H.; Deng, B. L.; Ribbe, A. E.; Hallenga, K.; Jacob, J.; Thiyagarajan, P., Entropically driven self-assembly of multichannel rosette nanotubes. *Proc. Natl. Acad. Sci. USA* **2002,** *99 Suppl 2*, 6487-92.
28. Israelachvili, J.; Pashley, R., The hydrophobic interaction is long range, decaying exponentially with distance. *Nature* **1982,** *300*, 341-342.
29. Li, Z.; Liu, M.; Ke, L.; Wang, L.-J.; Wu, C.; Li, C.; Li, Z.; Wu, Y.-L., Flexible polymeric nanosized micelles for ophthalmic drug delivery: research progress in the last three years. *Nanoscale Adv.* **2021,** *3*, 5240.
30. Zhang, X.; Zhang, H.; Gu, J.; Zhang, J.; Shi, H.; Qian, H.; Wang, D.; Xu, W.; Pan, J.; Santos, H. A., Engineered Extracellular Vesicles for Cancer Therapy. *Adv. Mater.* **2021,** *33* (14), e2005709.
31. Sorella, G. L.; Strukul, G.; Scarso, A., Recent advances in catalysis in micellar media. *Green Chem.* **2015,** *17*, 644-683.
32. Shen, T.; Zhou, S.; Ruan, J.; Chen, X.; Liu, X.; Ge, X.; Qian, C., Recent advances on micellar catalysis in water. *Adv. Colloid Interface Sci.* **2021,** *287*, 102299.
33. Bekus, R.; Schrader, T., Artificial Signal Transduction. *ChemistryOpen* **2020,** *9* (6), 667-682.
34. Barba-Bon, A.; Nilam, M.; Hennig, A., Supramolecular Chemistry in the Biomembrane. *Chembiochem* **2020,** *21* (7), 886-910.
35. Cortes-Clerget, M.; Akporji, N.; Zhou, J.; Gao, F.; Guo, P.; Parmentier, M.; Gallou, F.; Berthon, J. Y.; Lipshutz, B. H., Bridging the gap between transition metal- and bio-catalysis via aqueous micellar catalysis. *Nat. Commun.* **2019,** *10* (1), 2169.
36. Lipshutz, B. H.; Ghorai, S., Transitioning organic synthesis from organic solvents to water. What's your E Factor? *Green Chem.* **2014,** *16* (8), 3660-3679.
37. Lipshutz, B. H.; Ghorai, S.; Cortes-Clerget, M., The Hydrophobic Effect Applied to Organic Synthesis: Recent Synthetic Chemistry "in Water". *Chemistry* **2018,** *24* (26), 6672-6695.
38. Breslow, R., β-Cyclodextrinylbisimidazole, a model for ribonuclease. *J. Am. Chem. Soc.* **1978,** *100*, 3227-3229.
39. Nothling, M. D.; Xiao, Z.; Hill, N. S.; Blyth, M. T.; Bhaskaran, A.; Sani, M. A.; Espinosa-

Gomez, A.; Ngov, K.; White, J.; Buscher, T.; Separovic, F.; O'Mara, M. L.; Coote, M. L.; Connal, L. A., A multifunctional surfactant catalyst inspired by hydrolases. *Sci. Adv.* **2020,** *6* (14), eaaz0404.

40. Nothling, M. D.; Xiao, Z.; Bhaskaran, A.; Blyth, M. T.; Bennett, C. W.; Coote, M. L.; Connal, L. A., Synthetic Catalysts Inspired by Hydrolytic Enzymes. *ACS Catal.* **2018,** *9*, 168-187.
41. Ekici, O. D.; Paetzel, M.; Dalbey, R. E., Unconventional serine proteases: variations on the catalytic Ser/His/Asp triad configuration. *Protein Sci.* **2008,** *17* (12), 2023-37.
42. Polgar, L., The catalytic triad of serine peptidases. *Cell. Mol. Life Sci.* **2005,** *62* (19-20), 2161-72.
43. Whitty, A., Cooperativity and biological complexity. *Nat. Chem. Biol.* **2008,** *4* (8), 435-9.
44. Mahadevi, A. S.; Sastry, G. N., Cooperativity in Noncovalent Interactions. *Chem. Rev.* **2016,** *116* (5), 2775-825.
45. Perutz, M. F., Mechanisms of cooperativity and allosteric regulation in proteins. *Q. Rev. Biophys.* **1989,** *22* (2), 139-237.
46. Dill, K. A.; Fiebig, K. M.; Chan, H. S., Cooperativity in protein-folding kinetics. *Proc. Natl. Acad. Sci. USA* **1993,** *90* (5), 1942-6.
47. Ercolani, G., Assessment of cooperativity in self-assembly. *J. Am. Chem. Soc.* **2003,** *125* (51), 16097-103.
48. Allen, A. E.; Macmillan, D. W., Synergistic Catalysis: A Powerful Synthetic Strategy for New Reaction Development. *Chem. Sci.* **2012,** *2012* (3), 633-658.
49. Hunter, C. A.; Anderson, H. L., What is cooperativity? *Angew. Chem. Int. Ed.* **2009,** *48* (41), 7488-99.
50. Comba, P.; Gahan, L. R.; Hanson, G. R.; Mereacre, V.; Noble, C. J.; Powell, A. K.; Prisecaru, I.; Schenk, G.; Zajaczkowski-Fischer, M., Monoesterase activity of a purple acid phosphatase mimic with a cyclam platform. *Chemistry* **2012,** *18* (6), 1700-10.
51. Linjalahti, H.; Feng, G.; Mareque-Rivas, J. C.; Mikkola, S.; Williams, N. H., Cleavage and isomerization of UpU promoted by dinuclear metal ion complexes. *J. Am. Chem. Soc.* **2008,** *130* (13), 4232-3.
52. Chen, X.; Wang, J.; Sun, S.; Fan, J.; Wu, S.; Liu, J.; Ma, S.; Zhang, L.; Peng, X., Efficient enhancement of DNA cleavage activity by introducing guanidinium groups into diiron(III) complex. *Bioorg. Med. Chem. Lett.* **2008,** *18* (1), 109-13.
53. Mancin, F.; Scrimin, P.; Tecilla, P., Progress in artificial metallonucleases. *Chem. Commun.* **2012,** *48* (45), 5545-59.
54. Barnes, J. A.; Wilkie, J.; Williams, I. H., Transition-state structural variation and mechanistic change. *J. Chem. Soc., Faraday trans.* **1994,** *90* (12), 1709-1714.
55. Erxleben, A., Mechanistic Studies of Homo- and Heterodinuclear Zinc Phosphoesterase Mimics: What Has Been Learned? *Front. Chem.* **2019,** *7*, 82.
56. Iranzo, O.; Kovalevsky, A. Y.; Morrow, J. R.; Richard, J. P., Physical and kinetic analysis of the cooperative role of metal ions in catalysis of phosphodiester cleavage by a dinuclear Zn(II) complex. *J. Am. Chem. Soc.* **2003,** *125* (7), 1988-93.
57. Morrow, J. R.; Amyes, T. L.; Richard, J. P., Phosphate binding energy and catalysis by small and large molecules. *Acc. Chem. Res.* **2008,** *41* (4), 539-48.
58. Neverov, A. A.; Lu, Z. L.; Maxwell, C. I.; Mohamed, M. F.; White, C. J.; Tsang, J. S.; Brown, R. S., Combination of a dinuclear Zn^{2+} complex and a medium effect exerts a 10(12)-fold

rate enhancement of cleavage of an RNA and DNA model system. *J. Am. Chem. Soc.* **2006,** *128* (50), 16398-405.

59. Cacciapaglia, R.; Casnati, A.; Mandolini, L.; Reinhoudt, D. N.; Salvio, R.; Sartori, A.; Ungaro, R., Catalysis of diribonucleoside monophosphate cleavage by water soluble copper(II) complexes of calix[4]arene based nitrogen ligands. *J. Am. Chem. Soc.* **2006,** *128* (37), 12322-30.
60. Cacciapaglia, R.; Casnati, A.; Mandolini, L.; Peracchi, A.; Reinhoudt, D. N.; Salvio, R.; Sartori, A.; Ungaro, R., Efficient and selective cleavage of RNA oligonucleotides by calix[4]arene-based synthetic metallonucleases. *J. Am. Chem. Soc.* **2007,** *129* (41), 12512-20.
61. Manea, F.; Houillon, F. B.; Pasquato, L.; Scrimin, P., Nanozymes: gold-nanoparticle-based transphosphorylation catalysts. *Angew. Chem. Int. Ed.* **2004,** *43* (45), 6165-9.
62. Czescik, J.; Lyu, Y.; Neuberg, S.; Scrimin, P.; Mancin, F., Host-Guest Allosteric Control of an Artificial Phosphatase. *J. Am. Chem. Soc.* **2020,** *142* (15), 6837-6841.
63. Zaupa, G.; Scrimin, P.; Prins, L. J., Origin of the dendritic effect in multivalent enzyme-like catalysts. *J. Am. Chem. Soc.* **2008,** *130* (17), 5699-709.
64. Martin, M.; Manea, F.; Fiammengo, R.; Prins, L. J.; Pasquato, L.; Scrimin, P., Metallodendrimers as transphosphorylation catalysts. *J. Am. Chem. Soc.* **2007,** *129* (22), 6982-3.
65. Bonomi, R.; Selvestrel, F.; Lombardo, V.; Sissi, C.; Polizzi, S.; Mancin, F.; Tonellato, U.; Scrimin, P., Phosphate diester and DNA hydrolysis by a multivalent, nanoparticle-based catalyst. *J. Am. Chem. Soc.* **2008,** *130* (47), 15744-5.
66. Solís-Muñana, P.; Salam, J.; Ren, C. Z.-J.; Carr, B.; Whitten, A. E.; Warr, G. G.; Chen, J. L.-Y., An Amphiphilic (salen)Co Complex – Utilizing Hydrophobic Interactions to Enhance the Efficiency of a Cooperative Catalyst. *Adv. Synth. Catal.* **2021,** *363*, 3207-3213.
67. Fischer, E., *Chem. Ber.* **1894,** *27*, 2985-2993.
68. Lichtenthaler, F. W., 100 Years "Schlussel-Schloss-Prinzip" : What Made Emil Fischer Use this Analogy? *Angew. Chem. Int. Ed.* **1994,** *33*, 2364-2374.
69. Pauling, L., Molecular architecture and biological reactions. *Chem. Eng. News,* **1946,** *46*, 1375-1377.
70. Pauling, L., Nature of forces between large molecules of biological interest. *Nature* **1948,** *161*, 707-709.
71. Koshland, D. E., Application of a Theory of Enzyme Specificity to Protein Synthesis. *Proc. Natl. Acad. Sci. USA* **1958,** *44* (2), 98-104.
72. Daniel E. Koshland, J., The key-lock theory and the induced fit theory. *Angew. Chem. Inl. Ed.* **1994,** *33*, 2375-2378.
73. Thoma, I. A.; Jr., D. E. K., Competitive Inhibition by Substrate during Enzyme Action. Evidence for the Inducedfit Theory. *J. Am. Chem. Soc.* **1960,** *82*, 3329.
74. Yankeelov, J. A., Jr.; Koshland, D. E., Jr., Evidence for Conformation Changes Induced by Substrates of Phosphoglucomutase. *J. Biol. Chem.* **1965,** *240*, 1593-602.
75. Straub, F. B.; Szabolcsi, G., *Molecular Biology, Problems and Perspectives*. Izdat. Nauka, Moscow, **1964**.
76. Závodszky, P.; Abaturov, L. V.; Varshavsky, Y. M., Structure of glyceraldehyde-3-phosphate dehydrogenase and its alteration by coenzyme binding. *Acta Biochim. Biophys. Sin.* **1966,**

1, 389-403.
77. Ma, B.; Kumar, S.; Tsai, C. J.; Nussinov, R., Folding funnels and binding mechanisms. *Protein Eng.* **1999,** *12* (9), 713-20.
78. Tsai, C. J.; Kumar, S.; Ma, B.; Nussinov, R., Folding funnels, binding funnels, and protein function. *Protein Sci.* **1999,** *8* (6), 1181-90.
79. Frauenfelder, H.; Sligar, S. G.; Wolynes, P. G., The energy landscapes and motions of proteins. *Science* **1991,** *254* (5038), 1598-603.
80. Lange, O. F.; Lakomek, N. A.; Fares, C.; Schroder, G. F.; Walter, K. F.; Becker, S.; Meiler, J.; Grubmuller, H.; Griesinger, C.; de Groot, B. L., Recognition dynamics up to microseconds revealed from an RDC-derived ubiquitin ensemble in solution. *Science* **2008,** *320* (5882), 1471-5.
81. Boehr, D. D.; Nussinov, R.; Wright, P. E., The role of dynamic conformational ensembles in biomolecular recognition. *Nat. Chem. Biol.* **2009,** *5* (11), 789-96.
82. Grunberg, R.; Leckner, J.; Nilges, M., Complementarity of structure ensembles in protein-protein binding. *Structure* **2004,** *12* (12), 2125-36.
83. Wlodarski, T.; Zagrovic, B., Conformational selection and induced fit mechanism underlie specificity in noncovalent interactions with ubiquitin. *Proc. Natl. Acad. Sci. USA* **2009,** *106* (46), 19346-51.
84. Csermely, P.; Palotai, R.; Nussinov, R., Induced fit, conformational selection and independent dynamic segments: an extended view of binding events. *Trends Biochem. Sci.* **2010,** *35* (10), 539-46.
85. Hammes, G. G.; Benkovic, S. J.; Hammes-Schiffer, S., Flexibility, diversity, and cooperativity: pillars of enzyme catalysis. *Biochemistry* **2011,** *50* (48), 10422-30.
86. Nagel, Z. D.; Klinman, J. P., A 21st century revisionist's view at a turning point in enzymology. *Nat Chem Biol* **2009,** *5* (8), 543-50.
87. Tokuriki, N.; Tawfik, D. S., Protein dynamism and evolvability. *Science* **2009,** *324* (5924), 203-7.
88. Sanders, J. K. M., Supramolecular catalysis in transition. *Chem-Eur J* **1998,** *4* (8), 1378-1383.
89. Solis Munana, P.; Ragazzon, G.; Dupont, J.; Ren, C. Z.-J.; Prins, L. J.; Chen, J. L.-Y., Substrate-Induced Self-Assembly of Cooperative Catalysts. *Angew. Chem. Int. Ed.* **2018,** *57* (50), 16469-16474.
90. Sams, P. J.; Wynjones, E.; Rassing, J., New Model Describing Kinetics of Micelle Formation from Chemical Relaxation Studies. *Chem. Phys. Lett.* **1972,** *13*, 233.
91. Aniansson, E. A. G.; Wall, S. N.; Almgren, M.; Hoffmann, H.; Kielmann, I.; Ulbricht, W.; Zana, R.; Lang, J.; Tondre, C., Theory of Kinetics of Micellar Equilibria and Quantitative Interpretation of Chemical Relaxation Studies of Micellar Solutions of Ionic Surfactants. *J. Phys. Chem.* **1976,** *80*, 905.
92. Thomas, J. K.; Grieser, F.; Wong, M., Fast Reactions in Micelles. *Ber. Bunsenges. Phys. Chem.* **1978,** *82*, 937.
93. Kornberg, R. D.; McConnell, H. M., Inside-outside transitions of phospholipids in vesicle membranes. *Biochemistry* **1971,** *10* (7), 1111-20.
94. McLean, L. R.; Phillips, M. C., Mechanism of cholesterol and phosphatidylcholine exchange or transfer between unilamellar vesicles. *Biochemistry* **1981,** *20* (10), 2893-900.

95. Ren, C. Z.-J.; Solis Munana, P.; Dupont, J.; Zhou, S. S.; Chen, J. L.-Y., Reversible Formation of a Light-Responsive Catalyst by Utilizing Intermolecular Cooperative Effects. *Angew. Chem. Int. Ed.* **2019,** *58* (43), 15254-15258.
96. Salvio, R., The guanidinium unit in the catalysis of phosphoryl transfer reactions: from molecular spacers to nanostructured supports. *Chemistry* **2015,** *21* (31), 10960-71.
97. Salvio, R.; Volpi, S.; Cacciapaglia, R.; Sansone, F.; Mandolini, L.; Casnati, A., Upper Rim Bifunctional cone-Calix[4]arenes Based on a Ligated Metal Ion and a Guanidinium Unit as DNAase and RNAase Mimics. *J. Org. Chem.* **2016,** *81* (11), 4728-35.
98. Salvio, R.; Cacciapaglia, R.; Mandolini, L.; Sansone, F.; Casnati, A., Diguanidinocalix[4]arenes as effective and selective catalysts of the cleavage of diribonucleoside monophosphates. *RSC Adv.* **2014,** *4*, 34412-34416.
99. Schug, K. A.; Lindner, W., Noncovalent Binding between Guanidinium and Anionic Groups: Focus on Biological- and Synthetic-Based Arginine/Guanidinium Interactions with Phosph[on]ate and Sulf[on]ate Residues. *Chem. Rev.* **2005,** *105*, 67-113.
100. Blondeau, P.; Segura, M.; Perez-Fernandez, R.; de Mendoza, J., Molecular recognition of oxoanions based on guanidinium receptors. *Chem. Soc. Rev.* **2007,** *36* (2), 198-210.
101. Cotton, F. A.; Hazen, E. E., Jr.; Legg, M. J., Staphylococcal nuclease: proposed mechanism of action based on structure of enzyme-thymidine 3',5'-bisphosphate-calcium ion complex at 1.5-A resolution. *Proc. Natl. Acad. Sci. USA* **1979,** *76* (6), 2551-5.
102. Schug, K. A.; Lindner, W., Noncovalent binding between guanidinium and anionic groups: focus on biological- and synthetic-based arginine/guanidinium interactions with phosph[on]ate and sulf[on]ate residues. *Chem. Rev.* **2005,** *105* (1), 67-114.
103. Best, M. D.; Tobey, S. L.; Anslyn, E. V., Abiotic guanidinium containing receptors for anionic species. *Coord. Chem. Rev.* **2003,** *240*, 3-15.
104. Baldini, L.; Cacciapaglia, R.; Casnati, A.; Mandolini, L.; Salvio, R.; Sansone, F.; Ungaro, R., Upper rim guanidinocalix[4]arenes as artificial phosphodiesterases. *J. Org. Chem.* **2012,** *77* (7), 3381-9.
105. Salvio, R.; Cincotti, A., Guanidine based self-assembled monolayers on Au nanoparticles as artificial phosphodiesterases. *RSC Adv.* **2014,** *4*, 28678-28682.
106. Avenier, F.; Domingos, J. B.; Vliet, L. D.; Hollfelder, F., Polyethylene imine derivatives ('synzymes') accelerate phosphate transfer in the absence of metal. *J. Am. Chem. Soc.* **2007,** *129* (24), 7611-9.
107. Ren, C. Z.-J.; Solís-Muñana, P.; Warr, G. G.; Chen, J. L.-Y., Dynamic and Modular Formation of a Synergistic Transphosphorylation Catalyst. *ACS Catal.* **2020,** *10*, 8395-8401.
108. Brown, D. M.; Usher, D. A., Hydrolysis of Hydroxyalkyl Phosphate Esters: Effect of Changing Ester Group *J. Chem. Soc.* **1965**, 6558-6564.
109. Pezzato, C.; Chen, J. L.; Galzerano, P.; Salvi, M.; Prins, L. J., Catalytic signal amplification for the discrimination of ATP and ADP using functionalised gold nanoparticles. *Org. Biomol. Chem.* **2016,** *14* (28), 6811-20.
110. Ghosh, S.; Krishnan, A.; Das, P. K.; Ramakrishnan, S., Determination of critical micelle concentration by hyper-rayleigh scattering. *J. Am. Chem. Soc.* **2003,** *125* (6), 1602-6.
111. Rodriguez, J. R.; Czapkiewicz, J., Conductivity and dynamic light scattering studies on homologous alkylbenzyldimethylammonium chlorides in aqueous solutions. *Colloids Surf. A: Physicochem. Eng. Asp.* **1995,** *101*, 107-111.

112. Ysambertt, F.; Vejar, F.; Paredes, J.; Salager, J.-L., The absorbance deviation method: a spectrophotometric estimation of the critical micelle concentration (CMC) of ethoxylated alkylphenol surfactants. *Colloids Surf. A: Physicochem. Eng. Asp.* **1998,** *137*, 189-196.
113. Scholz, N.; Behnke, T.; Resch-Genger, U., Determination of the Critical Micelle Concentration of Neutral and Ionic Surfactants with Fluorometry, Conductometry, and Surface Tension-A Method Comparison. *J. Fluoresc.* **2018,** *28* (1), 465-476.
114. J.V.Prazeres, T.; MarianaBeija; V.Fernandes, F.; G.A.Marcelino, P.; S.Farinha, J. P.; J.M.G.Martinho, Determination of the critical micelle concentration of surfactants and amphiphilic block copolymers using coumarin 153. *Inorganica Chim. Acta* **2012,** *381*, 181-187.
115. Stuart, M. C. A.; Pas, J. C. v. d.; Engberts, J. B. F. N., The use of Nile Red to monitor the aggregation behavior in ternary surfactant–water–organic solvent systems. *J. Phys. Org. Chem.* **2005,** *18*, 929-934.
116. Mehreteab, A.; Chen, B., Fluorescence technique for the determination of low critical micelle concentrations. *J. Am. Oil Chem. Soc.* **1995,** *72*, 49-52.
117. Wilcox, D. E., Binuclear Metallohydrolases. *Chem. Rev.* **1996,** *96* (7), 2435-2458.
118. He, J.; Hu, P.; Wang, Y. J.; Tong, M. L.; Sun, H.; Mao, Z. W.; Ji, L. N., Double-strand DNA cleavage by copper complexes of 2,2'-dipyridyl with guanidinium/ammonium pendants. *Dalton Trans.* **2008,** (24), 3207-14.
119. Tjioe, L.; Joshi, T.; Brugger, J.; Graham, B.; Spiccia, L., Synthesis, structure, and DNA cleavage properties of copper(II) complexes of 1,4,7-triazacyclononane ligands featuring pairs of guanidine pendants. *Inorg. Chem.* **2011,** *50* (2), 621-35.
120. Salvio, R.; Cacciapaglia, R.; Mandolini, L., General base-guanidinium cooperation in bifunctional artificial phosphodiesterases. *J. Org. Chem.* **2011,** *76* (13), 5438-43.
121. Kneeland, D. M.; Ariga, K.; Lynch, V. M.; Huang, C.-Y.; Anslyn, E. V., Bis(alkylguanidinium) Receptors for Phosphodiesters: Effect of Counterions, Solvent Mixtures, and Cavity Flexibility on Complexation. *J. Am. Chem. Soc.* **1993,** *115*, 10042-10055.
122. Ariga, K.; Anslyn, E. V., Manipulating the Stoichiometry and Strength of Phosphodiester Binding to a Bisguanidine Cleft in DMSO/Water Solutions. *J. Org. Chem.* **1992,** *57*, 417-419.
123. Poojari, C.; Wilkosz, N.; Lira, R. B.; Dimova, R.; Jurkiewicz, P.; Petka, R.; Kepczynski, M.; Rog, T., Behavior of the DPH fluorescence probe in membranes perturbed by drugs. *Chem. Phys. Lipids* **2019,** *223*, 104784.
124. Ait-Haddou, H.; Sumaoka, J.; Wiskur, S. L.; Folmer-Andersen, J. F.; Anslyn, E. V., Remarkable cooperativity between a ZnII ion and guanidinium/ammonium groups in the hydrolysis of RNA. *Angew. Chem. Int. Ed.* **2002,** *41* (21), 4013-6.
125. He, J.; Sun, J.; Mao, Z. W.; Ji, L. N.; Sun, H., Phosphodiester hydrolysis and specific DNA binding and cleavage promoted by guanidinium-functionalized zinc complexes. *J. Inorg. Biochem.* **2009,** *103* (5), 851-8.
126. Liu, S.; Hamilton, A. D., Catalysis of phosphodiester transesterification by Cu(II)-terpyridine complexes with peripheral pendent base groups: implications for the mechanism. *Tetrahedron Lett.* **1997,** *38*, 1107-1110.
127. Belousoff, M. J.; Tjioe, L.; Graham, B.; Spiccia, L., Synthesis, X-ray crystal structures, and phosphate ester cleavage properties of bis(2-pyridylmethyl)amine copper(II) complexes

with guanidinium pendant groups. *Inorg. Chem.* **2008,** *47* (19), 8641-51.
128. Czescik, J.; Zamolo, S.; Darbre, T.; Mancin, F.; Scrimin, P., Factors Influencing the Activity of Nanozymes in the Cleavage of an RNA Model Substrate. *Molecules* **2019,** *24* (15).
129. Sheng, X.; Lu, X. M.; Zhang, J. J.; Chen, Y. T.; Lu, G. Y.; Shao, Y.; Liu, F.; Xu, Q., Synthesis and DNA cleavage activity of artificial receptor 1,4,7-triazacyclononane containing guanidinoethyl and hydroxyethyl side arms. *J. Org. Chem.* **2007,** *72* (5), 1799-802.
130. Sessa, L.; Concilio, S.; Martino, M. D.; Nardiello, A. M.; Miele, Y.; Rossi, F.; Brunetti, J.; Panunzi, B.; Piotto, S., A selective Nile Red based solvatochromic probe: A study of fluorescence in LUVs and GUVs model membranes. *Dyes Pigm.* **2021,** *196*.
131. Förster, T., Energiewanderung und Fluoreszenz. *Naturwissenschaften* **1946,** *33*, 166-175.
132. Chen, B.; Su, Q.; Kong, W.; Wang, Y.; Shi, P.; Wang, F., Energy transfer-based biodetection using optical nanomaterials. *J. Mater. Chem. B* **2018,** *6* (19), 2924-2944.
133. Gambin, Y.; Deniz, A. A., Multicolor single-molecule FRET to explore protein folding and binding. *Mol. Biosyst.* **2010,** *6* (9), 1540-7.
134. Struck, D. K.; Hoekstra, D.; Pagano, R. E., Use of Resonance Energy Transfer To Monitor Membrane Fusion. *Biochemistry* **1981,** (20), 4093-4099.
135. Bernitzki, K.; Schrader, T., Entirely artificial signal transduction with a primary messenger. *Angew. Chem. Int. Ed.* **2009,** *48* (43), 8001-5.
136. Gruber, B.; Balk, S.; Stadlbauer, S.; Konig, B., Dynamic interface imprinting: high-affinity peptide binding sites assembled by analyte-induced recruiting of membrane receptors. *Angew. Chem. Int. Ed.* **2012,** *51* (40), 10060-3.
137. Chudakov, D. M.; Matz, M. V.; Lukyanov, S.; Lukyanov, K. A., Fluorescent Proteins and Their Applications in Imaging Living Cells and Tissues. *Physiol. Rev.* **2010,** *90*, 1103-1163.
138. Wolfbeis, O. S., An overview of nanoparticles commonly used in fluorescent bioimaging. *Chem. Soc. Rev.* **2015,** *44* (14), 4743-68.
139. Chan, J.; Dodani, S. C.; Chang, C. J., Reaction-based small-molecule fluorescent probes for chemoselective bioimaging. *Nat. Chem.* **2012,** *4* (12), 973-84.
140. Wang, L.; Frei, M. S.; Salim, A.; Johnsson, K., Small-Molecule Fluorescent Probes for Live-Cell Super-Resolution Microscopy. *J. Am. Chem. Soc.* **2019,** *141* (7), 2770-2781.
141. Pushina, M.; Farshbaf, S.; Shcherbakova, E. G.; Anzenbacher, P., A dual chromophore sensor for the detection of amines, diols, hydroxy acids, and amino alcohols. *Chem. Commun.* **2019,** *55* (31), 4495-4498.
142. He, L.; Lin, W.; Xu, Q.; Wei, H., A new strategy to construct a FRET platform for ratiometric sensing of hydrogen sulfide. *Chem. Commun.* **2015,** *51* (8), 1510-3.
143. Zhai, Q.; Yang, S.; Fang, Y.; Zhang, H.; Feng, G., A new ratiometric fluorescent probe for the detection of thiophenols. *RSC Adv.* **2015,** *5*, 94216-94221.
144. Dong, B.; Song, W.; Lu, Y.; Kong, X.; Mehmood, A. H.; Lin, W., An ultrasensitive ratiometric fluorescent probe based on the ICT-PET-FRET mechanism for the quantitative measurement of pH values in the endoplasmic reticulum (ER). *Chem Commun (Camb)* **2019,** *55* (72), 10776-10779.
145. Zhou, X.; Su, F.; Lu, H.; Senechal-Willis, P.; Tian, Y.; Johnson, R. H.; Meldrum, D. R., An FRET-based ratiometric chemosensor for in vitro cellular fluorescence analyses of pH. *Biomaterials* **2012,** *33* (1), 171-80.
146. Jose, J.; Tavares, C. D. J.; Ebelt, N. D.; Lodi, A.; Edupuganti, R.; Xie, X.; Devkota, A. K.; Kaoud,

T. S.; Berg, C. L. V. D.; Anslyn, E. V.; Tiziani, S.; Bartholomeusz, C.; Dalby, K. N., Serotonin Analogues as Inhibitors of Breast Cancer Cell Growth. *ACS Med. Chem. Lett.* **2017,** *8*, 1072-1076.

147. Düdükcü, M.; Yazici, B.; Erbil, M., The effect of indole on the corrosion behaviour of stainless steel. *Mater. Chem. Phys.* **2004,** *87*, 138-141.
148. Gibson, M. S.; Bradshaw, R. W., The Gabriel synthesis of primary amines. *Angew. Chem. Int. Ed.* **1968,** *7*, 919-930.
149. Zhao, X. X.; Zhang, J. F.; Liu, W.; Zhou, S.; Zhou, Z. Q.; Xiao, Y. H.; Xi, G.; Miao, J. Y.; Zhao, B. X., A unique dansyl-based chromogenic chemosensor for rapid and ultrasensitive hydrazine detection. *J Mater Chem B* **2014,** *2* (42), 7344-7350.
150. Rouhani, S.; Gharanjig, K.; Nezhad, M. H., Facile synthesis of 4-nitro-N-substituted-1,8-naphthalimide derivatives using ultrasound in aqueous media. *Green Chem. Lett. Rev.* **2014,** *7*, 174-178.
151. He, L.; Dong, B.; Liu, Y.; Lin, W., Fluorescent chemosensors manipulated by dual/triple interplaying sensing mechanisms. *Chem. Soc. Rev.* **2016,** *45* (23), 6449-6461.
152. Xu, Z.; Yoon, J.; Spring, D. R., Fluorescent chemosensors for Zn(2+). *Chem. Soc. Rev.* **2010,** *39* (6), 1996-2006.
153. Zhuang, X.; Ha, T.; Kim, H. D.; Centner, T.; Labeit, S.; Chu, S., Fluorescence quenching: A tool for single-molecule protein-folding study. *Proc Natl Acad Sci U S A* **2000,** *97* (26), 14241-4.
154. Birks, J. B., Excimers. *Rep. Prog. Phys.* **1975,** *38*, 903-974.
155. Chen, R. F.; Knutson, J. R., Mechanism of fluorescence concentration quenching of carboxyfluorescein in liposomes: energy transfer to nonfluorescent dimers. *Anal. Biochem.* **1988,** *172* (1), 61-77.
156. Benderskii, V. A.; Brikenshtein, V. K.; Lavrushko, A. G.; Filippov, P. G., Non-linear fluorescence quenching in molecular crystals I. Recombination of localized excitons. *Phys. Status Solidi* **1978,** *86*, 449-458.
157. Klymchenko, A. S., Emerging field of self-assembled fluorescent organic dye nanoparticles. *J. Nanosci. Lett.* **2013,** *3* (21).
158. Huang, Y.; Xing, J.; Gong, Q.; Chen, L. C.; Liu, G.; Yao, C.; Wang, Z.; Zhang, H. L.; Chen, Z.; Zhang, Q., Reducing aggregation caused quenching effect through co-assembly of PAH chromophores and molecular barriers. *Nat. Commun.* **2019,** *10* (1), 169.
159. Meher, N.; Iyer, P. K., Spontaneously Self-Assembled Naphthalimide Nanosheets: Aggregation-Induced Emission and Unveiling a-PET for Sensitive Detection of Organic Volatile Contaminants in Water. *Angew. Chem. Int. Ed.* **2018,** *57* (28), 8488-8492.
160. Chen, S.; Yu, Y. L.; Wang, J. H., Inner filter effect-based fluorescent sensing systems: A review. *Anal. Chim. Acta.* **2018,** *999*, 13-26.
161. Ghosh, M.; Nath, S.; Hajra, A.; Sinha, S., Fluorescence self-quenching of tetraphenylporphyrin in liquid medium. *J. Lumin.* **2013,** *141*, 87-92.
162. Lee, H.; Hancock, R. D.; Lee, H. S., Role of fluorophore-metal interaction in photoinduced electron transfer (PET) sensors: time-dependent density functional theory (TDDFT) study. *J. Phys. Chem. A* **2013,** *117* (50), 13345-55.
163. De Silva, S. A.; Zavaleta, A.; Baron, D. E.; Allam, O.; Isidor, E. V.; Kasbimura, N.; Percarpio, J. M., A Fluorescent Photoinduced Electron Transfer Sensor for Cations with an Off-On-

Off Proton Switch. *Tetrahedron Lett.* **1997**, 2237-2240.
164. Lee, H.; Lee, H. S.; Reibenspies, J. H.; Hancock, R. D., Mechanism of "turn-on" fluorescent sensors for mercury(II) in solution and its implications for ligand design. *Inorg. Chem.* **2012,** *51* (20), 10904-15.
165. Xu, Z.; Baek, K. H.; Kim, H. N.; Cui, J.; Qian, X.; Spring, D. R.; Shin, I.; Yoon, J., Zn2+ triggered amide tautomerization produces a highly Zn2+-selective, cell-permeable, and ratiometric fluorescent sensor. *J. Am. Chem. Soc.* **2010,** *132* (2), 601-10.
166. Weiss, J. H.; Sensi, S. L.; Koh, J. Y., Zn(2+): a novel ionic mediator of neural injury in brain disease. *Trends Pharmacol. Sci.* **2000,** *21* (10), 395-401.
167. Kikuchi, K.; Komatsu, K.; Nagano, T., Zinc sensing for cellular application. *Curr. Opin. Chem. Biol.* **2004,** *8* (2), 182-91.
168. Joshi, T.; Kubeil, M.; Nsubuga, A.; Singh, G.; Gasser, G.; Stephan, H., Harnessing the Coordination Chemistry of 1,4,7-Triazacyclononane for Biomimicry and Radiopharmaceutical Applications. *Chempluschem* **2018,** *83* (7), 554-564.
169. Chua, M. H.; 2, K. W. S.; Zhou, H.; Xu, J., Recent Advances in Aggregation-Induced Emission Chemosensors for Anion Sensing. *Molecules* **2019,** *24*, 2711.
170. Luo, J.; Xie, Z.; Lam, J. W.; Cheng, L.; Chen, H.; Qiu, C.; Kwok, H. S.; Zhan, X.; Liu, Y.; Zhu, D.; Tang, B. Z., Aggregation-induced emission of 1-methyl-1,2,3,4,5-pentaphenylsilole. *Chem. Commun.* **2001,** (18), 1740-1.
171. Tang, B. Z.; Zhan, X.; Yu, G.; Lee, P. P. S.; Liu, Y.; Zhu, D., Efficient blue emission from siloles. *J. Mater. Chem* **2001,** *11*, 2974-2978.
172. Chen, J.; Xu, B.; Ouyang, X.; Tang, B. Z.; Cao, Y., Aggregation-Induced Emission of cis,cis-1,2,3,4-Tetraphenylbutadiene from Restricted Intramolecular Rotation. *J. Phys. Chem. A* **2004,** *108*, 7522-7526.
173. Mei, J.; Hong, Y.; Lam, J. W.; Qin, A.; Tang, Y.; Tang, B. Z., Aggregation-induced emission: the whole is more brilliant than the parts. *Adv. Mater.* **2014,** *26* (31), 5429-79.
174. He, Z.; Ke, C.; Tang, B. Z., Journey of Aggregation-Induced Emission Research. *ACS Omega* **2018,** *3* (3), 3267-3277.
175. Sturala, J.; Etherington, M. K.; Bismillah, A. N.; Higginbotham, H. F.; Trewby, W.; Aguilar, J. A.; Bromley, E. H. C.; Avestro, A. J.; Monkman, A. P.; McGonigal, P. R., Excited-State Aromatic Interactions in the Aggregation-Induced Emission of Molecular Rotors. *J. Am. Chem. Soc.* **2017,** *139* (49), 17882-17889.
176. Liu, X.; Ngo, H. T.; Ge, Z.; Butler, S. J.; Jolliffe, K. A., Tuning colourimetric indicator displacement assays for naked-eye sensing of pyrophosphate in aqueous media. *Chem. Sci.* **2013,** *4*, 1680-1686.
177. Liu, X.; Smith, D. G.; Jolliffe, K. A., Are two better than one? Comparing intermolecular and intramolecular indicator displacement assays in pyrophosphate sensors. *Chem. Commun.* **2016,** *52* (54), 8463-6.
178. Zwicker, V. E.; Long, B. M.; Jolliffe, K. A., Selective sensing of pyrophosphate in physiological media using zinc(II)dipicolylamino-functionalised peptides. *Org Biomol Chem* **2015,** *13* (28), 7822-9.
179. Butler, S. J.; Jolliffe, K. A., Selective pyrophosphate recognition by cyclic peptide receptors in physiological saline. *Asian J. Chem.* **2012,** *7* (11), 2621-8.
180. Zhu, J. H.; Yu, C.; Chen, Y.; Shin, J.; Cao, Q. Y.; Kim, J. S., A self-assembled amphiphilic

imidazolium-based ATP probe. *Chem Commun (Camb)* **2017,** *53* (31), 4342-4345.
181. Rao, A. S.; Kim, D.; Nam, H.; Jo, H.; Kim, K. H.; Ban, C.; Ahn, K. H., A turn-on two-photon fluorescent probe for ATP and ADP. *Chem. Commun.* **2012,** *48* (26), 3206-8.
182. Tarbah, F. A.; Kardel, B.; Pier, S.; Temme, O.; Daldrup, T., Acute poisoning with phosphamidon: determination of dimethyl phosphate (DMP) as a stable metabolite in a case of organophosphate insecticide intoxication. *J. Anal. Toxicol.* **2004,** *28* (3), 198-203.
183. Yang, F. W.; Zhao, G. P.; Ren, F. Z.; Pang, G. F.; Li, Y. X., Assessment of the endocrine-disrupting effects of diethyl phosphate, a nonspecific metabolite of organophosphorus pesticides, by in vivo and in silico approaches. *Environ. Int.* **2020,** *135*, 105383.
184. Ueyama, J.; Saito, I.; Takaishi, A.; Nomura, H.; Inoue, M.; Osaka, A.; Sugiura, Y.; Hayashi, Y.; Wakusawa, S.; Ogi, H.; Inuzuka, K.; Kamijima, M.; Kondo, T., A revised method for determination of dialkylphosphate levels in human urine by solid-phase extraction and liquid chromatography with tandem mass spectrometry: application to human urine samples from Japanese children. *Environ. Health Prev. Med.* **2014,** *19* (6), 405-13.
185. Bravo, R.; Caltabiano, L. M.; Weerasekera, G.; Whitehead, R. D.; Fernandez, C.; Needham, L. L.; Bradman, A.; Barr, D. B., Measurement of dialkyl phosphate metabolites of organophosphorus pesticides in human urine using lyophilization with gas chromatography-tandem mass spectrometry and isotope dilution quantification. *J. expo. anal. environ. epidemiol.* **2004,** *14* (3), 249-59.
186. Wulff, G.; Gross, T.; Schonfeld, R., Enzyme Models Based on Molecularly Imprinted Polymers with Strong Esterase Activity. *Angew. Chem. Int. Ed.* **1997,** *36* (18), 1962-1964.
187. Brisig, B.; Sanders, J. K.; Otto, S., Selection and amplification of a catalyst from a dynamic combinatorial library. *Angew. Chem. Int. Ed.* **2003,** *42* (11), 1270-3.
188. Muller, A.; Konig, B., Vesicular aptasensor for the detection of thrombin. *Chem. Commun.* **2014,** *50* (84), 12665-8.
189. Anzenbacher, P., Jr.; Lubal, P.; Bucek, P.; Palacios, M. A.; Kozelkova, M. E., A practical approach to optical cross-reactive sensor arrays. *Chem. Soc. Rev.* **2010,** *39* (10), 3954-79.
190. Lavigne, J. J.; Anslyn, E. V., Sensing A Paradigm Shift in the Field of Molecular Recognition: From Selective to Differential Receptors. *Angew. Chem. Int. Ed.* **2001,** *40* (17), 3118-3130.
191. Wright, A. T.; Anslyn, E. V., Differential receptor arrays and assays for solution-based molecular recognition. *Chem. Soc. Rev.* **2006,** *35* (1), 14-28.
192. Kostereli, Z.; Scopelliti, R.; Severin, K., Correction: Pattern-based sensing of aminoglycosides with fluorescent amphiphiles. *Chem. Sci.* **2015,** *6* (1), 842.
193. Zwicker, V. E.; Sergeant, G. E.; New, E. J.; Jolliffe, K. A., A colorimetric sensor array for the classification of biologically relevant tri-, di- and mono-phosphates. *Org Biomol Chem* **2021,** *19* (5), 1017-1021.
194. Liu, Y.; Bonizzoni, M., A supramolecular sensing array for qualitative and quantitative analysis of organophosphates in water. *J. Am. Chem. Soc.* **2014,** *136* (40), 14223-9.
195. He, H.; Li, C.; Tian, Y.; Wu, P.; Hou, X., Phosphorescent Differential Sensing of Physiological Phosphates with Lanthanide Ions-Modified Mn-Doped ZnCdS Quantum Dots. *Anal. Chem.* **2016,** *88* (11), 5892-7.
196. Du, S. Z.; Sun, Z.; Han, L.; Qing, M.; Luo, H. Q.; Li, N. B., Two 3d-4f metal-organic frameworks as fluorescent sensor array for the discrimination of phosphates based on different response patterns. *Sens. Actuators B Chem.* **2020,** *324*, 128757.

197. Pezzato, C.; Lee, B.; Severin, K.; Prins, L. J., Pattern-based sensing of nucleotides with functionalized gold nanoparticles. *Chem. Commun.* **2013,** *49* (5), 469-71.
198. Sokolova, A.; Whitten, A. E.; Campo, L. d.; Christoforidis, J.; Eltobaji, A.; Barnes, J.; Darmann, F.; Berry, A., Performance and characteristics of the BILBY timeof-flight small-angle neutron scattering instrument. *J. Appl. Cryst.* **2019,** *52*, 1-12.
199. Poznik, M.; Konig, B., Cooperative hydrolysis of aryl esters on functionalized membrane surfaces and in micellar solutions. *Org. Biomol. Chem.* **2014,** *12* (20), 3175-80.
200. Ohara, K.; Vasseur, J.-J.; Smietana, M., NIS-promoted guanylation of amines. *Tet. Lett.* **2009,** *50*, 1463-1465.
201. Brown, D. M.; Usher, D. A., Hydrolysis of Hydroxyalkyl Phosphate Esters: Effect of Changing Ester Group. *J. Chem. Soc.* **1965**, 6558-6564.
202. Tjioe, L.; Joshi, T.; Forsyth, C. M.; Moubaraki, B.; Murray, K. S.; Brugger, J.; Graham, B.; Spiccia, L., Phosphodiester cleavage properties of copper(II) complexes of 1,4,7-triazacyclononane ligands bearing single alkyl guanidine pendants. *Inorg. Chem.* **2012,** *51* (2), 939-53.
203. Tsukamoto, K.; Shimabukuro, S.; Mabuchi, M.; Maeda, H., A Naphthalimide-Based Cd(2+) Fluorescent Probe with Carbamoylmethyl Groups Working as Chelators and PET-Promoters under Neutral Conditions. *Chemistry* **2016,** *22* (25), 8579-85.

Appendix

Part A NMR for Synthesis of amphiphiles for multifunctional catalysts

***N*,*N*'-Bis(*tert*-butoxycarbonyl)-*N*''-hexadecylguanidine 27**

^{1}H NMR (400 MHz, $CDCl_3$)

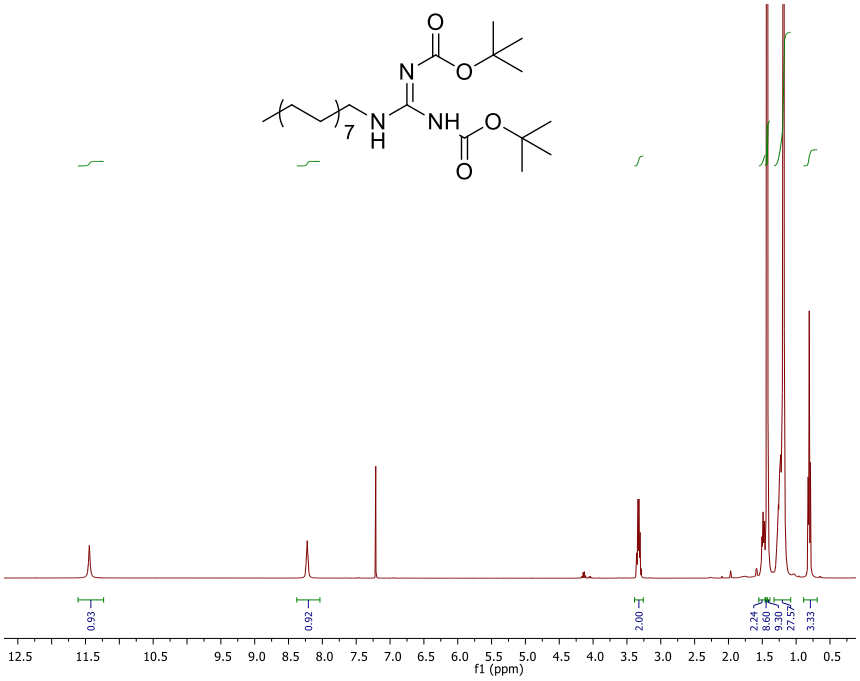

^{13}C NMR (100 MHz, $CDCl_3$)

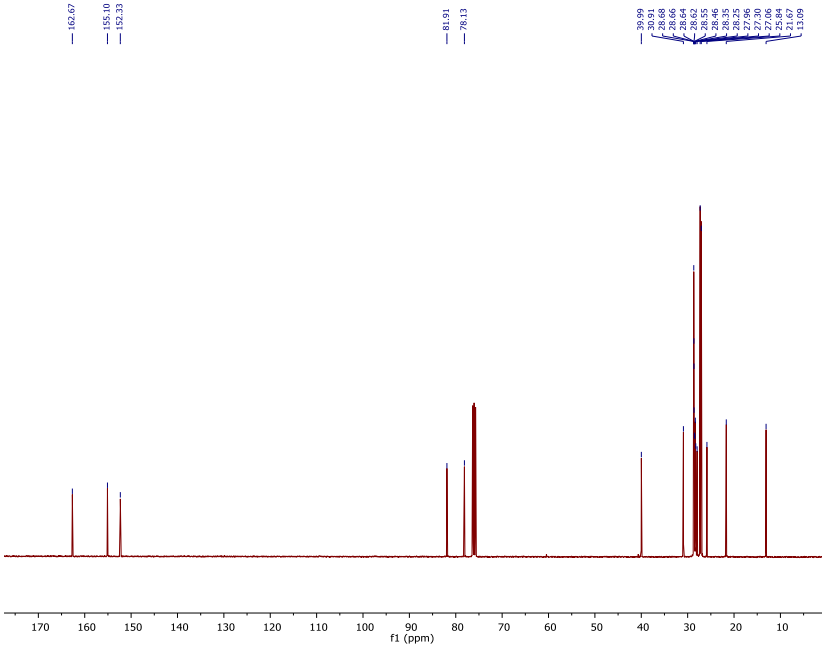

1-Hexadecylguanidinium chloride 23

^{1}H NMR (400 MHz, CD_3OD)

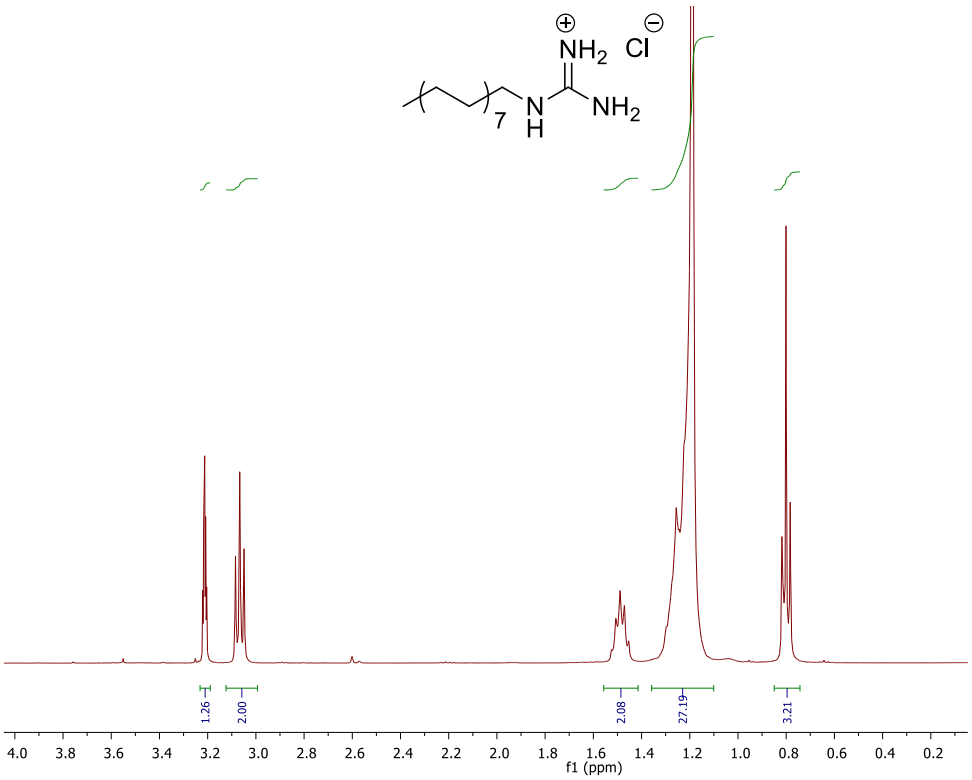

^{13}C NMR (100 MHz, CD_3OD)

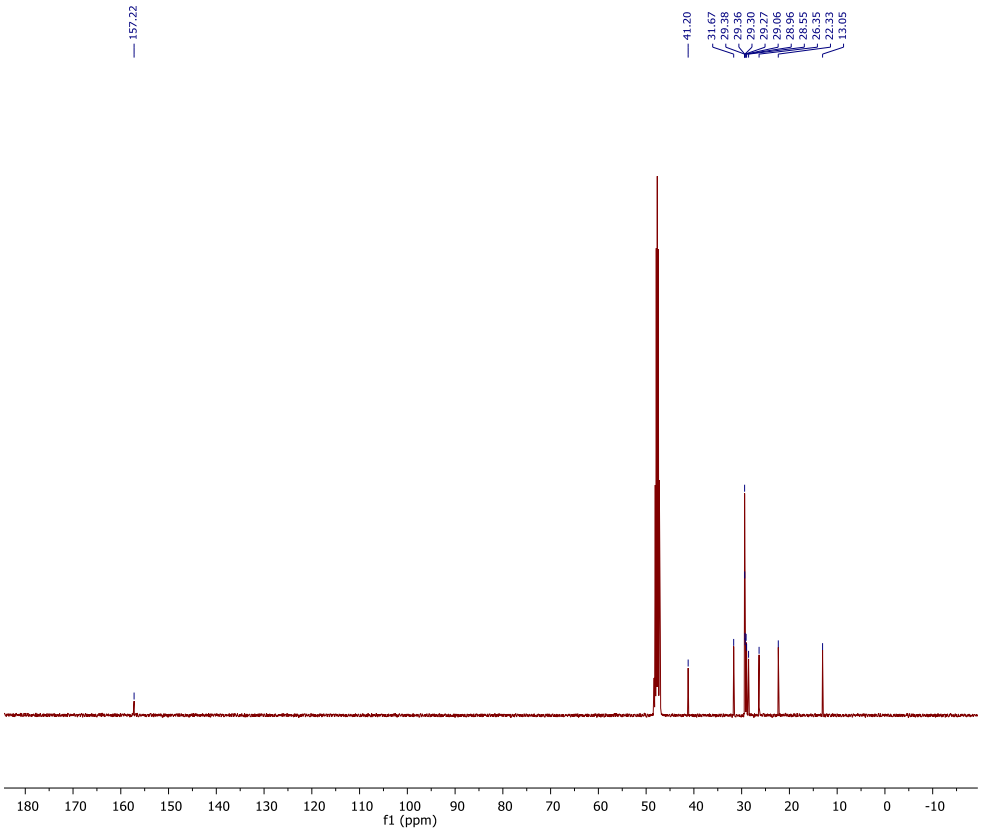

_N_,_N_'-Bis(_tert_-butoxycarbonyl)-_N_''-butylguanidine 28

^{1}H NMR (400 MHz, $CDCl_3$)

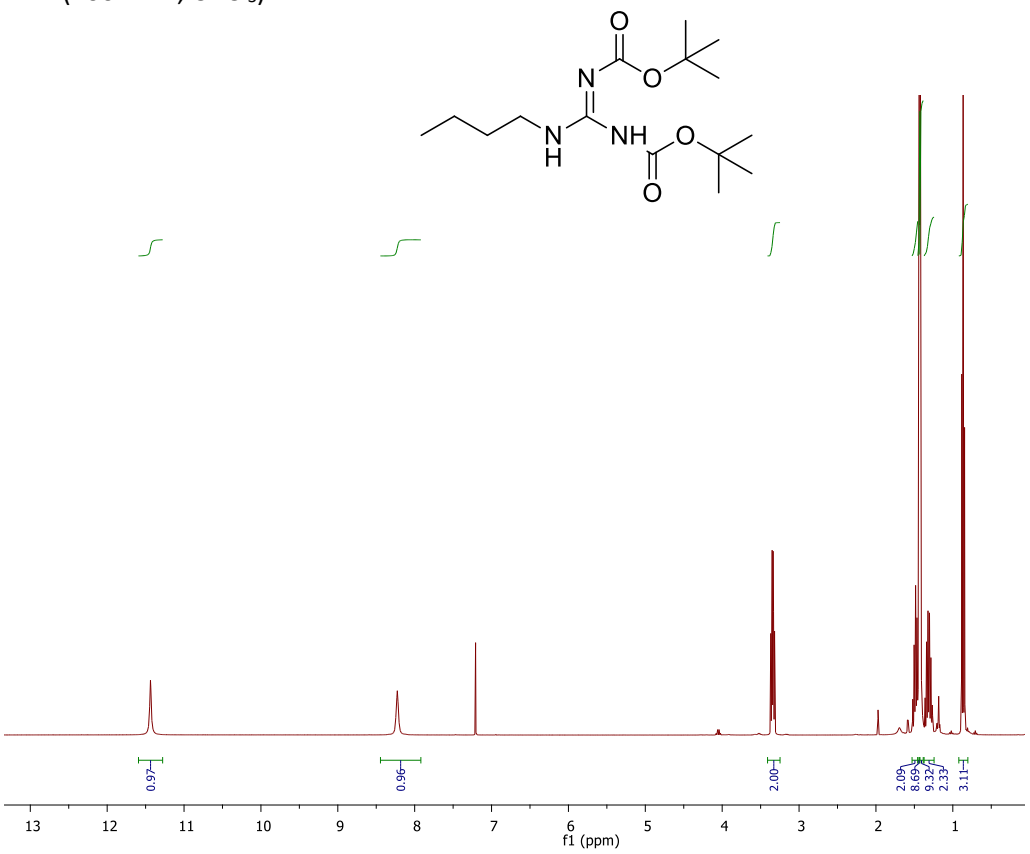

^{13}C NMR (100 MHz, $CDCl_3$)

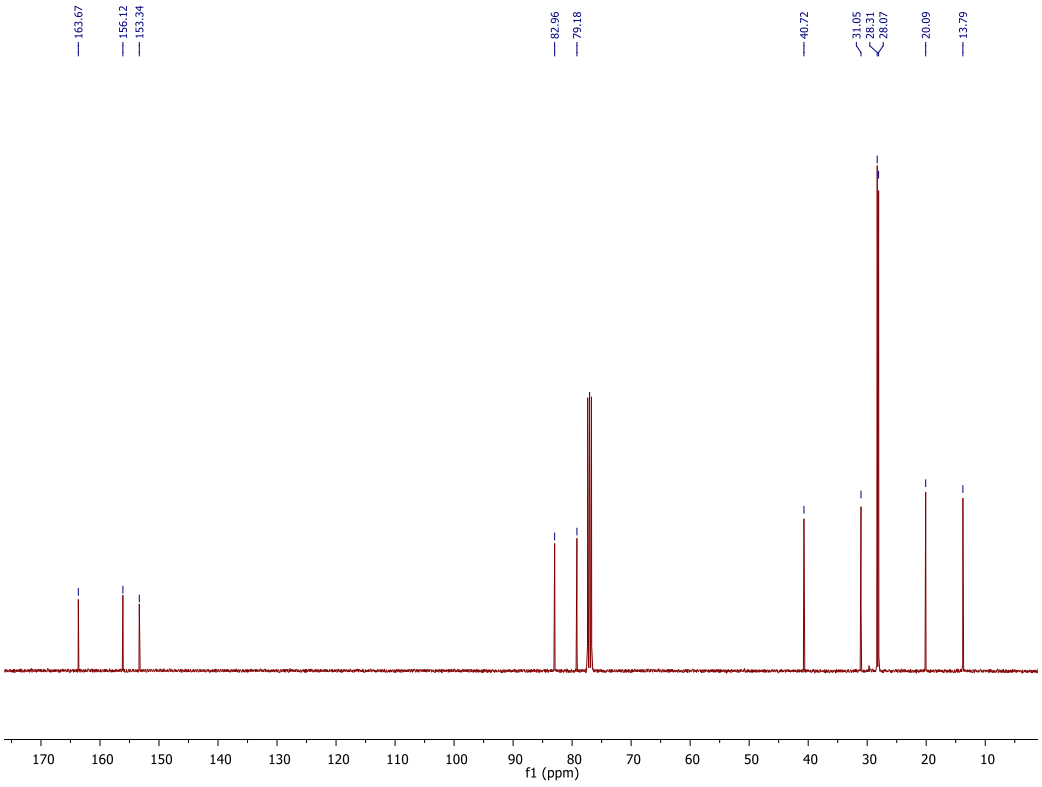

1-Butylguanidinium chloride 29

^{1}H NMR (400 MHz, CD_3OD)

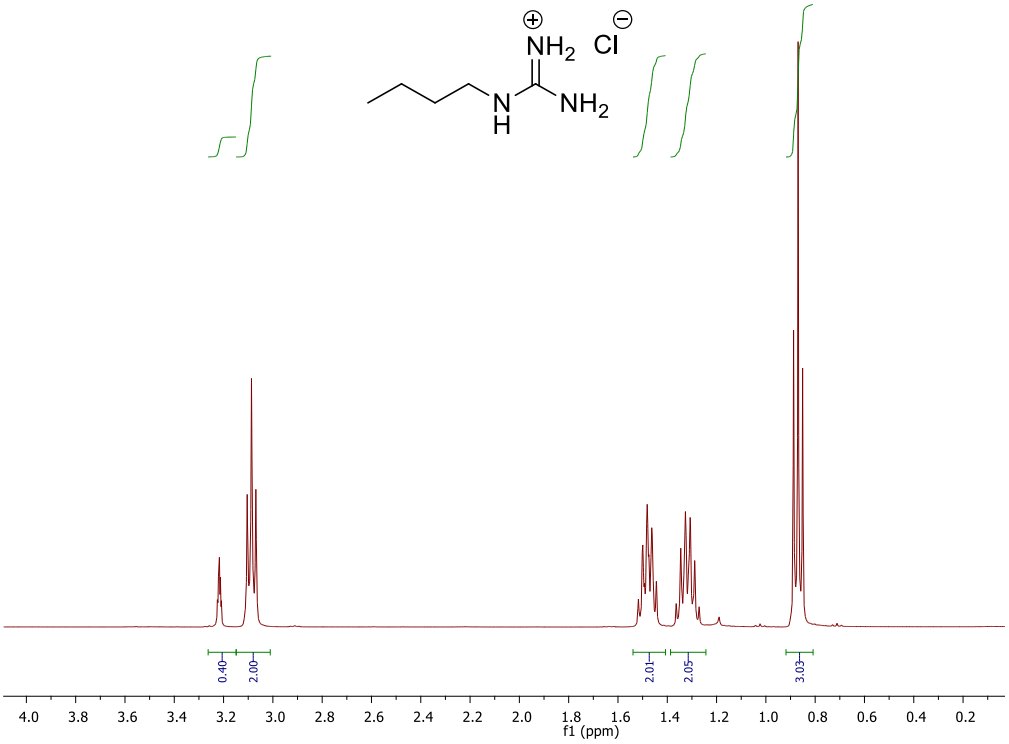

^{13}C NMR (100 MHz, CD_3OD)

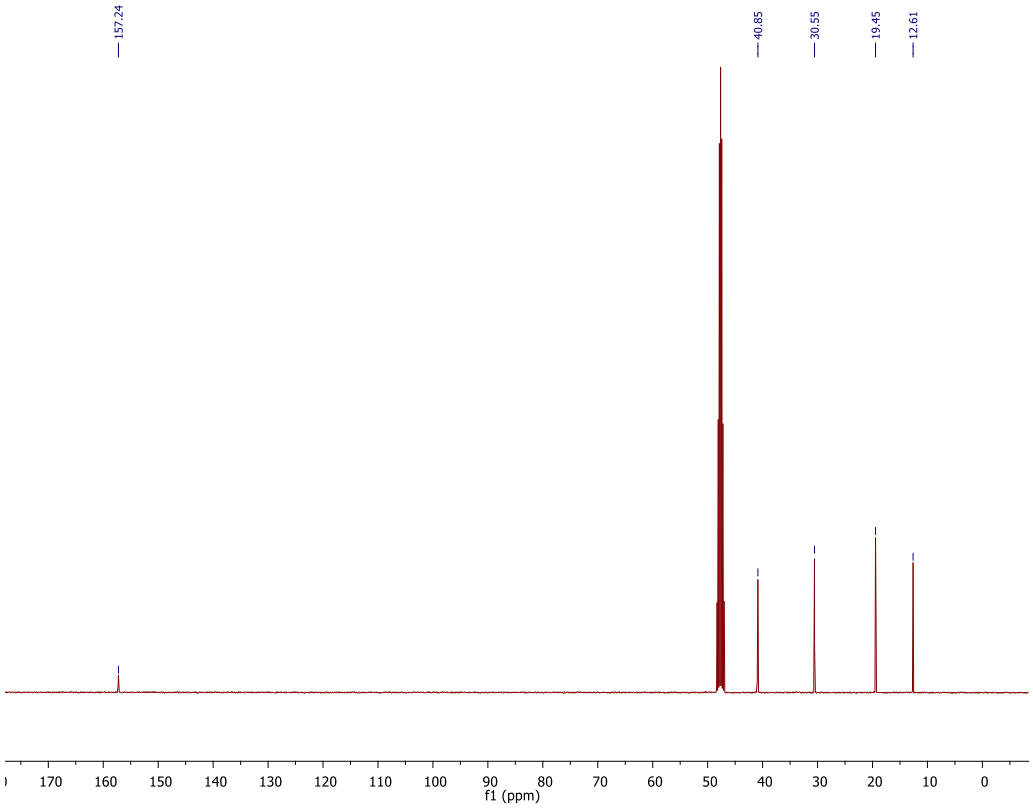

2-Hydroxypropyl *p*-nitrophenyl phosphate (HPNPP)

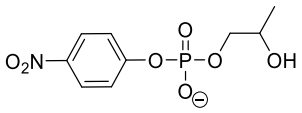

^{1}H NMR (400 MHz, D_2O)

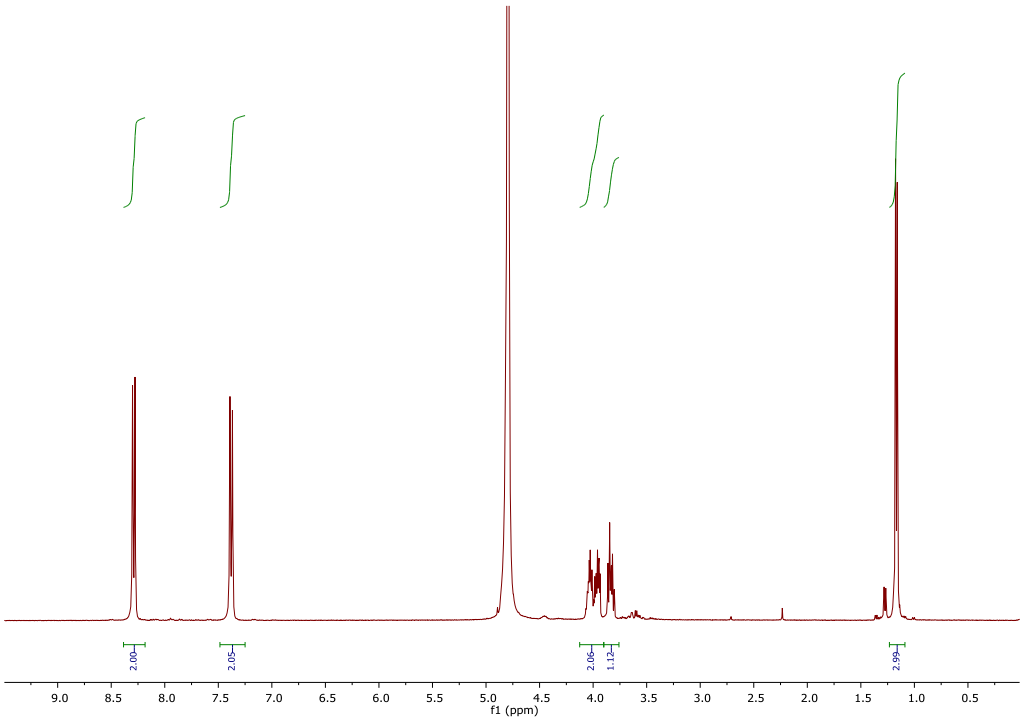

^{13}C NMR (100 MHz, D_2O)

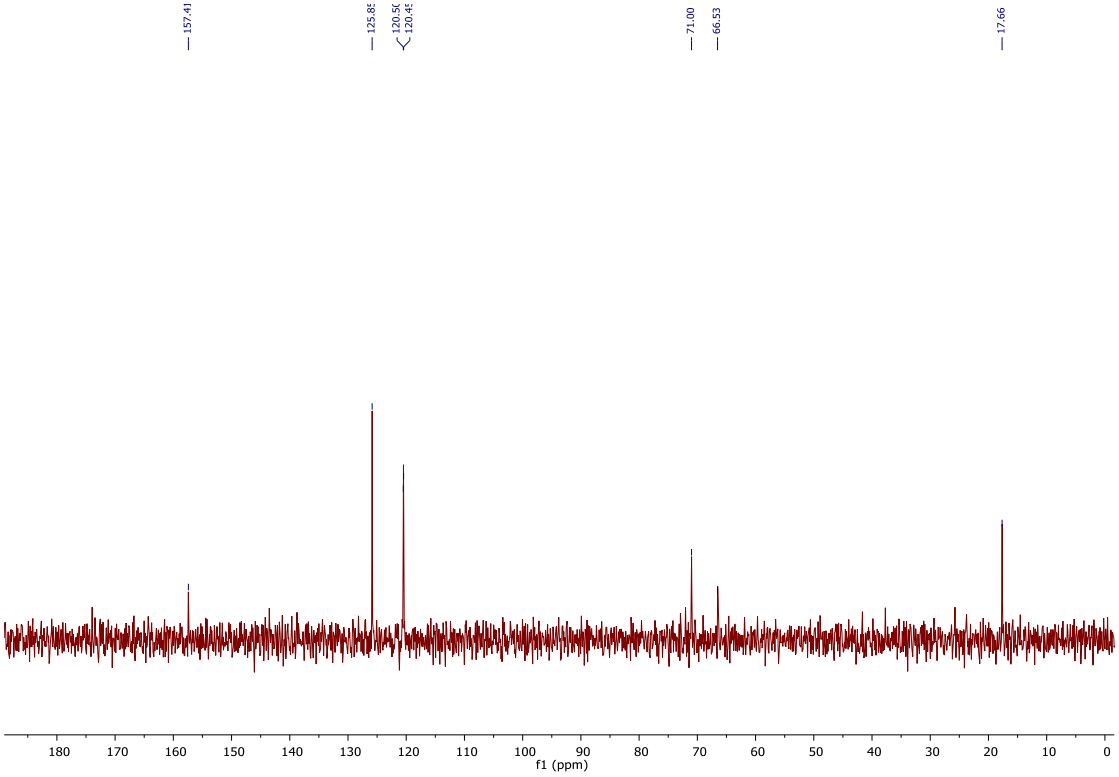

4-Nitrophenyl propyl hydrogen phosphate (Model HPNPP)

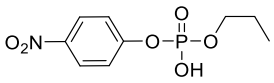

^{1}H NMR (400 MHz, D_2O)

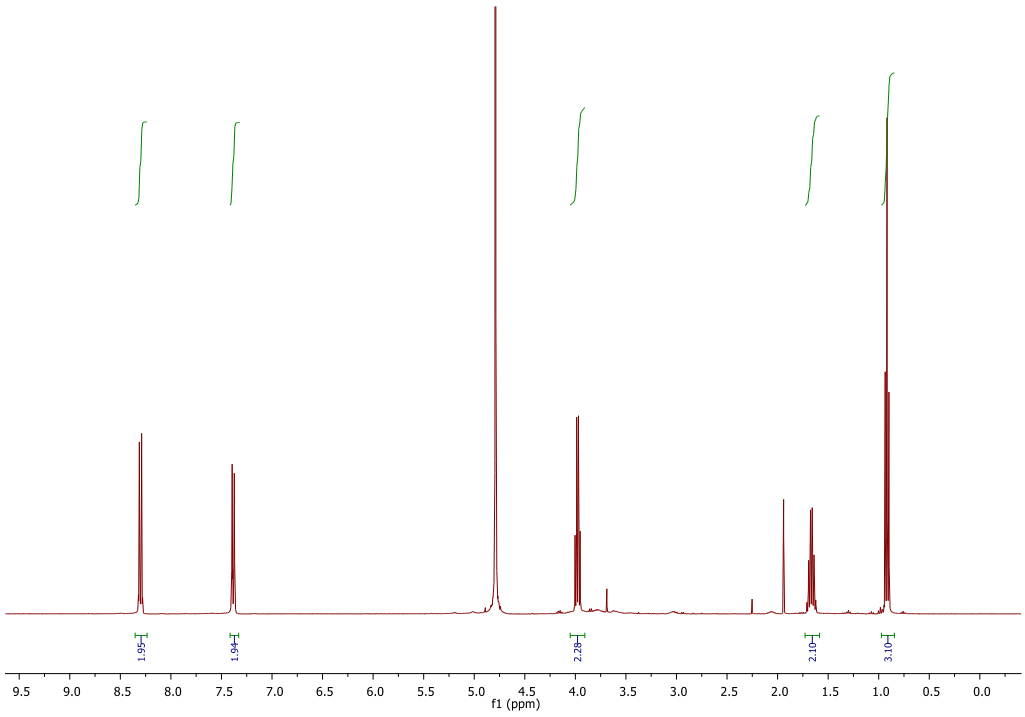

^{13}C NMR (100 MHz, D_2O)

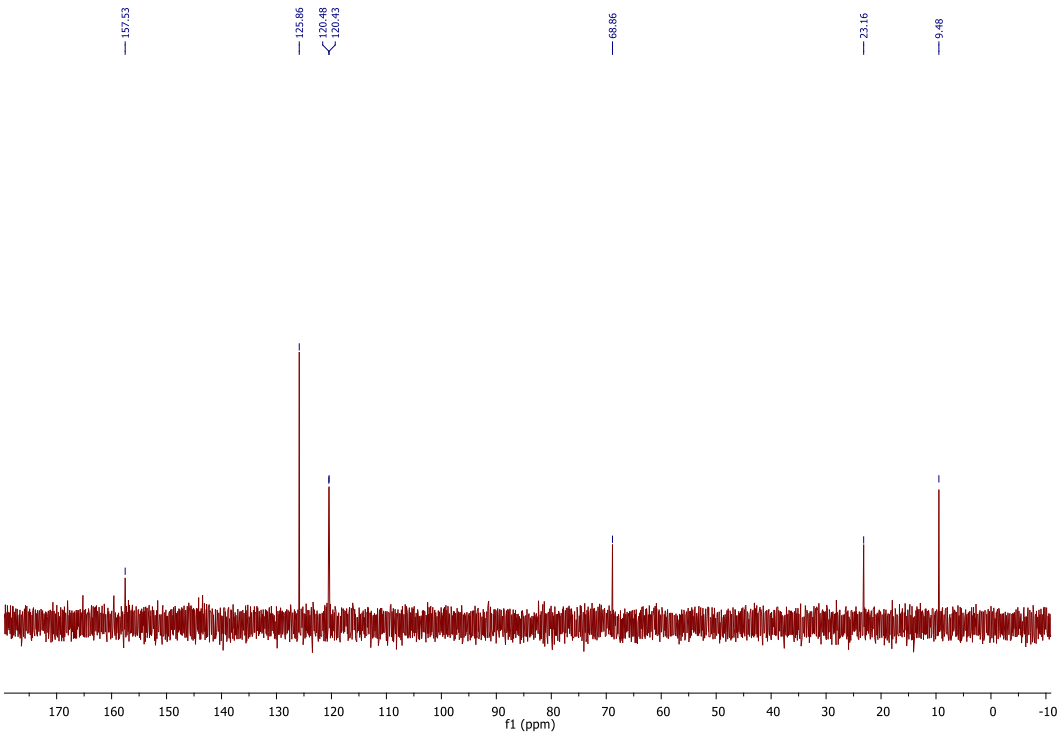

Part B NMR for Synthesis of FRET amphiphiles

di-tert-Butyl 1,4,7-triazonane-1,4-dicarboxylate 58

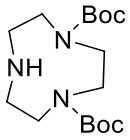

^{1}H NMR (400 MHz, $CDCl_3$)

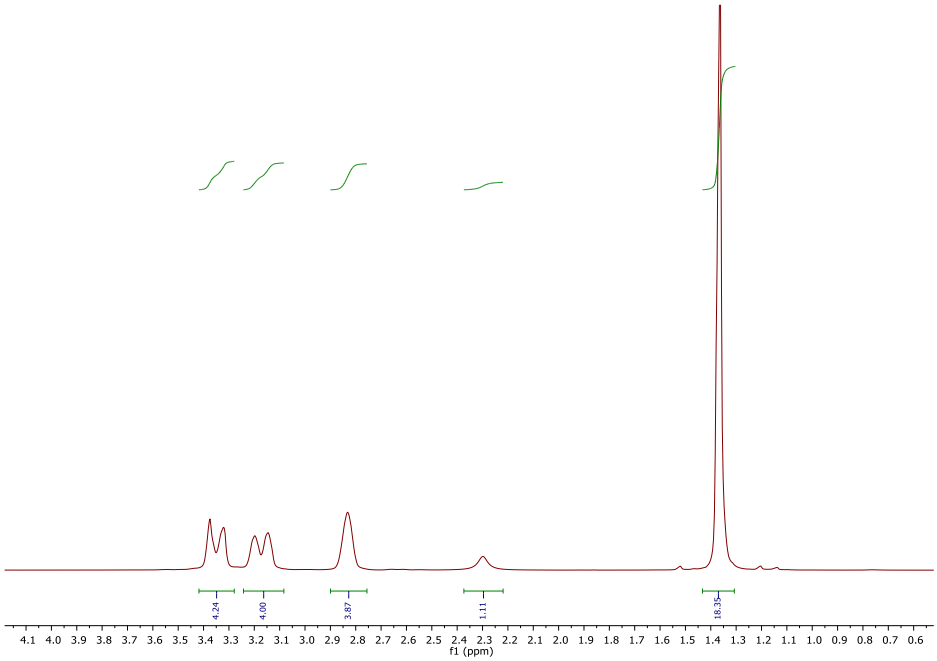

^{13}C NMR (100 MHz, $CDCl_3$)

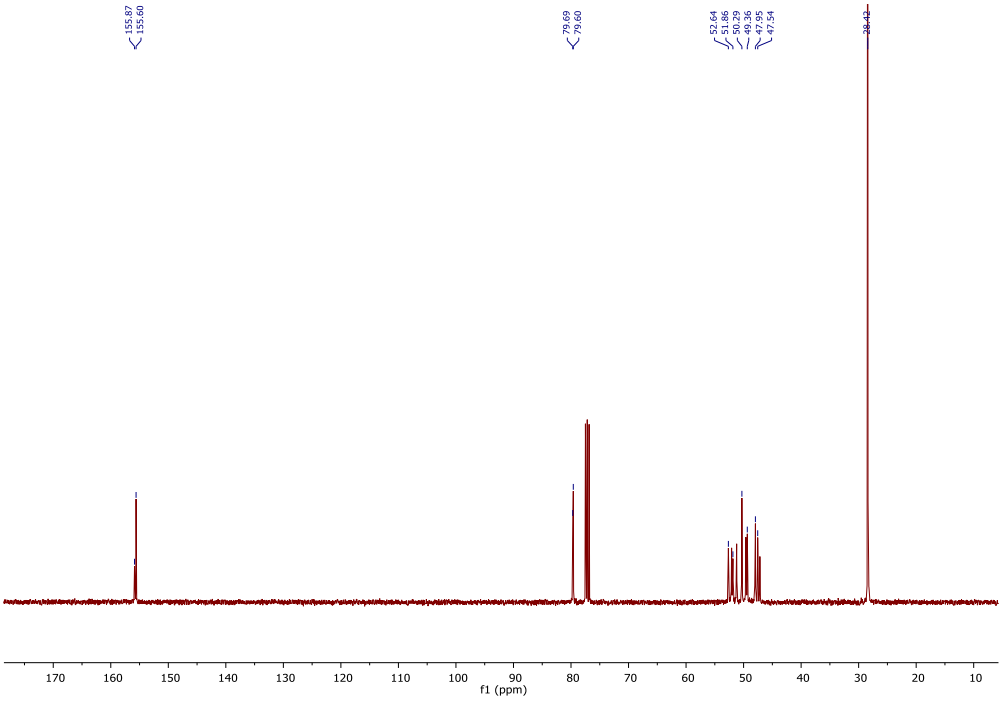

di-tert-Butyl 7-(3-(1,3-dioxoisoindolin-2-yl)propyl)-1,4,7-triazonane-1,4-dicarboxylate 68

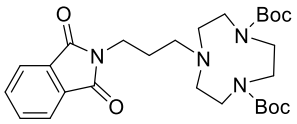

^{1}H NMR (400 MHz, $CDCl_3$)

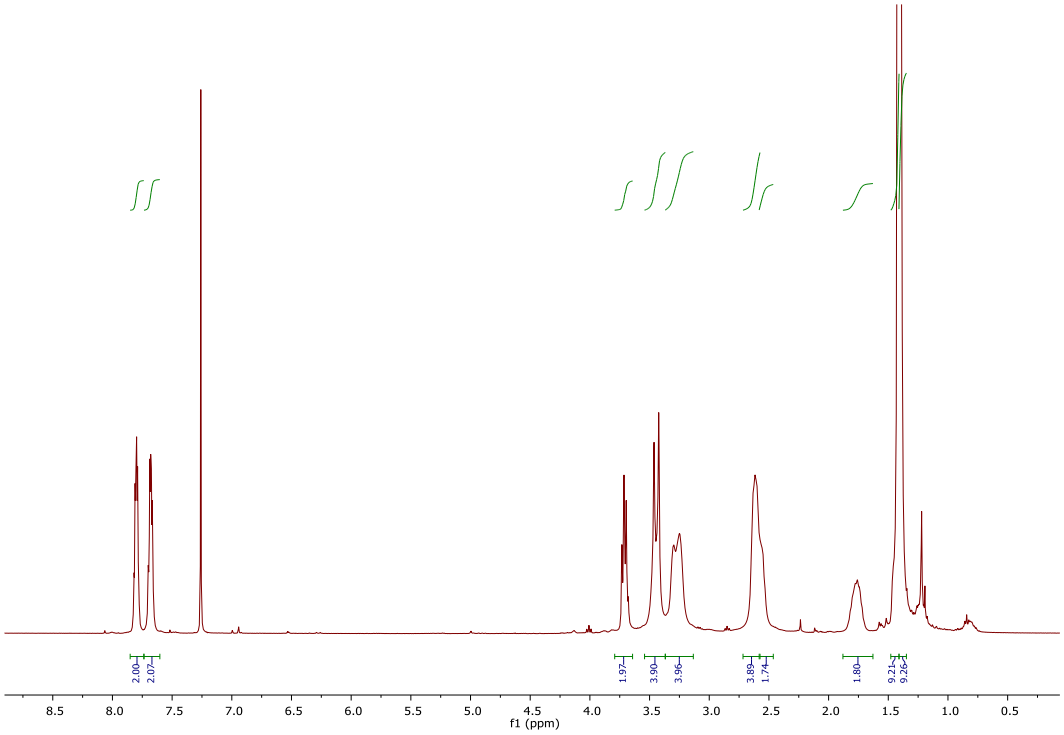

^{13}C NMR (100 MHz, $CDCl_3$)

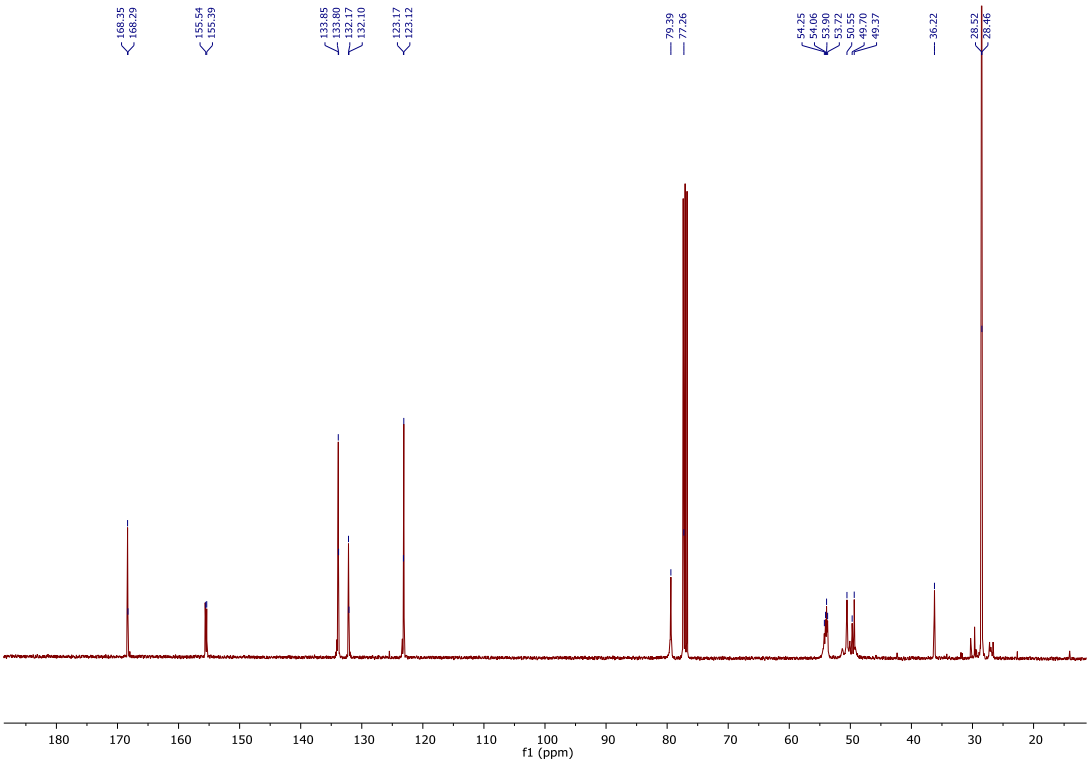

di-tert-Butyl 7-(3-aminopropyl)-1,4,7-triazonane-1,4-dicarboxylate 69

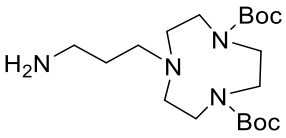

^{1}H NMR (400 MHz, $CDCl_3$)

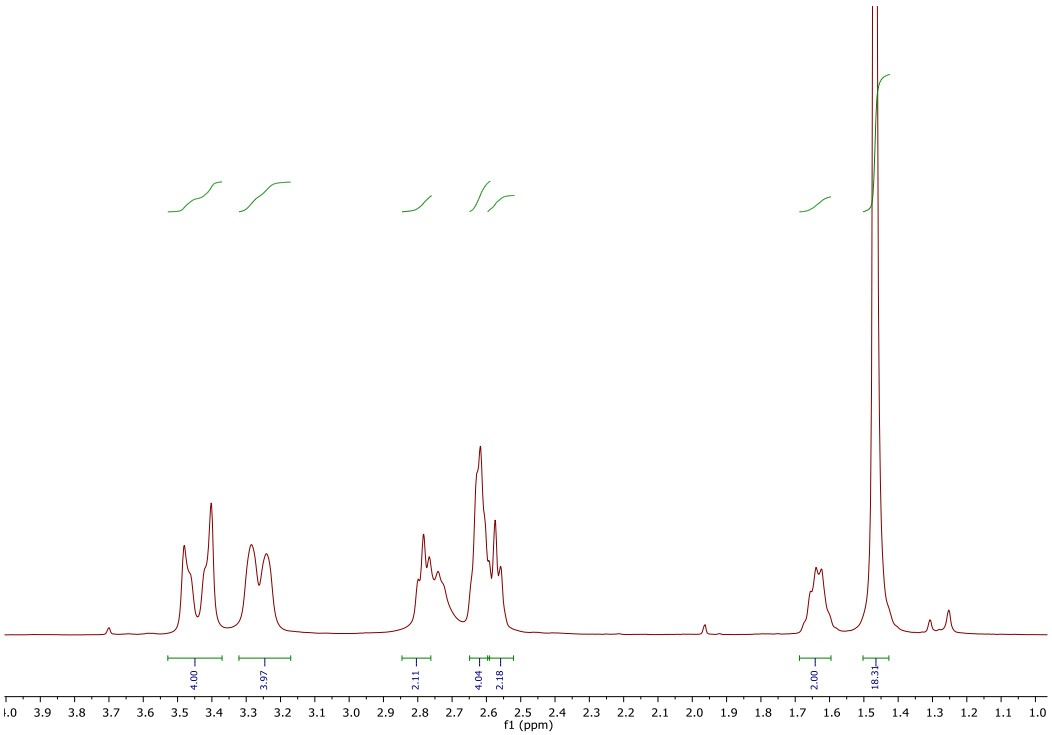

^{13}C NMR (100 MHz, $CDCl_3$)

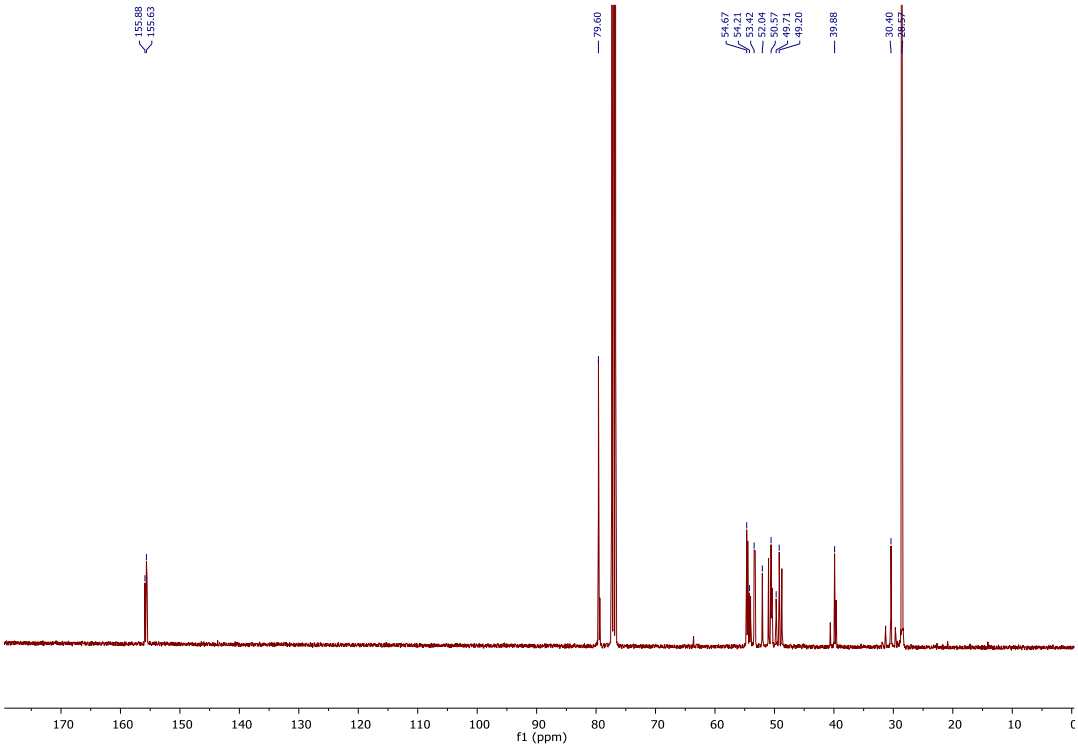

di-tert-Butyl 7-(3-(2-(7-hydroxy-2-oxo-2H-chromen-4-yl)acetamido)propyl)-1,4,7-triazonane-1,4-dicarboxylate 71

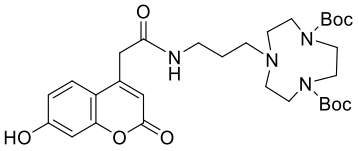

^{1}H NMR (400 MHz, $CDCl_3$)

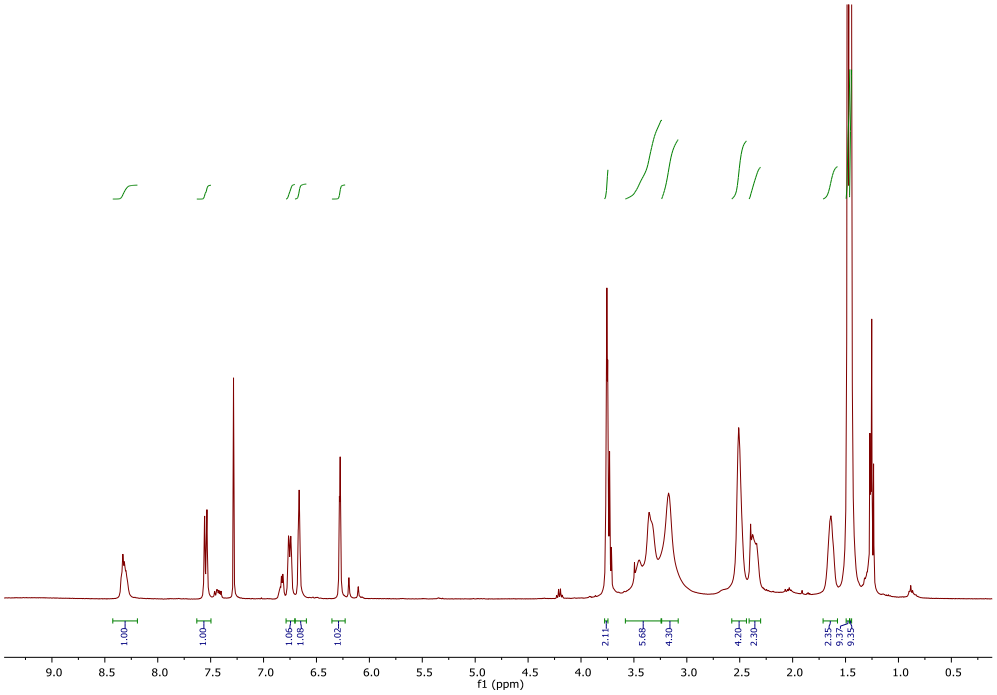

^{13}C NMR (100 MHz, $CDCl_3$)

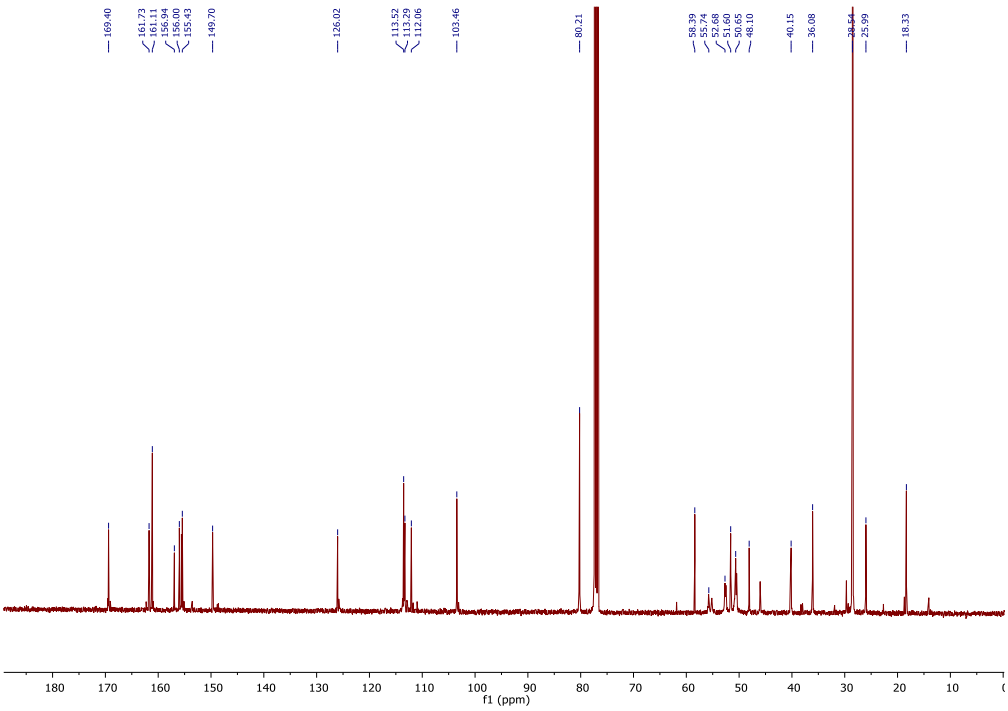

_N_-(3-(1,4,7-Triazonan-1-yl)propyl)-2-(7-hydroxy-2-oxo-2H-chromen-4-yl)acetamide trihydrochloride 96

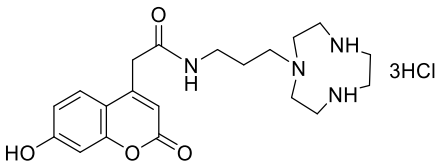

^{1}H NMR (400 MHz, D_2O)

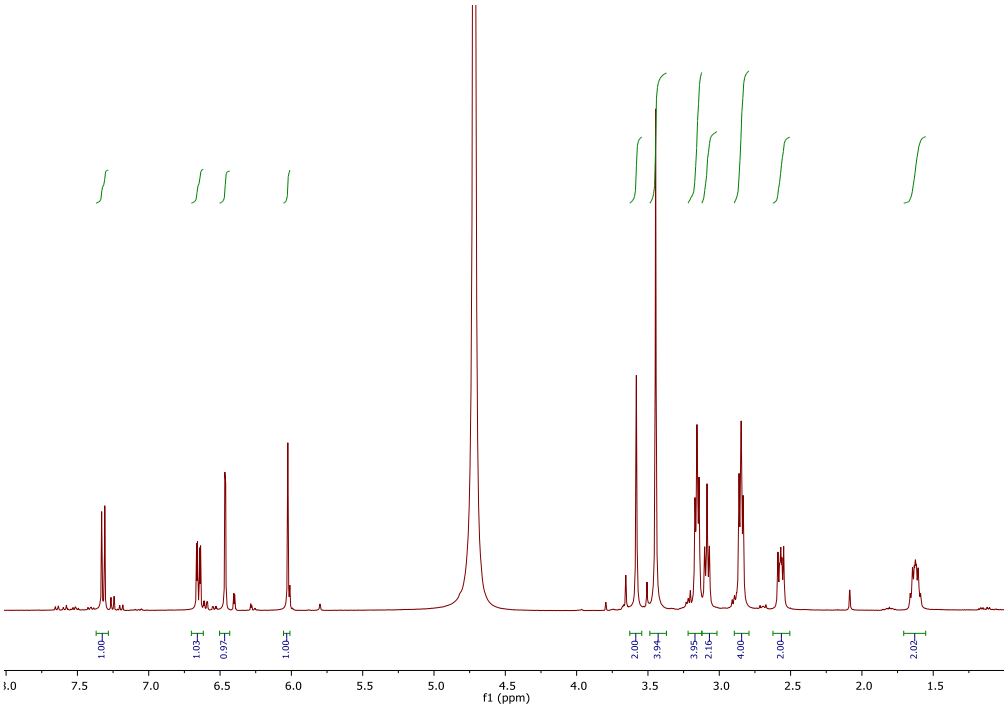

^{13}C NMR (100 MHz, D_2O)

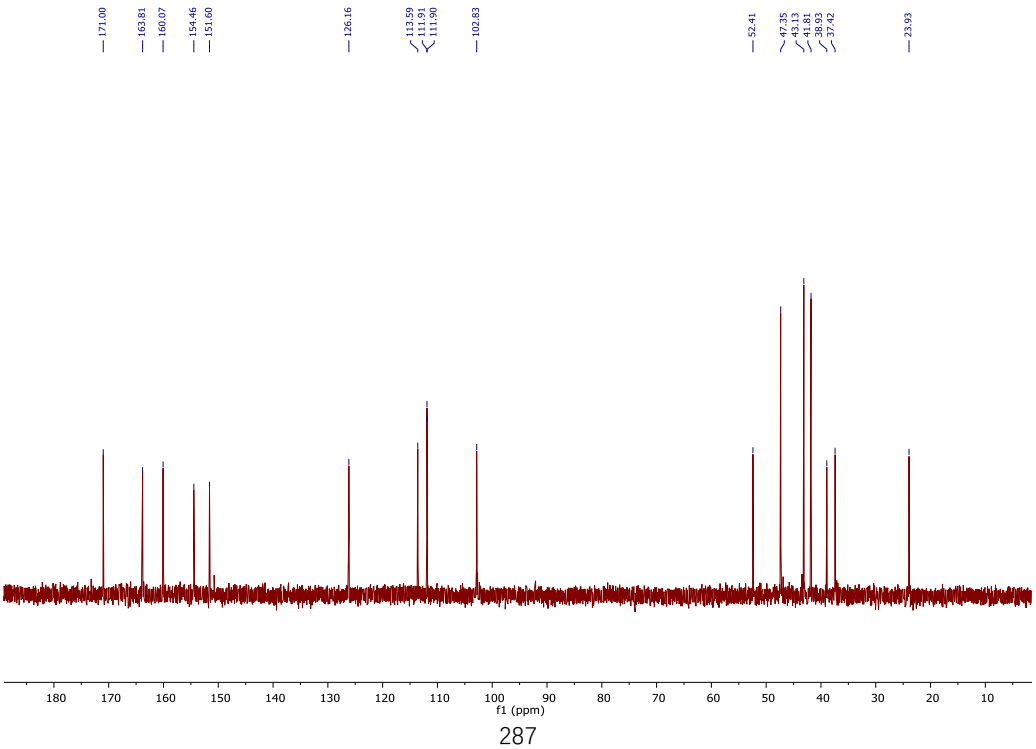

di-tert-Butyl 7-(3-(2-(7-(dodecyloxy)-2-oxo-2H-chromen-4-yl)acetamido)propyl)-1,4,7-triazonane-1,4-dicarboxylate 72

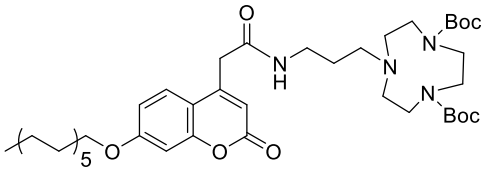

^{1}H NMR (400 MHz, $CDCl_3$)

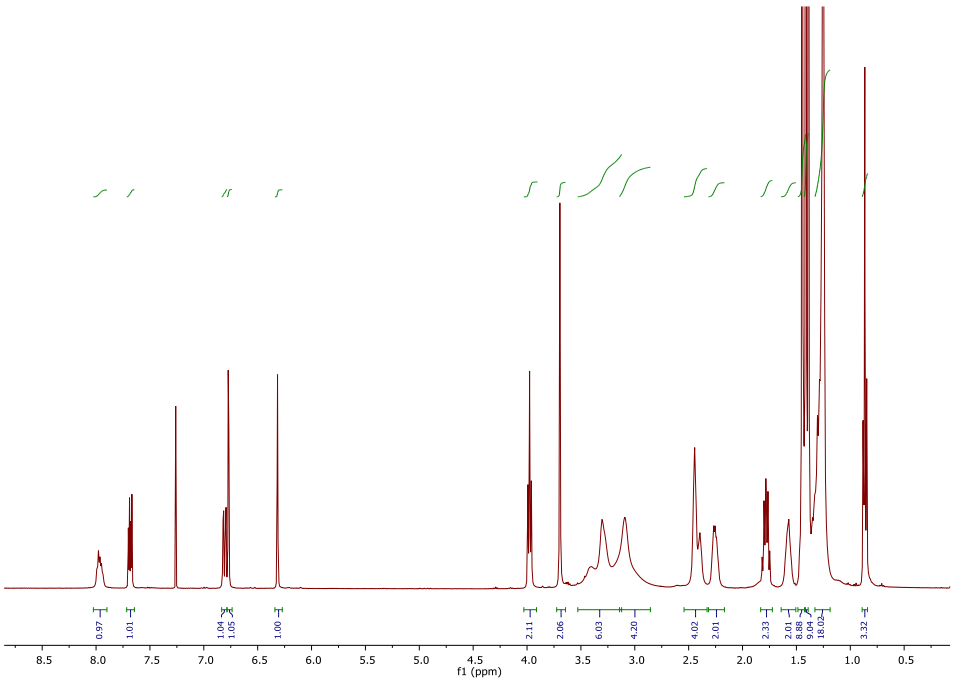

^{13}C NMR (100 MHz, $CDCl_3$)

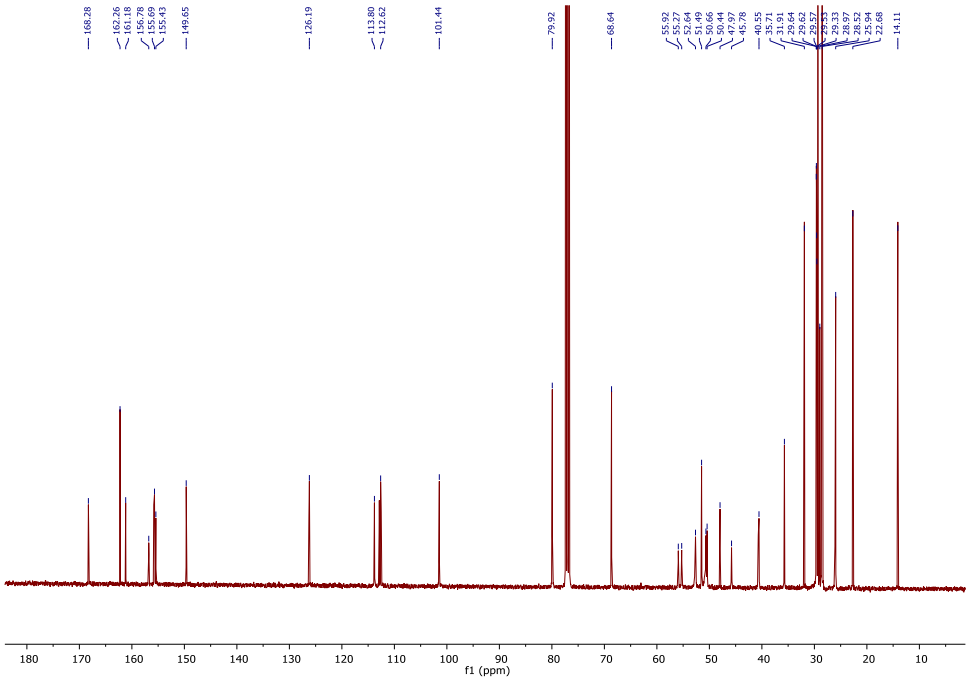

_N_-(3-(1,4,7-Triazonan-1-yl)propyl)-2-(7-(dodecyloxy)-2-oxo-2H-chromen-4-yl)acetamide trihydrochloride 97

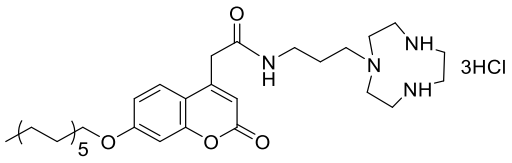

^{1}H NMR (400 MHz, CD_3OD)

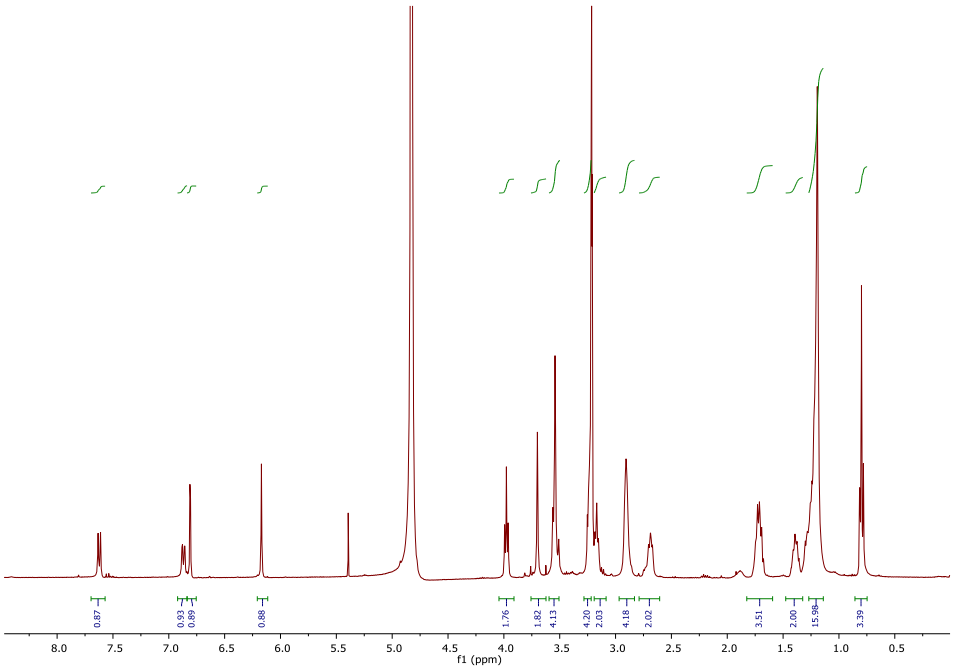

^{13}C NMR (100 MHz, CD_3OD)

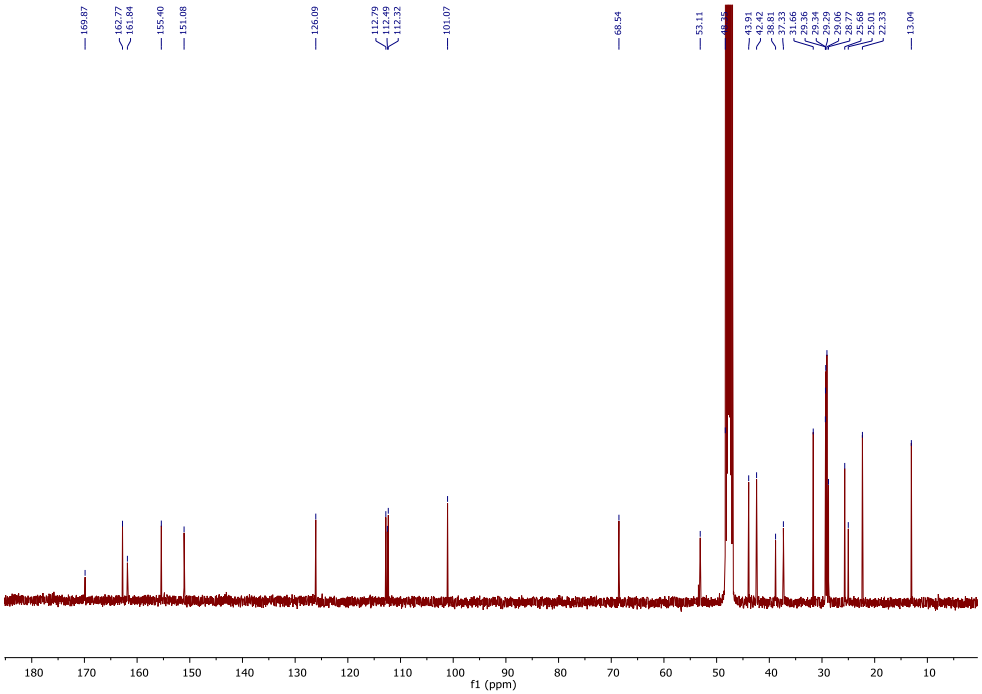

***N*-(3-(1,4,7-Triazonan-1-yl)propyl)-2-(7-butoxy-2-oxo-2H-chromen-4-yl)acetamide trihydrochloride 97**

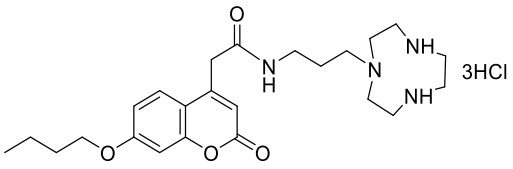

^{1}H NMR (400 MHz, D_2O)

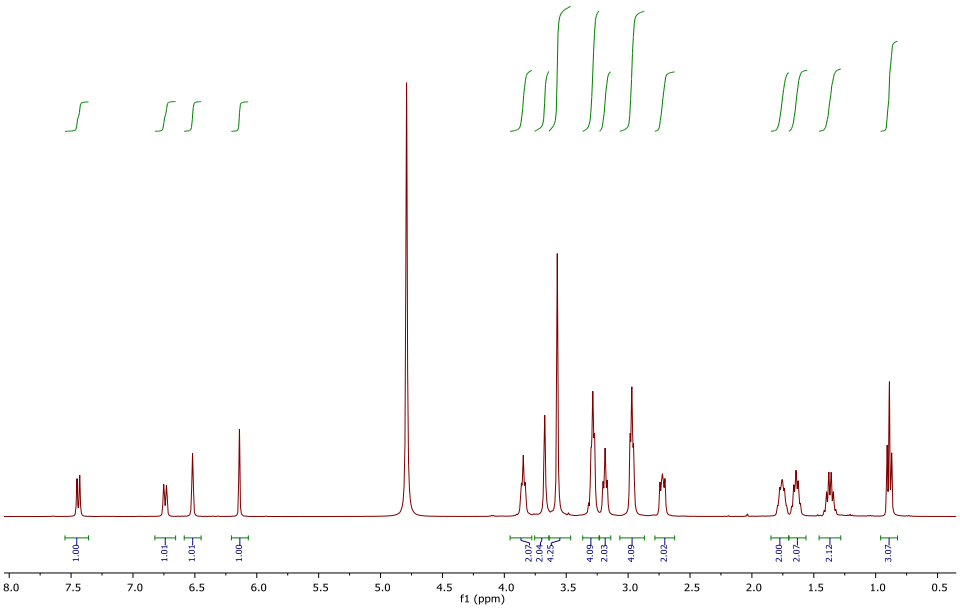

^{13}C NMR (100 MHz, D_2O)

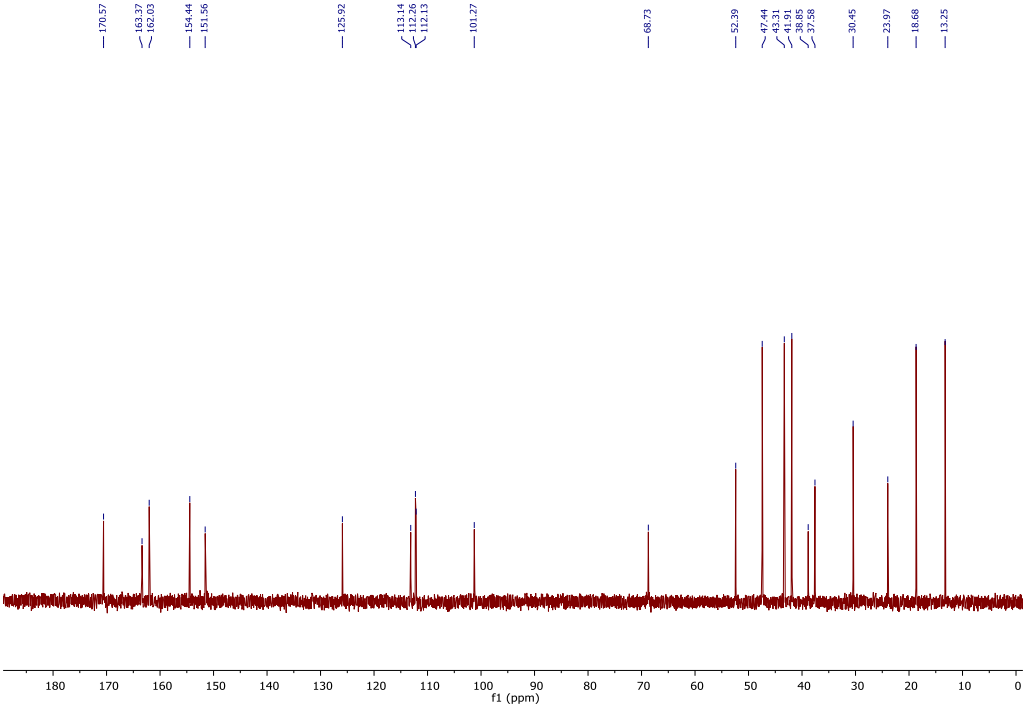

6-Hydroxy-1H,3H-benzo[de]isochromene-1,3-dione 81

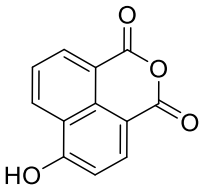

^{1}H NMR (400 MHz, DMSO-d6)

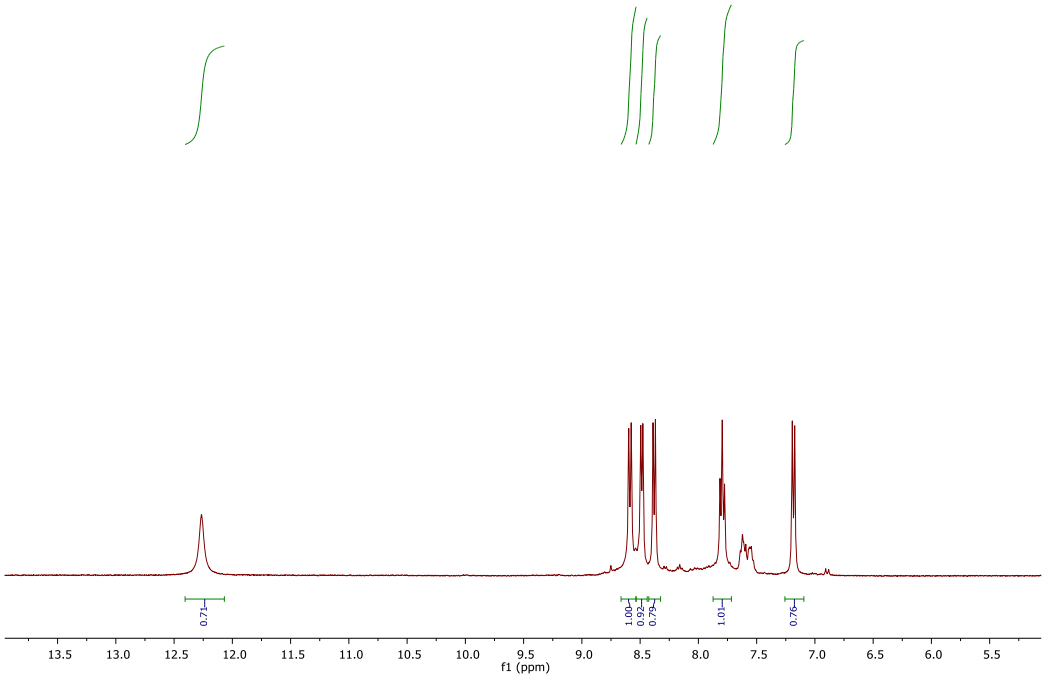

^{13}C NMR (100 MHz, DMSO-d_6)

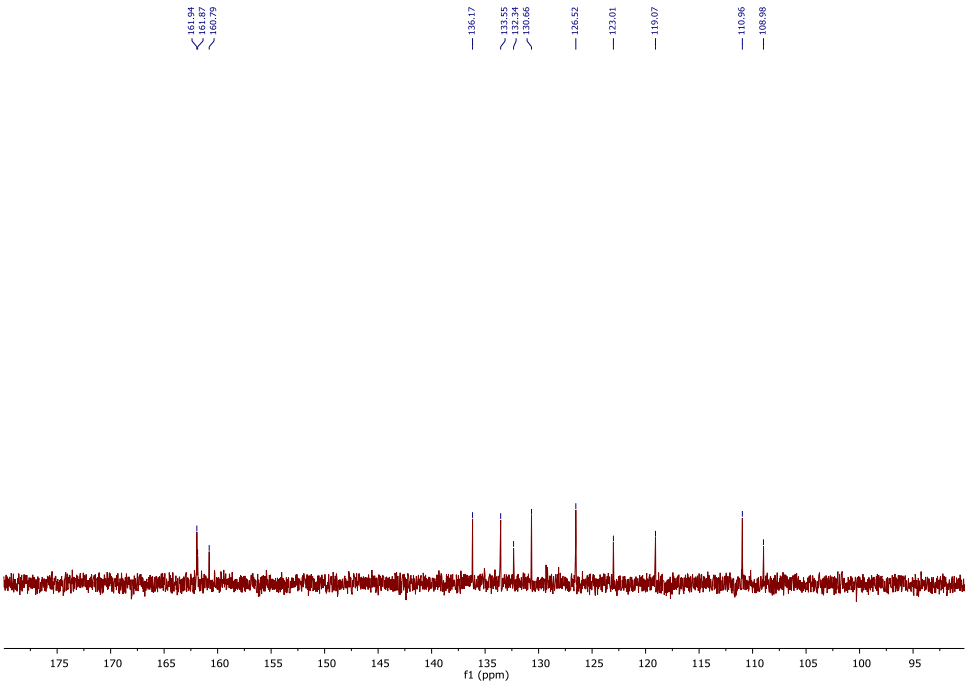

tert-Butyl (3-(6-hydroxy-1,3-dioxo-1H-benzo[de]isoquinolin-2(3H)-yl)propyl)carbamate 83

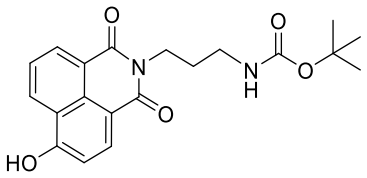

^{1}H NMR (400 MHz, $CDCl_3$)

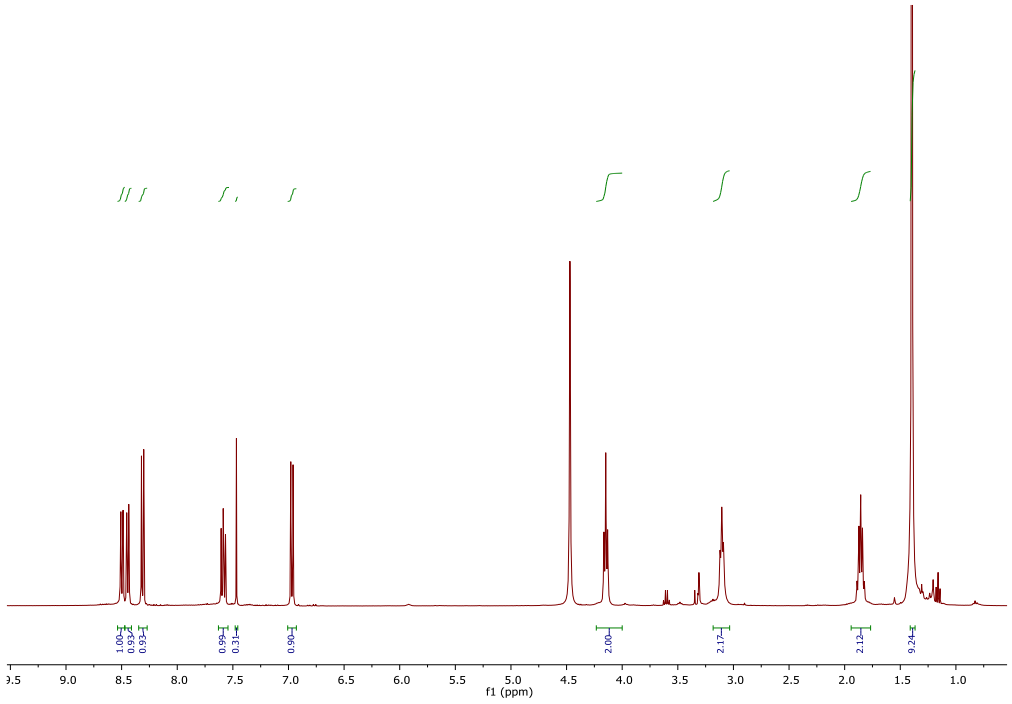

^{13}C NMR (100 MHz, $CDCl_3$)

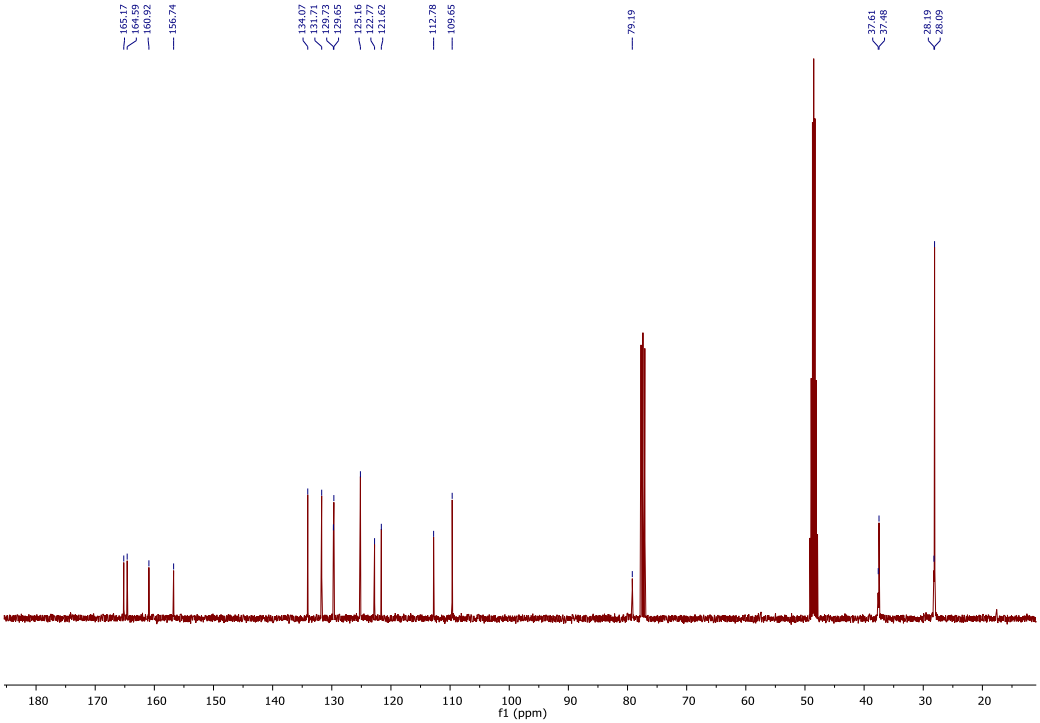

2-(3-aminopropyl)-6-hydroxy-1H-benzo[de]isoquinoline-1,3(2H)-dione hydrochloride 84

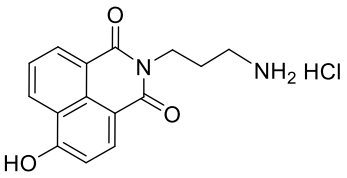

^{1}H NMR (400 MHz, D_2O)

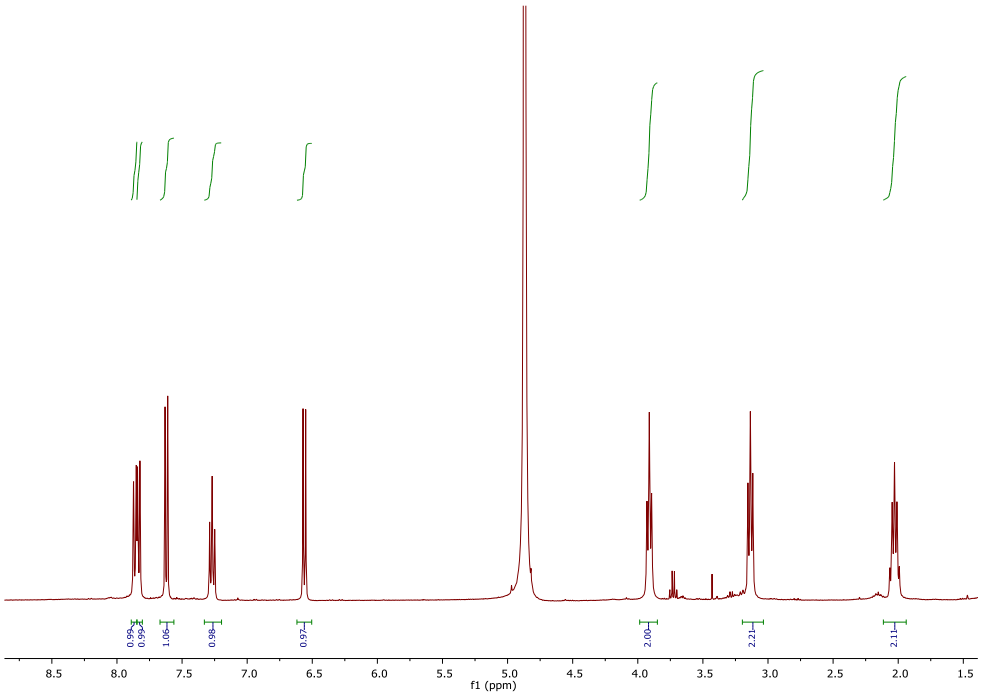

^{13}C NMR (100 MHz, D_2O)

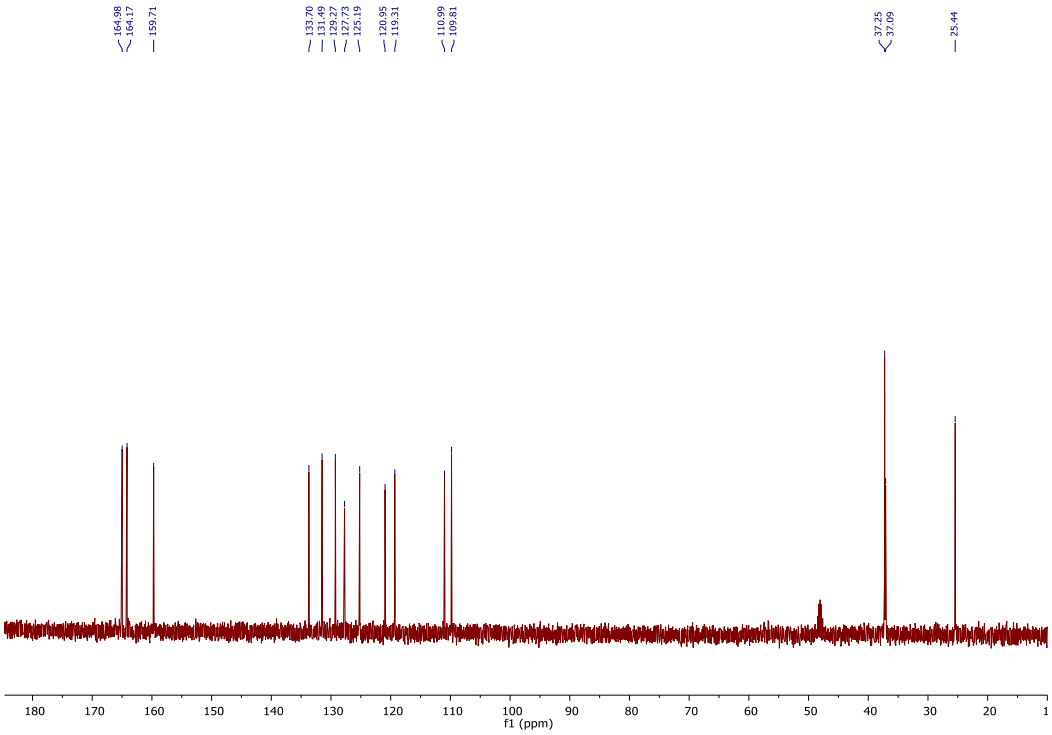

Napthalimide 85

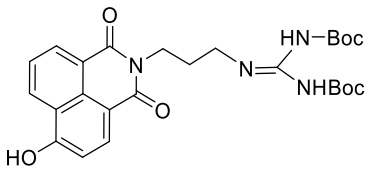

^{1}H NMR (400 MHz, $CDCl_3$)

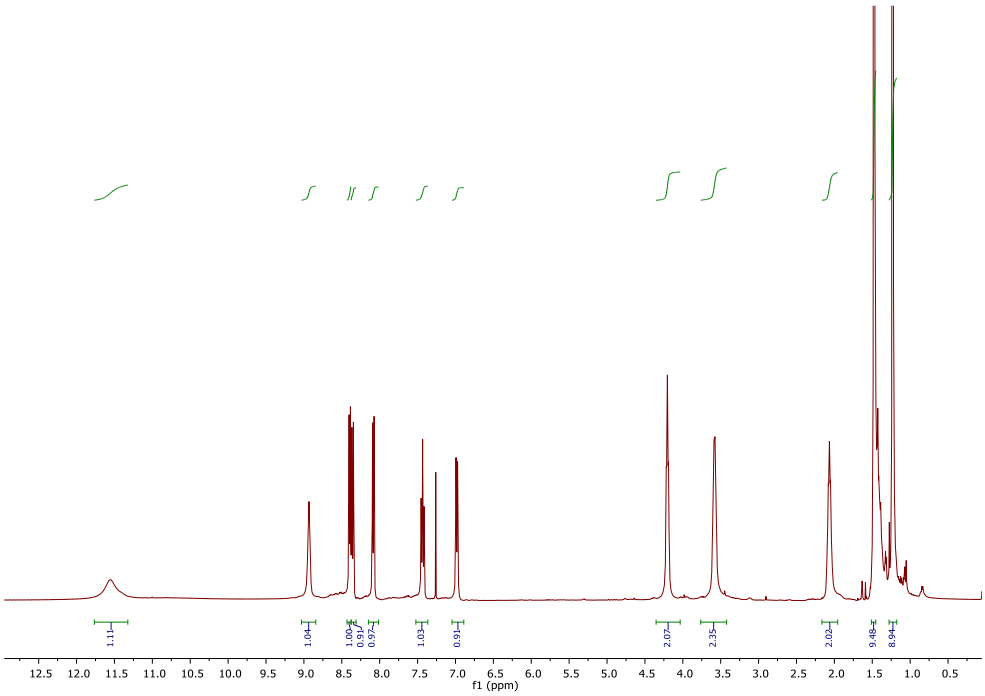

^{13}C NMR (100 MHz, $CDCl_3$)

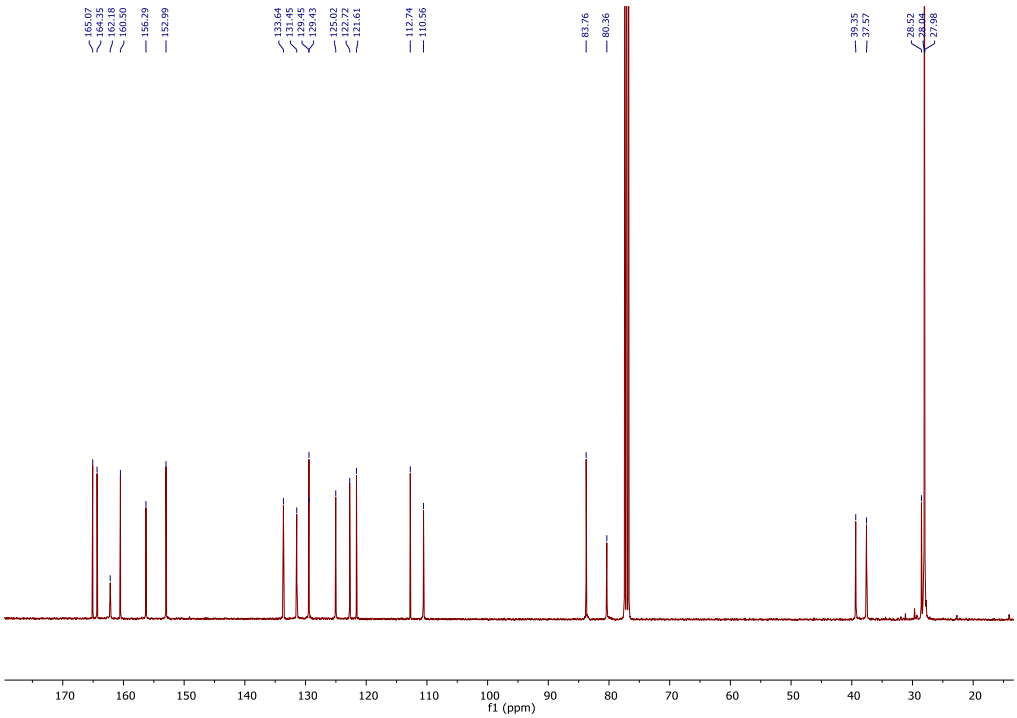

Napthalimide 86

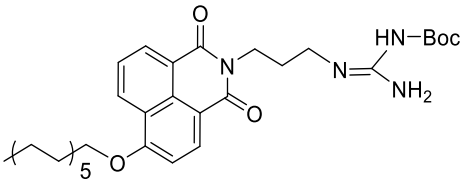

^{1}H NMR (400 MHz, $CDCl_3$)

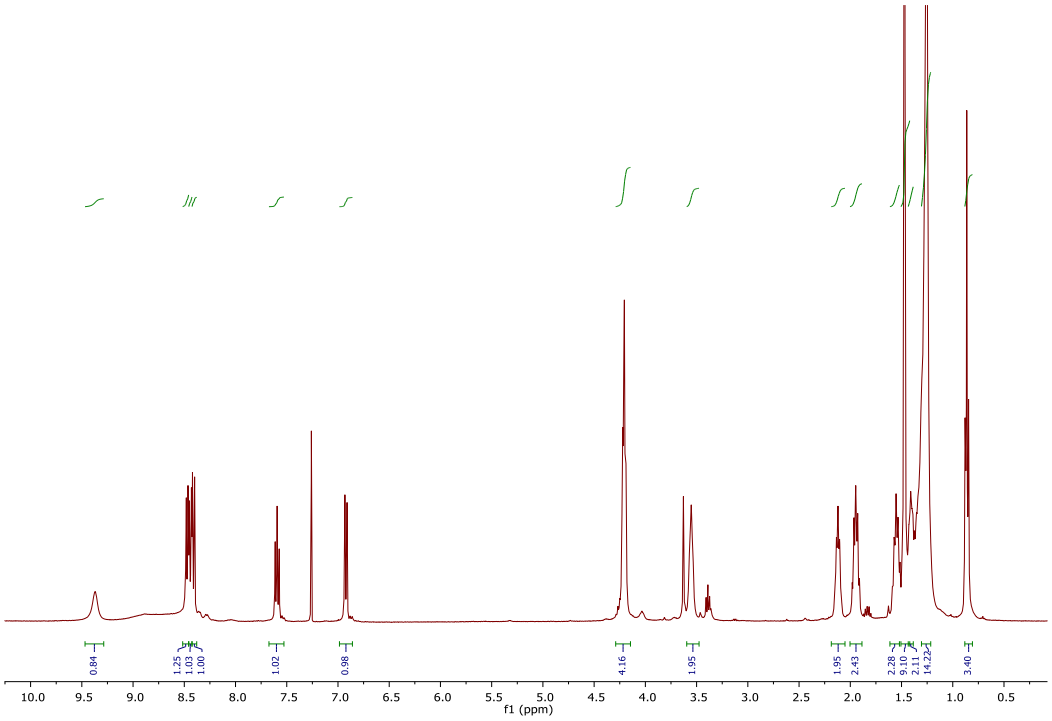

^{13}C NMR (100 MHz, $CDCl_3$)

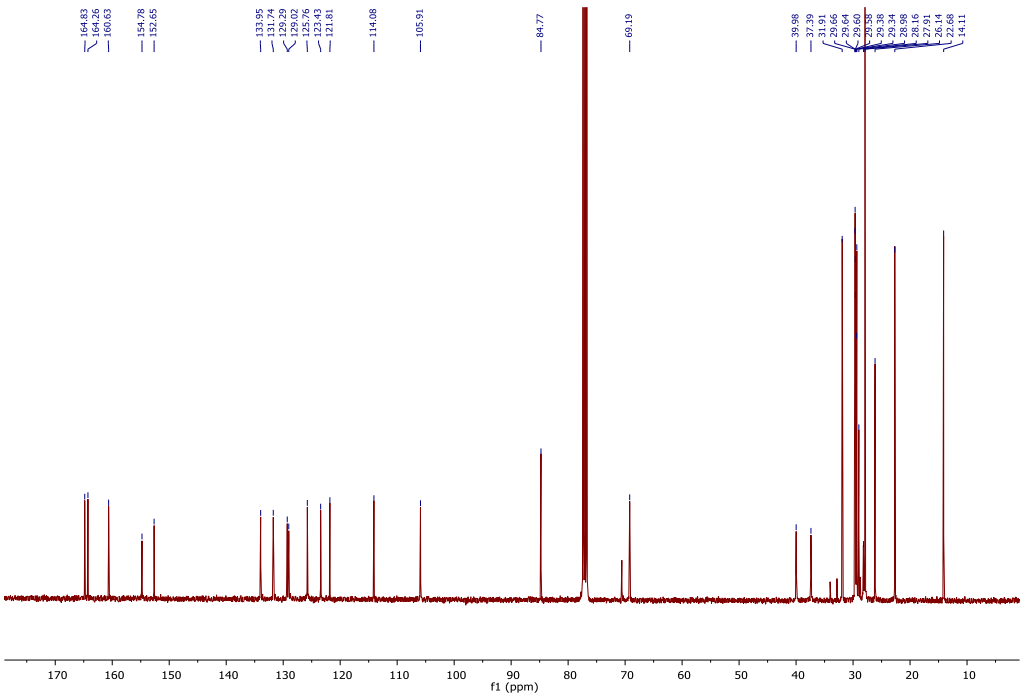

2-(3-(6-(Dodecyloxy)-1,3-dioxo-1H-benzo[de]isoquinolin-2(3H)-yl)propyl)guanidine dihydrochloride 55

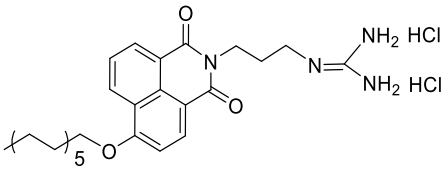

^{1}H NMR (400 MHz, CD_3OD)

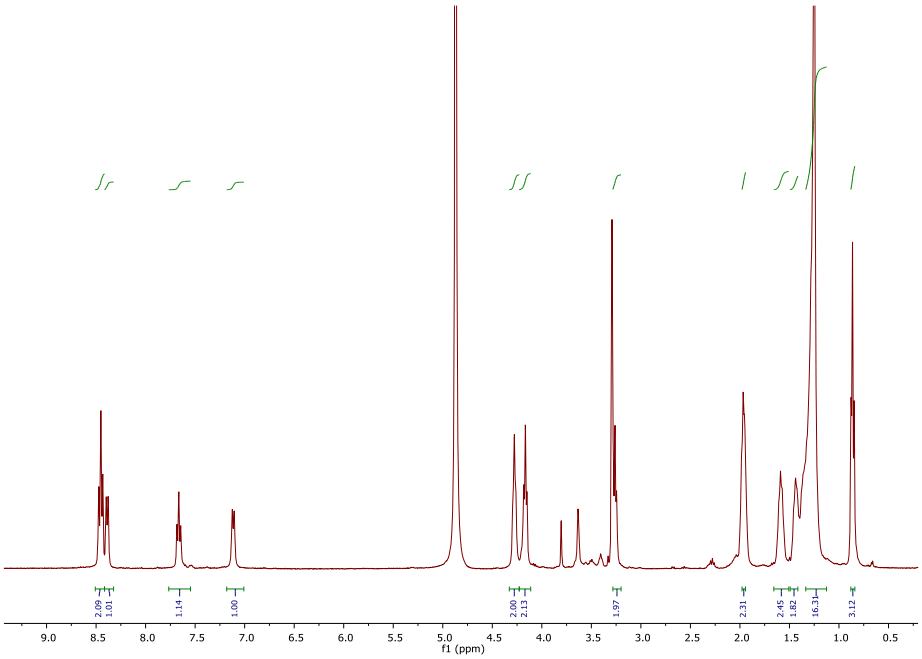

^{13}C NMR (100 MHz, CD_3OD)